

DISCOTIC COLLOIDS

A Dissertation

by

ANDRES FERNANDO MEJIA MEJIA

Submitted to the Office of Graduate Studies of
Texas A&M University
in partial fulfillment of the requirements for the degree of

DOCTOR OF PHILOSOPHY

Chair of Committee,	Zhengdong Cheng
Co-Chair of Committee,	M. Sam Mannan
Committee Members,	Abraham Clearfield
	Victor Ugaz
Head of Department,	M. Nazmul Karim

August 2013

Major Subject: Chemical Engineering

Copyright 2013 Andres Fernando Mejia Mejia

ABSTRACT

Many materials and biological systems in nature are suspensions composed of disks, such as clay, asphaltenes, and red blood cells. Despite their natural abundance and wide industrial application, disks are least studied compared to spheres and rods, due to the lack of model systems. In our research, disks at micro-scale were mass-produced with unprecedented uniformity in size and shape, and unique flexibility in the control of lateral size, lateral size polydispersity, shape, and aspect ratio (ξ = diameter/thickness). This dissertation focuses on two main areas: the study of the discotic colloidal liquid crystal phase transitions and the application of disk-like colloidal systems as Pickering emulsion and Pickering foam stabilizers.

First, we engineered two discotic colloidal systems made from organic and inorganic materials. The former is made of α -eicosene, which is an alkene of 20 carbons. The latter is composed of nano-sheets from exfoliated zirconium phosphate (α -ZrP). Both discotic systems were used to experimentally investigate the liquid crystalline phase transitions (Isotropic-Nematic, Isotropic-Cubic and Isotropic-Columnar). Also, the nematic crystalline phase was studied in detail by embedding it in a translucent and thermo-sensitive hydrogel. This was possible since nematic textures could be formed instantly by ZrP nano-sheets due to their high diameter-thickness ratio.

Second, we developed Pickering emulsions and Pickering foams stabilized by high-aspect-ratio nano-sheets. We have also demonstrated for the first time the fabrication of the thinnest amphiphilic Janus and Gemini nano-sheets, which are either

surface- or edge-modified plates with a thickness at atomic scale. These nano-sheets were obtained by exfoliating α -ZrP crystals grafted with a coupling agent of hydrophobic molecules on their edges and outer surfaces. Extending this work, we studied crucial fundamental mechanisms that allow Pickering interfacial stabilization, including the effect on the adsorption properties of particle aspect ratio, concentration, and hydrophobicity. Our study is of great interest in the scientific community due to the difficulty in generating a discotic colloidal system of controllable parameters.

To

God

My parents Julio and Olga

My siblings Olga, Carlos and Paquita

The love of my life Diana

ACKNOWLEDGEMENTS

There are many people who have contributed and made an impact on the development of this work. I would like to thank every person that was part of Dr. Cheng's group during the last four years; each one of them has helped me learn in one way or the other. I would like to especially thank my lab mates Dr. Srinivasa Pullela, Dr. Peng He, Dr. Peng Lian, Dr. Jingyi Shen, Dr. Ya-Wen Chang, Dr. Karym Kinnibrugh, Dr. Nasser Alenzi, Dr. Min Shuai, Yi-Hsien Yu, Xuezheng Wang, Ilse Nava, Yuly Lopez, and Scott Henderson for many interesting discussions, and their friendship. I would also like to acknowledge Ratna Ng, Juan Sebastian Guevara, Michael Simonetty, Peter Nguyen, Emma Risinger, Elliott Joo, and Mark Netemeyer for their valuable help, which was crucial for the development of part of this work.

I am very grateful to my advisor, Dr. Cheng, for sharing his enthusiasm for science and inspiring a bit in me, and for giving out all the knowledge possible every time.

I am highly thankful to my co-advisor, Dr. M. Sam Mannan, for his personal advice during my PhD and financial support through the Mary Kay O'Connor Process Safety Center.

Additionally, I would like to thank the members of my committee, Dr. M. Sam Mannan, Dr. Abraham Clearfield, and Dr. Victor Ugaz for their assistance, interest, and time through the completion of this work.

I would like to express my sincere gratitude to Mr. Randy Marek and his undergraduates of the machine shop who helped me on designing and repairing our autoclaves.

Finally, I would like to thank my parents Julio Eduardo Mejia and Olga Maria Mejia for their always unconditional support and freedom throughout the years, which has been essential in making difficult decisions that come with every undertaking. I would like to thank my sister Olga Liliana Mejia and my brother Carlos Eduardo Mejia for being my role models and inspiration throughout my life. I would also thank to my American family Majdi Alkarmi, Donna Alkarmi, Nathan Massotti, Amanda Massotti, Laith Alkarmi, and Pele.

Especially, I would like to thank my girlfriend, Diana Castellanos, whose encouragement during hard times greatly helped me to keep perspective and move forward, for all the support given since the very beginning and until today.

TABLE OF CONTENTS

	Page
ABSTRACT	ii
DEDICATION	iv
ACKNOWLEDGEMENTS	v
TABLE OF CONTENTS.....	vii
LIST OF FIGURES.....	x
LIST OF TABLES	xxi
CHAPTER I INTRODUCTION	1
1.1 Colloids of Different Shapes	1
1.2 Fabrication.....	4
1.2.1 Colloidal Disks	4
1.2.2 Monolayers from Inorganic Lamellar Crystals	13
1.3 Discotic Liquid Crystals.....	16
1.3.1 Theoretical Approximations.....	18
1.3.2 Computer Simulations	20
1.3.3 Experimental Work	26
1.4 Applications of Discotic Colloids	34
1.4.1 Interfacial Stabilizers.....	34
1.4.2 Polymer Composite Nanofillers	36
1.4.3 Rheological Modifiers.....	37
1.4.4 Manipulation of Liquid Crystals Using External Forces.....	38
1.4.5 Catalytic Frameworks.....	40
1.5 Summary and Conclusions.....	40
1.6 Outline of the Dissertation	41
CHAPTER II LOW ASPECT RATIO COLLOIDAL DISKS	43
2.1 Synopsis	43
2.2 Uniform Discotic Wax Particle Synthesis by Electrospray Emulsification	44
2.2.1 Introduction	44
2.2.2 Materials and Methods	47
2.2.3 Results and Discussion.....	49
2.2.4 Summary	61

2.3 Surface-controlled Shape Design of Discotic Micro-particles.....	62
2.3.1 Introduction	62
2.3.2 Experimental	65
2.3.3 Discussion	70
2.3.4 Summary	88
 CHAPTER III HIGH ASPECT RATIO COLLOIDAL DISKS	 89
3.1 Synopsis	89
3.2 Aspect Ratio and Polydispersity Dependence of Isotropic-nematic Transition in Discotic Suspensions	90
3.2.1 Introduction	90
3.2.2 Previous Results from Simulations	96
3.2.3 Experimental Results with Monolayers of α -ZrP.....	100
3.2.4 Summary	115
3.3 Thermo-responsive Discotic Nematic Hydrogels	117
3.3.1 Introduction	117
3.3.2 Experimental	121
3.3.3 Results and Discussion.....	124
3.3.4 Summary	134
 CHAPTER IV INTERFACIAL STABILIZATION USING NANO-SHEETS	 136
4.1 Synopsis	136
4.2 Pickering Emulsions Stabilized by Amphiphilic Nano-sheets.	137
4.2.1 Introduction	137
4.2.2 Experimental	142
4.2.3 Results and Discussion.....	145
4.2.4 Summary	161
4.3 Stabilization of Pickering Foams by High-aspect-ratio Nano-sheets.....	163
4.3.1 Introduction	163
4.3.2 Experimental	166
4.3.3 Results and Discussion.....	170
4.3.4 Summary	188
 CHAPTER V CONCLUSIONS AND FUTURE WORK	 190
5.1 Summary	190
5.2 Future Research and Ongoing Projects	193
5.2.1 Liquid Crystalline Phase Behavior of Zirconium Phosphate - Silica Suspensions	193
5.2.2 Phase Behavior and Self-assembly of Wax Disks and SDS Micelles.....	197
 REFERENCES	 203

APPENDIX A ADDITIONAL FIGURES FOR CHAPTER II	238
APPENDIX B ADDITIONAL FIGURES FOR CHAPTER IV	242
APPENDIX C PEER-REVIEWED PUBLICATIONS.....	253

LIST OF FIGURES

	Page
Figure 1. Different length scales in the world.....	2
Figure 2. Phases for spheres, rods, and disks <i>versus</i> concentration.....	4
Figure 3. Representative examples of recently synthesized colloidal disks. α -Eicosene disks synthesized via shape-change of wax emulsions having an aspect ratio of (a) ~ 2 , (b) ~ 4 . (c) and (d) Lithographically designed colloidal disks. (e) Custom-shaped microscale pentagonal Lithoparticles. (f) Replicated hydrogel red blood cell-like discotic microparticles synthesized via non-wetting templates (PRINT®) technique. (g) Toroidal particles via solidification of a polymer solutions. (h) Red blood cell-like polymer particles via consolidation of charged droplets. (i) Disk-like polymer particles produced by seeded dispersion polymerization method of methacrylate and polystyrene seeds.....	6
Figure 4. Colloidal disk-like systems. (a) γ -Al(OH) ₃ , (b) Co, (c) Ni(OH) ₂ , (d)LaF ₃ , (e) Ag-SO, and (f) Cu ₂ S colloidal nano-platelets.....	11
Figure 5. Discotic liquid crystalline phase diagram and states. (a) Discotic phase diagram predicted by Veerman and Frenkel ¹³⁹ (b) Schematic representation of nematic, columnar, and smectic states for plate-like particles (c) ZrP I-N transition (d) Gibbsite plate-like suspensions present I-N, N-C and C textures (e) White and crossed polarized light of a gibbsite platelet suspension presenting a triphasic (I-N-C) transition via ion screening and sedimentation (f) Representation of OHSC particles at the cubic phase (g) Cubic phase of nickel hydroxide platelets (h) Columnar phase ordering of nickel hydroxide platelets (i) Copper sulfide nanodisks stacked in a columnar state.....	25
Figure 6. Applications of discotic colloidal systems. (a) Optical micrograph of a Pickering emulsion stabilized by Janus and Gemini nano-sheets of ZrP. (b) SEM image of a Pickering foam stabilized by amphiphilic and high-aspect-ratio ZrP nano-sheets. (c) TEM micrograph of an epoxy/ α -ZrP nanocomposite. (d) Magnetic-field-induced birefringence in the isotropic phase of a gibbsite platelet suspension at horizontal magnetic fields of 0, 0.5, 1, 1.5, and 2 T, respectively. (e) SEM image (top view) of an uniform and well-packed deposit composed of highly-oriented nano-sheets made by filtration of an MFI nano-sheet suspension through an anodized alumina membrane (pore size of ~ 200 nm).....	34

Figure 7. Electrospray emulsification. (a) Schematic setup. A strong electric field is generated between a capillary needle and a ground wire-ring. The collection fluid is heated to tune the density and surface tension, and stirred to facilitate drop entrainment. (b) Micrograph showing a stable cone-jet mode of electrospray captured by a fast camera.....	48
Figure 8. Size control of emulsions with flow rate. Data are plotted for size variation of wax droplets by flow rate from 1 ml/h to 30 ml/h. The line is the power law fitting to the data, $d = (2.1 \pm 0.2)Q^{0.38 \pm 0.03}$	50
Figure 9. Polydisperse wax emulsions when the density and the surface tension of wax mismatch that of the continuous phase. (a) Size polydispersity is evidenced when wax droplets are collected in solution. (b) Droplet size distribution. The polydispersity is estimated as high as 25%. The collection fluid is 20 mM SDS aqueous solution. The flow rate is 4 ml/h and the applied voltage is 2.8 kV.	51
Figure 10. Monodisperse wax emulsions produced with a collection solution of 80 %wt. ethanol, 20 %wt. water, 0.005 %wt. of Tergitol 15-S-9 and 20mM SDS. The flow rate is 4 ml/h and the voltage is 2.8 kV. (a) Micrograph of the hexagonal lattices of emulsion droplets confirms size uniformity. (b) Droplet size distribution measured by dynamic light scattering. The diameter of the droplets is $1.02 \pm 0.03 \mu\text{m}$, and the polydispersity is $2.7 \pm 0.1\%$ (Standard deviation of the size distribution divided by the mean size).....	53
Figure 11. Time sequential optical microscopy images of wax particles after 36 hour-storage at 4°C. The disks (No. 1, 2, 3, 5 and 6) are uniform and have the same inversed aspect ratio of about 1:2. Some of the particles (No. 4 and 7) were still in a spherical shape. Time interval between two consecutive images is 2 seconds.....	55
Figure 12. The dependence of shape changing time as a function on the initial size of emulsions. (a) Apparent size of the disks measure by DLS in the course of shape changing. The solid line is the exponential growth fit to the data: $D = (341.5 \pm 4.8) - (61.2 \pm 10.5) \exp\left(-\frac{\tau}{1.28 \pm 0.52}\right)$ (b) Shape changing time as a function of initial emulsion size.	57
Figure 13. Columnar morphology of rods that are stacked from the wax disks. (a)(b) Rods from polydisperse disks fabricated by emulsification with variation in flow rates. (c)(d) Rods from uniform disks fabricated by emulsification with the same flow rate (4 ml/h).....	57

Figure 14. Self-assembling of micro wax disks observed by evaporating a droplet. (a) A droplet of homogeneous suspension was deposited on a glass slide under observation of a polarized optic microscope. Solvent-evaporation starts once the drop is placed on the slide. (b) Influenced by Marangoni's effect, the colloidal disks are taken into the center of the droplet by convection as indicated on the top panel. (c) The evaporation of the droplet continues and the concentration of disks and SDS become higher. Depletion attraction between disks due to the high concentration of SDS micelle leads to the formation of a condensed phase. (d) The disks start to self-assemble into rods inside the condensed phase and flow out. (e) Rods suspension is finally formed toward the end of the evaporation. Pictures below the schematics are cross-polarization optical microscopic images near the top center of the drop. 60

Figure 15. Biconcave α -eicosene disks. Dimples are visible on the circular faces of the disks, indicated by the arrows. Short stacks of the disks are observed as well. (See supplementary Figure A1a for the Brownian motion of a disk.) These disks have an aspect ratio ξ about 2, with $\xi = \text{diameter}/\text{thickness}$, and a single defect of a focal conic domain (FCD). See Figure 17c and supplementary Figure A2 for the defect configurations of a layered structure.) The micrograph was taken at room temperature using a Nikon microscope TE-2000U with magnification 60 \times 64

Figure 16. Biconcave α -eicosene disks. (a) Confocal micrographs. Biconcave disks coated with Nile red are displayed as rings. Magnification 60 \times . (b) Confocal reflective image at the same position as (a). (c) The spindle torus that represents the surface coating of the Nile red dye on the disks. The dimples of the torus appear as black dots on the circular faces in Figure 15. (d) Sequential confocal images cutting through a single disk. Magnification 150 \times . (d') Regenerated image slices using Matlab from a tiled spindle torus as illustrated in (c), where gray stripes stand for imaging slices. (a),(b) and (d) were taken at room temperature using a Leica confocal microscope TCS SP5. 66

Figure 17. Coalescence of two biconcave colloidal disks into a flat disk. (a) The disks were attracted to each other at high sample SDS concentrations. Temperature was raised and lowered for several times between 20 $^{\circ}\text{C}$ and 60 $^{\circ}\text{C}$, cycling above and below the melting point of α -eicosene ($T_m=26^{\circ}\text{C}$). This procedure produced disks of a larger volume with a larger aspect ratio, $\xi=4$, than the original biconcave disks with $\xi=2$. (b) Disk obtained after temperature oscillations. Images were taken of a single disk at different times to examine the shape from various view angles. The first two images are optic micrographs, and the third image is a polarizing microscope micrograph. Images were taken at room temperature using 20 \times lens. (c)

Illustration of the FCD defect of the layered structure of a biconcave disk. Molecules in the rotator phase pack into layers, in which they rotate freely. (d) Illustration of the $+\pi$ edge disclination loop defect of the flat disk.68

Figure 18. Flat disks. Disks have an aspect ratio of $\xi = 4$. (a) Disks begin to stack into rods at relatively dilute concentration comparing to the biconcave disks. Magnification 60x. (b) AutoCAD illustration of disk stacking. Disks are brighter due to their inclination at the end of the stack as observed in (a). (c) Confocal micrograph of rods formed at a high disk concentration. Magnification: 60x. Figure 18a and Figure 18c were taken at room temperature. Figure 18a and Figure 18c were taken using confocal microscopy (TCS SP5, Leica).69

Figure 19. The morphology control of colloidal disks by varying surfactant composition. Decanol increases the surfactant molecular packing density at the wax-water interface and lowers the curvature c_0 of the interface. The particles are composed of equidistant layers in topological equivalence to a sphere of concentric layers. Without decanol, the spontaneous curvature c_0 is larger than c_0^* , and the surface membrane of the particle takes a torus structure due to the FCD defect (note the dimples on the circular surfaces, see supplementary Figure A1a). With enough decanol, the spontaneous curvature is reduced to be smaller than a critical value c_0^* , and the disk assumes the flat coin-like shape with the $+\pi$ disclination loop defect⁴²³ (Supplementary Figure A2b). The aspect ratio of the particles increases if the surface tension $\sigma_{||}$ is reduced by the addition of decanol. The scale bar is 4 μm . Images were taken at room temperature using confocal microscopy (TCS SP5, Leica) with 100X lens. Note: $c_{o \text{ SDS only}} > c_{o \text{ 10:1}} > c_{o \text{ 1:1}}$ 76

Figure 20. Structure of the wax particles. (a-c) The surface membranes formed by surface freezing. (a) and (b) are biconcave membranes and (c) is flat membrane. (d) Biconcave disk geometry with FCD region (I), flat surface region (II) and $+\pi$ edge disclination region (III). The radial lengths of the FDC region and the flat region are $a/2$ and l , respectively. (a) is the surface for particles with $l = 0$ and (c) is the surface for particles with $a = 0$. (e) Flat disk geometry with the same thickness and lateral size as the biconcave disk shown in (d), divided into three corresponding regions.77

Figure 21. Dependence of the alkene/liquid interfacial tension (a) and the aspect ratio on decanol/SDS composition (b). The aspect ratio of the disks was measured using their phase transition by dynamic light scattering. The solid line is a polynomial fit.80

Figure 22. Correlation between aspect ratio and interfacial surface tension. The solid lines are fittings to the theoretical prediction (Eq. 17). The triangles are the

experimental data. The square is for the sample using SDS only. The left regions (I and II) correspond to flat disks produced at low membrane spontaneous curvature C_o . The right region (III) represents the biconcave disks with a FCD defect due to large C_o83

Figure 23. Self-assembly of colloidal disks due to depletion attraction. (a) Cross-polarizing micrograph of rods formed at a high flat disk concentration. Magnification 20x. (b) Micrograph showing the assembly of biconcave disks. The disks tend to stack at high concentration resembling the red blood cells. Magnification 35x, (c-f) Possible interactions between disks. (c) and (d) Assembly of a pair of flat and biconcave disks (e) oriented face-to-face and (f) disks oriented side-to-side. Images were taken at room temperature.84

Figure 24. Self-assembling of the flat disks in an evaporating droplet observed under cross-polarizing microscopy. Disks are fabricated using 1:10 surfactant ratio (decanol:SDS) in a 10mM SDS aqueous solution. The microdisks are uniform in diameter ($R = 4 \pm 0.25 \mu\text{m}$) and aspect ratio ($\xi = 4$). (a) Disks just after the deposition of the droplet on the glass slide. (b) Cloud of disks formed as a result of the depletion attraction. Pink color is evident under a pair of crossed polarisers. (c) Some rods started to flow out from the cloud when the droplet is flatten over the glass. (d) Alignment of rods in flow direction. (e), (f), (g) Different rod organizations are exhibited. (h), (i) Rods began to assemble side by side. Images were taken at room temperature using 20x.87

Figure 25. Phase diagrams for discotic systems in volume fraction (ϕ) versus inversed aspect ratio obtained from simulations. (a) A general diagram for cut spheres (NVT MC). The dashed lines represent simulation data reported by Veerman *et al.*, for $\xi^* < 0.1$,¹³⁹ (b) Short cylinders (Onsager-Parsons theory)¹³⁷, (c) Oblate hard spherocylinders (NPT MC),¹⁵⁹ and (d) Oblate hard spherocylinders (free energy calculations).¹⁶⁰ The insets at the bottom left of each graph illustrate the side view and the three-dimensional shape of the disks.95

Figure 26. Pristine α -zirconium phosphate crystals. Scanning electron microscope (SEM) micrographs of different ZrP sizes prepared at different conditions (a) 9M-5h, (b) 12M-5h, (c) 15M-5h, (d) 9M-24h, (e) 12M-24h, and (f) 15M-24h.99

Figure 27. Structure of zirconium phosphate crystals and the exfoliation process. (a) Structure of crystalline zirconium phosphate (ZrP). (b) Guest molecule: n-tetrabutylammonium hydroxide (TBA+OH-) (c) Schematic process of

lamellar crystals going through exfoliation by using excess of TBA. After exfoliation, monolayers were obtained having a thickness of 26.8Å. 101

Figure 28. Size distribution for exfoliated ZrP platelets as measured by DLS. Aspect ratio and polydispersity obtained are listed in Table 3. The non-fractionated and the fractionated samples are represented by the green-dashed (gray-dashed) red circles and the blue-lined (black-lined) black squares, respectively. The lines are fit to the extreme distribution function. 103

Figure 29. Suspensions of ZrP monolayers at various aspect ratios and different concentrations. (A1) through (A6) are the non-fractionated suspensions, and (B1) through (B6) are the fractionated suspensions. (C2) through (C6) are additional ZrP suspensions. Photographs were taken for samples set between cross polarizers to distinguish between upper isotropic and lower birefringent nematic liquid crystalline phase. 106

Figure 30. Cross-polarized optical microscopic images of nematic Schlieren textures at different aspect ratios. Inversed aspect ratio increases from (a) to (f) which are from samples of B1 to B6, and $\phi =$ (a) 0.0053, (b) 0.01, (c) 0.014, (d) 0.02, (e) 0.0420, and (f) 0.06. The micrographs were taken using a Nikon microscope TE-2000U with crossed polarizers. Picture of (a) was taken using 10x magnification and pictures of (b to f) using 4x magnification. 107

Figure 31. The relative fraction percentage of the nematic phase as a function of the monolayer volume fraction ϕ . (a) The non-fractionated suspensions, (b) the fractionated suspensions, and (c) the additional ZrP suspensions. Inversed aspect ratio increases from A1 to A6, from B1 to B6 and from C2 to C6. The values for inversed aspect ratio and polydispersity can be found in Table 1. 109

Figure 32. Volume fraction (ϕ) of the isotropic (solid black circles) and nematic (open red (gray) circles) volume fraction of the cloud phases as a function of polydispersity (σ) at fixed inversed aspect ratios of around (a) 0.010 and (b) 0.0020. The concentrations at zero polydispersity for both graphs were obtained from simulations of Fartaria *et al.*¹⁵⁸ The lines are guides for the eye. The solid and open blue (black) squares are the theoretical ϕ_I and ϕ_N , respectively, from Martinez-Raton *et al.*, using a DFT calculation with Zwanzig approximation.¹⁶⁸ The solid and the open purple (black) diamonds are the theoretical ϕ_I and ϕ_N , respectively, from Frenkel *et al.*, for infinitely thin plates.³³⁵ 111

Figure 33. Comparison of the experimental ϕ_I and ϕ_N and simulation data. a) Linear-log diagram illustrating the correspondence of the ϕ_I with the Onsager-

Parson theory and the OHSC free energy calculations. The difference in ϕ_N is due to effect of polydispersity of the ZrP platelets. The lines are guides for the eye. b) Log-log diagram showing power law scaling of inversed aspect ratio for $\phi_{I, i, ii \text{ and } iii} = 23.1 \pm 8.1(\xi^*)^{1.36 \pm 0.10}$, and $\phi_{N, i} = 115.5 \pm 78.6(\xi^*)^{1.41 \pm 0.20}$, $\phi_{N, ii} = 68.6 \pm 48.3(\xi^*)^{1.36 \pm 0.10}$, and $\phi_{N, iii} = 36.9 \pm 6.9(\xi^*)^{1.32 \pm 0.04}$ for groups i, ii and iii, confirming that the width of the biphasic transition is affected by aspect ratio and polydispersity. 112

Figure 34. The study of ZrP isotropic-nematic (I-N) transition (a) ZrP-embedded PAAm-PNIPAm hydrogel. Schematic representation of ZrP nano-sheets dispersed in solvent between PAAm and PNIPAm polymer networks. (b) Transmission electron micrographs (TEM) of ZrP nano-sheets. (c) The discotic I-N phase diagram of ZrP nano-sheets. The sequence, left to right, corresponds to nano-sheet volume fractions of $\phi_{ZrP} = 0.0037, 0.0045, 0.0047, 0.0053, 0.0078,$ and 0.0093 respectively. (d) The nematic percentage as a function of volume fraction depicting the I-N transition. The arrows indicate the isotropic (ϕ_I) and nematic (ϕ_N) volume fraction transitions. 121

Figure 35. Schlieren texture of ZrP nano-sheet having a size of 2436 ± 562 nm (a) in aqueous suspension at $\phi_{ZrP} = 0.010 \pm 0.001$ and (b) in PNIPAm-PAAm hydrogel at $\phi_{ZrP} = 0.023 \pm 0.001$ 124

Figure 36. The effect of initiator (APS) and catalyst (TEMED) on the texture of the nematic hydrogels. (a) Crossed polarized pictures of the nematic hydrogels at various initiator and catalyst concentrations. The ZrP nano-sheet volume fraction is $\phi_{ZrP} = 0.0035 \pm 0.0005$. The scale bar is 1 cm. (b) Plot of the number of nematic domains as a function of catalyst concentration. The black squares, red circles, blue triangles and pink diamonds correspond to an initiator concentration of $0.5 \pm 0.1, 1.0 \pm 0.1, 1.5 \pm 0.1$ and 2.0 ± 0.1 %wt., respectively. 126

Figure 37. Crossed polarizing images of several nematic ZrP suspensions and hydrogels at different ZrP nano-sheet concentrations. (a) Discotic I-N phase transition of ZrP nano-sheet in aqueous suspensions. From left to right, the ZrP nano-sheet concentration corresponds to $\phi_{ZrP} = 0, 0.0037, 0.0045, 0.0047, 0.0053, 0.0078,$ and 0.0093 . (a') Nematic hydrogels at the same concentration as (a). (i) At room temperature. (ii-iv) Volume shrinking of the nematic hydrogels at 333 K after 5, 48, and 310 h, respectively. The scale bar is 2 cm. (b) Normalized hydrogel volume as a function of time for samples in (a'). 127

Figure 38. Birefringent color pattern variation due to temperature-shrinkage of the polymer hydrogels. The incrementing of ϕ_{ZrP} and S_2 during hydrogel

collapsing initiated a birefringent color transition in the hydrogels. The samples contains a ZrP volume fraction (ϕ_{ZrP}) of: (a) 0.0045 (b) 0.0047, and (c) 0.0093. The scale bar is 0.5 cm. The samples were stored at 333 K. 131

Figure 39. Time-sequential crossed polarized optical microscopy images of a sealed capillary tube containing ZrP nano-sheet hydrogels at $\phi_{\text{ZrP}} = 0.0030 \pm 0.0005$ during deswelling and swelling. (a-f) Deswelling of the nematic hydrogel at 333 K. At the edge, the isotropic-to-nematic transition takes place as evidenced from the visualization of nematic defects. Defects of +1 and -1 are characterized from their four lobes. (g-l) Swelling of the nematic hydrogel at ambient temperature. Reversible nematic-to-isotropic transition occurs as the concentration of ZrP nano-sheets on the hydrogel edge decrease during water absorption. 133

Figure 40. The α -zirconium phosphate crystals. (a) SEM micrograph. (b) Zoomed view of a particular crystal showing cracks along the lamellar layers. (c) Idealized structures of the alpha phase of zirconium phosphate (α -ZrP). 139

Figure 41. FTIR of α -Zirconium phosphate surface with grafted octadecylisocyanate groups. (1) α -ZrP, (2) octadecyl isocyanate, and (3) the grafted product..... 146

Figure 42. XPS and TGA spectra of the product obtained from the reaction of ODI with α -ZrP (a). Deconvolution of the C(1s) spectrum exhibits three peaks, consistent with the presence of the N-C(=O)- and carbon atoms. (b) N(1s) spectra. (c) The thermal stability of pristine α -ZrP (blue line) and α -ZrP grafted with ODI (green line) analyzed by TGA. 148

Figure 43. Characterization of stable emulsions stabilized by α -ZrP-ODI nano-sheets and unstable emulsions using non-modified α -ZrP nano-sheets. Representative (a) optical micrograph and (b) confocal laser scanning micrograph of o/w emulsions using α -ZrP-ODI as surface-active agents. (c) Observation of o/w emulsions stabilized by non-modified α -ZrP monolayers. The emulsion coalesced and quickly creamed. (d) Optical micrographs of the o/w emulsion right after emulsification and (e) after 24 days, which indicates that non-modified α -ZrP nano-sheets are not good emulsifiers due to the observed coalescence. (f) Creaming of o/w emulsions stabilized by α -ZrP-ODI nano-sheets. The emulsion presents less creaming compared to (c) due to the less degree of coalescence. (g) Micrograph showing the oil-in-water droplets after emulsification. (h) o/w emulsion micrograph from the top and (i) from the middle after 24 days, where no coalescence was observed. Pictures of (a, d, e, g, h, and i) were taken using a Nikon microscope TE-2000U with 20x magnification. (b) was taken using a Leica confocal microscope TCS SP5 with magnification of 100x. (c and f)

digital photographs were taken using a Sony DSC-220W digital still camera.....	152
Figure 44. (a) Toluene-in-water emulsion droplet diameter as a function of α -ZrP-ODI nano-sheet concentration after one week. The toluene volume fraction is $\phi_o=0.085$. (b) Droplet diameter of toluene-in-water emulsions as a function of time. The concentration of α -ZrP-ODI nano-sheets is 0.45 wt. %.....	153
Figure 45. Toluene-in-water emulsions stabilized by α -ZrP-ODI and non-modified α -ZrP nano-sheets, where toluene concentration was $\phi_o=0.12$. (a) Micrograph of uniform toluene-in-water droplets stabilized by α -ZrP-ODI nano-sheets. The diameter of the droplets is $3.05 \pm 0.42 \mu\text{m}$. (b) Micrograph of polydispersed toluene-in-water emulsion droplets stabilized by non-modified α -ZrP nano-sheets. (c) Toluene-in-water emulsions stabilized by non-modified α -ZrP (right) showing strong creaming due to large drop size and stabilized by α -ZrP-ODI nano-sheets (left) with a less creaming effect. The picture is taken at 200 h after emulsification.....	155
Figure 46. Pickering miniemulsion polymerization of styrene using α -ZrP-ODI nano-sheets as stabilizers. Average polystyrene particle diameter as a function of weight percent of platelets.....	157
Figure 47. Polymerization of Pickering miniemulsions of styrene-in-water. (a) SEM image of platelet-armored-polystyrene particles. (b), (c) and (d) TEM images of nano-sheet-armored polystyrene particles.	159
Figure 48. Concentration of amphiphilic nano-sheets on the surface ($C_{surface}$) vs. total concentration of platelets (C_o).	161
Figure 49. Pristine α -ZrP crystals. Transmission (a) and scanning (b, c) electron microscope micrographs of different ZrP sizes prepared at varying conditions (a) 3M-24 h (RM). (b) 15M-5h (HM), and (c) 15M-24 h (HM). (d) Size distribution of the ZrP crystals fabricated at different reaction conditions.....	167
Figure 50. Effect of ZrP-PA nano-sheet concentration on foam stabilization. (a) Aqueous foams 7 days after preparation as a function of ZrP-PA nano-sheet concentration. The nano-sheet suspension of batch A were used in this experiment at a PA:ZrP molar ratio of 2.16 ± 0.05 . The nano-sheet concentrations are 0.5 ± 0.1 , 1 ± 0.1 , 1.5 ± 0.1 and 2 ± 0.1 % wt. (b) Foam volume as a function of nano-sheet concentration at different times after preparation. The green apex-down triangles, blue triangles, red circles, and black squares correspond to 0, 60, 150, and 270 min., respectively. Lines are guide to the eye.....	170

- Figure 51. Foams stabilized by ZrP-PA nano-sheets using (a) batch A (b) batch B, and (c) batch C, for different PA:ZrP molar ratios at 1 h and 7 days after foam stabilization. The concentration of ZrP-PA nano-sheets is 2 ± 0.1 % wt. 172
- Figure 52. Aqueous foam stability at varying nano-sheet aspect ratio and PA:ZrP molar ratio. (a1–e1) Foam and (a2–e2) drainage volume as a function of time. The black squares, red circles and blue triangles correspond to batches A, B, and C, respectively. The PA:ZrP molar ratios were set to (a) 1.32 ± 0.05 , (b) 1.53 ± 0.05 , (c) 1.74 ± 0.05 , (d) 1.95 ± 0.05 , and (e) 2.16 ± 0.05 173
- Figure 53. The two-time scales, t_1 and t_2 , observed during water drainage as a function of the PA:ZrP molar ratio at different aspect ratios. (a) Creaming and (b) Coarsening time. The black squares, red circles, and blue triangles correspond to batches A, B, and C, respectively. 177
- Figure 54. Foam decay (red squares) and water drainage rate (blue triangles) as a function of PA:ZrP molar ratio of aqueous foams obtained from nano-sheet suspensions of batch (a) A (b) B, and (c) C. The foam decay and water drainage rate were calculated from the foam and water volume at the 10th day with respect to the volume right after preparation, respectively..... 180
- Figure 55. Optical micrographs of bubbles extracted from the aqueous foams in Figure 51. The micrographs were taken 1 h after foam stabilization. The aqueous foams were obtained by shaking suspensions containing nano-sheets from (a) batch A, (b) batch B, and (c) batch C. From (1) to (4) the molar ratios were set to (1) 1.32 ± 0.05 , (2) 1.53 ± 0.05 , (3) 1.74 ± 0.05 , and (4) 2.16 ± 0.05 , respectively. The scale bar is 100 μm 183
- Figure 56. Aqueous foams obtained from nano-sheet suspensions at varying aspect ratios and PA:ZrP molar ratios. (a) batch A, (b) batch B, and (c) batch C. The water is blocked at the top of the tube due to the jammed ZrP-PA nano-sheets in the bulk and on the air bubbles. 184
- Figure 57. The contrast between optical and crossed-polarized micrographs of the foams. The micrographs were taken 1 h after foam stabilization. The foams are obtained from suspensions of batch C. (a) and (c) are optical micrographs at a molar ratio of PA:ZrP of 1.32 and 1.95, respectively. (b) and (d) are cross-polarized micrographs at a molar ratio of PA:ZrP of 1.32 and 1.95, respectively. The nano-sheet concentration is fixed at 2 ± 0.1 % wt. The scale bar is 50 μm 186
- Figure 58. SEM micrographs of dried aqueous foam stabilized by ZrP-PA nano-sheets of different batches as labelled. (a) Batch A, (b) batch B, and (c)

batch C. The zoomed-in images show the nano-sheets at the air-water interface. The PA:ZrP molar ratios were set as labelled.	188
Figure 59. Transmission electron micrographs of (a) ZrP nano-sheets and (b) silica spheres.	193
Figure 60. Photographs of ZrP/silica suspensions between crossed polarizers. From left to right, ZrP volume fraction corresponds to 0.0009, 0.0018, 0.0027, 0.0036, 0.0045, 0.0054, 0.0063, 0.0070, 0.0081, 0.009, 0.01, 0.0108, 0.0117, 0.0126, 0.0153, and 0.018, respectively. From top to bottom, silica concentration corresponds to 0, 0.12, 1.78, and 2 wt.%, respectively.	194
Figure 61. Cross-polarized optical microscopic images of nematic Schlieren textures (a) N_1 , $\phi_d = 0.0081$ and silica concentration of 0 wt.%. and (b) N_2 , $\phi_d = 0.018$ and silica concentration of 1.78 wt.%. The micrographs were taken using a Nikon microscope TE-2000U with crossed polarizers. Pictures were taken using 4 \times magnification.	195
Figure 62. Phase diagram as a function of ZrP and silica concentration. Phase states include isotropic (I, blue circle), nematic-1(N_1 , red-vertical rectangle), nematic-2(N_2 , red-horizontal rectangle), and smectic (S).	196
Figure 63. Nonadecane wax disks. (a) Confocal micrographs. Wax disks coated with Nile red. Magnification 100 \times . (b) Confocal reflective image at the same position as (a) (c, d) Self-assembling of wax disks in an evaporating droplet observed under cross-polarizing microscopy. Magnification 20 \times	198
Figure 64. Different states observed for nonadecane wax disks of aspect ratio around 5. Isotropic (blue circle), short rods (red triangle), long rods (yellow star), and random aggregations (purple square).	199
Figure 65. Different states observed for nonadecane wax disks of aspect ratio around 5. Isotropic (blue circle), short rods (red triangle), long rods (yellow star), and random aggregations (purple square).	200
Figure 66. Selective interaction tuned with depletion attraction from SDS micelles. Diagram of the different states observed in suspensions of wax disks of aspect ratio around 4, at various concentrations of SDS. We identified states such as isotropic (blue circle), short rods (red triangle), long rods (yellow star), and random aggregations (purple square).	201

LIST OF TABLES

	Page
Table 1. The history of self-assembly disk-shaped colloids	18
Table 2. Comparison of different methods for the production of emulsions and colloids.....	54
Table 3. Characterization of the exfoliated ZrP platelets	104
Table 4. The biphasic gap ($\Delta\phi_{I-N} = \phi_N - \phi_I$) values for different aspect ratios and polydispersities.	108
Table 5. Isotropic (ϕ_I) and nematic (ϕ_N) volume fractions for inversed aspect ratios (ξ^*) of 0.010 ± 0.003 and 0.0020 ± 0.0005 at different polydispersity (σ). The concentrations at zero polydispersity for both graphs were obtained from simulations of Fartaria and Sweatman. ¹⁵⁸	111
Table 6. Classification of ZrP suspensions according to polydispersity.	113
Table 7. Comparison of experimental and simulations isotropic (ϕ_I) and nematic (ϕ_N) lines on power law ξ^* scaling.	116
Table 8. Nano-sheet lateral size and aspect ratio	168
Table 9. Melting temperature (T_m) and rotator phase range of different waxes	198

CHAPTER I

INTRODUCTION

1.1 Colloids of Different Shapes

Colloids are defined as particles or droplets dispersed in a continuous phase, characterized by at least one dimension in a range between 1 nm to 1 μm (**Figure 1**) and subject to thermal motion or *Brownian* motion. Colloids are well suitable systems for fundamental research and observable under microscopy. There are many examples of colloidal systems in nature, such as mayonnaise (oil droplets suspended in water, an emulsion), fog (liquid droplets suspended in a gas, an aerosol), and human blood (red blood cells are solid particles suspended in a liquid, a suspension). Colloidal systems are tunable in size, shape, interactions, and can evolve from one state to another (*i.e.*, *phase transitions*) when changing temperature, concentration, or other factors. Colloids exist in a variety of shapes,¹ such as spheres, rods, and disks. Spherical colloids can crystallize at relatively high particle concentrations ($\phi=0.494$, for hard spheres).² In contrast, rod- and disk-like particles, due to their *anisotropy*, can form a variety of *lyotropic* liquid crystalline phases at low particle concentrations as shown in **Figure 2**, which makes them particularly interesting. In addition, their interaction potential can be adjusted to achieve gels, glasses, liquid crystal, and crystal phases. Regardless of their natural abundance, studies of disks are less commonly undertaken than studies of rods.^{3,4}

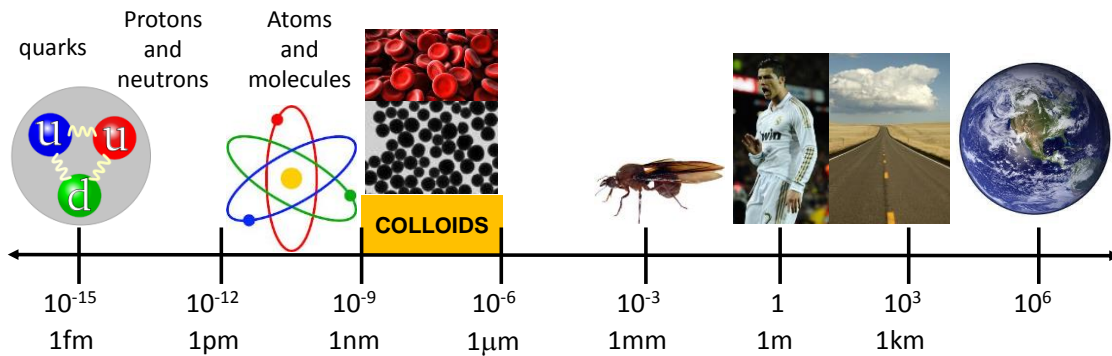


Figure 1. Different length scales in the world

In 1938 the first liquid crystal study of disk-like particles was reported by Langmuir, who studied lathlike natural hectorite clay particles (*i.e.*, California bentonite).⁵ Inspired by this experiment and others, Onsager developed a theory to predict the capability of cylindrical objects (*i.e.*, rods and disks) with diameter D and height L to evolve a liquid crystalline transition, which interact via hard-core repulsions, to make phase transitions.⁶ His theory was based on the excluded volume and applies for both rods and disks, $L \gg D$ and $L \ll D$, respectively. In the disk case, the excluded volume b per real volume, v_p , at thermodynamic equilibrium is $b/v_p \sim \pi D/4L$. At high particle concentration and large aspect ratio ($\xi = \text{diameter/thickness} = D/L$), if the particle dismisses orientational entropy, it is compensated by the increase in excluded volume entropy (*i.e.*, translational entropy), hence stabilizing a liquid crystalline phase.^{6,7}

Colloidal discotic liquid crystals are finding increasing potential applications in a large variety of fields including liquid crystal displays and nanocomposites. By controlling the anisotropy of the system at the colloidal scale, the self-assembly of these

particles have provided a powerful methodology to enhance the properties of composite materials. This chapter summarizes the recent significant developments in fabricating colloidal disks, the experimental and theoretical phase transitions, and their prospective usage. Colloidal disks can be obtained from natural and synthetic crystals and various fabrication methods. However, there is a great need for a large-scale production and process of synthetic disks. Furthermore, we reviewed theoretical and computational studies as potential predictive tools of phase transitions. These transitions are the result of the balance of excluded volume, electrostatic, and van der Waals interactions. The literature up to date has revealed the presence of various discotic liquid crystalline phases, projected by theoretical and computational models. Factors such as polydispersity, shape, external forces, and particle-particle interactions are prone to enrich the phase diagram. Disk-like particles and their phase transitions have become an emerging fundamental research area; therefore, there has been a call to develop scalable approach to disk production and find novel applications of these materials.

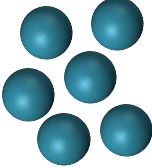
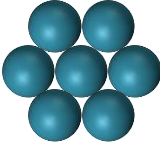



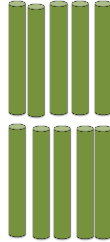





PHASE PARTICLE	ISOTROPIC	NEMATIC	SMECTIC	COLUMNAR	CRYSTAL
spheres					
rods					
disks					
ORDER	none	orientational	1D	2D	3D

Figure 2. Phases for spheres, rods, and disks *versus* concentration.

1.2 Fabrication

1.2.1 Colloidal Disks

There is an outstanding need for methods to fabricate discotic colloidal particles that can self-assemble into useful structures. Significant progress has been made in recent years toward particle synthesis, which has led to disk-like particle systems of varying compositions, aspect ratio, and functionalities. Certainly, disk-like colloidal particles have long been known in science. For instance, clay,⁸⁻¹⁰ asphaltenes,^{11, 12} histone octamer disks in nucleosomes,¹³ and red blood cells¹⁴ are systems found in nature that are mainly composed of disks. So far, a significant amount of work has been carried out on making micrometer-sized platelets,¹⁵⁻¹⁷ nanometer-sized disks in clay,¹⁸⁻²¹

synthetic clay²²⁻²⁵ or nano-crystals,²⁶ and lithographically fabricated particles.²⁷⁻²⁹ However, narrow industrial applications of such similar systems have been reported due to the low yield, highly polydispersity in size and low shape selectivity of current synthesis methods. There is a critical need to establish a model system of discotic colloidal particles with uniform size in nanometer to a few microns.³⁰⁻³⁶ Current synthetic discotic colloidal systems often have a broad size distribution, as large as 17%.^{15, 17} But, particle polydispersity has an important effect on the structure and phase transitions of the suspensions.^{37, 38} A dispersion in particle size can suppress crystallization in hard sphere colloids.³⁹ In discotic liquid crystals, polydispersity influences both the isotropic-nematic⁴⁰⁻⁴² and the nematic-smectic^{43, 44} transitions. In this section we discuss the recent progress made in the synthesis of discotic colloidal systems and their self-assembly into three-dimensional structures.

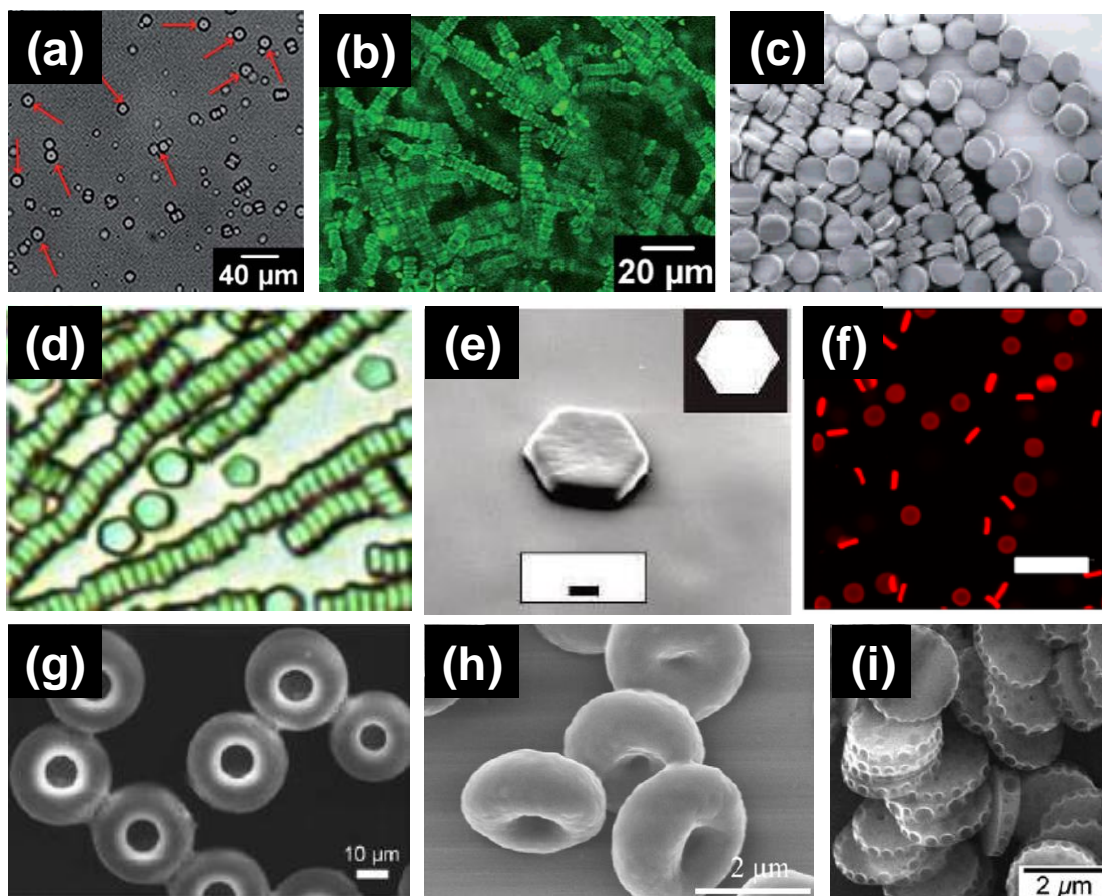


Figure 3. Representative examples of recently synthesized colloidal disks. α -Eicosene disks synthesized via shape-change of wax emulsions having an aspect ratio of (a) ~ 2 , (b) ~ 4 . (c) and (d) Lithographically designed colloidal disks. (e) Custom-shaped microscale pentagonal Lithoparticles. (f) Replicated hydrogel red blood cell-like discotic microparticles synthesized via non-wetting templates (PRINT®) technique. (g) Toroidal particles via solidification of a polymer solutions. (h) Red blood cell-like polymer particles via consolidation of charged droplets. (i) Disk-like polymer particles produced by seeded dispersion polymerization method of methacrylate and polystyrene seeds.

1.2.1.1 Fabrication Methods

Great effort has been dedicated to the invention of new methodologies to mass produce discotic colloidal systems. We summarize here the most emerging strategies for disk-like particles fabrication using electrospray, photolithography, microfluidic, and particle replication in non-wetting templates (PRINT). In addition, these techniques are

also characterized of their excellent control in size, shape, composition, and surface chemistry.

1.2.1.1.1 Wax Disks via Electrospray Emulsification

Mason^{45, 46} pioneered the preparation of discotic wax particles via shearing hot α -Eicosene into a highly concentrated SDS aqueous solution and lowering the temperature to induce the shape-change of the wax emulsions. However, his conventional emulsification methodology lacked to control the size and size distribution of the final particles. Our group synthesized for the first time uniform wax emulsions by a newly developed emulsification method: electrospraying melted α -eicosene at 60°C and collecting the emulsions in 20mM sodium dodecyl sulfate (SDS) solution to produce micron-sized emulsions.⁴⁷ Subsequently, uniform wax discotic particles were obtained via surface freezing and phase transition of wax molecules inside the emulsions. The emulsion size was controlled by varying experimental electrospray parameters, such as the wax flow rate, the electric conductivity, and the applied voltage. In addition, they found that the uniformity of the emulsions was influenced by the surface tension and the density of the collection liquid. Recently, they demonstrated experimentally and theoretically the principle to control the morphology of the discotic particles with a layered internal structure.⁴⁸ Setting of the surfactant and co-surfactant concentration on the wax surface, biconcave and flat disks have been obtained (**Figure 3a, b**).

1.2.1.1.2 Photolithography

Discrete monodisperse anisotropic colloidal particles of well-defined shapes and surface chemistry have been designed via photolithography^{29, 49, 50} and have served as platform to systematically study the effect of shape, surface roughness and colloidal interactions (*e.g.* depletion, van der Waals, electrostatic, etc.) on particle self-assembly.^{29, 49, 50} Badaire *et al.*,^{29, 49} studied the effect of surface roughness, and colloidal interactions using cylindrical disk-like particles as shown in **Figure 3c**, that exhibited self-assembly of ordered structures at various aspect ratios. They found that both depletion and van der Waals interactions can be attenuated ~20 fold in comparison with calculations for smooth particle surfaces. Similarly, Zhao *et al.*,⁵¹ fabricated polymeric pentagonal platelets of 1.8 and 1 μm in diameter and thickness, respectively, and stabilized in aqueous solution by trisodium salt of triacetic acid (**Figure 3d**). From these custom-shaped micro-platelets, depletion attraction was suppressed when surface asperities became larger than the depletant size.⁵¹ Hernandez *et al.*,²⁸ used the shape versatility of lithography to develop a monodispersed, microscopic and fluorescent colloidal alphabet particles at micro-scale. These unique anisotropic particles presented a strong Brownian motion similar to standard colloids, which makes them a good candidate to study the influence of particle shape on self-assembly and phase transitions.

1.2.1.1.3 Microfluidic facilitated Lithography

There is a tremendous call to create monodisperse anisotropic particles with a greater control of their shape and surface chemistry. A versatile technology commonly

used by scientists to produce disk-like particles is microfluidic fabrication. Microfluidic reactors have the capability to produce nano-meter sized droplets through channels at micro-scale. Eventually, these droplets can be solidified into solid particles via temperature cooling, solvent evaporation, chemical reaction, or thermal polymerization. Dendukuri *et al.*,^{52, 53} combined photolithography and microfluidic to mass produce complex shapes (*e.g.* triangles, cubes, platelets, etc) at the colloidal length-scale. The shape is defined by the channel architecture and lithographic mask. A disk-like particle produced via this technique is shown in **Figure 3e**. Although microfluidic fabrication is a useful tool to produce highly anisotropic particles, it is limited to polymerizable precursors, where the continuous phase should be chemical compatible with material that is used to make the microfluidic device such as poly(dimethylsiloxane) (PDMS).

1.2.1.1.4 Particle Replication in Non-wetting Templates (PRINT®)

Anisotropic discotic particles have been replicated using non-wetting templates (PRINT®) technique. PRINT is a template-nanofabricated process that offers cost-effective colloidal particles. This methodology allows the fabrication of anisotropic particles with a unique control of shape, size, surface chemistry, and composition.⁵⁴⁻⁵⁶ PRINT allows the targeting to different chemistries that enhance the cargo of drug delivery particles. For instance, Merkel *et al.*,⁵⁵ fabricated red blood cell (RBC) –like particles that were characterized by a similar size, shape, and deformability (**Figure 3f**).

1.2.1.2 Polymer-discotic Colloidal Particles

Researchers have tried to produce anisotropic particles via consolidation of polymer droplets. However, it is difficult to control the geometry of polymer particles due to the minimization of the interfacial energy between the particle and its surrounding, which usually is prone to produce spherical particles. As previously mentioned, typical methodologies to produce anisotropic particles were based on lithography in microfluidics via temperature cooling or photopolymerization reactions. As a breakthrough, Weitz lab generated toroidal particles (**Figure 3g**) via solidification of different polymer solutions of poly(ether sulfone) (PES), polysulfone (PSF), poly(methyl methacrylate) (PMMA), and poly(vinylidene fluoride) (PVDF) inside a micro-channel.⁵⁷ A glass device was utilized to produce polymer emulsions dissolved in dimethylformamide (DMF) and dispersed in PDMS. Monodisperse toroidal particles are created during polymer drop solidification in a range of 6-120 μm . Similarly, Park *et al.*,⁵⁸ synthesized polyurethane monodispersed toroidal particles by varying the surrounding temperature, solvent characteristics, and polymer concentration (**Figure 3h**). Remarkably, the monodispersed charged droplets produced by electrospray solidified into a torus structure above a critical droplet size to induce the asymmetry diffusivities.⁵⁸

In another approach, similar particles have been recently produced by seeded dispersion polymerization method of various methacrylates using polystyrene seeds of 1.57 μm (**Figure 3i**).⁵⁹ Also, polyethylene (PE) nano-platelets were successfully synthesized under mild conditions (15 °C) via nickel-catalyzed polymerizations in

aqueous solution. These reactions resulted in nano-platelets of 12 and 6 nm in radius and thickness, respectively.⁶⁰

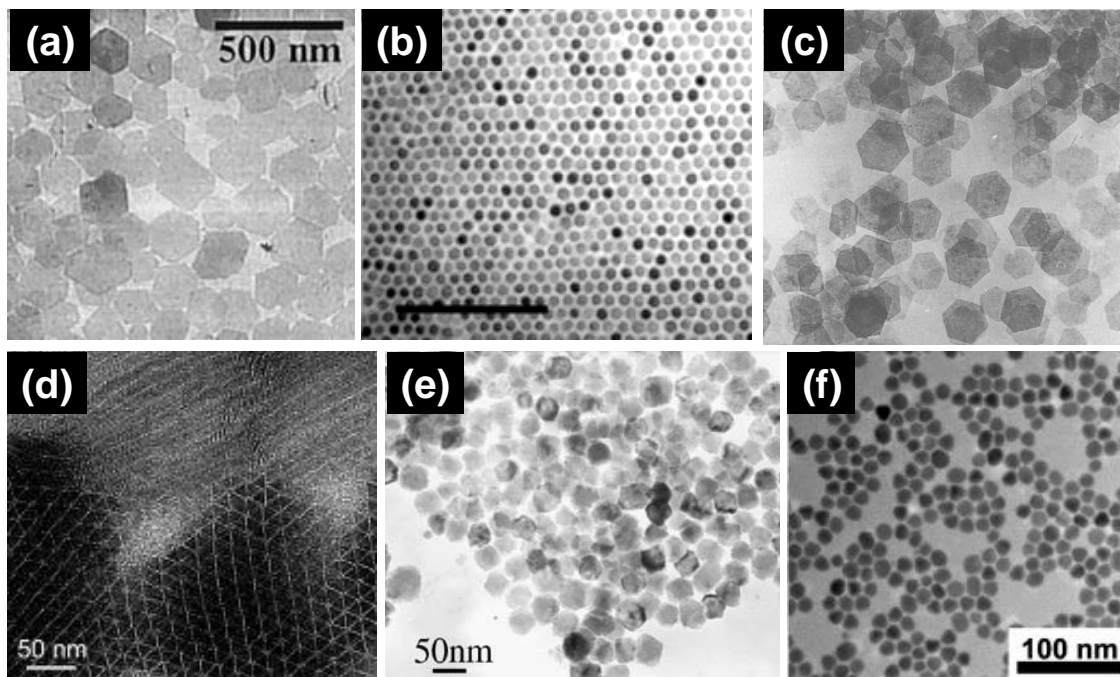


Figure 4. Colloidal disk-like systems. (a) γ -Al(OH)₃, (b) Co, (c) Ni(OH)₂, (d) LaF₃, (e) Ag-SO, and (f) Cu₂S colloidal nano-platelets

1.2.1.3 Controlled Crystal Growth Plate-like Particles

Nowadays, the synthesis of colloidal nanoparticles with well-defined size, shape, composition, and structure, underpins a gamut of applications and fundamental science research.⁶¹ The goal of this section is to present a brief review of recent research progress that center on the disk-like shape-controlled synthesis possessing great applicability in the field of mineral liquid crystals. Inorganic discotic particles have caught good attention due to several unique properties such as rigid structure, high thermal stability, and high aqueous and non-aqueous suspension stability. A typical synthesis of inorganic disk-like particles consists in nucleation, nuclei evolution into

seeds, and seed-growth into nanoparticles. To date the following are some examples of nanoplatelets that have been reported in literature: γ -Al(OH)₃,⁶² Ni(OH)₂,⁶³⁻⁶⁵ Co,⁶⁶ Ag-SO,⁶⁷ LaF₃,⁶⁸ Cu₂S,⁶⁹ CuS,⁷⁰ Ni₃S₄,⁷⁰ In₂S₃,⁷¹ and CdSe, CdS, and CdTe nanoplatelets.⁷² **Figure 4** shows some examples of inorganic nanoplatelets. They are characterized by their hexagonal, pentagonal, and triangular shapes. Gibbsite (γ -Al(OH)₃) nanoplatelets is the most recognized model of disk-like colloidal system to study liquid crystal phase transitions (**Figure 4a**). Hexagonal nanoplatelets of 150-200 nm with a polydispersity of ~25% can be obtained by heating a solution of aluminum alkoxide.⁶² Colloidal gibbsite can be coated with silica^{73, 74} and the size polydispersity enhanced via seed-growth.⁷⁵ In addition to gibbsite disk-like particles, similar systems have been recently reported. Puntero *et al.*,⁶⁶ reported the fabrication of hcp-Co nanodisks from the rapid decomposition of cobalt carbonyl in the presence of surfactants and susceptible to a magnetic field (**Figure 4b**). Surfactants played a significant role in the enhancement of the shape control, size polydispersity, and particle stability. By introducing a magnetic field, the disks spontaneously self-assembled into stacks. Ithurria *et al.*,⁷² synthesized highly anisotropic two-dimensional colloidal nanoplatelets of SnSe composed of about 4-11 monolayers. Brown *et al.*,^{63, 64} developed Ni(OH)₂ platelets of 180 nm and 10 nm in diameter and thickness, respectively (**Figure 4c**). Finally, the crystal morphology of Cu₂S disk-like particles of 14–20 nm and 5 nm in diameter and thickness, respectively, was controlled by tailoring the face-surface-reactivity of the seeds as shown in **Figure 4f**. In general, the aforementioned platelet colloidal systems self-assembled into columns of platelets and most of them served to study the discotic liquid crystal phase diagram.

1.2.2 Monolayers from Inorganic Lamellar Crystals

The family of lamellar compounds has been found to be the most valuable source of two-dimensional systems. Lamellar crystals are mainly composed of atomically flat two-dimensional nano-sheets hold together by attraction due to van der Waals, electrostatic interactions, or hydrogen bonds. They can be inorganic crystals, such as clay⁷⁶, α -zirconium phosphates (α -ZrP),⁷⁷⁻⁸⁰ niobates,⁸¹⁻⁸³ titanates,⁸⁴⁻⁸⁶ or organic crystals, such as graphite, which is made of stacks of graphene layers.⁸⁷ These layers are valuable for energy storage, electronics, and catalytic applications. Lamellar crystals are characterized by their weak interactions between their layers, therefore, can go through exfoliation by guest species to obtain single nano-sheets (*e.g.*, molecules, ions, solvents, polymers, etc).^{77, 80, 88-91} A wide variety of mineral crystals have been exfoliated, such as layered double hydroxides,⁹² niobates,^{81-83, 93-98} phosphates,^{81, 82, 99-101} titanium oxides,^{81, 84} and metal chalcogenides (*e.g.*, MoS₂, WS₂, etc.).¹⁰²⁻¹⁰⁴ After exfoliation, stable nano-sheet suspensions can be obtained due to counteractions presented on the particle surface. In nature, these materials exist in a great variety of specific surface areas, surface chemistries, and compositions. Inorganic nano-sheets are commonly used for several industrial applications such as rheological modifiers for drilling fluids, cosmetics, pharmaceutical products, and paints,^{10, 105} and polymer fillers.¹⁰⁶⁻¹⁰⁹ For fundamental science, due to the high anisotropic character of the nano-sheets, they are currently being exploited as lyotropic model systems to study the discotic liquid crystal phase diagram. A review regarding the recent application of these highly anisotropic nano-sheets on the study of liquid crystals will be discussed in **Section 1.4**.

1.2.2.1 Natural Clay

Clay minerals are commonly classified under *silicates*. However, their chemical formula contains more oxygen compared to other elements such as silicon, aluminium, or magnesium and can be considered as *hydroxides* as well. Clay minerals are composed of tetrahedral and octahedral nano-sheets. In the tetrahedral nano-sheets, each silicon atom is enclosed by four oxygen atoms, and the tetrahedral silicon unit is linked to one another one through shared oxygen. The shared oxygen atoms form a basal plane. On the other hand, the octahedral nano-sheets have aluminum and magnesium cations covalently linked and coordinated with six oxygens or hydroxyls. The tetrahedral and octahedral nano-sheets are covalently linked through tetrahedral oxygen atoms. Depending of their substitution on the tetrahedral or octahedral nano-sheets, natural clay can be classified as kaolin-serpetine, pyrophyllite-talc, smectite, vermiculite, illite, palygorskite-sepiolite, chlorite, and mica. Amongst them, smectites have become the most chemically interesting for surface modification and application. In the following liquid crystal section, we will focus on liquid crystals reported using smectite natural clay with tetrahedral (beidellite and saponite) and octahedral (montmorillonite and hectorite) substitutions. We will also mention liquid crystal phases formed of nontronite system, another well-known iron-rich smectite mineral.

1.2.2.2 Synthetic Clay

In the literature it is possible to find a myriad of smectite-type layered inorganic materials such as silicates, phosphates, oxides, niobates, chalcogenides, and sulfides.

They have received a tremendous attention due to their great potential on catalysis, ion exchange applications, and liquid crystal formation. One of the advantages of these materials relies on crystal exfoliation due to guest accommodation inside the inter-galleries, increasing the inter-lamellar spacing and decreasing the van der Waals interactions between the nano-sheets. One good example among these various layered inorganic materials is the crystalline α -zirconium (IV) phosphate (α -ZrP) with chemical formulas $\text{Zr}(\text{HPO}_4)_2 \cdot \text{H}_2\text{O}$. The α -ZrP crystal layer is composed of a ZrO_6 sheet coordinated with HPO_4^{2-} tetrahedrons forming a covalent network.^{79, 110} The thickness of a monolayer of α -ZrP is about 0.66 nm⁸⁹. The obtained mono-layers have excellent mechanical properties and are chemically stable in acid and basic conditions. Layered crystals of α -ZrP can be synthesized at varying crystal size and size polydispersity. Shuai *et al.*,¹¹¹ reported the tailoring of these parameters by varying phosphoric acid concentration, reaction time, and reaction temperature.

Another type of synthetic clay materials are layered double hydroxide (LDHs), metal oxides, and metal chalcogenides. LDHs consist of positively charged layers containing hydroxides of two different metal cations. LDHs can be synthesized in the laboratory via coprecipitation and hydrothermal treatment of an aqueous solution having salts of two metal ions and a base.¹¹² Xu *et al.*,¹¹² reported that LDH particles between 40 and 300 nm can be synthesized by adjusting the hydrothermal treatment conditions. Layered metal oxides such as niobates have been utilized to study the liquid crystalline transitions. These materials can be prepared by a solid-state reaction by mixing starting material powders. Layered metal chalcogenides have called remarkable attention due to

the fascinating structural and physical properties of these quasi two-dimensional inorganic materials. Examples of metal chalcogenides are MoS₂, WS₂, MoTe₂, TaSe₂, NiTe₂, BN, and Bi₂Te₃. Similar to phosphates and oxides, the weak interaction between the nano-sheets enables crystal exfoliation.¹⁰²⁻¹⁰⁴

1.2.2.3 Graphene and Graphene Oxide

Graphene and graphene oxide nano-sheets are rising materials commonly applied in soft condensed matter physics. However, graphene nano-sheets are not easy to obtain. Highly anisotropic graphene nano-sheets were first obtained by graphite exfoliation via scotch tape method.^{113, 114} Later, single layers of graphene have been obtained by a spontaneous exfoliation using chlorosulfonic acid solution.^{115, 116} Graphene is a new class of material having thickness of single layer of atoms (2D crystal) and possesses tremendous potential applications. In contrast, graphene oxide is commonly obtained from chemical oxidation of graphene via chemical oxidation and water dispersion. Recently, both graphene and graphene oxide have been applied to the study of the discotic liquid crystalline phase diagram.¹¹⁵⁻¹¹⁸

1.3 Discotic Liquid Crystals

Self-organization of colloids has attracted interest due to the intriguing *lyotropic* liquid crystalline phases and crystals that can be produced. At the beginning, scientists focused on experiments and simulation from spherical-like particles having a hard-core repulsion.¹¹⁹⁻¹²¹ In the last decades, the study of liquid crystals has extended to anisotropic colloidal particles, such as rods and disks (**Table 1**).^{1, 122} The study of liquid

crystalline dispersions of anisotropic particles is of great interest due to the possibility to fabricate photonic crystals and integrated photonic circuits. It is well-known that highly anisotropic particles are capable to enter in a liquid crystalline phase transition at low concentrations. Recently, the study of these transitions has been extended to a variety of colloidal interactions.¹²³ The self-assembly of these structures is possible by the *engineering* of the attraction (depletion,^{45, 124-126} van der Waals,^{127, 128} or Coulomb^{127, 129}) and/or repulsion (steric¹³⁰ or Coulomb¹³¹) inter-particle forces. In the past, attraction and repulsion forces have been applied to manipulate the self-assembly of complementary shapes¹³² and DNA strands.¹³³⁻¹³⁶

Langmuir and Onsager were pioneers in the study of the liquid crystal phase formation in disk-like colloidal suspensions.^{5, 6} In this section, we summarize theoretical,^{137, 138} computer simulations,¹³⁹ and experimental work,¹⁵ developed to comprehend the discotic phase diagram. As we discuss in this section, the ability of a given discotic colloidal system to induce self-assembly and transfer into a liquid crystal phase depends on both inter-particle interactions and aspect ratio ($\xi = \text{diameter} / \text{thickness}$).^{80, 139}

Table 1. The history of self-assembly disk-shaped colloids

Year	Autor	Description
1938	Langmuir	Nematic phase observation from a clay suspension
1949	Onsager	Theoretical prediction of cylindrical objects at the I-N transition
1977	Chandrasekhar	Physical treatment of disk-shaped molecule phase transitions
1992	Frenkel <i>et al.</i>	Discotic phase diagram from Monte Carlo simulations
1998	Lekkerkerker <i>et al.</i>	Observation of columnar phase at relatively low polydispersity
2000	Lekkerkerker <i>et al.</i>	Nematic-to-columnar and nematic-to-smectic phase sequence
2002	Mason	Columnar stack of wax disks via depletion forces
2009	Sun <i>et al.</i>	Smectic phase of polydisperse colloidal platelets with identical thickness
2010	Behabtu <i>et al.</i>	Graphene liquid crystals
2010	Mejia <i>et al.</i>	Mass production and self-assembly of uniform wax disks
2011	Gao and Xu	Graphene oxide chiral liquid crystals and macroscopic assembled fibers
2011	Ruzicka <i>et al.</i>	Empty liquid and equilibrium gels from a colloidal clay suspension

1.3.1 Theoretical Approximations

Theoretical and computer simulation work of discotic systems is perhaps one of the most significant approaches as it allows the prediction of different states of matter and properties. This section reviews most of the works published in the last decades related to the discotic liquid crystalline phases. The possibility of anisometric colloidal systems to present a first-order isotropic-nematic transition was first reported by Onsager⁶. Based on his work, the third- and higher-body correlations cannot be ignored for rods of relatively small thickness-to-diameter ratio (*i.e.*, disks). Therefore, it is anticipated that the second-virial coefficient treatment will present better results.⁷

Simulations of infinitely thin disks reported by Eppenga *et al.*,¹⁴⁰ stated that ϕ_I and ϕ_N are smaller and the coexistence region ($\Delta\phi_{I-N} = \phi_N - \phi_I$) narrower than predicted by Onsager.⁶ By increasing the disk-shaped particle concentration, the nematic phase can evolve into a columnar order, distinguished by a 2D hexagonal organization of disk stacks. At the nematic-to-columnar (N-C) transition, the system loses configurational entropy but gains translational entropy. Attempts to improve Onsager's theory on platelet dispersions has been reported.¹⁴¹ Density functional theory approaches have been developed for isotropic fluids,^{142, 143} models with parallel or restricted orientation,¹⁴⁴ and vanishing thickness.^{145, 146} An approach of a discotic colloidal system presenting liquid crystalline order was made utilizing shaped hard convex bodies.¹⁴⁷ High-body virial term correlations of disk-like colloidal systems can only be performed via computer simulation.¹⁴⁸ In the case of cut spheres, eight virial terms have been calculated for both isotropic and nematic phases.^{149, 150} However, an inaccurately description of states at higher concentrations (*e.g.*, nematic and columnar) was obtained. Scaled particle theory (SPT) has been used as an alternative methodology to introduce higher virial terms. Although good results were obtained for thin disk-like particles,¹⁵¹ poor predictions at the isotropic-to-nematic (I-N) transition were obtained at higher inversed aspect ratios ($\xi^* = \text{thickness} / \text{diameter}$). One popular methodology to account high-virial term is the Parson-Lee (PL) approximation.¹⁵²⁻¹⁵⁴ This approach has been used for short hard spherocylinders,^{3, 155} disk-like hard cylinders,¹³⁷ and disk mixtures.¹⁵⁶ The hard cylinder phase diagram is in good agreement with computer simulations.^{139, 157-}
¹⁶⁰ The values of ϕ_I and ϕ_N are the same as the ones predicted by Onsager's second virial

theory at $\xi^* \sim 0$ ¹⁶¹ and increase with ξ^* . The nematic-columnar (N-C) transition stays constant at varying ξ . The triple point (I-N-C) position occurs at $\xi^* = 0.175$ in comparison to other simulations, which occurs at $\xi^* \sim 0.126$ ^{162, 163} and $\xi^* \sim 0.14$.^{139, 164} Recently, an accurate analytical form of the equation of state was developed by introducing an extra term to incorporate contributions at high particle concentration and compared with simulation data.¹⁶⁵ In recent publications, our group in collaboration with others has carefully studied the effect of polydispersity, aspect ratio, and soft interactions on the I-N and N-S transitions using DFT calculations with Zwanzig approximation.¹⁶⁶⁻¹⁶⁸

1.3.2 Computer Simulations

The configuration of stable clusters possesses significant importance in both colloidal and biological sciences.^{169, 170} Discotic colloidal systems are useful models to comprehend colloidal aggregation into 3D structures. Although numerous publications about theoretical and computer simulations can be found in literature, it is still little in contrast to the abundance of experimental studies. Previous studies have utilized ellipsoidal core models.¹⁷¹⁻¹⁷⁵ In early 1990s, Veerman and Frenkel introduced the hard cut sphere (CS) model.¹³⁹ Interestingly, the reported discotic liquid crystalline phase diagram showcased nematic and columnar states, which were dependent on the particle aspect ratio. Recently, the phase diagram of oblate hard spherocylinder (OHSC) has been established via direct simulations^{159, 176, 177} and free energy calculations.¹⁶⁰ We discuss here the discotic liquid crystalline phase transitions for cut spheres using different kinds of Monte Carlo (MC) simulations such as NVT-Gibbs ensemble,¹³⁹ NPT-

Gibbs ensemble (GE),¹⁵⁷ and umbrella sampling (US).¹⁵⁸ We also study the liquid crystalline phase transitions reported for hard cylinders¹³⁷ and oblate hard spherocylinders (OHSC).^{159, 160, 176, 177}

1.3.2.1 Isotropic-Nematic and Nematic-Columnar Transitions

Hard cut spheres suspensions, depending on their aspect ratio, are known to exhibit isotropic, nematic, columnar, and crystalline solid states. Particularly, the I-N transition has been extensively studied at various aspect ratios and different simulation conditions. The pioneer work from Veerman *et al.*,¹³⁹ introduced the cut sphere phase diagram using NVT-MC simulations for inversed aspect ratios of 0.1, 0.2, and 0.3 and a system size of 256 and 288 particles. Using NPT-GEMC simulations, Piñeiro *et al.*,¹⁵⁷ studied the phase diagram at $\xi^* = 0.1$ for a system size of 1500 and 3000. Piñeiro's I-N transition densities¹⁵⁷ were in agreement with Veerman and Frenkel's data.¹³⁹ Recently, Fartaria *et al.*,¹⁵⁸ using NPT-USMC simulations, analyzed the low inversed aspect ratio region at $\xi^* = 0.001, 0.01, 0.04, 0.07,$ and 0.1 for a system size of 288 and 2048. Interestingly, Fartaria *et al.*,¹⁵⁸ reported a constant I-N biphasic gap occurred at inversed aspect ratios lower than 0.04. Both simulations of Veerman *et al.*,¹³⁹ and Fartaria *et al.*,¹⁵⁸ found that the nematic phase formation considerably reduced at $\xi^* \geq 0.1$, where a columnar organization is preferred.¹⁵⁸

In the literature is possible to find studies at inversed aspect ratios smaller than^{158,}¹⁶⁴ or larger than 0.1.^{139, 157, 178} The study of the I-N transition first-order behavior has been elusive via computer simulations and some efforts have been done by increasing

the system size, where a weak first order I-N transition has been observed $\xi^* = 0.1$.¹³⁹ Both cut sphere phase diagrams presented a nematic-to-columnar transition at $\xi^* = 0.1$. Similarly to cut spheres, Bates *et al.*,¹⁶⁴ reported for hard cylinders a first-order nematic-to-columnar transition for infinitely thin disks (*i.e.*, $\xi^* \sim 0$).

A colloidal system consisting of oblate hard spherocylinders particles has been broadly studied as well.^{159, 160, 176, 177, 179} The liquid crystalline phase diagram has been calculated by Monte Carlo simulations.^{159, 160} Similar to the cut spheres,^{139, 157, 158} the liquid crystal states of the OHSC phase diagram is mainly dependent on particle aspect ratio.^{159, 160} The nematic state is favored at $\xi^* \leq 0.1$. The similarity in the I-N transition is attributed to the circular face shape of the particles. Bates *et al.*,¹⁸⁰ reported that the I-N transition width is constant at various non-circular shapes (*e.g.*, regular hexagons, pentagons, squares, triangles, ellipses, rectangles, etc.) and decreases in concentration if the shape differs from circular. It is worth to mention the manifest of the first-order I-N transition at $\xi^* = 0.1$, in comparison to the neglectable one for cut spheres.¹⁵⁷

Similarly to cut spheres, OHSCs present nematic-to-columnar transition in an inversed aspect ratio range of $0 \leq \xi^* \leq 0.12$. Marechal *et al.*,¹⁶⁰ explained the presence of nematic state due to the low inversed aspect ratio of the particles, which does not favor edge disk interactions. However, as inversed aspect ratio increments, the edge-surface-area becomes significant to that of the face-surface-area at a fixed particle concentration, thereby allowing the disks to pack in bundles and crystallize laterally.¹⁷⁹

Martinez-Haya *et al.*,¹⁷⁶ performed computer simulations of spherocylinder and ellipsoidal discotic suspensions having an inversed aspect ratio of 0.2. A variation of the

dispersive interactions was induced to test the stability of the columnar phase. Robust hexatic columnar phases from these discotic systems were observed. Interestingly, the formation of a nematic state is dominant with respect to columnar state at $\xi^* = 0.2$.¹³⁹ The nematic state becomes stable if weak edge-to-edge interactions are larger than face-to-face interactions.¹⁷⁶ By inducing strong face-to-face or edge-to-edge interactions the columnar state is favored. In the case of ellipsoidal disk-like particles, the nematic state happens to be stable even if face-to-face interactions are induced.¹⁷⁶ Thus, spherocylinder and ellipsoidal discotic suspensions differ in the phase diagram configuration. Finally, in a recent paper, Morales-Anda *et al.*,¹⁸¹ simulated a thin and charged colloidal plate-like system and predicted the formation of a novel columnar nematic phase composed of interpenetrating columns.

1.3.2.2 Isotropic-Columnar Transition

Veerman *et al.*,¹³⁹ reported isotropic-to-columnar transitions at a range between $\xi^* = 0.15-0.3$. Cuetos *et al.*,¹⁵⁹ explored the discotic phase diagram of hard spherocylinder suspensions via Monte Carlo simulations for inversed aspect ratios within 0.2-0.5. Interestingly, three columnar phases were found, namely, a hexatic interdigitated phase (D_{hi}), a hexatic ordered phase (D_{ho}), and a hexatic disordered phase (D_{hd}), where the columns are fluid-like.¹⁵⁹ Due to their shape difference, hard spherocylinder particles can arrange either into columnar variations in a range of $0.1 \leq \xi^* \leq 0.5$. Similarly, Marechal *et al.*,^{160, 182} investigated the phase behavior of OHSCs and compared the results to the cut sphere and the hard spherocylinder phase diagrams.

Isotropic-to-columnar transitions at a range of $0.13 \leq \xi^* \leq 0.3$ were observed. Surprisingly, OHSCs differ with hard spherocylinders at the columnar state ($0.3 \leq \xi^* \leq 0.5$). Although similar phases were observed, Marechal *et al.*,¹⁶⁰ described these three columnar phases from Cuetos *et al.*,¹⁵⁹ as variants of the OHSC crystal phases.

1.3.2.3 Isotropic-Cubic and Cubic-Columnar Transitions

The isotropic-cubic and cubic-columnar transition were first predicted by Veerman and Frenkel using a hard cut-sphere model with Monte Carlo simulations.¹³⁹ In the cubic phase, the particles aggregate into short stacks of disks and align along three perpendicular axes. This cubic orientational order phase is characterized by not having translational order.¹³⁹ Blaak *et al.*,¹⁸³ investigated the possibility of cylinders of inversed aspect ratio equal to 0.9 to exhibit a cubic state. Although theoretical arguments state that a cubic state might occur, computer simulations could not find it. The cubic phase has not been extensively studied. The stability of the cubic phase is under current investigation.^{149, 160, 183-185} Veerman *et al.*,¹³⁹ focused on inversed aspect ratios of 0.1, 0.2, and 0.3. Duncan *et al.*,¹⁴⁹ extended the study to inversed aspect ratios of 0.15 and 0.25 and found the cubic phase at $\xi^* = 0.15-0.3$. By performing long runs and increasing the high-order virial expansion to the eighth term, the stability of the cubic phase was studied. In good agreement with theoretical results, at $\xi^* = 0.1$, the cubic was found to be metastable, however, at $\xi^* = 0.15$, the cubic phase dominated over the nematic phase.¹⁴⁹ Interestingly, at $\xi^* = 0.2$, even after extremely long runs the cubic phase did not convert into columnar or vice versa. Recently, Marechal *et al.*,^{160, 186} reported a

transient cubic phase using three model of hard platelets. Structures of locally perpendicular-oriented particle stacks neglect the formation of columnar phase. Surprisingly, the cubic phase lifetime is strongly dependent to the particle confinement that leads geometric frustration.¹⁸⁶

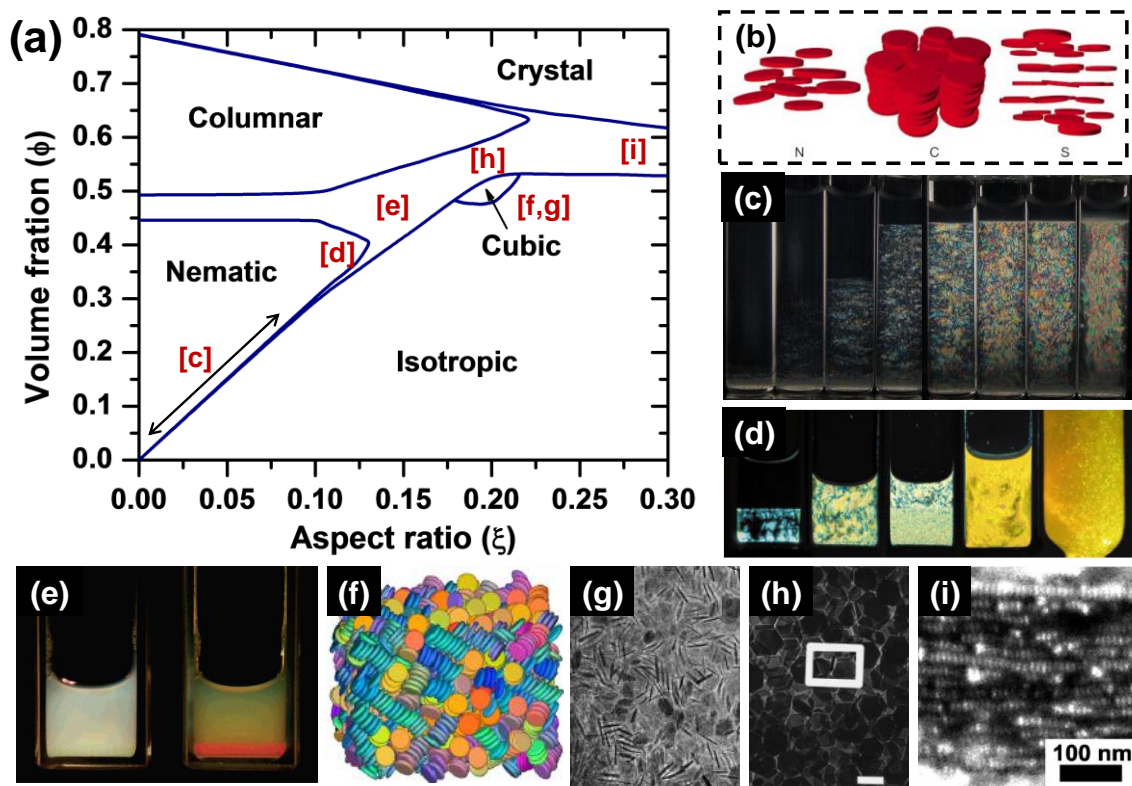


Figure 5. Discotic liquid crystalline phase diagram and states. (a) Discotic phase diagram predicted by Veerman and Frenkel¹³⁹ (b) Schematic representation of nematic, columnar, and smectic states for plate-like particles (c) ZrP I-N transition (d) Gibbsite plate-like suspensions present I-N, N-C and C textures (e) White and crossed polarized light of a gibbsite platelet suspension presenting a triphasic (I-N-C) transition via ion screening and sedimentation (f) Representation of OHSC particles at the cubic phase (g) Cubic phase of nickel hydroxide platelets (h) Columnar phase ordering of nickel hydroxide platelets (i) Copper sulfide nanodisks stacked in a columnar state.

1.3.3 Experimental Work

1.3.3.1 Isotropic-Nematic Transition

In 1938, Langmuir first demonstrated the isotropic-to-nematic transition in disk-like clay suspensions.⁵ However, clay suspensions present a singular challenge due to gelation, which makes them difficult to present a reproducible I-N phase transition.¹⁸⁷⁻¹⁹¹ Recently, scientists have reported the presence of nematic states for natural and synthetic clays on specific conditions.^{187, 192, 193} Early attempts focused on the structure of the electric double layer¹⁹⁴⁻¹⁹⁶ or around a single platelet.¹⁹⁷ The I-N transition has gained interest during the last 25 years^{122, 198, 199} and is now the most studied liquid crystalline phase transition.^{15, 16, 122, 168, 192, 200} Lekkerkerker *et al.*,^{16, 193, 201} reported liquid crystalline states using suspensions of polydisperse gibbsite platelets of around 170 nm and 15 nm in diameter and thickness, respectively (**Figure 5b and d**). These platelets were sterically stabilized in toluene¹⁶ and electrostatically stabilized in water.^{193, 201} Similarly, discotic nematic liquid crystals have been obtained from Mg/Al layered double hydroxides (LDH) aqueous²⁰² and toluene²⁰³ suspensions.

Gabriel *et al.*,¹⁰¹ rediscovered the ability of mineral nano-sheet suspensions of layered phosphate ($K_3Sb_3P_2O_{14}$) to give liquid crystalline states. From this breakthrough, inorganic layers suspensions with a thickness of several nanometers obtained from exfoliation of layered crystals gained attention due to their high anisotropy.^{122, 198, 199, 204} We have recently investigated the I-N transition at low inverted aspect ratios ($\xi^* \ll 0.1$) and different polydispersities using layers of α -zirconium phosphate (ZrP) as shown in **Figure 5c**. The aspect ratio of ZrP nano-sheets was controlled in an extensive range^{79, 80}.

^{110, 111} by fabricating crystals of varying lateral dimensions with subsequent exfoliation using tetrabutylammonium cations (TBA⁺).⁸⁸ We found that the transition volume fractions scale with aspect ratio $\phi_{I,N}=m(\xi^*)^{1.36 \pm 0.07}$, where the prefactor m strongly depends on size polydispersity for ϕ_N , but does not depend on size polydispersity for ϕ_I .^{80, 167} The effect on the I-N coexistence might be due to a particle demixing mechanism^{44, 80, 167}. Martinez-Raton and Velasco explained these results using a density functional model for hard board-like platelets with Zwanzig approximation.¹⁶⁷ The huge I-N coexistence gap of the ZrP nano-sheet suspensions could be explained by considering a bimodal size distribution in the lateral size, which may not be apparent through a direct visual observation.¹⁶⁷

Lateral and thickness size polydispersity can highly affect the behavior of the discotic suspensions in the coexistence region (I-N).¹⁶⁷ For instance, van der Kooij *et al.*,⁴² observed for gibbsite plate-like suspensions a phase separation having an isotropic and a nematic phase at the bottom and at the top of the sample, respectively. This behavior was attributed to fractionation caused by platelet thickness polydispersity. Wensink *et al.*,²⁰⁵ studied the phase behavior of a binary mixture containing thin and thick hard platelets using Onsager's theory. In agreement with van der Kooij *et al.*,⁴² their calculations confirmed a significant fractionation that caused the inversion of the isotropic and nematic phases.

Metal oxides such as exfoliated niobate and titanate colloidal suspensions have been previously utilized to study the I-N region.^{81, 84, 97} Miyamoto *et al.*,²⁰⁶ studied the aspect ratio dependence on the I-N transition of low inversed aspect ratio niobate

($\text{K}_4\text{Nb}_6\text{O}_{17}$) nano-sheets ranging from 0.0015 to 0.0035 for highly polydisperse suspensions using a well-defined sonication procedure. Nakato *et al.*,²⁰⁷ reported liquid crystal suspensions of exfoliated HNb_3O_8 and HTiNbO_5 that can behave as hydrogels depending on pH.^{207, 208} Very recently, graphene and graphene oxide colloidal systems have revealed Schlieren nematic textures.^{116-118, 209, 210} Graphene oxide nano-sheet systems are able to enter into a nematic state at low isotropic volume fraction transitions at extremely low inversed aspect ratios,²⁰⁹ reproduce a fully I-N transition,²¹⁰ and present novel liquid crystalline states (*i.e.*, chiral liquid crystal).¹¹⁸

1.3.3.2 Isotropic- and Nematic-Columnar Transitions

By increasing the particle volume fraction, discotic colloidal suspensions can present an orientational and two-dimensional (2D) positional ordered structure called columnar phase. Based on the disk aspect ratio, suspensions can transfer into a columnar state from isotropic or nematic states (**Figure 5a**).⁴³ Brown *et al.*,⁶³ and Saunders *et al.*,²⁶ reported the I-C transition that resulted in a hexagonal columnar state using nickel hydroxide ($\text{Ni}(\text{OH})_2$) and copper sulfide (CuS) disk-like particles (**Figure 5h and i**), respectively. In both studies, the structure of the columnar phase was analyzed using small-angle x-ray scattering (SAXS). van der Kooij *et al.*,¹⁵ reported the I-N and N-C transitions for relatively low polydisperse sterically stabilized gibbsite platelets (**Figure 5b and d**). Additionally, the high-density liquid-crystalline phase was presumably described as a hexagonal columnar phase in agreement with Brown *et al.*,⁶³ Lekkerkerker *et al.*,²¹¹⁻²¹³ confirmed this observation from large and oriented domains of

columnar phase, which were analyzed using high-resolution SAXS. Lateral size polydispersity also has a disruptive effect on the columnar phase crystallization. van der Kooij *et al.*,¹⁵ nicely illustrated that the two-dimensional crystallization (*i.e.*, columnar phase) nucleated for a lateral size polydispersity of up to 25%. The columnar state was also reported for charged gibbsite aqueous suspensions.¹⁹³ Interestingly, the effective platelet aspect ratio was adjusted by tailoring the ionic strength via salt addition. As expected from **Figure 5a**, I-N and N-C transitions were observed for low and large particle inversed aspect ratios, respectively. The nucleation of the columnar phase has been studied in droplets.²¹⁴ Additionally, charged gibbsite colloidal systems at varying salt concentrations possess the ability to transfer from a nematic to a columnar nematic state with a subsequent evolution into hexagonal columnar or repulsive gel.²¹⁵

1.3.3.3 Nematic-Smectic Transition

When liquid crystalline phases present a one-dimensional (1D) long-range positional order structure is called smectic phase. This phase has been rarely observed in discotic suspensions and has received much less attention than nematic and columnar states. A smectic-like crystalline state is expected for relatively high polydispersities ($\sigma > 17\%$) and high volume fractions.^{40, 41, 168, 216} van der Kooij *et al.*,¹⁵ reported a smectic-like structure from polydisperse in diameter and thickness gibbsite plate-like suspensions at high volume fractions. Long-range interacting colloidal plate-like systems have led to the formation of interesting liquid crystalline phases. Charged colloidal plate-like suspensions have demonstrated to present not only a I-N-C transition, but also a lamellar

phase.^{101, 118, 168} Our group reported a nematic-to-smectic (N-S) transition in colloidal suspension of ZrP monolayers.¹⁶⁸ Suspensions of exfoliated ZrP nano-sheets are characterized by a strong lateral-dimension polydispersity but identical thickness (*i.e.*, 2.68 nm). The spatial ordering of the nano-sheets was characterized using x-ray diffraction (XRD).¹⁶⁸ Very recently, the smectic B (Sm_B) was first reported by Kleshchanok *et al.*,²¹⁷ in charged colloidal gibbsite plate-like particles stabilized in dimethylsulfoxide (DMSO). Sm_B can be described as a phase composed of hexagonally ordered plate-like particles oriented along the particle layer's normal and was only observed in thermotropic rod-like liquid crystal suspensions.²¹⁷ Interestingly, the Coulombic repulsion long-range forces are attributed to the formation of the layered crystalline state. Finally, Yamaguchi *et al.*,²¹⁸ published the evolution of niobate plate-like colloidal system from the nematic into the smectic-layered structure by varying the nano-sheet aspect ratio and the nano-sheet volume fraction using x-ray scattering data.

1.3.3.4 Other Phases

1.3.3.4.1 Cubic

As previously mentioned, the discotic liquid crystal phase diagram predicted by Veerman and Frenkel¹³⁹ present a remarkable cubic phase. This liquid crystalline state is characterized by small disk stacks aligned perpendicular to each other. Although computer simulations have disputed the stability of the cubic phase (**Figure 5f**),^{149, 160, 183-185} Qazi *et al.*,¹⁸⁴ gave a first evidence in $Ni(OH)_2$ plate-like suspensions apparently in the dynamical arrested state as shown in **Figure 5g**.

1.3.3.4.2 Chiral

Chiral liquid crystals of 2D colloids have not been explored extensively. Chirality is frequently expressed in biology as the molecule helical assembly. Xu *et al.*,¹¹⁸ reported for the first time the presence of a chiral liquid crystal in a twist-grain-boundary phase-like model with lamellar ordering using 2D nano-sheet suspensions of graphene oxide at a particle volume fraction of 0.39%. This liquid crystal phase has only been observed for molecular liquid crystals and is commonly known as the cholesteric phase. The graphene oxide nano-sheets were characterized by having a particle diameter and thickness of $\sim 0.81 \mu\text{m}$ and 0.8 nm, respectively.

1.3.3.4.3 Gel and Glass

Arrested states for highly anisotropic suspensions are one of the central interests for condensed matter physics and many industrial applications. These states such as gel and glasses are basically a difficulty in the study of the discotic liquid crystalline phase transitions. They have commonly been observed in charged colloidal systems and evolve in time.^{187, 188, 201} The most known example of an arrested state (*i.e.*, gelation) during a liquid crystalline phase transition was observed by Irvine Langmuir⁵. Although scientists have observed the presence of nematic textures for selected natural and synthetic clays,^{187, 192, 193} little work has been dedicated to understand the factors (*e.g.*, ionic strength) that influence an arrested phase. Interestingly, recent studies have revealed the presence of large nematic order parameters in kinetic arrested phases.^{21, 188, 189, 191} Particle configuration in a kinetic-arrested colloidal system have been explained in terms

of *house of cards* and glass-like structures and can be induced via several ways.²³ For instance, gels can be created through attractive interactions at low particle concentration. On the other hand, repulsive or attractive glasses are formed at high particle concentration via electric repulsions or short-ranged attractive and repulsive interactions, respectively.^{219, 220} Common routes to induce arrested states are via depletion attraction^{221, 222} or charge screening.^{91, 221, 222}

In our lab, we have recently developed a detailed study to elucidate gelation of ZrP nano-sheet suspensions that usually result into liquid crystal suspensions at normal conditions.⁹¹ We found that the phase behavior of charged discotic suspensions displays a strong dependence on ionic strengths that resulted in liquid crystal, glasses, and gel states. Interestingly, the nano-sheet ion exchange capacity controlled the inter-particle interaction that resulted in isotropic- and nematic-gel and nematic states.⁹¹ The particle surface electrical charge is great importance due to the influence of the ionic strength on the suspension properties¹⁸⁷. Nakato *et al.*,^{207, 208} revealed that layered niobate suspensions can exhibit a pH-induced gelation. Wijnhoven *et al.*,²²³ demonstrated that sedimentation and particle size can also play a crucial role on the gel formation.

Attractive glass was produced in a gibbsite plate-like system via short-range depletion attraction caused by silica spheres.²²¹ At enough sphere concentration, the platelet colloidal suspension could not enter into a liquid crystalline state and glass formation occurred. Surprisingly, after several months the upper phase evolved into I-C phase on top of the glass phase.²²² Kinetically arrested glass has been formed from the same colloidal suspension at high particle concentration and salt concentrations of 10^{-2} M.

Devitrification of the glassy state occurred, where iridescent grains of hexagonal columnar phase were created in a period between months and years.²²⁴

1.3.3.5 The Effect of Gravity

Gravitational compression plays a crucial role in addition to the shape-dependent thermodynamic force on colloidal suspensions.²²⁵ Although anisotropic particles such as rods and disks show a richer phase behavior compared to spheres, experiments are greatly limited. The effect of gravity has permitted the existence of more than two liquid crystalline states simultaneously. van der Beek *et al.*,¹⁶³ reported on an I-N biphasic sample of sterically stabilized gibbsite plate-like suspension that developed a columnar phase on the bottom after a year. This observation was in agreement with an osmotic compression model obtained using the equation of state for cut spheres ($\xi^* = 1/15$).¹⁶³ As an extension of the previous study, Van der Beek *et al.*,¹⁹³ also elucidated the effect of gravity and aspect ratio through variation of the ionic strength. Similarly, an I-N biphasic suspension became triphasic (I-N-C) after several months. Wijnhoven *et al.*,²²³ analyzed the competition between sedimentation, gelation and liquid crystal formation in gibbsite platelet suspensions for five different platelet size and three different ionic strengths. For the final macroscopic appearance, sedimentation is the most decisive factor for large platelets, whereas for small particles phase separation occurs first and sedimentation has a lower influence.²²³ Very recently, Kleshchanok *et al.*,²²² observed for gibbsite platelet suspensions subjected to depletion attraction by silica spheres that sedimentation after several months could induce liquid crystal formation. Surprisingly, this sedimentation

conducted to a highly organized columnar state, which was confirmed via x-ray diffraction.

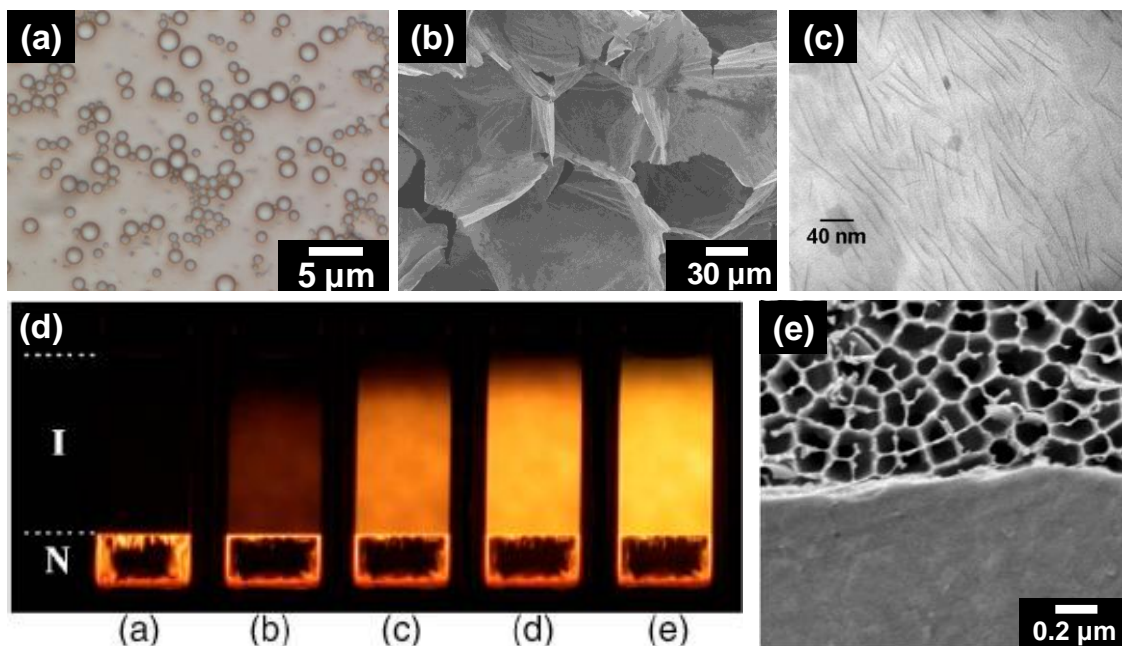


Figure 6. Applications of discotic colloidal systems. (a) Optical micrograph of a Pickering emulsion stabilized by Janus and Gemini nano-sheets of ZrP. (b) SEM image of a Pickering foam stabilized by amphiphilic and high-aspect-ratio ZrP nano-sheets. (c) TEM micrograph of an epoxy/ α -ZrP nanocomposite. (d) Magnetic-field-induced birefringence in the isotropic phase of a gibbsite platelet suspension at horizontal magnetic fields of 0, 0.5, 1, 1.5, and 2 T, respectively. (e) SEM image (top view) of a uniform and well-packed deposit composed of highly-oriented nano-sheets made by filtration of an MFI nano-sheet suspension through an anodized alumina membrane (pore size of ~ 200 nm).

1.4 Applications of Discotic Colloids

1.4.1 Interfacial Stabilizers

There is a renewed interest of Pickering stabilized systems in recent years. Pickering systems such as emulsions and foams are solely stabilized by solid particles. The ability of solid particles to stabilize gas-liquid and liquid-liquid interfaces has been

fully investigated during the last decades.²²⁶ Interfacial stabilization is achieved once the energy of the system is reduced as solid particles are adsorbed onto the liquid-liquid or the air-liquid interface. The high desorption energy and the resulting capillary effects of solid particles have been recently explained.²²⁷⁻²²⁹ Pickering stabilization is indeed influenced on size,^{230, 231} shape,^{232, 233} aspect ratio,²³⁴ concentration,²³⁵⁻²³⁸ and hydrophobicity²³⁸⁻²⁴¹ of particles at the interface.^{234, 242-245} Previous theoretical studies have demonstrated that spherical,²⁴⁶ rod-like,²⁴⁶ and discotic²⁴⁷ particles can be utilized as Pickering stabilizers. Particularly, discotic particles having a high aspect ratio ($\zeta = 2R_d/h$) can be good interfacial stabilizers.^{234, 248} Amphiphilic nano-sheets were fabricated from block-copolymer cross-linking,^{249, 250} graphite exfoliation,^{251, 252} block-copolymer graphene modification,^{253, 254} and crushing of inorganic^{255, 256} and polymer-inorganic²⁵⁷ hollow silica spheres. These type of particles have been applied to emulsify immiscible liquids,^{251, 255, 258} and to develop polymer composites.²⁵⁸ Recently, we successfully stabilized oil- and air-water interfaces (**Figure 6a,b**) using amphiphilic nano-sheets obtained from the exfoliation of ZrP crystals.^{259, 260} Suspensions of ZrP nano-sheets are not able to stabilize air-water or liquid-liquid interfaces, since these highly anisotropic particles are extremely hydrophilic due to the presence of hydroxyl (–OH) groups on the particle surface.⁷⁸ In our work, Pickering foams and emulsions were stabilized using surface-functionalized nano-sheets with propylamine (C₃H₇NH₂, PA)²⁵⁹ and octadecyl-isocyanate²⁶⁰ as shown in **Figure 6b** and **Figure 6a**, respectively. In the former study, we found that using low and high aspect ratio nano-sheets having a high and an intermediate degree of hydrophobicity, respectively, is the successful formula to

obtain high foam stability. Highly stable Pickering aqueous foams have been previously obtained from suspensions containing plate-like Laponite particles and nonionic²⁶¹ and cationic surfactants.^{232, 262} The effect of laponite hydrophobicity was studied using short chain amphiphile molecules like sodium butyrate on LDH²⁶³ and hexylamine on Laponite.²⁶⁴

Lagaly *et al.*,^{265, 266} revealed that highly anisotropic plate-like clay particles along with nonionic surfactants could be used as stabilizers for Pickering emulsions by creating a mechanical barrier to prevent coalescence. In the same way, Laponite only²⁶⁷ and along with amines and surfactants^{232, 261, 262, 264} and layered double hydroxides (LDH) modified with sodium butyrate,²⁶³ have served as interfacial stabilizers. Interestingly, phase inversion has also been observed.²⁶⁸ Laponite suspensions have also been applied to fabricate latex via Pickering miniemulsion polymerization.^{269, 270} These latex particles were obtained from microcapsules composed of a coagulated particle shell that resulted from Pickering stabilization, also called colloidosomes.²⁷¹⁻²⁷⁴

1.4.2 Polymer Composite Nanofillers

Polymer nanocomposites filled with inorganic layered materials at nano-scale have received enormous research attention due to the potential improvement of the polymer properties such as permeability,²⁷⁵ mechanical and structural properties,²⁷⁶ and electrical and thermal conductivity.²⁷⁷ Whilst the polymer light weight is typically maintained by using little nanofiller amounts (~1-3%),¹⁰⁶⁻¹⁰⁹ optimal cost and reinforcement efficiency is of great importance. Although several layered materials can

be found in literature (*e.g.*, Laponite,⁷⁶ LDHs,⁹² niobates,^{81-83, 93-98} phosphates,^{81, 82, 99-101} titanium oxides,^{81, 84} and metal chalcogenides,¹⁰²⁻¹⁰⁴ etc) scientists have commonly embedded exfoliated layered silicate crystals on a wide variety of polymer matrix.²⁷⁸⁻²⁸² For instance, layered materials have been utilized to fabricate biodegradable polymer composites.^{283, 284} Synthetic clay has also been applied to obtain polymer nanocomposites. Compounds such as epoxy-ZrP nanocomposites (**Figure 6c**)^{285, 286} have been fabricated, where the mechanical properties have been characterized²⁸⁷⁻²⁸⁹ and the effect of nano-sheet aspect ratio was elucidated.²⁹⁰ The useful properties of graphene and its derivatives have been utilized to produce functional composites. Some applications can be highlighted such as the Li-ion batteries, supercapacitors, fuel cells, photocatalysis,²⁹¹ paper,²⁹² and photovoltaic devices.²⁹³

1.4.3 Rheological Modifiers

As previously mentioned, clay is commonly known as a great family of minerals composed of elements such as magnesium, aluminum, silicon, and oxygen arranged in a sheet-like structure. In the oil and gas industry, clay is mined from surface pits and utilized in drilling fluids.²⁹⁴ A common clay material used as additive to increase the density of drilling muds for oil extraction is sodium montmorillonite (*i.e.*, bentonite).^{105, 295} Due to its plate-like shape, bentonite suspensions behave differently compared to sphere suspensions.^{296, 297} In fact, due to difficult interactions between highly anisotropic colloidal particles, suspensions can evolve into sol-gel transitions. For instance, as the nano-sheet concentration increases, the particles present a rotation reduction due to their

large excluded volume interactions as well as long inter-particle forces. Namely, for large aspect ratio nano-sheets the excluded volume is greater than the physical volume. Therefore, particle motion is geometrically constrained at reduced volume fractions.²⁹⁶ In addition electrostatic interactions play an important role in the sol-gel transition. Mourchid *et al.*,¹⁸⁷ reported the phase diagram of plate-like charged colloidal dispersions in terms of particle concentration and ionic strengths and shear rheology was applied to localize the sol-gel phase transition. Finally, Paineau *et al.*,²⁹⁸ presented a systematic study to assess in depth the static and dynamic rheological behavior of aqueous suspensions to analyze the repulsion influence on the mechanical properties. Interestingly, they found a better orientation of clay particles for stronger repulsive orientations and a sol-gel transition dependency on particle size.

1.4.4 Manipulation of Liquid Crystals Using External Forces

There is a renewed considerable attention in mineral colloidal liquid crystals because of their remarkable optical properties and potential applications. External forces such as shear,²⁹⁹⁻³⁰⁴ magnetic,^{305, 306} and electric^{295, 307} forces have been utilized to re-orient nano-sheet suspensions due to their high susceptibility. Shear flow aligning can be initiated by shaking a suspension of highly anisotropic nano-sheets. During this process, a transient birefringence from a temporal ordering of these anisotropic nano-sheets has been visualized through crossed polarizers for isotropic montmorillonite^{299, 300}, hectoritepoly (ethyleneoxide),³⁰¹⁻³⁰³ and montmorillonite-polybutadiene systems³⁰⁴

suspensions. Eventually, the birefringence vanishes after a certain period of time (*i.e.*, relaxation time), which is proportional to nano-sheet concentration.

During the I-N transition, a gain in the orientational order is expected; therefore the influence of an external-aligning force along with the anisotropic morphology of the nano-sheets will positively influence on the phase transition. A system hard colloidal plate-like gibbsite were magnetically-induced from the isotropic into a *paranematic* state, shifting the I-N transition to lower volume fractions (**Figure 6d**).^{305, 306} Interestingly, a nematic single domain was obtained using a rotating field.³⁰⁶ Liquid crystals of nano-sheet suspensions have also been aligned at various magnetic fields and times. For instance, suspensions of V_2O_5 ³⁰⁸⁻³¹⁰, nontronite/Fe,^{21, 311} $H_3Sb_3P_2O_{14}$,¹⁰¹ fluorohectorite,³¹² and niobates.³¹³ This birefringent alignment can also be enhanced by doping the nano-sheets with magnetic molecules. Kim *et al.*,³¹⁴ presented a magnetic-aligned colloidal suspension of surface-modified niobate nano-sheets with magnetic nanoparticles.

Using electric fields, liquid crystals of nano-sheet suspensions have also been investigated. Dozov *et al.*,³¹⁵ and Nakato *et al.*,³¹⁶ studied the electro-optic response of beidellite and niobate nano-sheet suspensions, respectively. Paineau *et al.*,³¹⁷ also aligned beidellite plate-like suspensions by applying electric fields and obtained an increase in the nematic order parameter of about 0.8. An interesting point for niobate suspensions was that the larger lateral-dimension (*i.e.*, large anisotropy) nano-sheets presented a greater response compared to the smaller ones. Also, by switching the

electric field on and off several times, the growth of a large crystalline domain was induced.

1.4.5 Catalytic Frameworks

Tsapatsis *et al.*,³¹⁸⁻³²⁰ have introduced a highly-selective and -crystalline set of frameworks with tailored properties made from orthogonally-linked zeolite nano-sheets (**Figure 6e**). The synthesis of these materials applies the *house-of-cards* described in an earlier section to allow them to pack into mesoporous supports.³¹⁹ Microporous structures have gained great attention due to their gamut of applications such as adsorption, catalysis, and ion exchange. These novel materials are characterized of an extremely large external surface area and reduced pore diffusion length in comparison to conventional MFI zeolites that allows an easy access to chemical catalysts.^{320, 321} We believe that branching zeolites nano-sheets via twinning or intergrowth processes is a low-cost approach to produce hierarchical materials with an interconnected microporous structure.³²⁰

1.5 Summary and Conclusions

We have reviewed the recent progress on synthesis, liquid crystals states, and current applications of discotic colloidal suspensions. The recent explosion of discotic systems at colloidal scale has resulted in the study of the previous predicted self-assembled structures. Due to their two-dimensional morphology and tailored colloidal interactions, these systems are versatile in a myriad of applications.

1.6 Outline of the Dissertation

The central aim of this dissertation was originally motivated to experimentally investigate the effects of particle aspect ratio and size polydispersity on the phase diagram of discotic colloids. We also demonstrated the development of the thinnest amphiphilic disk-like particle reported in literature called Janus and Gemini, which were eventually used to stabilize long-lasting Pickering emulsions. Similarly, amphiphilic nano-sheets were utilized to produce Pickering foams. The different studies reported in this dissertation have been triggered off by the motivation to mass-produce novel discotic colloids with well-controlled uniformity in size, shape, and aspect ratio.

This dissertation is organized as follows:

In **Chapter II**, we deal with the synthetic and theoretical principle to control the disk morphology of uniform wax discotic particle fabricated by inducing an intermolecular phase transition of wax molecules inside the emulsion droplets.

Subsequently, in **Chapter III**, we investigate the strong dependency of the I-N transition of discotic suspensions on the aspect ratio via control of the sizes of pristine zirconium phosphate (ZrP) layered crystals and subsequent exfoliation to monolayers. Also, a new temperature-responsive discotic nematic hydrogel was synthesized using extremely large aspect ratio ZrP nano-sheets embedded into a polymer network.

In **Chapter IV**, we develop Pickering emulsions and foams stabilized by high-aspect-ratio nano-sheets. We also demonstrate the fabrication of Janus and Gemini nano-sheets, which are either surface- or edge-modified plates with a thickness at atomic scale. In addition to the generation of amphiphilic and high aspect ratio nano-sheets,

crucial fundamental mechanisms that allow Pickering interfacial stabilization are also investigated, including the effect on the adsorption properties of particle aspect ratio, concentration, and hydrophobicity. Our study is of great interest in the scientific community due to the difficulty in generating a discotic colloidal system of controllable parameters that allows a systematic study in this regard.

Finally, in **Chapter V** we present the main conclusions, ongoing projects and future work of this dissertation.

CHAPTER II

LOW ASPECT RATIO COLLOIDAL DISKS*

2.1 Synopsis

We present here a novel colloidal discotic system: the formation and self-assembling of wax microdisks with a narrow size distribution. Uniform wax emulsions are first fabricated by electrospraying of melt α -eicosene. The size of the emulsions can be flexibly tailored by varying the flow rate of the discontinuous phase, its electric conductivity, and the applied voltage. The process of entrainment of wax droplets, vital for obtaining uniform emulsions, is facilitated by the reduction of air-water surface tension and the density of the continuous phase. Then uniform wax discotic particles are produced via phase transition, during which the formation of a layered structure of the rotator phase of wax converts the droplets, one by one, into oblate particles. The time span for the conversion from spherical emulsions to disk particles is linearly dependent on the size of droplets in the emulsion, indicating the growth of a rotator phase from surface to the center is the limiting step in the shape transition. Using polarized light microscopy, the self-assembling of wax disks is observed by increasing disk concentration and inducing depletion attraction among disks, where several phases, such

* Reprinted with permission from “Uniform discotic wax particles via electrospray emulsification” by A. F. Mejia, P. He, D. Luo, M. Marquez and Z. Cheng, 2009. *Journal of Colloid and Interface Science*, 334, 22-28, Copyright 2009 by Elsevier.

Reprinted with permission from “Surface-controlled shape design of discotic micro-particles” by A. F. Mejia, P. He, M. Netemeyer, D. Luo, M. Marquez and Z. Cheng, 2010. *Soft Matter*, 6, 4885-4894, Copyright 2010 by The Royal Society of Chemistry.

as isotropic, condensed, columnar stacking, and self-assembly of columnar rods are present sequentially during solvent evaporation of a suspension drop.

We also demonstrated experimentally and theoretically the principle to control the discotic morphology of particles with a layered internal structure. The packing of surfactants tailored the curvature and set the shape of the elastic membrane produced as the surface of the emulsions crystallized via surface freezing. Using these membranes as the nuclei, emulsions crystallized from the surface to the centre, forming a layered structure. The final shape of the disks could be either biconcave or flat circular depending on the defect structures of the layers. We confirmed that the final aspect ratio of these disks could be controlled varying co-surfactant concentration on the surface. We also showed that the morphology of anisotropic particles is vital to their self-assembling behaviours. This surface controlled organization of molecules and colloids offers novel routes for soft material design, fabrication, and utilization at micro-scales.

2.2 Uniform Discotic Wax Particle Synthesis by Electrospray Emulsification

2.2.1 Introduction

Wax emulsions find wide applications in cosmetics,³²² waterproof paints,^{323, 324} adhesives,³²⁵ oil well fracturing,³²⁶ self-polishing emulsions for floor care,³²⁷ and fruit preservatives.³²⁸ They are also good model systems to investigate crystal nucleation and the growth of hydrocarbons, polymers, surfactants, and lipids.³²⁹⁻³³²

Here, however, we are interested in the shape transition of wax emulsions^{45, 46} to fabricate discotic colloids. Colloids exist in a variety of shapes,¹ such as spheres, rods,

and disks. Disks are the least studied despite of their significance in research in petroleum (asphaltenes in the heavy oil are nano-disks),¹¹ biology (red blood cells are micro-platelets),¹⁴ and agriculture (soils are aggregations of nano-disks).^{8, 333} Estimating the amount of research on spheres, rods, and disks, Lekkerkerker (<http://www.engr.udel.edu/Colloids2007/plenary.html> and private communications) found that spheres account for about four times the amount of research as rods, and about 80 times the amount as disks. Research has been conducted on micrometer-sized platelets,¹⁵⁻¹⁷ nanometer-sized disks in clay,¹⁸⁻²¹ synthetic clay²²⁻²⁵ or nano-crystals,²⁶ and lithographically fabricated particles²⁷⁻²⁹; however, there is a critical need to establish a model system of discotic colloidal particles with uniform size in a few microns.³⁰⁻³⁶ Current synthetic discotic colloidal systems often have a size distribution, as large as 17%.^{15, 17} Particle polydispersity, which is a collection of particles in a broad range of size dimensions, affects phase transitions of suspensions.^{37, 38} For an example, a dispersion in particle size can suppress crystallization in hard sphere colloids.³⁹ As for liquid crystals, polydispersity influences both the isotropic-nematic^{40, 41} and the nematic-smectic^{43, 44} transitions. Recent experiments demonstrated a fractionation in the thickness of platelets between the coexisting phases, where the thicker platelets accumulated in the isotropic phase.⁴² Therefore, the insight into the dependence of liquid-crystalline phases on the polydispersity in diameter and thickness of disks requires further study through experiments,¹⁷ theories, and simulations.^{205, 334, 335} The pioneering work of preparing discotic wax particles was done by Mason⁴⁵ via shearing hot α -eicosene into a highly concentrated aqueous solution of sodium dodecyl sulfate (SDS) and lowering the

temperature to induce the shape-change of the wax emulsions. It was difficult, however, to control the size and size distribution of the final particles obtained with this conventional emulsification method. Here, we seek ways to produce uniform wax emulsions with the aid of the electric field, thereby creating uniform colloidal disks.

The production of monodisperse aerosols using electrospray has been thoroughly studied³³⁶⁻³⁴⁴ and extensively applied.^{343, 345-354} Loscertales and Barrero *et al.*,³⁵⁵ have demonstrated the production of stable electrospray in insulator baths with potential application in microencapsulation^{352, 356} and the possibility of scale-up using multiple nozzles.³⁵⁶ When a high electric field is applied to a liquid in a capillary, the liquid forms a conical meniscus through which a fine liquid ligament is ejected. The liquid ligament further breaks into a spray of droplets downstream. The production of fine droplets is governed by the voltage applied to the capillary, the liquid flow rate and electric conductivity, surface tension, viscosity, and dielectric constant of the liquid.³⁵⁷⁻³⁶⁰

We produce uniform wax emulsions using electrospray. The process sequence is droplet formation via electrospray, suspension formation via droplet entrainment (drop entering into the collection fluid) into the continuous phase, and emulsion stabilization in mixed ethanol and water solutions. The emulsion droplets are further converted into disks by lowering the temperature to solidify the wax. The shape-changing kinetics from emulsions to disks are characterized by dynamic light scattering. Finally, self-assembling of microdisks is achieved by solvent evaporation from a droplet of the suspensions.

2.2.2 Materials and Methods

2.2.2.1 Discontinuous Phase Preparation

The wax of α -eicosene (Sigma-Aldrich, St. Louis) was used as received, with 1% (w/w) of Stadis-450³³⁷ (Octel Starreon, Newark, Delaware) added to increase electrical conductivity.

2.2.2.2 Continuous Phase Preparation

A mixture of 200 mL of ethanol and water (80/20 w/w) was prepared, to which 0.005 wt% of Tergitol 15-S-9 (Sigma-Aldrich) and 20 mM of sodium dodecyl sulfate (SDS) was added. This mixture was used to collect the wax droplets in a 500-mL beaker, as illustrated in **Figure 7(a)**.

2.2.2.3 Electrospray Setup

Liquid wax was introduced through a metallic needle using a syringe pump. An electric heater was used to maintain the temperature of α -eicosene above its melting point (26°C). A digital signal generator (Model DS345, Stanford Research System, Sunnyvale, Calif.) and a high-voltage amplifier (Model 609E-6, Trek, Inc. Medina, N.Y.) provided the required high electric voltage. The positive electrode was connected to the top end of the needle, beneath which was a grounded circular wire. The distance between the tip of the needle and the surface of the collection solution was kept constant at 7 cm. The solution was heated to adjust the density and surface tension of the collection fluids. A magnetic stirrer was used to homogenize the resulted emulsions. A

stable Taylor cone was observed (**Figure 7 (b)**) with a voltage range from 2.6 to 2.9 kV using a fast camera Phantom V4.2 (Vision Research, Wayne, N.J.). For α -eicosene flow rate ranging from 1 ml/hr to 30 ml/hr, the jetting liquid from the cone broke into fine droplets with a fairly narrow size distribution.

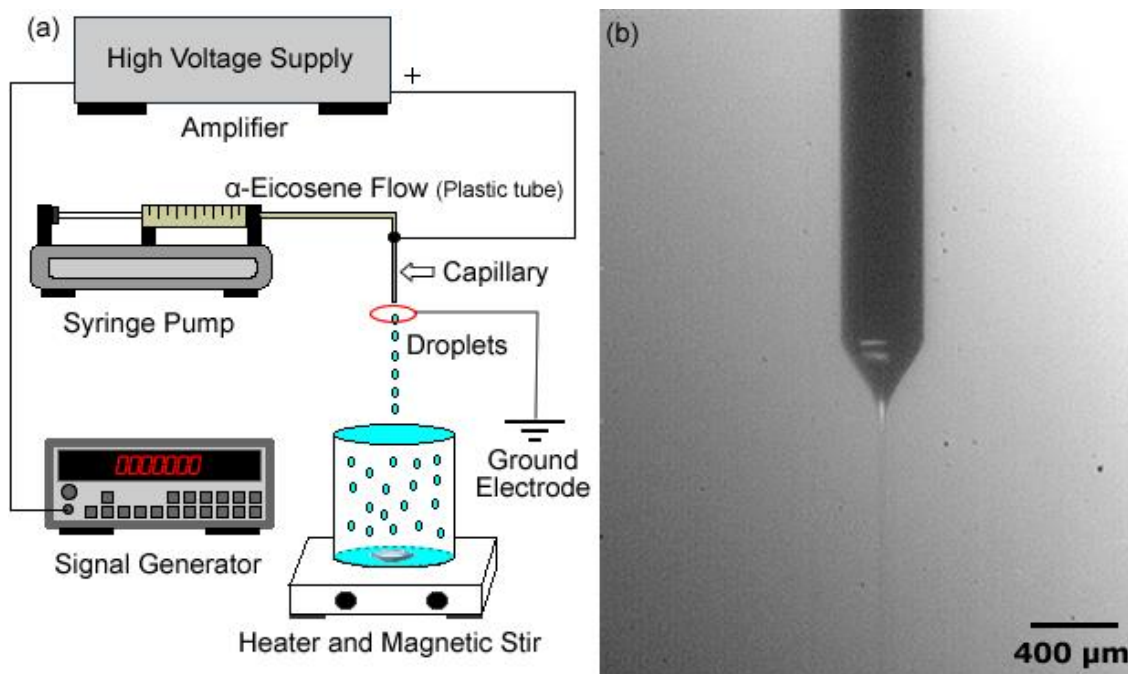


Figure 7. Electrospray emulsification. (a) Schematic setup. A strong electric field is generated between a capillary needle and a ground wire-ring. The collection fluid is heated to tune the density and surface tension, and stirred to facilitate drop entrainment. (b) Micrograph showing a stable cone-jet mode of electro-spray captured by a fast camera.

2.2.2.4 Emulsion Preparation

Ethanol was added to the collection solution to match the density of wax, and was later evaporated at room temperature to reduce the solubility of α -eicosene. Before the evaporation of ethanol, another 160 mL of water was added to prevent aggregation arising from the increase of SDS concentration after evaporation. (SDS micelles will

introduce depletion attraction between wax droplets⁴⁵.) By controlling the surfactant concentration, we were able to obtain stable emulsions. The sample was kept at low temperature (4°C), and checked frequently for morphological changes of wax particles using polarizing optical microscopy (TE-2000U, Nikon). The dynamic light scattering (DLS) measurement was performed on a ZetaPALS zeta potential analyzer (Brookhaven Instrumentation Corporation, Holtsville, N.Y.).

2.2.3 Results and Discussion

2.2.3.1 Conductivity, Flow Rate and Applied Voltage of the Disperse Phase

In electrospray, the droplet size is controlled predominantly by the liquid flow rate and secondarily by the applied voltage (**Figure 8**), but is independent of the capillary size.³³⁷ The power law fit shows the dependence of the wax droplet size on the flow rate. The final droplet size increases with the flow rate. The data also shows that the final size of the emulsions can be flexibly manipulated. For a given liquid, the Taylor cone can only be established in a certain range of liquid flow rates and voltages, which depend on the electrical conductivity of the liquid. As the conductivity increases, the range shifts toward smaller flow rates, and smaller droplets are generated in the spray.³³⁷ The electrical conductivity of wax is linearly dependent on the concentration of the added Stadis-450. In our experiments, the desired conductivity ($4.1 \times 10^{-8} \text{ S}\cdot\text{m}^{-1}$) is achieved at 1 wt.% of Stadis-450 concentration.

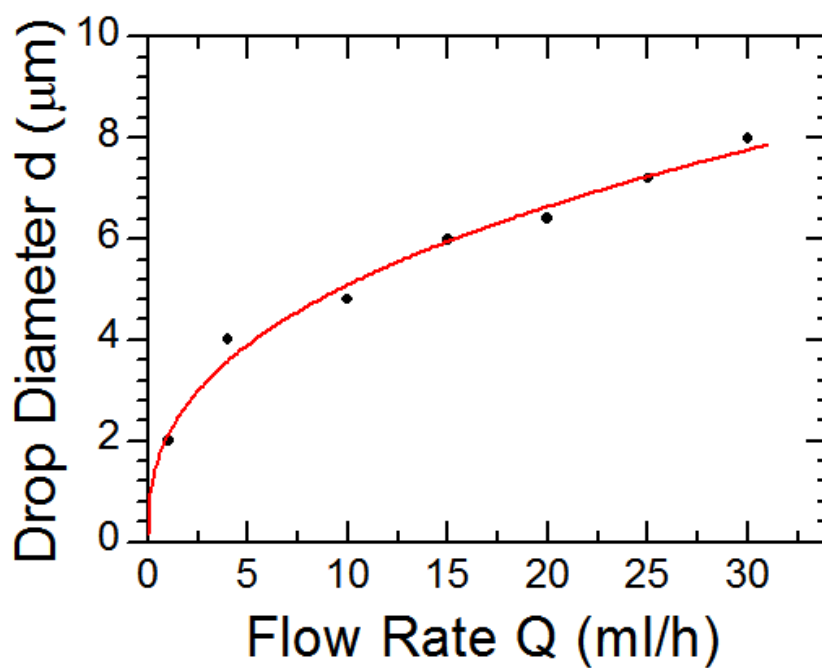
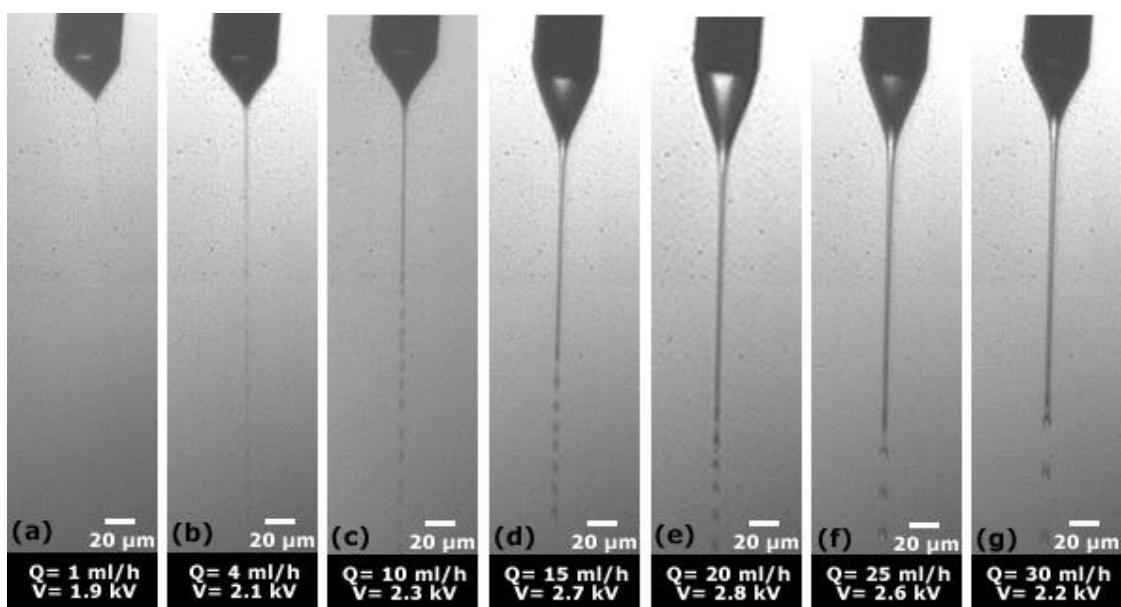


Figure 8. Size control of emulsions with flow rate. Data are plotted for size variation of wax droplets by flow rate from 1 ml/h to 30 ml/h. The line is the power law fitting to the data, $d = (2.1 \pm 0.2)Q^{0.38 \pm 0.03}$.

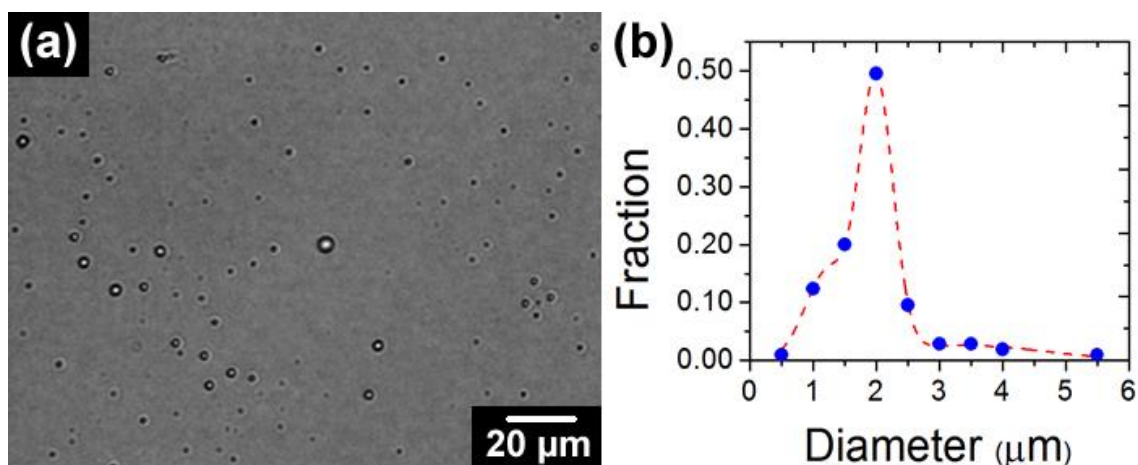


Figure 9. Polydisperse wax emulsions when the density and the surface tension of wax mismatch that of the continuous phase. (a) Size polydispersity is evidenced when wax droplets are collected in solution. (b) Droplet size distribution. The polydispersity is estimated as high as 25%. The collection fluid is 20 mM SDS aqueous solution. The flow rate is 4 ml/h and the applied voltage is 2.8 kV.

2.2.3.2 Characterization of α -Eicosene Droplets

The micrographs captured by the fast camera, as shown in **Figure 8**, demonstrate the uniform wax droplets produced in electrospray. We measure the size distributions of the wax droplets using optic microscopy after cooling the emulsions to room temperature. **Figure 9** shows the particles collected using pure water, with no ethanol added. The polydispersity in size was evident (**Figure 9(b)**). When particles rise to the water-air interface due to buoyancy force, they coalesce with the incoming newly produced droplets from electrospray, as indicated by the chunks of wax found on the air-water interface. Using an ethanol-water solution and optimizing collection temperature, we were able to reduce the mismatch in density and surface tension. The droplets enter the solution immediately after they touch the solution surface.²⁰ We found that surface aggregation of the droplets was prevented by using 80/20 w/w ethanol/water solution

with density close to that of the α -eicosene. At 40°C, the density of water is 0.992 kg/m³; ethanol, 0.773 kg/m³; α -eicosene, 0.795 kg/m³; and 80/20 w/w ethanol/water solution, 0.817 kg/m³.³⁶¹

Drop entrainment is also complicated due to the finite difference in interfacial tension between air-water and air-wax droplets. Experiment by Li and Wang showed that the falling drops of wax often spread on the surface rather than entering the water. Due to the hydrophobic nature of wax, a positive spreading coefficient S is obtained by the following definition,³⁶²

$$S = 2\sqrt{\sigma_p}(\sqrt{\sigma_c} - \sqrt{\sigma_p}) \quad (1)$$

Where $\sigma_c = 23.5 \times 10^{-3} N/m$ is the surface tension of ethanol/water solution³⁶¹ at 80/20 and $\sigma_p = 29 \times 10^{-3} N/m$ is the α -eicosene surface tension,³⁶³ both at 40°C. When the surface tension of water is greater than the wax droplet, the spreading coefficient is positive, causing the droplet to spread out. The spreading coefficient must be made negative to allow the droplets to enter the water intact. This requirement can be met by reducing the surface tension of water using ethanol and surfactants. We add Tergitol 15-S-9, a nonionic secondary ethoxylated alcohol to the collection liquid, which controls the surface tension effectively.³⁶⁴

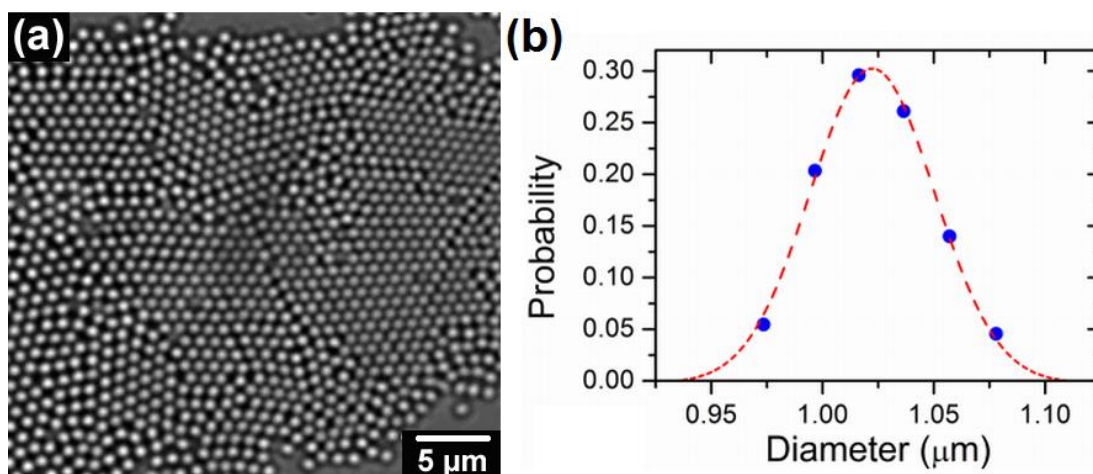


Figure 10. Monodisperse wax emulsions produced with a collection solution of 80 %wt. ethanol, 20 %wt. water, 0.005 %wt. of Tergitol 15-S-9 and 20mM SDS. The flow rate is 4 ml/h and the voltage is 2.8 kV. (a) Micrograph of the hexagonal lattices of emulsion droplets confirms size uniformity. (b) Droplet size distribution measured by dynamic light scattering. The diameter of the droplets is $1.02 \pm 0.03 \mu\text{m}$, and the polydispersity is $2.7 \pm 0.1\%$ (Standard deviation of the size distribution divided by the mean size).

Figure 10 shows the DLS measurement and an optical image of wax droplets collected using 80/20 (w/w) ethanol/water mixture and 0.005% Tergitol surfactant. The spherical wax droplets were $1.02 \pm 0.03 \mu\text{m}$ in diameter, according to the DLS measurement. The polydispersity was $2.7 \pm 0.1\%$ (**Figure 10(b)**). Ordered lattice structures were observed by increasing the concentration of droplets using evaporation, which confirms the narrow size distribution of the droplets (**Figure 10(a)**). We can fabricate monodisperse wax emulsions (which later transform into monodisperse discotic particle suspensions) ranging from $1 \mu\text{m}$ to $5 \mu\text{m}$ by varying the flow rate. Sub-micron emulsions can be produced by further reducing the flow rate and increasing conductivity. We have obtained some $0.5 \mu\text{m}$ emulsions.

Table 2. Comparison of different methods for the production of emulsions and colloids

	Microfluidics	Heating and shear mixing	Inorganic Crystal growth	Membrane Emulsification	Emulsification in Viscoelastic Media	Electrospray (This work)
Typical Production Rates	$\leq 10,000$ particles per second	Mass production ~ 500 grams per batch	Mass production ~ 10 grams per batch	Continuous but low production ~60 kg/(m ² *h)	~ 0.1 g/batch	Mass production 0.03 – 15 ml/h
Size	33 - 55 μm	1 – 100 μm	~ 0.2 μm	4.25 – 12.3 μm	1 – 30 μm	0.5 - 10 μm
Polydispersity	2%	25%	17 - 25%	37-65%	5%	2.7%

2.2.3.3 Electrospray Method Compared to Other Emulsification Techniques

We compare the various emulsification techniques in **Table 2**. The electrospray emulsification method can mass produce particle suspensions (mass flux $\sim 0.03\text{--}15$ ml/h), and can control the size and polydispersity by tailoring the physical properties of the materials involved or parameters of the process. By contrast, the emulsification in viscoelastic media³⁶⁵ and the flow focusing microfluidic methods can achieved a good control of the particles size but they cannot mass produce particles as electrospray does. Other methods, such as the heating-shear mixing method⁴⁵ and the inorganic crystal growth produced by Lekkerkerker *et al.*,¹⁶ are lack of controlling the polydispersity of the particles in the suspensions. Finally, the membrane emulsification method³⁶⁶ is not quite good at controlling polydispersity and the particle flux rate is limited.

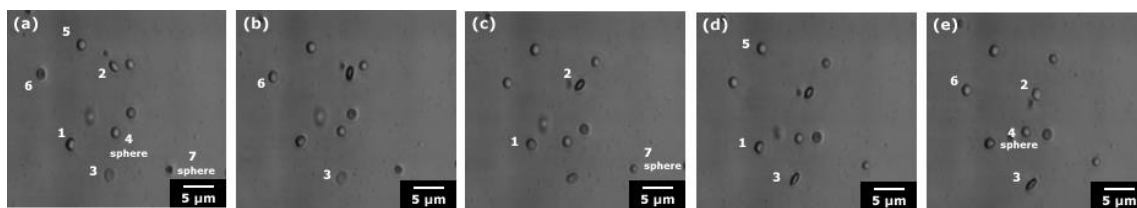


Figure 11. Time sequential optical microscopy images of wax particles after 36 hour-storage at 4°C. The disks (No. 1, 2, 3, 5 and 6) are uniform and have the same inverted aspect ratio of about 1:2. Some of the particles (No. 4 and 7) were still in a spherical shape. Time interval between two consecutive images is 2 seconds.

2.2.3.4 Phase Changing of Wax Emulsions

The samples are kept at low temperature (4°C), and checked frequently for morphological changes of the emulsions/particles using polarizing light microscopy. After 1 day, the shape change of wax emulsions to discotic particles with an inverted

aspect ratio of 0.5 (thickness/diameter) was observed. Depending on time, some wax droplets switch into disks while some others remain as spheres, as shown in **Figure 11**.

No separation procedure of spheres from disks (as done by Mason⁴⁵) are performed. The conversion from spheres to disks requires several days for large-sized droplets, and the percentage of conversion increases with time. We use DLS to monitor the change of the apparent size, which increases as the emulsions solidify (**Figure 12(a)**) from spheres into disks. An ultrasonic emulsification method is used to produce the small-sized emulsions. **Figure 12(b)** shows that the shape-changing time depends on the size of the initial emulsions. Due to the surface freezing of α -eicosene,³⁶³ the phase transition initiates (*i.e.*, nucleates) at the surface, and grows inward to the center to complete. The linear dependence (power law fit to the data in **Figure 12(b)** gives $n=0.75\pm 0.33$) on size demonstrates that growth process is the time-limiting step. If nucleation of the rotator phase at the surface is the limited step, the power-law exponent n should be approximately equal to 2.

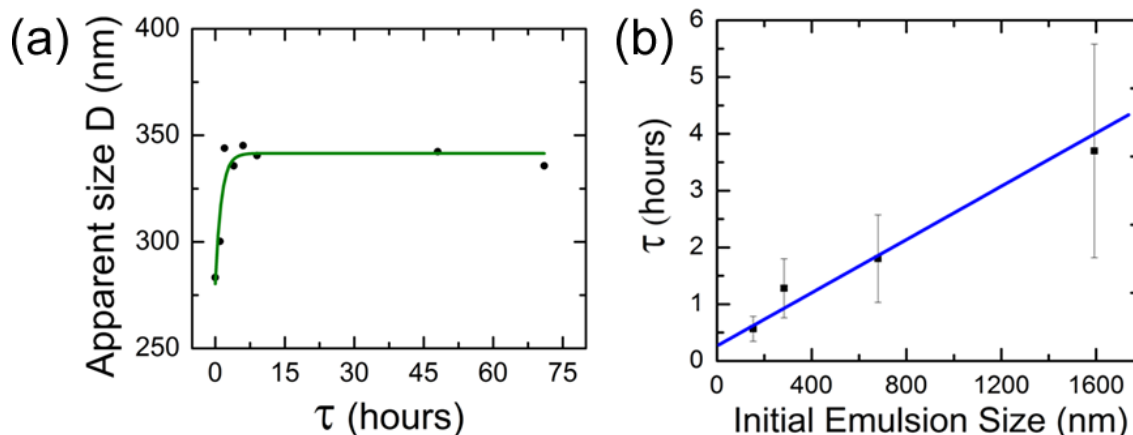


Figure 12. The dependence of shape changing time as a function on the initial size of emulsions. (a) Apparent size of the disks measure by DLS in the course of shape changing. The solid line is the exponential growth fit to the data:

$$D = (341.5 \pm 4.8) - (61.2 \pm 10.5) \exp\left(-\frac{\tau}{1.28 \pm 0.52}\right). \text{ (b) Shape changing time as a function of initial emulsion size.}$$

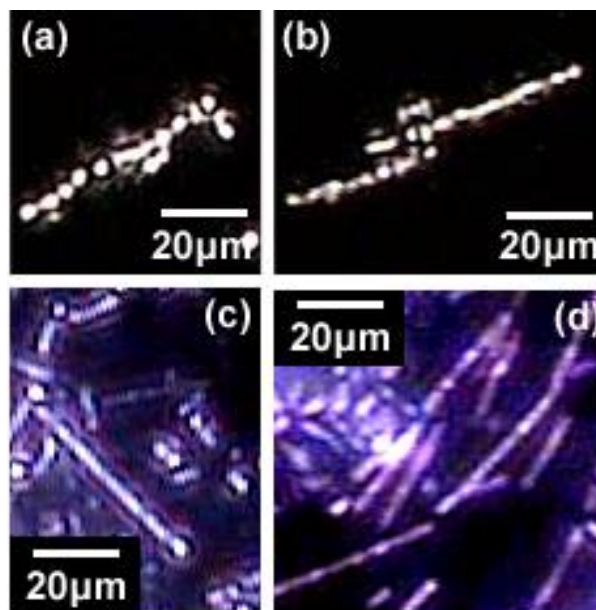


Figure 13. Columnar morphology of rods that are stacked from the wax disks. (a)(b) Rods from polydisperse disks fabricated by emulsification with variation in flow rates. (c)(d) Rods from uniform disks fabricated by emulsification with the same flow rate (4 ml/h).

2.2.3.5 Uniform Discotic Wax Particles

Starting from emulsions of uniform volume, a suspension of uniform disks in diameter and thickness is resulted after the shape change. The straight columnar morphology of the rods from the stacking of the disks and the monodispersity of the columnar width observed in **Figure 13(c)** and **(d)** demonstrates the narrow size distribution of the discotic particles that are transformed from the monodisperse wax droplets. The structure of rods is similar to the stacking of red blood cells in the rouleaux.^{29, 367, 368} As a further demonstration of monodispersity in disk diameters, we contrast the micrographs of rods formed from polydisperse disks and uniform disks. **Figure 13(a)** and **(b)** shows the width variation of rods comprising polydisperse disks fabricated by emulsification varying the flow rate. Rods of higher polydisperse disks can be found in ⁴⁵. **Figure 13(c)** and **(d)** shows rods made from uniform disks fabricated by emulsification keeping the same flow rate (4 ml/h). The polydisperse-disk-rods are less straight with apparent breaks along the rod.

By observation, the disks can be approximated as short circular cylinders.⁴⁵ Consistent with the structure of the rotator phase is the fact that the α -eicosene molecules are perpendicular to the faces as the molecules form layers which stack on each other. The free rotation of the α -eicosene in the molecular layer leads to a two-dimensional symmetry in the layer; hence, the circular faces of the cylinders. Therefore, let us assume two phenomenological surface tensions between α -eicosene molecules and water, σ_1 and σ_2 , being the surface tensions for the circular faces and the edge of the cylinder, respectively.

The total surface energy of the disk is,

$$E_{TOTAL} = 2\pi r^2 \sigma_1 + 2\pi r l \sigma_2 \quad (2)$$

where, l is the thickness and r is the radius of the disk. Assuming a constant volume, V , for each disk, we have,

$$l = \frac{V}{\pi r^2}. \quad (3)$$

Minimization of E_{TOTAL} via the variation of r leads to

$$r = \sqrt[3]{\frac{V\sigma_2}{2\pi\sigma_1}}. \quad (4)$$

Therefore, the inversed aspect ratio of the disk is

$$\xi^* = \frac{l}{2r} = \frac{\sigma_1}{\sigma_2}. \quad (5)$$

This is to say, the physical properties of the rotator phase of α -eicosene determine the aspect ratio of the disks via the surface tensions (σ_1, σ_2). Hence, all disks should have the same aspect ratio. The uniform emulsions produced by electrospray will produce a uniform suspension of disks. Equation (5) shows that the inversed aspect ratio becomes smaller with decreasing σ_1 .

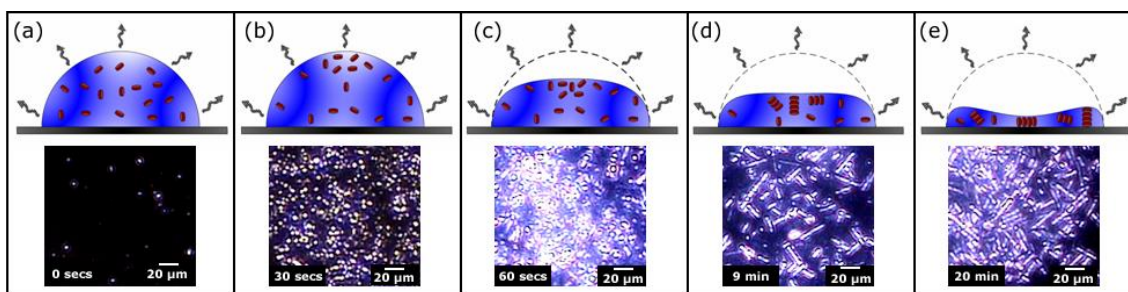


Figure 14. Self-assembling of micro wax disks observed by evaporating a droplet. (a) A droplet of homogeneous suspension was deposited on a glass slide under observation of a polarized optic microscope. Solvent-evaporation starts once the drop is placed on the slide. (b) Influenced by Marangoni's effect, the colloidal disks are taken into the center of the droplet by convection as indicated on the top panel. (c) The evaporation of the droplet continues and the concentration of disks and SDS become higher. Depletion attraction between disks due to the high concentration of SDS micelle leads to the formation of a condensed phase. (d) The disks start to self-assemble into rods inside the condensed phase and flow out. (e) Rods suspension is finally formed toward the end of the evaporation. Pictures below the schematics are cross-polarization optical microscopic images near the top center of the drop.

2.2.3.6 Discotic Liquid Crystalline Phases of Micro Wax Disks via Droplet Solvent-evaporation

The self-assembling of the wax disks is briefly studied by polarizing optical microscopy using solvent-evaporation method from a drop of suspension. At the beginning of this process, the suspension is in the isotropic phase (**Figure 14(a)**). As the solvent evaporates,³⁶⁹ the concentrations of the wax disks and SDS increase, the latter introduces depletion attraction between disks (**Figure 14(b)**) and a condensed fluid phase is obtained (**Figure 14(c)**). In the simulation⁴³ and the experiments on Gibbsites,¹⁵ this condensed phase was not observed due to the absence of attraction. Then, a columnar stacking of disks is formed flowing out from the condensed phase. (**Figure 14(d)**). Finally, the self-assembly of columnar rods is observed (**Figure 14(a)**) as previously reported.⁴⁵

We are able to mass-produce discotic particle suspensions at the rate of a few milliliters per hour (between 0.03 ml/h to 15 ml/h). This new emulsification method is a natural extension to the microfluidic emulsification to produce monodisperse emulsion droplets of tens of microns.^{341, 370, 371} It opens doors to further characterization of discotic colloids, one of the least studied type of colloids, such as their phase transitions and rheology.^{18, 22, 26, 28}

2.2.4 Summary

We have established a new model system of discotic colloids via electrospray of melted wax and demonstrated the phase transitions of the produced suspensions. Using a stable cone-jet mode, spherical droplets of α -eicosene with uniform size are obtained. By tuning the flow rate and conductivity, suspensions of monodisperse wax emulsions with sizes ranging from 0.5 μ m to 5 μ m are obtained. The emulsions can be mass produced at rate between 0.03 ml/h to 15 ml/h. We find that the properties of collection solution, such as density and surface tension, are crucial to the formation of monodisperse suspensions. When the density and the surface tension of wax mismatch that of the continuous phase, the wax particles spread on the air-water interface, producing aggregates of wax and increase the polydispersity of the final emulsions. The formation of the rotator phase of wax converts the emulsions into oblate disks with an aspect ratio determined by the surface tension anisotropy, and the growth of the rotator phase from the surface to the center is the rate determining step in the shape transition. The self-assembling of wax disk is observed by solvent evaporation to induce depletion

attraction. Along with evaporation, phases such as isotropic, condensed, columnar stacking, and self-assembly of columnar rods are revealed. The advantage of producing anisotropic particles in a wide range of sizes with a narrow size distribution will initiate novel routines to the understanding of colloidal behaviors. We anticipate that the novel emulsification method we elaborated here can be also used in biomaterial development and drug delivery.

2.3 Surface-controlled Shape Design of Discotic Micro-particles

2.3.1 Introduction

Surfactants can tailor interfaces essential to many chemical, physical, and biological processes.³⁷² For example, they are used as stabilizers for foam and emulsions, size-controllers for droplets made in microfluidics,³⁷³ adjustors for the organization of liquid crystals,³⁷⁴ growth-regulators for nano particles,³⁷⁵ and area-maintainers for drop evaporation to make DNA chips.³⁷⁶ Here, we use surfactants as a shape transformer for emulsions.

Alkenes crystallize via anomalous surface freezing³⁷⁷ and formation of a rotator phase. The rotator phase is a layered crystalline phase that lacks rotational order about the molecular axis.³⁶³ Colloidal particles of the rotator phase are then composed of equidistant layers. Decreased temperatures cause surface freezing of the alkene droplets. Surfactant adsorption exert forces that shape the solidifying alkene droplets into colloidal disks. When surface freezing establishes an elastic shell for the emulsion droplets, we have found that a mixture of surfactant and co-surfactant can prescribe the

spontaneous curvature of this shell, which in turn leads to the defect structure of the produced micro-disks after the interior of the emulsion crystallizes. Depending on the defect type, the shape of the disks is either flat-circular or biconcave with dimples on their circular faces. The surfactants also set the magnitude of surface-tension anisotropy; hence, the aspect ratio of the produced micro-disks.

Anisotropic particles are models for the study of liquid crystals.^{15, 124} Conventionally, they are either taken directly from nature, such as filamentous viruses,³⁷⁸ DNA,³⁷⁹ microtubules,³⁸⁰ and minerals,¹²² or they are synthesized in the form of inorganic crystals,³⁸¹ polymeric colloids,³⁸² and lithographic particles.²⁸ Colloidal disks are one of the least studied anisotropic particles due to the lack of model systems. Although many examples of platelike particles at the colloidal scale can be found in the literature,^{29, 383, 384} biconcave particles small enough to experience Brownian motion, as we fabricated here, have not been demonstrated so far.³⁸⁵ In addition, self-assembly configuration of the anisotropic particles is determined by their geometric shape and inter-particle interactions; hence, our capability to control their surface roughness and anisotropy dimensions can provide excellent tools for investigation.^{1, 45, 49} Colloidal disks with controllable aspect ratio and polydispersity are vital to the understanding of discotic liquid crystals. Therefore, our results can help to establish a better comprehension of the self-assembly mechanisms in systems of non-spherical colloidal particles such as red blood cells, soils, and asphaltenes.

Our research is closely related to liquid crystal dispersions due to the internal layered structure of our particles. To date, the majority of research in liquid crystal

dispersions has been on nematic droplets,³⁸⁶⁻³⁸⁸ the shape of which is still close to spherical due to the bipolar structure with two defects anchored on the surface.³⁸⁹ Though defect structures of smectic liquid crystals in confinement have long been studied,³⁹⁰⁻³⁹⁷ systematic study on the smectic emulsions has not been performed.³⁹⁸ However, faceted droplets of smectic liquid crystals³⁹⁹⁻⁴⁰² and the laminar (layered) phase of diblock copolymers⁴⁰³ are observed on solid substrates. Smectic phase growth in the isotropic phase has been studied experimentally^{404, 405} and theoretically.⁴⁰⁶⁻⁴⁰⁸

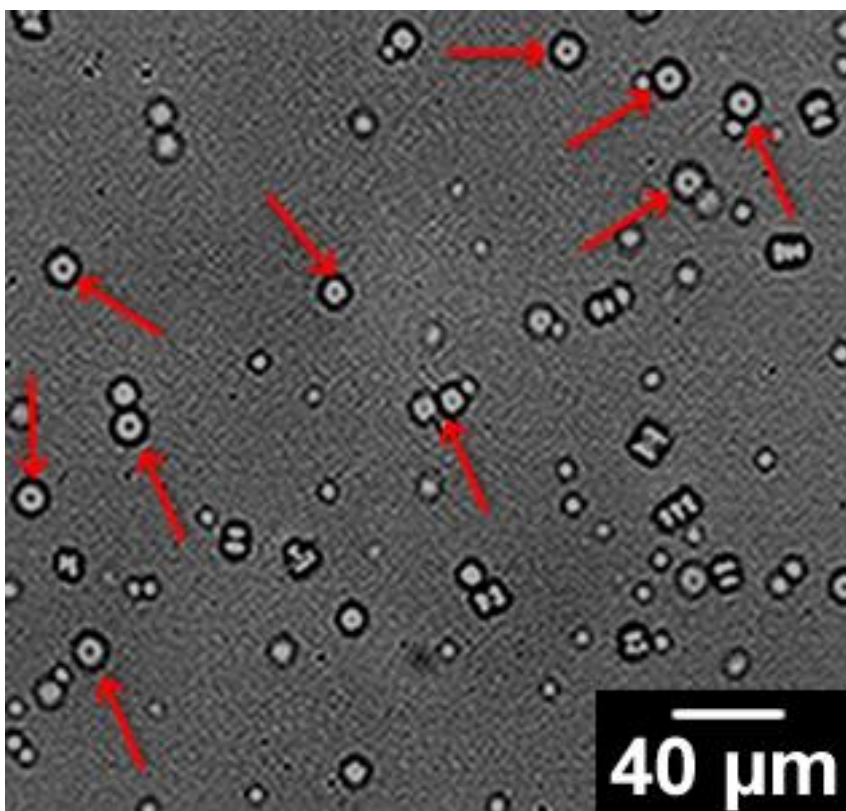


Figure 15. Biconcave α -eicosene disks. Dimples are visible on the circular faces of the disks, indicated by the arrows. Short stacks of the disks are observed as well. (See supplementary **Figure A1a** for the Brownian motion of a disk.) These disks have an aspect ratio ξ about 2, with $\xi = \text{diameter}/\text{thickness}$, and a single defect of a focal conic domain (FCD). See **Figure 17c** and supplementary **Figure A2** for the defect configurations of a layered structure.) The micrograph was taken at room temperature using a Nikon microscope TE-2000U with magnification 60 \times .

2.3.2 Experimental

We fabricated uniform alkene (α -eicosene, a wax) emulsions by a newly developed emulsification method: electrospraying melted α -eicosene at 60°C and collecting the emulsions in 20mM sodium dodecyl sulfate (SDS) solution producing micron-sized emulsions.⁴⁷

The emulsions were cooled down to room temperature and kept at 4°C in a refrigerator. Alkenes go through surface freezing that their surfaces crystallize at temperature right above their bulk melting temperature.⁴⁰⁹ At the melting temperature of α -eicosene 26°C, surface freezing created a crystalline monolayer around our wax droplets that would act as the nuclei of the rotator phase as temperature decreased. Then rotator phase grew from the surface towards the center, fabricating the disks. The surface freezing process took place at the early stage of the cooling, where the temperature was higher than 20°C; hence, the Krafft temperature, which is about 15°C, did not affect the surface freezing.

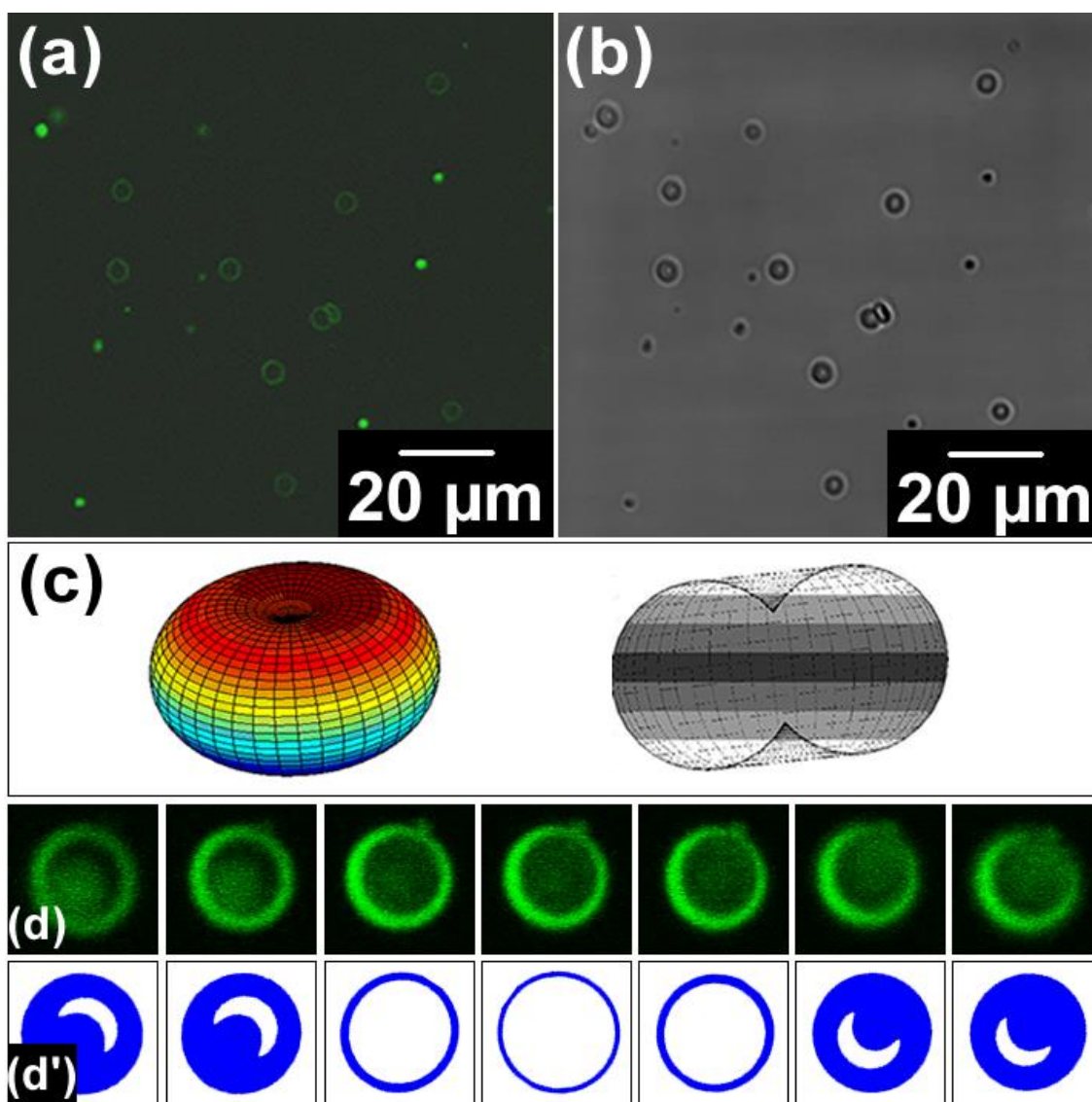


Figure 16. Biconcave α -eicosene disks. (a) Confocal micrographs. Biconcave disks coated with Nile red are displayed as rings. Magnification 60x. (b) Confocal reflective image at the same position as (a). (c) The spindle torus that represents the surface coating of the Nile red dye on the disks. The dimples of the torus appear as black dots on the circular faces in **Figure 15**. (d) Sequential confocal images cutting through a single disk. Magnification 150x. (d') Regenerated image slices using Matlab from a tiled spindle torus as illustrated in (c), where gray stripes stand for imaging slices. (a),(b) and (d) were taken at room temperature using a Leica confocal microscope TCS SP5.

The disks were imaged under polarizing optical microscopy (TE-2000U, Nikon) at room temperature. (See Supplement **Figure A1**.) The obtained solidified particles

exhibited a morphology that remarkably resembles that of red blood cells (RBCs) as shown in **Figure 15**. Dimples were obvious on the circular faces of the disks (Supplementary **Figure A1a**). They manifest in the torus structure as molecular layers of the rotator phase (**Figure 16c** and **Figure 17c**). **Figure 16d** shows slides of confocal images when the laser scanned through a single disk as illustrated in **Figure 16c**. Since the Nile red dye coated only the surface, the middle slices were rings (**Figure 16a**), while the slices near the top and bottom were partially filled rings due to the tilt of the disk with respect to the laser scanning plane. Images regenerated (**Figure 16d'**) from a tilted spindle torus using Matlab reproduced well the experimental 3D image stack (**Figure 16d**). To our knowledge, this is the first observation of solid colloidal particles with a biconcave shape.

Using the Langmuir isotherm of SDS adsorption to self-assembled monolayers (SAMs),⁴¹⁰ we estimated the surface adsorption density of SDS to be about $\Gamma_{10\text{mM}} = 0.71$ molecules/nm² with 10mM SDS aqueous solution. This value is about 27% of the density of dehydrated SDS crystalline packing. Therefore, our experiment indicates that 27% mixing of SDS into α -eicosene at the surface is not a high enough concentration to make flat surface disks.

Elevating the concentration of SDS to 60mM introduced a stronger depletion attraction between alkene emulsions due to the increase of SDS micelle concentration.⁴¹¹ Increasing and decreasing the temperature of the suspensions several times caused coalescence of the dimmer aggregates (**Figure 17a**). The surface area decreased by 21% when two spherical droplets coalesced into one. Assuming the adsorbed SDS molecules

did not re-dissolve into the solvent, the SDS density on the surface became about 0.89 molecules/nm², so the SDS occupied about 35% of the surface. To our surprise, these disks showed two flat circular surfaces instead of dimples on both faces. (**Figure 17b, d**).

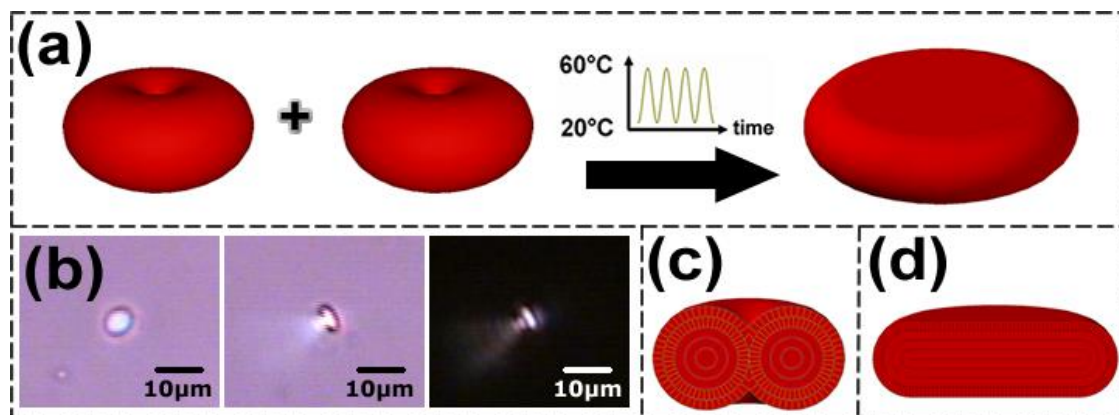


Figure 17. Coalescence of two biconcave colloidal disks into a flat disk. (a) The disks were attracted to each other at high sample SDS concentrations. Temperature was raised and lowered for several times between 20 °C and 60 °C, cycling above and below the melting point of α -eicosene ($T_m=26^\circ\text{C}$). This procedure produced disks of a larger volume with a larger aspect ratio, $\xi=4$, than the original biconcave disks with $\xi=2$. (b) Disk obtained after temperature oscillations. Images were taken of a single disk at different times to examine the shape from various view angles. The first two images are optic micrographs, and the third image is a polarizing microscope micrograph. Images were taken at room temperature using 20 \times lens. (c) Illustration of the FCD defect of the layered structure of a biconcave disk. Molecules in the rotator phase pack into layers, in which they rotate freely. (d) Illustration of the $+\pi$ edge disclination loop defect of the flat disk.

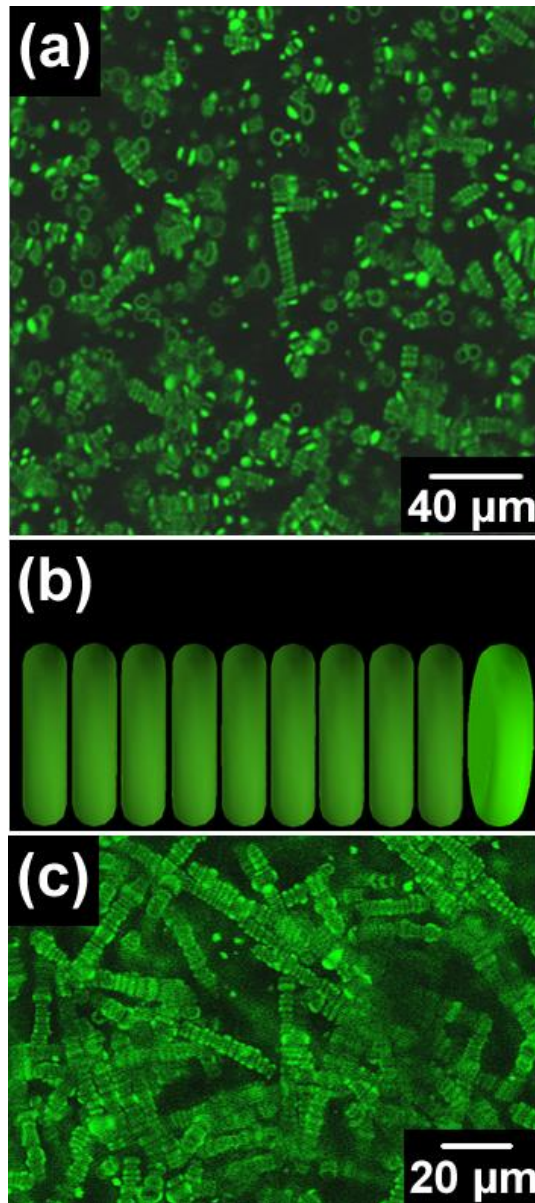


Figure 18. Flat disks. Disks have an aspect ratio of $\xi = 4$. (a) Disks begin to stack into rods at relatively dilute concentration comparing to the biconcave disks. Magnification 60x. (b) AutoCAD illustration of disk stacking. Disks are brighter due to their inclination at the end of the stack as observed in (a). (c) Confocal micrograph of rods formed at a high disk concentration. Magnification: 60x. **Figure 18a** and **Figure 18c** were taken at room temperature. **Figure 18a** and **Figure 18c** were taken using confocal microscopy (TCS SP5, Leica).

From this experiment, we realized that the high surface concentration or dense packing of surfactants—hence low surface tension—is required to fabricate flat disks. Therefore, we used a co-surfactant, decanol, to tune the organization of molecules at the wax-water interface. It is known that decanol increases the surfactant molecular packing density at the interface and lowers the curvature of the surfactant monolayer.^{412, 413} In a previous work, it was used to induce dewetting to modify the shape of solidifying droplets.⁴¹⁴ Using mixtures of decanol and SDS at a weight ratio of 1 to 10 in a 10mM SDS aqueous solution, flat-surfaced disks quickly emerged in the emulsions in less than 12 hours at 4°C, as shown in **Figure 18**.

2.3.3 Discussion

2.3.3.1 Morphology of the Disks

Therefore, two distinct kinds of disks can be obtained by varying the composition of surfactant and co-surfactant (**Figure 19**). Hydrocarbons have particular physical properties, such as the formation of a rotator phase and surface freezing.^{415, 416} Surface freezing appears a few degrees above the melting temperature creating a crystalline monolayer at the surface, usually of a rotator phase that is in equilibrium with the bulk liquid.⁴¹⁷ Colloidal particles of the rotator phase are composed of equidistant layers, topologically equivalent to a sphere of concentric layers. Crystallization converts wax emulsions themselves into disks in a two-step process. Surface freezing³⁶³ first forms an elastic membrane at the alkene-water interface. This membrane then serves as the nucleus of the rotator phase. However, the final shape of the disk is dictated by elastic deformation of this membrane and defects of the rotator phase, satisfying global free

energy minimization. The role of the co-surfactant decanol is to achieve a high surfactant concentration to form a condensed phase at the alkene-water interface, which in turn leads to an enhanced surface freezing.³⁷⁷ The rotator phase propagates from the alkene-water interface to the center of the emulsions to form the final disk shape.

As described below in detail, the shape of the disks is determined by the surfactants through two specific control parameters, the spontaneous curvature, c_0 , and the anchoring or orientation of the alkene molecules at the alkene-water interface. c_0 determines the defect type of the resultant disks by selecting the shape of the elastic membrane, either flat at small c_0 or biconcave at large c_0 . The biconcave membrane can create a single FCD defect during the rotator phase growth, which acts to form the emulsion into red-blood-cell-like (RBC-like) shape. The flat membrane, though, creates a $+\pi$ edge disclination to connect the top layers to the bottom layers form the emulsion into flat disks. (Defects of the layered structure are illustrated in supplement **Figure A2**). On the other hand, the anchoring sets the aspect ratio of the resulted disks.

2.3.3.1.1 Disk Morphology Selection by the Spontaneous Curvature of the Surface

Membrane

Spontaneous curvature, c_0 , plays an important role as a shape selector of the elastic membrane. It varies with the surfactants pack in a monolayer on the surface. When only SDS is used, c_0 is large, and a biconcave membrane will be obtained. However, if the mixture of decanol and SDS reduces c_0 to a critical value. c_0^* , a flat

membrane can be achieved. Here we establish the theoretical considerations for this c_0 induced disk morphology transition.

2.3.3.1.1 Shape of the Elastic Membrane

For an elastic membrane of surface area A enclosing a fixed volume V , the free energy⁴¹⁸ is:

$$E = \frac{1}{2} k_{membrane} \int (c_1 + c_2 - c_o)^2 dA + \int \delta p dV + \int \lambda dA., \quad (6)$$

where $k_{membrane}$ is the elastic modulus, c_0 is its spontaneous curvature, c_1 and c_2 are the two principle curvatures of the membrane. Minimization of this free energy leads to a second-order differential equation for the rotation-symmetric shape of the membrane:⁴¹⁹

$$\begin{aligned} \cos^2 \varphi \frac{d^2 \varphi}{dr^2} - \frac{\sin(2\varphi)}{4} \left(\frac{d\varphi}{dr} \right)^2 + \frac{\cos^2 \varphi}{r} \frac{d\varphi}{dr} - \frac{\sin(2\varphi)}{2r^2} \\ - \frac{\delta p r}{2k \cos \varphi} - \frac{\sin \varphi}{2 \cos \varphi} \left(\frac{\sin \varphi}{r} - c_o \right)^2 - \frac{\lambda \sin \varphi}{k \cos \varphi} = \frac{C}{r \cos \varphi}. \end{aligned} \quad (7)$$

Since a cylindrical coordinate system was used, $c_1 = \sin \varphi / r$ is the curvature along the parallels and $c_2 = d \sin \varphi / dr$ is that along the meridian, where φ is the angle made by the surface tangent and the r axis, and r is the distance to the z axis. In Eq. (7), C is an integration constant ($C = 2c_0$).

We can assume $\delta p = 0$ since there is no material transport across the membrane during surface freezing. Let us consider $\lambda = 0$ since area are created favorably during surface freezing. An analytic solution for Eq. (7) under such conditions is:⁴¹⁹

$$\sin \varphi = r/R_o + c_o r \ln r, \quad (8)$$

which describes the shape of the membrane, where R_o is a constant.

When only SDS is used as surfactant, it is well known that the spontaneous curvature c_0 of the interface is relatively large due to the large size of the charged head group compared to the relatively small hydrophobic chain, giving the surfactant molecule a conical shape.⁴²⁰ Even at a low decanol concentration, the surfactant packing is still not tight and the surfactant mixture still produces a wax-water interface with a relatively large spontaneous curvature c_0 . For a non zero c_0 , Eq. (8) gives a biconcave shape of the membrane. An example with $c_o = 1.8$ and $R_o = 1$ is shown in **Figure 20a**.

As decanol/SDS weight ratio increases, the enhanced surfactant molecular packing at the wax-water interface reduces the curvature of the membrane.⁴²¹ At the limit of, $c = 0$, there are two solutions for the membrane⁴¹⁹: the sphere with $\sin \varphi = r/R$ with R_o as the radius and the flat plane with $\sin \varphi = 0$. Obviously, the flat plane has lower free energy than the sphere. However, the flat membrane needs to have a curved edge to connect the top to the bottom portion of the membrane, as shown in **Figure 20c**.

2.3.3.1.1.2 Influence of c_0 on Final Shape of the Disk after Emulsion

Crystallization

Even a biconcave membrane, which is formed at non-zero c_0 , might lead to the formation of a flat disk due to the competition of surface and bulk deformation. It is instructive to compare the free energy for both the biconcave (FCD) and the flat disks (**Figure 20**). Ignoring here the surface tension contribution in Eqs, 9 and 10 as they

should cancel out in Eq. 11 due to roughly the same surface area for both cases, the free energy for the biconcave disk can be expressed as

$$\begin{aligned}
 E_{biconcave} &= E_{gd_{III}} + \frac{1}{2} k_{membrane} \int_{I+II} (c_1 + c_2 - c_o)^2 dA \\
 &\quad + \frac{1}{2} k_{rotator} \int_{I+II} (c_{r1} + c_{r2})^2 dV.
 \end{aligned} \tag{9}$$

Where E_{gd} is the energy of the $+\pi$ disclination located on the edge of the disk (**Figure 20d** and supplementary **Figure A2g**), the second term corresponds to the elastic free energy of the membrane (**Figure 20b**), and third term corresponds to the enclosed rotator phase (**Figure 20d**). c_{r1} , c_{r2} and $k_{rotator}$ are the curvatures of the rotator phase and its modulus, respectively.

The free energy of a flat disk is (**Figure 20c** and **Figure 20e**)

$$\begin{aligned}
 E_{flat} &= E_{gd_{III}} + \frac{1}{2} k_{membrane} \int_{I+II} (c_1 + c_2 - c_o)^2 dA \\
 &\quad + \frac{1}{2} k_{rotator} \int_{I+II} (c_{r1} + c_{r2})^2 dV \\
 &= E_{gd_{III}} + \frac{1}{2} k_{membrane} \int_{I+II} (c_o)^2 dA.
 \end{aligned} \tag{10}$$

Assuming the same thickness t and lateral size, the free energy difference is

$$\begin{aligned}
\Delta E &= E_{biconcave} - E_{flat} \\
&= \frac{1}{2} k_{membrane} \int_I [(c_1 + c_2 - c_o)^2 - c_o^2] dA \\
&\quad + \frac{1}{2} k_{rotator} \int_I (c_{r1} + c_{r2})^2 dV.
\end{aligned} \tag{11}$$

Letting H be the mean curvature of the surface membrane, *i.e.*, $H = -(c_1 + c_2)/2$, integrating Eq. (11), we obtain:⁴²²

$$\Delta E \approx \frac{1}{2} k_{membrane} [(2H + c_o)^2 - c_o^2] a^2 + \frac{1}{2} k_{rotator} a. \tag{12}$$

Where a is the size of the torus defect (Region I). Since a is smaller than $1/(-H)$, let $a = \eta/(-H) = \eta R/\xi$ with $\eta < 1$; R is the lateral radius of the disk; and $\xi = 2R/t$ is the aspect ratio.

Setting $\Delta E = 0$ to obtain c_0^* , which is the critical spontaneous curvature for the transition between biconcave and the flat disk:

$$\frac{1}{2} k_{membrane} [4H^2 + 4Hc_o^*] a^2 + \frac{1}{2} k_{rotator} a = 0, \tag{13}$$

$$c_0^* = \frac{\xi^\#}{R} + \frac{1}{4\eta} \frac{k_{rotator}}{k_{membrane}}. \tag{14}$$

where $\xi^\#$ is the aspect ratio of the disks produced at c_0^* , $2.0 < \xi^\# < 4.0$ according to observation made in **Figure 19**. When decanol is used in a sufficient amount so that c_o can be reduced to less than c_0^* , flat disks will be obtained. Flat disks are certain to be produced when the decanol/SDS weight ratio is larger than 0.25 because there co-surfactant and surfactant mixtures were observed to form the lamellar phase (a flat

layered structure, indicating small c_0).⁴²¹ Eq. (14) indicates that the *elasticity* of the internal structure of the particle ($k_{rotator}$) leads to the formation of flat disks at a non-zero spontaneous curvature value c_0^* . It also indicates that small sized disks (small R) are ready to be flat due to the relatively large value of c_0^* .


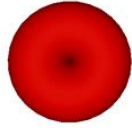
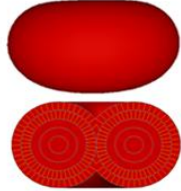
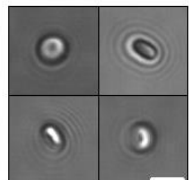


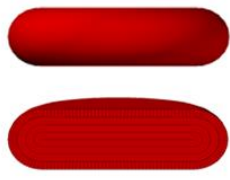
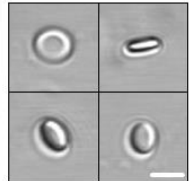



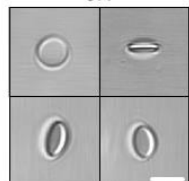
Surfactant Concentration Ratio	Top View	Side View & Defect Structure	Aspect Ratio	Defect Type
<p>SDS Only</p>  <p>$C_{0, \text{SDS only}} > C_0^*$</p>			<p>2:1</p> 	Focal Conical Domain (FCD)
<p>SDS : Decanol = 10:1</p>  <p>$0 < C_{0, 10:1} < C_0^*$</p>			<p>4:1</p> 	+ π disclination loop
<p>SDS : Decanol = 1:1</p>  <p>$C_{0, 1:1} \approx 0$</p>			<p>6:1</p> 	+ π disclination loop

Figure 19. The morphology control of colloidal disks by varying surfactant composition.

Decanol increases the surfactant molecular packing density at the wax-water interface and lowers the curvature c_0 of the interface. The particles are composed of equidistant layers in topological equivalence to a sphere of concentric layers. Without decanol, the spontaneous curvature c_0 is larger than c_0^* , and the surface membrane of the particle takes a torus structure due to the FCD defect (note the dimples on the circular surfaces, see supplementary **Figure A1a**). With enough decanol, the spontaneous curvature is reduced to be smaller than a critical value c_0^* , and the disk assumes the flat coin-like shape with the $+\pi$ disclination loop defect⁴²³ (Supplementary **Figure A2b**). The aspect

ratio of the particles increases if the surface tension $\sigma_{||}$ is reduced by the addition of decanol. The scale bar is 4 μm . Images were taken at room temperature using confocal microscopy (TCS SP5, Leica) with 100X lens. Note: $c_{o, \text{SDS only}} > c_{o, 10:1} > c_{o, 1:1}$.

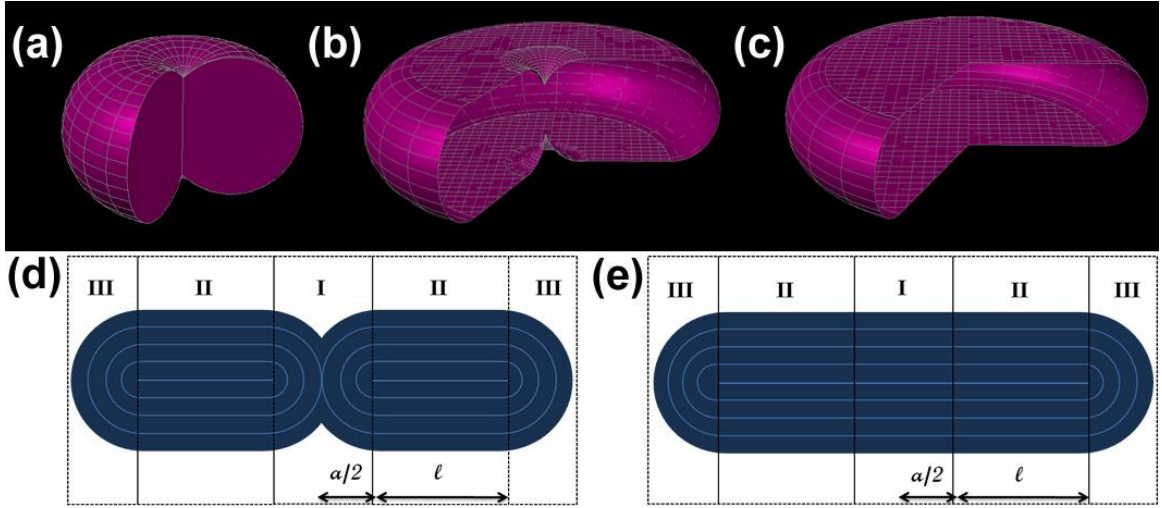


Figure 20. Structure of the wax particles. (a-c) The surface membranes formed by surface freezing. (a) and (b) are biconcave membranes and (c) is flat membrane. (d) Biconcave disk geometry with FCD region (I), flat surface region (II) and $+\pi$ edge disclination region (III). The radial lengths of the FCD region and the flat region are $a/2$ and l , respectively. (a) is the surface for particles with $l = 0$ and (c) is the surface for particles with $a = 0$. (e) Flat disk geometry with the same thickness and lateral size as the biconcave disk shown in (d), divided into three corresponding regions.

2.3.3.1.2 Aspect Ratio of Disks is Tailored by Molecular Anchoring and c_o

Anchoring controls the aspect ratio of the disk through the magnitude of surface tension anisotropy $\Delta\sigma$, with $\Delta\sigma = \sigma_{\perp} - \sigma_{\parallel}$, σ_{\parallel} being the surface tension with the molecular layers parallel to the surface, and σ_{\perp} perpendicular to the surface. To avoid exposure of high energetic interface involving σ_{\perp} , the alkene layers bend to adopt a configuration of parallel layers with a disclination loop defect (the III region of **Figure 20d** and **Figure 20e**; supplementary **Figure A2d**). It is a defect in the orientation of molecules. The energy for the $+\pi$ edge-disclination in the flat disk can be expressed as:⁴²³

$$E_{gd} = 2\pi R \left\{ E_c + \frac{t\sqrt{KB}}{2} + \frac{\pi}{2} K \ln n \right\}. \quad (15)$$

Where, E_c represents the core energy of the $+\pi$ disclination. The second term is the elastic self-energy of the giant dislocation. K and B are the curvature and compressibility moduli of the molecular layers, respectively; R is the radius of the disk; t is the thickness of the disk; and n is the number of layers. The third term is the curvature energy of the layers. Assuming the second term in E_{gd} dominates and R to be constant ($R = a/2 + l + t/2$), where $a/2$ and l are the length of the defect and the flat surface, respectively, as shown in **Figure 20d** and **Figure 20e**, the total energy for the disk is:

$$\begin{aligned}
E_{disk} &= \pi \left(l^2 / 2 + al \right) \left(\sigma_{\parallel} + \frac{1}{2} k_{membrane} c_0^2 \right) + E_{gd} + E_I + E_{II, internal} \\
&\approx \pi \left(l^2 / 2 + al \right) \left(\sigma_{\parallel} + \frac{1}{2} k_{membrane} c_0^2 \right) \\
&\quad + \pi (a/2 + l) t \sqrt{KB} + E_I + E_{II, internal}.
\end{aligned} \tag{16}$$

Where, the first term corresponds to the surface energy of region II. The second term is related to the $+\pi$ giant disclination (region III). The third term represents the energy of region I, either FCD-I⁴²² (**Figure 20d**) or flat (**Figure 20e**), which is constant when varying l . The last term is the energy of the internal structure of region II, which is also constant (zero) when varying l . Therefore, the aspect ratio of the disks can be calculated by minimizing this energy expression for a fixed disk volume:

$$\xi = \frac{2(a/2 + l + t/2)}{t} = \frac{\sqrt{KB}}{2(\sigma_{\parallel} + \frac{1}{2} k_{membrane} c_0^2)} + 1. \tag{17}$$

This relationship shows that the aspect ratio of the disks increases with reduced surface tension σ_{\parallel} and spontaneous curvature c_0 . We confirmed this correlation experimentally in **section 2.3.3.1.2.3**.

2.3.3.1.2.1 Surface Tension for Wax-water Interface at Different Decanol and SDS Weight Ratios

A KSV CAM-200 optical goniometer instrument (Monroe, CT) with auto-dispenser, video camera, and drop-shape analysis software was used to measure the surface tension of the wax/liquid interface. The liquid-air interfacial tension was roughly approximated to a pure ethanol-air system using a solution of 80% ethanol and 20% water. To mimic the wax-liquid interface, a glass slide was coated with α -eicosene using a Cee® Model 100 spin coater (Brewer Science Inc, Rolla, Mo.). The static contact angles were measured for five different decanol/SDS weight ratios, as shown in **Figure 21a**. From the obtained static contact angles, the following equation was used to measure the wax-liquid interfacial tension.

$$\gamma_{wl} = \gamma_{wa} - \gamma_{la} \cos \theta, \quad (18)$$

where θ is the contact angle and γ_{wl} , γ_{wa} and γ_{la} are the wax-liquid, wax-air, and liquid-air interfacial tension. Values for γ_{wa} and γ_{la} were taken as 25.6 dyn/cm³⁶³ and 22.4 dyn/cm,⁴²⁴ respectively.

Figure 21a shows that the surface tension changes only slightly in a weight ratio between 0 and 0.4, but there is a relatively large reduction in the range 0.4 to 1 range.

2.3.3.1.2.2 Aspect Ratio Measurement using Dynamic Light Scattering

Dynamic light scattering measurements were carried out to calculate the aspect ratio (ξ) of the colloidal disks at different decanol/SDS weight ratios applying Eq. (19). The diffusion coefficient for the emulsions (D_{sphere}) and for the disks (D_{disk}) were

measured using ZetaPALS (Brookhaven Instrumentation Corporation, Holtsville, N.Y.).⁴²⁵

$$\frac{\arctan(\sqrt{\xi^2 - 1})}{\sqrt{\xi^2 - 1}} \xi^{2/3} = \left(\frac{2}{3}\right)^{1/3} \left(\frac{D_{disk}}{D_{sphere}}\right). \quad (19)$$

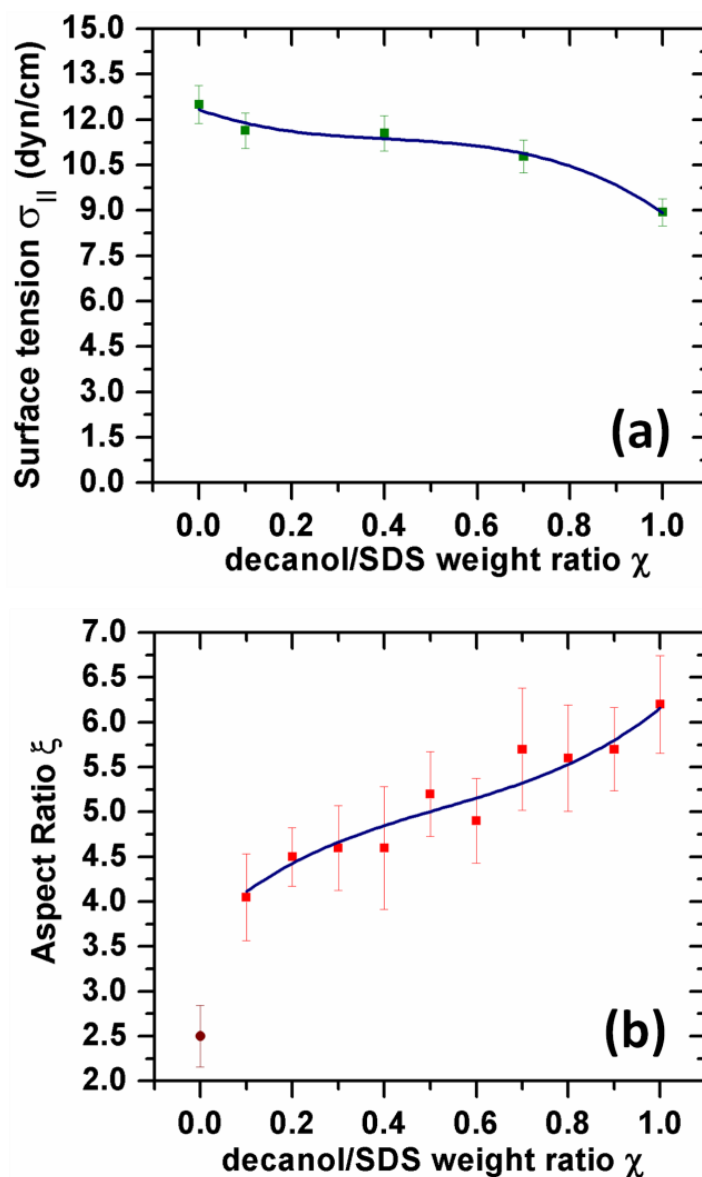


Figure 21. Dependence of the alkene/liquid interfacial tension (a) and the aspect ratio on decanol/SDS composition (b). The aspect ratio of the disks was measured using their phase transition by dynamic light scattering. The solid line is a polynomial fit.

The results are shown in **Figure 21b**. A transition between decanol/SDS weight ratio 0 and 0.1 was observed. It is known that the spontaneous curvature of the α -eicosene changes dramatically at low decanol concentrations.⁴²¹ From decanol/SDS weight ratio 0.1 to 1, an approximate linear tendency was observed for aspect ratio.

2.3.3.1.2.3 Correlation of aspect ratio and surface tension for disks

Figure 22 confirms the relationship predicted by Eq. 17 between the aspect ratio and the surface tension. The graph is divided into three regions. For region I, $c_o \sim 0$ due to the use of a large amount of decanol,⁴²¹ the fitting of Eq. 17 to the data gave $\sqrt{KB}/2 = 45.76 \pm 1.17$ dyn/cm. Regions II and III are separated by the critical spontaneous curvatures c_o^* or critical aspect ratio ξ^* . We found that a linear dependence of $\frac{1}{2}k_{membrane}c_o^2$ on $\sigma_{||}$ fits the data well in regions II and III: $\frac{1}{2}k_{membrane}c_o^2 = (12.06 \pm 4.16)\sigma_{||} - (136.76 \pm 47.43)$. The limit value $\xi = 1$ at large interfacial tension was taken for $\sigma_{||} = 100$ dyn/cm. However, the position of the dashed line was uncertain, since the transition from biconcave to flat disks cannot be yet determined experimentally.

In summary, region III produces biconcaved disks due to the large spontaneous curvature c_o of the elastic membrane. Region I produces flat disks because spontaneous curvature c_o equals zero, which favors a flat elastic membrane. In region II, it is the

competition between the elastic membrane and layer-packing of the internal rotator phase that determines the final shape of the disks to be flat.

2.3.3.2 Depletion Attraction between Disks of Various Shapes.

The depletion energy of the wax disks system was manipulated increasing the concentration of the SDS nanospheres by evaporation of a suspension droplet (For evaporation method, see Supplementary **Figure A1**.) The evaporation method lacks precise control of the concentration of SDS and wax disks. The depletion attraction for two disks oriented face to face is larger than side to side, hence aggregations face to face as shown in **Figure 23c** and **Figure 23d** are observed rather than side to side as depicted in **Figure 23e** and **Figure 23f**. As a result the wax disks tend to form rods. It was found that there is a large difference in the depletion attraction energies between two biconcave and two flat disks. The rods stacked by the flat disks are longer, straighter, and more rigid (**Figure 23a**) as measured by less sideways Brownian motion, compared with the short rods obtained from the biconcave disks (**Figure 23b**). Mason⁴⁵ showed these aggregations are explained by the depletion caused by the SDS micelles between different surfaces. In **Figure 23** we show here how the geometry of anisotropic particles affects their self-assembled structures.

The flat disks prefer to aggregate into condensed structures, as shown in **Figure 24b**. The contact energy for two disks approaching face to face can be calculated as⁴⁵ shown in Eqs. 20 and 21. (Note: Here the aspect ratio is defined as $\xi = 2R_d / t$, Mason⁴⁵ used $\xi^* = t / 2R_d$.)

$$U_{flat}^{f-f} = -2\pi R_m R_d^2 \Pi_m, \quad (20)$$

$$U_{flat}^{s-s} = \frac{-2^{7/2} R_m^{3/2} R_d^{3/2} \Pi_m}{\xi}, \quad (21)$$

where U^{f-f} is the depletion energy between two flat disks in the orientation of face to face, U^{s-s} is the depletion energy side to side, R_m is the micelle size, R_d is the disks face radius and Π_m the micellar osmotic pressure.

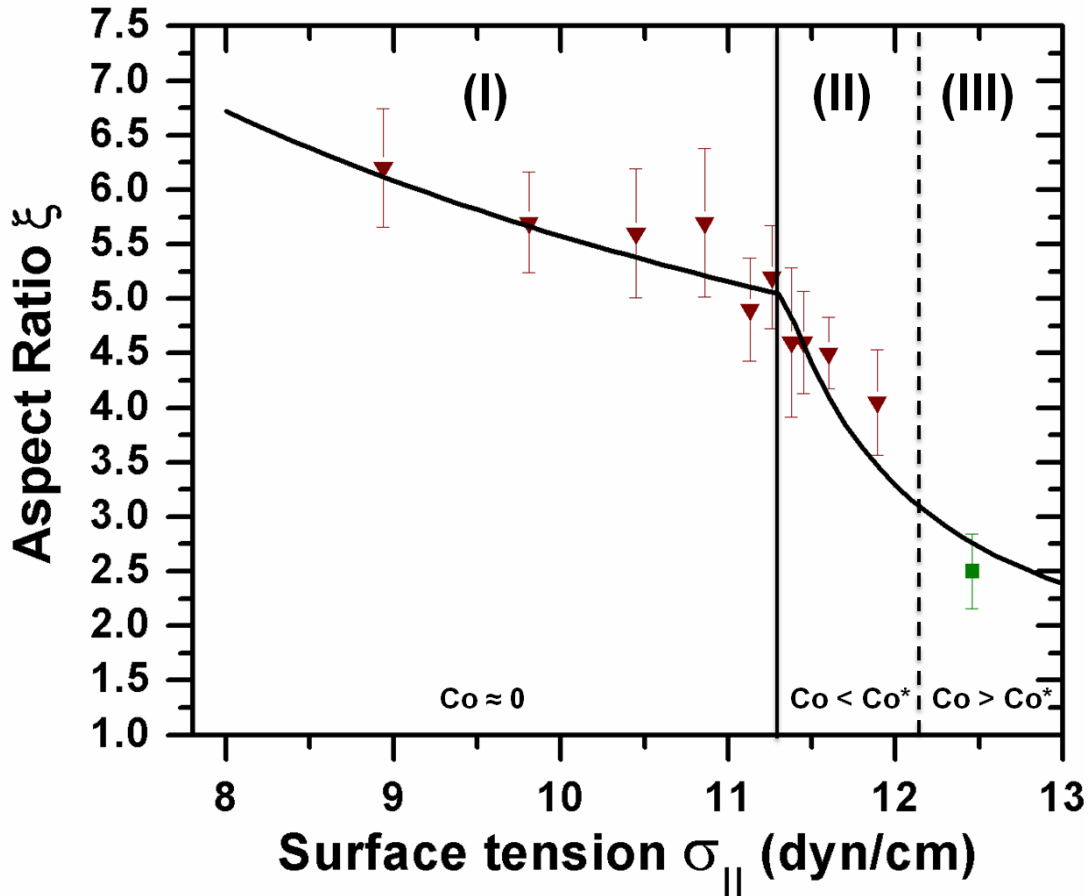


Figure 22. Correlation between aspect ratio and interfacial surface tension. The solid lines are fittings to the theoretical prediction (Eq. 17). The triangles are the experimental data. The square is for the sample using SDS only. The left regions (I and II) correspond to flat disks produced at low membrane spontaneous curvature C_o . The right region (III) represents the biconcave disks with a FCD defect due to large C_o .

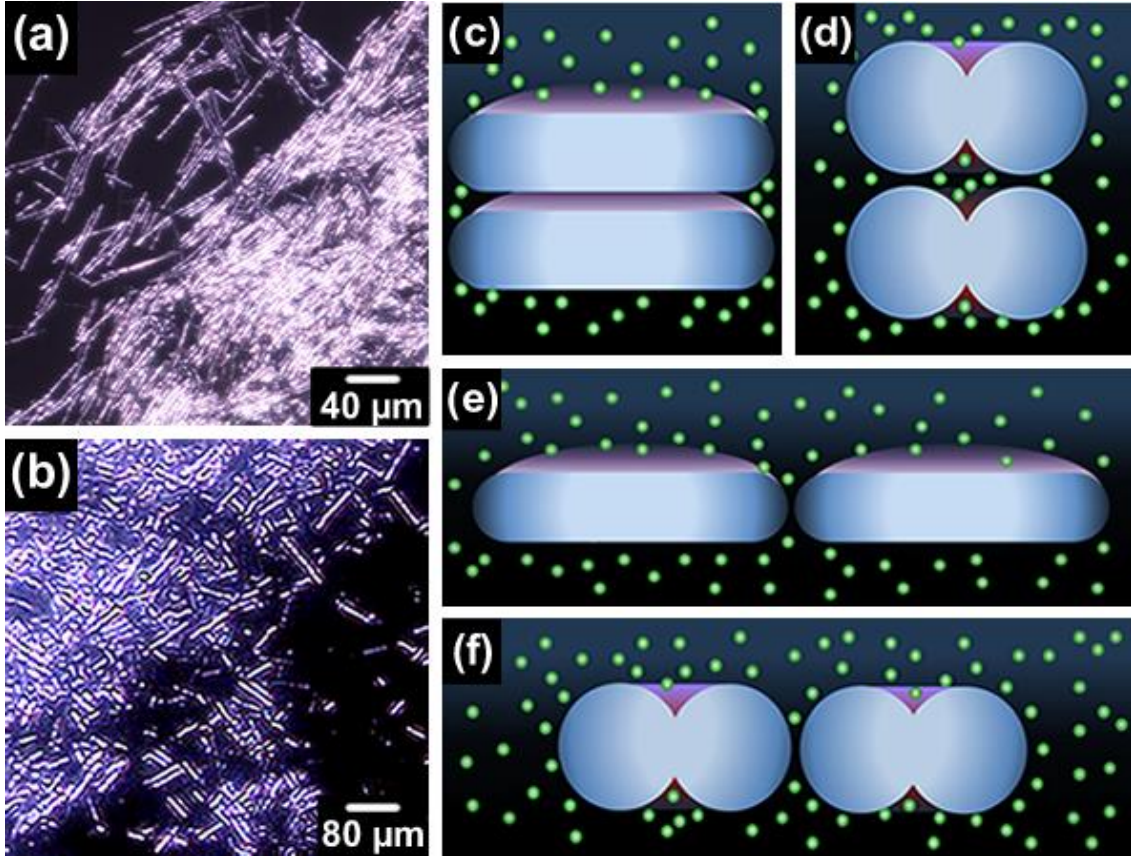


Figure 23. Self-assembly of colloidal disks due to depletion attraction. (a) Cross-polarizing micrograph of rods formed at a high flat disk concentration. Magnification 20x. (b) Micrograph showing the assembly of biconcave disks. The disks tend to stack at high concentration resembling the red blood cells. Magnification 35x, (c-f) Possible interactions between disks. (c) and (d) Assembly of a pair of flat and biconcave disks (e) oriented face-to-face and (f) disks oriented side-to-side. Images were taken at room temperature.

Rewriting the above depletion energy equations for particles and assuming the volume of each particle is V ($V = \pi R_d^2 L$), the depletion energy can be expressed as:

$$U_{flat}^{f-f} = V^{2/3} \xi^{2/3}. \quad (22)$$

$$U_{flat}^{s-s} = V^{1/2} \xi^{-1/2}. \quad (23)$$

These equations indicate that the aspect ratio (ξ) influences disk assembly through the magnitude of depletion attraction, confirming the observation in **Figure 23a** for the flat disks ($\xi \sim 4$) and **Figure 23b** for the biconcave disks ($\xi \sim 2$). We can see that U_{flat}^{f-f} is an increasing function of ξ , while U_{flat}^{s-s} is a decreasing function of ξ . So, when ξ increases, the flat disks more likely stack upon each other into rods.

The shape and the surface roughness of the particles can influence the strength of the depletion attraction. Badaire⁴⁹ studied the dependency of the depletion energy on the global shape and roughness of platelets. In addition Zhao⁵¹ stated that the depletion energy can be attenuated when the roughness is larger than the depletant agent. Here, we take into account the depletion attraction difference between smooth biconcave and flat disks. The depletion attraction energy between two biconcave disks (**Figure 23d**) is generally smaller compared to the energy between two flat disks (**Figure 23c**) due to the reduction in the excluded volume allowing depletant agent to fill the dimples. The contact energy for the biconcave disks can be expressed as:⁴⁵

$$U_{biconcave}^{f-f} = -2^{5/2} \pi R_t R_m^{3/2} R_c^{1/2} \Pi_m . \quad (24)$$

where R_c is the radius from the center to the edge of the disk and R_t is the radius to the core of the spindle torus defect.

Assuming $R_c \approx R_d$, a ratio between the depletion attraction energy of the biconcave and the flat disks can be obtained:

$$U_{biconcave}^{f-f} / U_{flat}^{f-f} = 2^{3/2} (R_m / R_d)^{1/2} (R_t / R_d) . \quad (25)$$

where $R_m \approx 20 \text{ \AA}$, $R_d \approx 2 \mu m$ and $R_t \approx 1 \mu m$.

Hence,

$$U_{biconcave}^{f-f}/U_{flat}^{f-f} \approx 0.05. \quad (26)$$

As a result, we conclude that a smaller concentration of SDS or lower Π_m is required to induce depletion attraction of flat disks into columnar stacks as compared to biconcave disks. The micelles can fill the void between the dimples of biconcave disks stacked face-to-face to reduce the depletion energy. In consequence a poor alignment for stacks formed by biconcave disks was observed in **Figure 23b**. In contrast, flat disks can successfully form long and straight rods as shown in **Figure 23a** and **Figure 24**. In general, when the stacks become longer during the increment of the disk concentration, the formation of bundles could be observed,²⁹ as exhibited in **Figure 23a** and **Figure 24g, h** and **i**. Sideways aggregation occurs for the rods when their lateral surface becomes larger, increasing the side-to-side depletion energy. We predict with a further increase in the concentration of flat disks, they might form colloidal crystals.¹³⁹

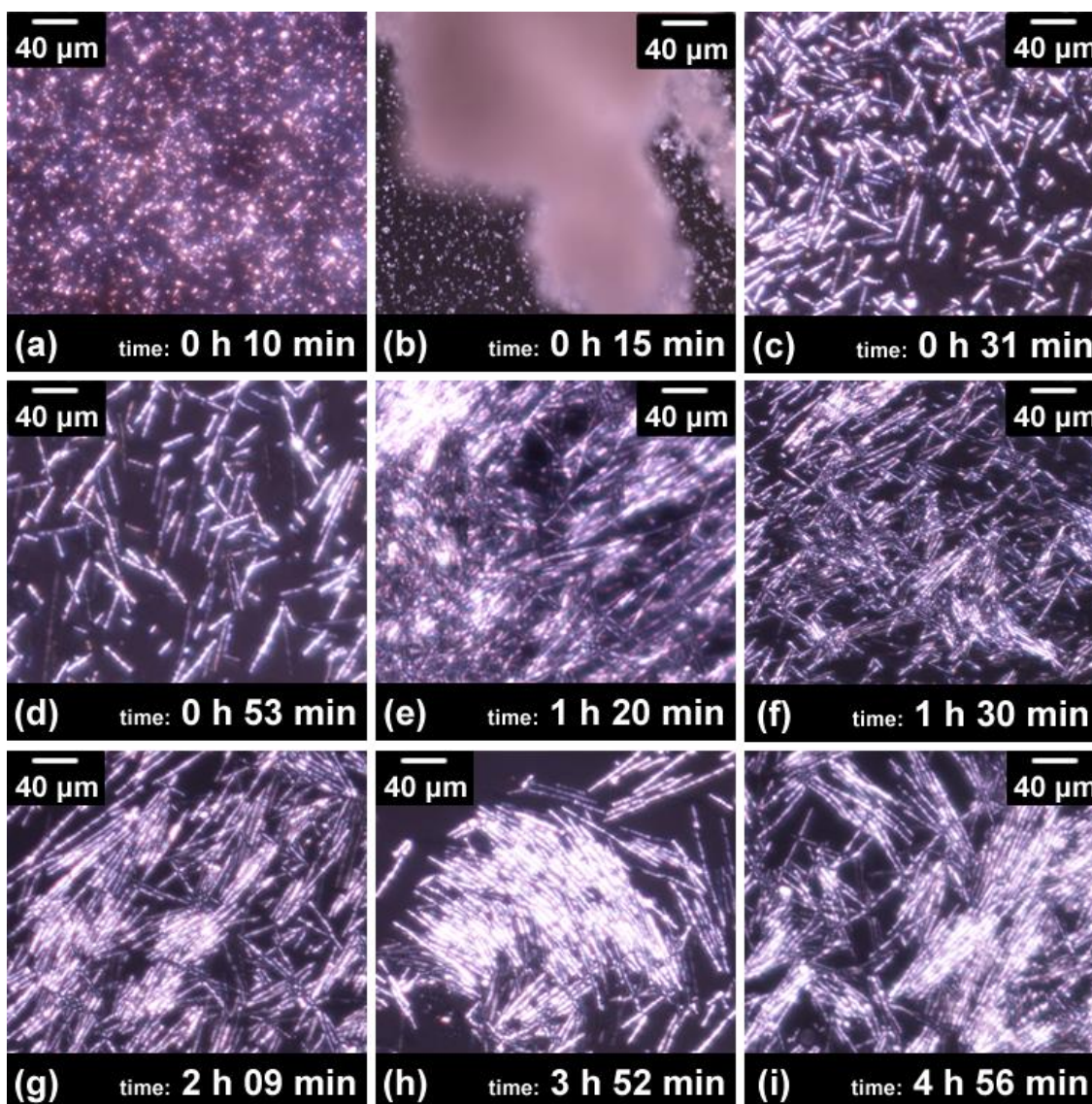


Figure 24. Self-assembling of the flat disks in an evaporating droplet observed under cross-polarizing microscopy. Disks are fabricated using 1:10 surfactant ratio (decanol:SDS) in a 10mM SDS aqueous solution. The microdisks are uniform in diameter ($R = 4 \pm 0.25 \mu\text{m}$) and aspect ratio ($\xi = 4$). (a) Disks just after the deposition of the droplet on the glass slide. (b) Cloud of disks formed as a result of the depletion attraction. Pink color is evident under a pair of crossed polarisers. (c) Some rods started to flow out from the cloud when the droplet is flattened over the glass. (d) Alignment of rods in flow direction. (e), (f), (g) Different rod organizations are exhibited. (h), (i) Rods began to assemble side by side. Images were taken at room temperature using 20x.

2.3.4 Summary

In conclusion, we demonstrated both experimentally and theoretically the feasibility of molding phase-changing emulsions by controlling their surfaces using a mixture of surfactants and co-surfactants. The α -eicosene molecules in the emulsions exhibit a controllable surface freezing transition, which we demonstrated by the packing of interfacial molecules. Using the surface membranes as the nuclei, the layers of the rotator phase of α -eicosene propagate inward from the surface to complete the phase transition of the whole emulsion droplet, thus changing the shape of the emulsions from spherical to disk-like. The shape of the resultant particles is adjusted by two control parameters, the anchoring and the spontaneous curvature c_0 . The aspect ratio of the flat disks can be varied by setting the magnitude of the surface tension anisotropy using different ratios of decanol and SDS at the interface. c_0 selects the shape of elastic membrane. Elasticity of the internal structure establishes a non-zero critical spontaneous curvature c_0^* ; where the transition between biconcave and flat disks occurs. We can adjust c_0 using surfactant composition. Such surface-bound sculpturing of emulsions should have profound application in design of complex particles^{426, 427}, control of phase-changing materials,⁴²⁸ and study of liquid crystals of anisotropic mesogenes.¹⁵ We also showed that the morphology of anisotropic particles is vital to their self-assembling behaviors. Our observations showed that flat disks possess twenty times stronger depletion attraction than biconcave disks, so that the disks tend to assemble in more straight stacks than biconcave disks. These wax colloidal disks offers an experimental system to test the prediction of the liquid crystalline phase behaviors of cut spheres.¹³⁹

CHAPTER III

HIGH ASPECT RATIO COLLOIDAL DISKS*

3.1 Synopsis

We demonstrate the strong dependency of the I-N transition of discotic suspensions on the inversed aspect ratio ($\xi^* = 1/\xi = \text{thickness/diameter}$) via control of the sizes of pristine ZrP crystals and subsequent exfoliation to monolayers. The size-fractionation of the I-N transition facilitates the analysis of the effect of polydispersity. A systematic variation of ξ^* in the low ξ^* region ($0.001 < \xi^* < 0.01$) showed that the I-N transition volume fraction increases with ξ^* in agreement with computer simulations. It was found that the transition volume fractions scale with inversed aspect ratio $\phi_{I,N} = m(\xi^*)^{1.36 \pm 0.07}$, where the prefactor m strongly depends on size polydispersity for ϕ_N , but does not depend on size polydispersity for ϕ_I , with ϕ_I and ϕ_N being the volume fractions of the isotropic and the nematic phases on the cloud curves, respectively.

We also synthesized a novel thermo-responsive discotic nematic hydrogel. This liquid crystalline polymer nanocomposite was fabricated using extremely high-aspect-ratio ($\xi = \text{diameter/thickness} \sim 10^3$) zirconium phosphate (ZrP) nano-sheets embedded into a polymeric network. These nano-sheets were immersed into a solution of constituent monomers of N-isopropylacrylamide (NIPAm) and acrylamide (AAm) with

* Reprinted with permission from “Aspect ratio and polydispersity dependence of isotropic-nematic transition in discotic suspensions” by A. F. Mejia, Y.-W. Chang, R. Ng, M. Shuai, M. S. Mannan and Z. Cheng, 2012. Physical Review E, 85, 061708, Copyright 2012 by the American Physical Society.

a subsequent polymerization in situ to obtain a hydrogel embedded with the nematic liquid crystal of the nano-sheets. We analyzed the effect of initiator (APS) and catalyst (TEMED) concentration on the nematic domains at ZrP nano-sheet volume fractions (ϕ_{ZrP}) near the isotropic-nematic (I-N) transition. The mixing during hydrogel preparation allowed the aligning of the nano-sheets into highly ordered domains, which were eventually disturbed by the effect of APS and TEMED on the polymer matrix. The effect of ZrP nano-sheet concentration and temperature on the nematic hydrogels was also studied. By increasing the temperature above the LCST of PNIPAm, the hydrogels entered into a hydrophilic-to-hydrophobic transition. Interestingly, hydrogels containing ZrP nano-sheets presented increased hydrogel rigidity. In addition, we observed that the variation of the nematic ordering (S_2) and ϕ_{ZrP} within the system manipulated the birefringent color patterns of the hydrogels. Finally, a nematic hydrogel placed into a thin-rectangular capillary from 298 K to 333 K presented edge-wrinkling. Surprisingly, an isotropic-to-nematic transition guided by the increment in the ZrP nano-sheet nematic ordering was observed at a nano-sheet concentration slightly below the isotropic concentration (ϕ_I).

3.2 Aspect Ratio and Polydispersity Dependence of Isotropic-nematic Transition in Discotic Suspensions

3.2.1 Introduction

Many materials and biological systems in nature are mainly suspensions composed of disks, such as clay,⁸⁻¹⁰ asphaltenes,^{11, 12} histone octamer disks in

nucleosomes,¹³ and red blood cells.¹⁴ Theoretical studies^{6, 7} and computer simulations^{139, 140, 429} have confirmed that disks can undergo different liquid crystal transitions at high concentrations due to their excluded volumes. The discotic liquid crystalline phases can acquire exceptional thermal, electrical, and mechanical properties.^{430, 431} Liquid crystals^{6, 7, 15, 335} with distinctive flow behaviors are of great fundamental and technological importance. Regardless of their natural abundance, studies of disks are less commonly undertaken than studies of rods.^{3, 4} However, two-dimensional disks behave quite differently comparing to one-dimensional rods as manifested by the following observation in the limit case: infinitesimally thin disks in thickness have a non-zero excluded volume proportional to $0.5\pi D^3 \langle \sin\gamma \rangle$, where D is the disk diameter, γ is the angle between two disks' orientation, and $\langle \rangle$ stands for the thermodynamic average⁷; while rods of vanishing diameter have a zero excluded volume proportional to $2l_r^2 D_r \langle \sin\gamma \rangle$, where l_r is the length of rods, and D_r is the diameter.⁴³² For liquid crystals, the discotic nematic phase has long been elusive of observation;¹⁹⁸ whereas, nematic phases are frequently observed for calamitic (rod) liquid crystals.

The discotic isotropic-to-nematic (I-N) transition will play an important role in understanding the fundamentals of soft condensed matter in science and technology.⁴³³ The study of this transition can facilitate understanding of the behavior of asphaltenes,¹² to produce soft matrices of functional molecules,⁹⁷ to promote the disk-like mesogens to be used as templates for the preparation of mesoporous materials,^{308, 434} and to initiate the use of nano-platelets in semiconductors⁴³³ and solid state photovoltaic cells.⁴³⁵ In addition, a better understanding of the optical and electronic properties^{436, 437} of the

nematic discotic phase can serve in the development of new liquid crystal display (LCD) devices.^{98, 308, 438} The importance to LCDs relies on the fact that the discotic nematic phase is characterized by low viscosity and can easily be reoriented by applying electric fields, magnetic fields, and shear stimuli.

A representative phase diagram of colloidal disks contains phases such as isotropic (**I**), nematic (**N**), columnar (**C**), smectic (**S**), and crystalline (**X**). The diagrams depend substantially on the disk inversed aspect ratio ($\xi^* = 1/\xi = L/D = \text{thickness/diameter}$)¹³⁹ and polydispersity in terms of particle diameter (σ).³⁸ Generally speaking, polydispersity greatly alters the phase diagram. It is well known that crystallization of hard spheres can be suppressed by the presence of a moderate polydispersity ($\sigma \sim 10\%$).³⁹ There are I-N and N-C transitions for relatively low polydispersed discotic suspensions ($\sigma < 17\%$),^{43, 44} and an N-S transition for high polydispersities ($\sigma > 17\%$).^{40, 41, 168, 216}

Discotic suspensions have intrigued scientists since Langmuir in 1938 demonstrated that clay particles can exhibit a discotic nematic phase.⁵ Around the 1940s, Onsager predicted the capability of platelets to make an I-N transition.⁶ His theory was based on the excluded volume of disks with increasing translational entropy to compensate for the dismissing of orientational entropy.^{6, 7} The I-N transition has now become the most studied phase transition in science.^{15, 16, 122, 168, 192, 200} Computer simulations of the I-N transition have been carried out for cut spheres at inversed aspect ratios smaller than ^{158, 164} or larger than 0.1,^{139, 157, 178} but due to the system size, it is not possible to confirm the first-order nature of the I-N transition. By increasing system size,

some simulations have revealed the possibility for a weak first order I-N transition with an inversed aspect ratio equal to 0.1.¹³⁹ Interesting experimental results have also been published; for example, Lekkerkerker's group used sterically stabilized gibbsite particles ($\text{Al}(\text{OH})_3$) at $\xi^* \sim 0.1$ in toluene¹⁶, or electrostatically stabilized ones in water^{42, 193, 201, 205} to produce I-N transitions. Van der Beek *et al.*,¹⁹³ described how gravity developed a columnar phase at the bottom of an initial I-N biphasic sample elucidating the I-N-C triple point at $\xi^* \sim 0.143$. A study related to the competition between sedimentation, gelation, and liquid crystal formation of gibbsite suspensions was reported by Wijnhoven *et al.*,²²³. Aqueous suspensions of $\text{Ni}(\text{OH})_2$ at $\xi^* \sim 0.11$ were reported to present a columnar phase coexisting at equilibrium with an isotropic phase.⁶³

We are interested in studying the I-N transition at low inversed aspect ratios ($\xi^* \ll 0.1$), which thus far has only been occasionally investigated. Inorganic layers obtained from exfoliation of lamellar crystals possess a highly anisotropic shape with a thickness of several nanometers and can exhibit liquid crystals.^{97, 122, 198} A wide variety of mineral crystals have been exfoliated, such as layered double hydroxides,⁹² niobates,^{81-83, 93-98} clay,^{5, 187-189} phosphates,^{81, 82, 99-101} titanium oxides,^{81, 84} and graphite.⁴³⁹ I-N transitions have been achieved by using layers of Mg-Al double hydroxides (LDH),²⁰² and exfoliated niobate colloidal suspensions of $\text{K}_4\text{Nb}_6\text{O}_{17}$.⁹⁷ The niobate crystal layers have a low inversed aspect ratio, ranging from 0.0015 to 0.0035, so that birefringence occurs at low volume fractions. Dependence on aspect ratio has been studied for the I-N transition of $\text{K}_4\text{Nb}_6\text{O}_{17}$ layers obtained by exfoliating pristine crystals using a well-defined sonication procedure.²⁰⁶ It was found that the I-N transition occurred at higher

volume fractions when the inversed aspect ratio was increased. The polydispersity of the nanosheets, however, was not controlled, and the effect on the I-N was not carefully studied. Liquid crystalline behavior has also been reported for exfoliated HNb_3O_8 and HTiNbO_5 .²⁰⁷ Clay presented a particular challenge for scientists due to gelation, even though laponite suspensions could exhibit an I-N phase transition,¹⁸⁷ and these laponite suspensions presented clear-cut nematic textures and orientational ordering.¹⁸⁸⁻¹⁹¹

Here we study the I-N transition using exfoliated α -zirconium phosphate (ZrP) at different aspect ratios. The ability to control the lateral dimension of the ZrP crystals allows us to tune the aspect ratio of the nanoplates in a wide range. ZrP is a crystal configured by layers having the same thickness.^{79, 110} A layer of ZrP is composed of a ZrO_6 sheet coordinated with HPO_4^{2-} tetrahedrons. The aspect ratio can be easily varied by fabricating ZrP crystals of different sizes followed by exfoliation through intercalation of guest molecules (*i.e.*, tetrabutylammonium TBA^+).⁸⁸ Using this technique, we are able to study the sedimentation for high and low aspect ratio platelets using ZrP.⁴⁴⁰ Our work here examined the effects of aspect ratio and shape on I-N transition at the low inversed aspect ratio region ($0.001 < \xi^* < 0.01$). The dependence of the positions of the biphasic gap for a fixed aspect ratio ZrP nanoplate on size polydispersity was elucidated. A power law scaling was found for the aspect ratio dependence of the phase transition volume fractions $\phi_{\text{I,N}}(\xi^*)$. Platelet size polydispersity was observed to separate the nematic volume fraction, $\phi_{\text{N}}(\xi^*)$, further from the isotropic volume fraction, $\phi_{\text{I}}(\xi^*)$, while the position of $\phi_{\text{I}}(\xi^*)$ was not dramatically affected;

hence, the effect of polydispersity would be more dramatic at higher inversed aspect ratios (*i.e.*, low degree of anisotropy).

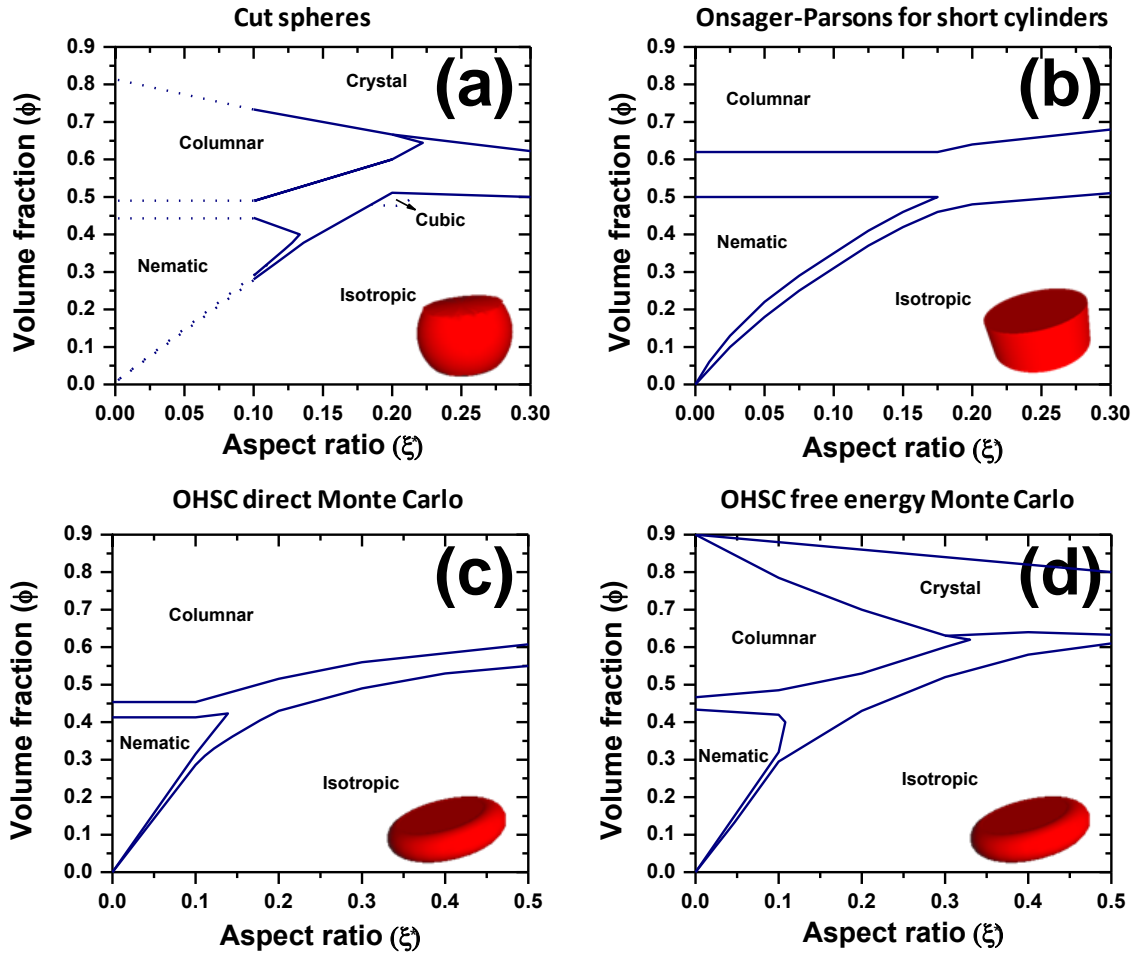


Figure 25. Phase diagrams for discotic systems in volume fraction (ϕ) versus inversed aspect ratio obtained from simulations. (a) A general diagram for cut spheres (NVT MC). The dashed lines represent simulation data reported by Veerman *et al.*, for $\xi^* < 0.1$,¹³⁹ (b) Short cylinders (Onsager-Parsons theory)¹³⁷, (c) Oblate hard spherocylinders (NPT MC),¹⁵⁹ and (d) Oblate hard spherocylinders (free energy calculations).¹⁶⁰ The insets at the bottom left of each graph illustrate the side view and the three-dimensional shape of the disks.

3.2.2 Previous Results from Simulations

We compare here the aspect ratio-dependent phase diagrams in the literature for cut spheres using NVT-Gibbs ensemble,¹³⁹ NPT-Gibbs ensemble (GE),¹⁵⁷ and umbrella sampling (US),¹⁵⁸ which are different kinds of Monte Carlo (MC) simulations. We also examine the phase diagrams of hard plate-like cylinders from Onsager-Parsons second virial theory,¹³⁷ and of the oblate hard spherocylinders (OHSC), also known as discotic spherocylinders, which were obtained using direct energy calculations,¹⁵⁹ and free energy calculations¹⁶⁰ via MC simulations.

3.2.2.1 Cut Spheres

Veerman and Frenkel ($\xi^* = 0.1, 0.2$ and 0.3 , the number of particles $N = 256$ and 288 NVT-MC),¹³⁹ Piñeiro ($\xi^* = 0.1$, $N = 1500$ and 3000 NPT-GEMC)¹⁵⁷, and Fartaria ($\xi^* = 0.001, 0.01, 0.04, 0.07$ and 0.1 , $N = 288$ and 2048 NPT-USMC)¹⁵⁸ studied the I-N phase transition in suspensions of hard cut spheres at various aspect ratios. A phase diagram for cut spheres is shown in **Figure 25(a)**. Piñeiro's results¹⁵⁷ were in agreement with Veerman and Frenkel's data.¹³⁹ For both simulations, the phase behavior of hard cut spheres was found to be strongly dependent on the aspect ratio. At $\xi^* = 0.1$. Both nematic and columnar phases were reported; however, Piñeiro obtained larger I-N transition concentrations compared to Veerman and Frenkel.¹⁵⁷ This variation was attributed to the difference of system size or to a change in simulation technique (NPT versus NVT ensembles). Around $\xi^* = 0.2$, Veerman *et al.*,¹³⁹ found a columnar phase and a phase with cubic orientational order but no translational order, which was called the

“cubic phase”. The cubic phase is still under investigation to determine if the stability is only temporary.^{149, 160, 183, 184} For $\xi^* = 0.3$, only isotropic and crystal phases were obtained. For cut spheres at low aspect ratios, Fartaria¹⁵⁸ found that the nematic order parameter, S_2 , depended strongly on inversed aspect ratio ξ^* . $S_2=1/2(\cos\theta^2-1)$ is a measure of the average relative orientation of the disks that is close to zero in the isotropic phase and nonzero in the nematic phase,⁴⁴¹ where θ is the average inclination of the platelets to the director. The nematic order parameter presents a value close to 1 for the nematic phase at $\xi^* = 0.1$ and approximately 0.5 for the smaller inversed aspect ratios ($\xi^* = 0.001, 0.01$ and 0.04). Fartaria¹⁵⁸ found that in simulations, a constant I-N transition gap occurred for low inversed aspect ratios ($\xi^* \leq 0.04$). At $\xi^* \geq 0.1$ the possibility for formation of the nematic phase was reduced, and the formation of the columnar phase was preferred.¹⁵⁸

3.2.2.2 Onsager-Parsons Approximation for Flat Cylinders

Wensink and Lekkerkerker¹³⁷ studied the hard colloidal platelet phase diagram for different aspect ratios using Onsager’s second virial theory with the Parson-Lee decoupling approximation for multiple body interactions. The phase diagram shown in **Figure 25(b)** is compatible with other simulations.^{139, 157-160} As $\xi^* \sim 0$, the I-N concentrations are the same as those predicted by Onsager’s second virial theory.¹⁶¹ When the aspect ratio varies, the I-N transition concentrations increase with ξ^* , but the nematic-columnar (N-C) density stays constant. The nematic order appears when the excluded volume exceeds a value about 4, while the columnar order becomes stable at a

volume fraction (ϕ) around 0.4. The calculated triple point (I-N-C) position, which occurs at $\xi^* = 0.175$, deviates considerably from the aspect ratio values predicted by the other simulations, which occur at $\xi^* \sim 0.126$ ^{162, 163} and $\xi^* \sim 0.14$.^{139, 164} This deviation was caused mainly by the theoretical concentration value of the N-C transition exceeding that of the other simulations, resulting in a much higher intersection point. When $\xi^* > \xi^*_{\text{I-N-C}}$, the disks no longer exhibit an I-N transition, but rather an I-C transition. This theory, however, does not consider the cubic phase that was reported by Veerman *et al.*¹³⁹ In general, this approximation shows a good agreement with the other simulations featured in **Figure 25** at $\xi^* > 0.1$.

3.2.2.3 Oblate Hard Sphero-cylinders

The OHSCs have been extensively studied in recent years.^{159, 160, 176, 177, 179} **Figure 25c** and **Figure 25d** show the phase diagrams for OHSCs obtained using direct¹⁵⁹ and free energy calculations,¹⁶⁰ respectively, using MC simulations. Both phase diagrams show similar tendencies when compared to the other simulations. The OHSCs^{159, 160} [**Figure 25(c,d)**] and the cut spheres [**Figure 25(a)**]^{139, 157, 158} phase diagrams are similar based on the presence of their circular face shape.¹⁸⁰ In general, the isotropic phase is present for all aspect ratios, while the nematic phase appears only at low inversed aspect ratios ($\xi^* \leq 0.1$). The first order I-N transition at $\xi^* = 0.1$ evident for the MC OHSC simulations [**Figure 25(c,d)**] is comparable to that of the cut spheres¹⁵⁷ [**Figure 25(a)**]. In the cut spheres simulation, an I-N biphasic gap was not obtained due to the inadequate number of particles used. Marechal *et al.*,¹⁶⁰ stated that the packing

fractions between cut spheres and OHSCs at low aspect ratios differed. By increasing the disk concentration at a range of $0 \leq \xi^* \leq 0.3$, the OHSCs can form either straight or tilt columns due to their shape. In the N-C transition ($0 \leq \xi^* \leq 0.1$), the self-assembly of the disks at a very low aspect ratio ($\xi^* \ll 0.1$) does not favor disk interactions on the edge since the edge has a lower surface area than the faces of the disks, which leads to the disks having a greater chance of maintaining a nematic order. But at higher inversed aspect ratios in the N-C transition region, the edge surface area becomes comparable to that of the face surface area. Disks are able to pack laterally much more easily due to the greater surface area, and have a greater tendency to transition from a nematic to a columnar order.¹⁷⁹ Also, a difference of the phase diagram of the OHSCs from the cut spheres phase diagram is the absence of the cubic phase. At $\xi^* = 0.2$, a possible cubic phase was found for the OHSC phase diagram but ended up converting to the columnar phase.¹⁶⁰

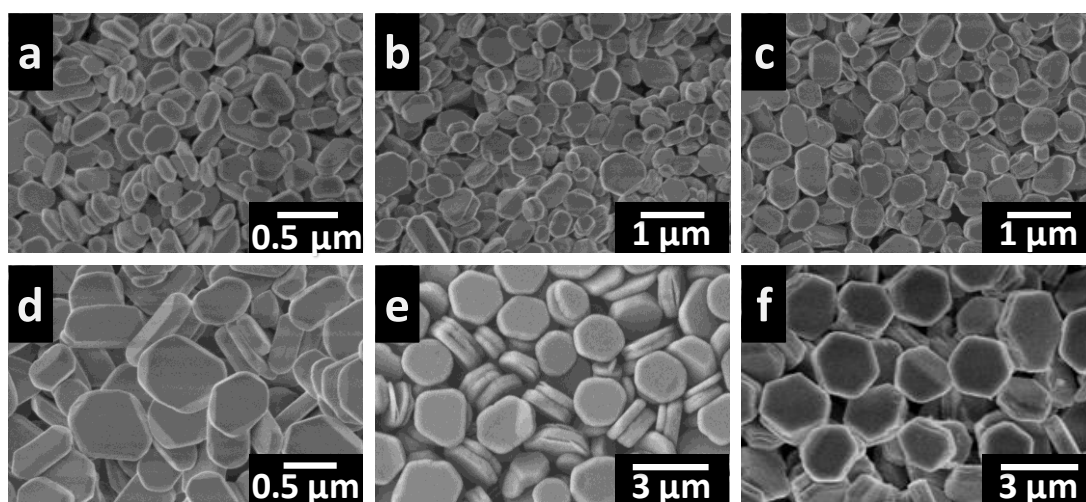


Figure 26. Pristine α -zirconium phosphate crystals. Scanning electron microscope (SEM) micrographs of different ZrP sizes prepared at different conditions (a) 9M-5h, (b) 12M-5h, (c) 15M-5h, (d) 9M-24h, (e) 12M-24h, and (f) 15M-24h.

3.2.3 Experimental Results with Monolayers of α -ZrP

3.2.3.1 Control of the Size and Aspect Ratio of ZrP Nanoplates

The pristine α -zirconium phosphate (ZrP) crystals were synthesized by a hydrothermal method.⁷⁸ In a typical reaction, 6 g of $\text{ZrOCl}_2 \cdot 8\text{H}_2\text{O}$ was added to 60.0 mL of phosphoric acid (H_3PO_4) solution. The mixture was enclosed in an autoclave and left in an oven at 200°C. In **Figure 26**, crystals with a lateral size of 331 ± 87 , 400 ± 146 , 653 ± 206 , 957 ± 147 , 1276 ± 303 and 2233 ± 807 nm were obtained from the following conditions (H_3PO_4 concentration - reaction time): 9M-5h, 12M-5h, 15M-5h, 9M-24h, 12M-24h, and 15M-24h, respectively. The crystals at different sizes possessed irregular hexagonal shapes as shown in [**Figure 26(a-f)**] (SEM - JEOL JSM-7500F). To obtain monolayers of ZrP that were uniform in thickness, these layered crystals [**Figure 27(a)**] were exfoliated by dispersing the crystals in deionized (DI) water and subsequently adding tetra-(n-butyl ammonium) hydroxide (TBA^+OH^- , Aldrich, 40% in water) at a molar ratio of 1:1 (ZrP: TBA^+OH^-) at 0°C. The TBA^+OH^- molecule is depicted in **Figure 27(b)**. The concentrated suspensions were treated under sonication for 1 h and left for 3 days to ensure full intercalation of the TBA and complete exfoliation of the crystals.¹⁰⁰ A general exfoliation process is illustrated in **Figure 27(c)**. The size and varying polydispersities (σ) of the exfoliated platelets were calculated using a dynamic light scattering instrument (DLS, ZetaPALS, Brookhaven Instruments Corporation, Long Island, NY) to measure the translational and rotational diffusion of ZrP monolayers,⁴⁴⁰ since all the platelets have a fixed thickness of 2.68 ± 0.02 nm.¹⁰⁰ The size distributions are shown in **Figure 28(A1-A6)**, as represented by the green-dashed (gray-dashed) red

circles. The polydispersity values were obtained by an extreme distribution fit of the data and listed in **Table 3**.

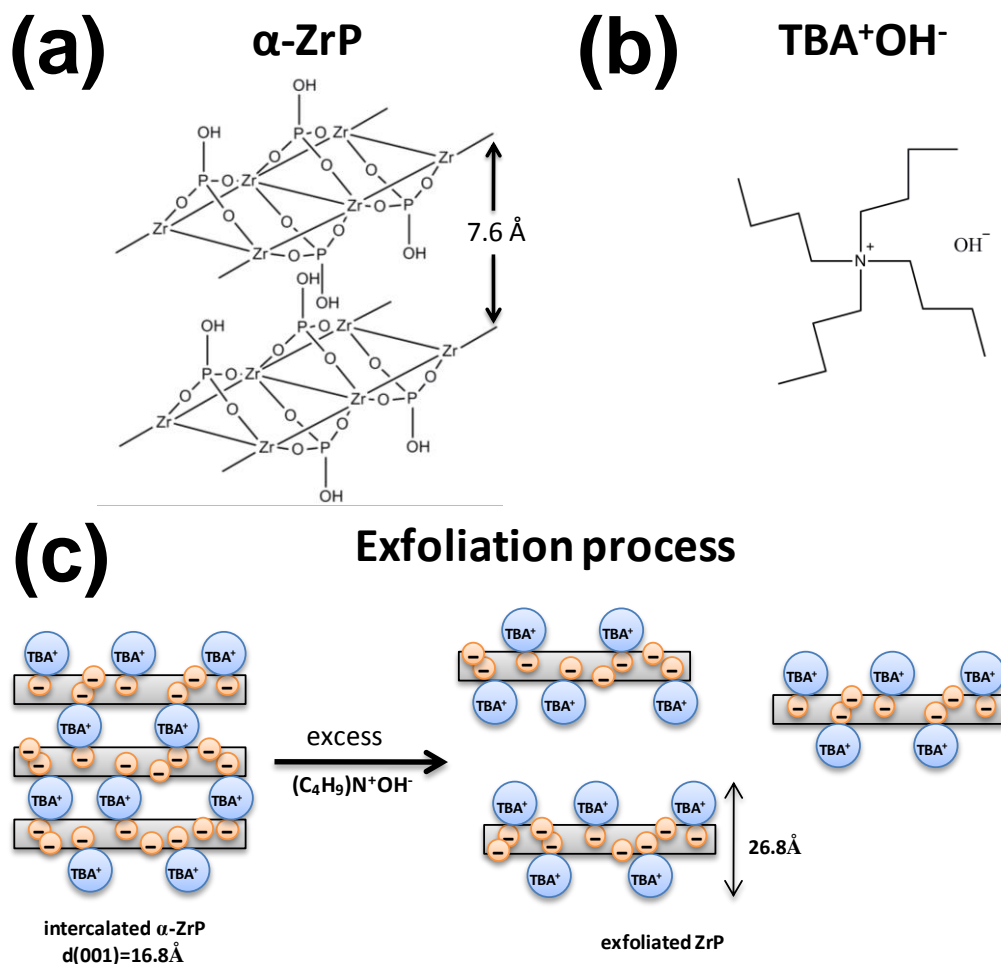


Figure 27. Structure of zirconium phosphate crystals and the exfoliation process. (a) Structure of crystalline zirconium phosphate (ZrP). (b) Guest molecule: n-tetrabutylammonium hydroxide (TBA⁺OH⁻) (c) Schematic process of lamellar crystals going through exfoliation by using excess of TBA. After exfoliation, monolayers were obtained having a thickness of 26.8 Å.

3.2.3.2 Control of the Size Polydispersity of ZrP Nanoplates via I-N Fractionation

To analyze the effect of polydispersity at different aspect ratios, we performed I-N fractionation to control the polydispersity of our samples. For each aspect ratio, the

concentrated ZrP monolayers' mother suspension was diluted to the I-N coexistence region, where the nematic volume occupies approximately 50% of the total suspensions after complete phase separation. Particle size segregation occurred as described in previous simulations,³³⁵ with larger-sized monolayers populating the nematic phase, reducing the size-polydispersity of both the lower (N) and upper (I) phases. This nematic phase was collected and the size distribution, labeled B1 to B6 in **Figure 28**, was compared to the original suspension A1 to A6 in **Figure 28**. The results show a slight increase in platelet size, and a significant reduction of polydispersity (more than 5%) for highly polydispersed samples ($\sigma > 25\%$). Furthermore, we fabricated more ZrP suspensions using ZrP crystals synthesized from the following conditions: 12M-24h, 9M-24h, 12M-5h, and 9M-5h to expand the experimental set of samples, but the I-N crystal fractionation was not performed. The size distributions of these additional samples labeled as C2, C3, C5, and C6 in **Figure 28**, for notation and comparison purposes.

For each aspect ratio of varying polydispersities, samples of decreasing concentrations were prepared by diluting a concentrated suspension into 8 mm \times 40 mm borosilicate glass cylinders (Fisher Scientific, Pittsburgh, PA). The suspensions were left at room temperature for five days until equilibrium was reached and the phases separated by sedimentation with a clear interface. The I-N phase behavior was analyzed by placing the tubes between two crossed polarizers and photographing using a Sony DSC-W220 digital camera [**Figure 29**].

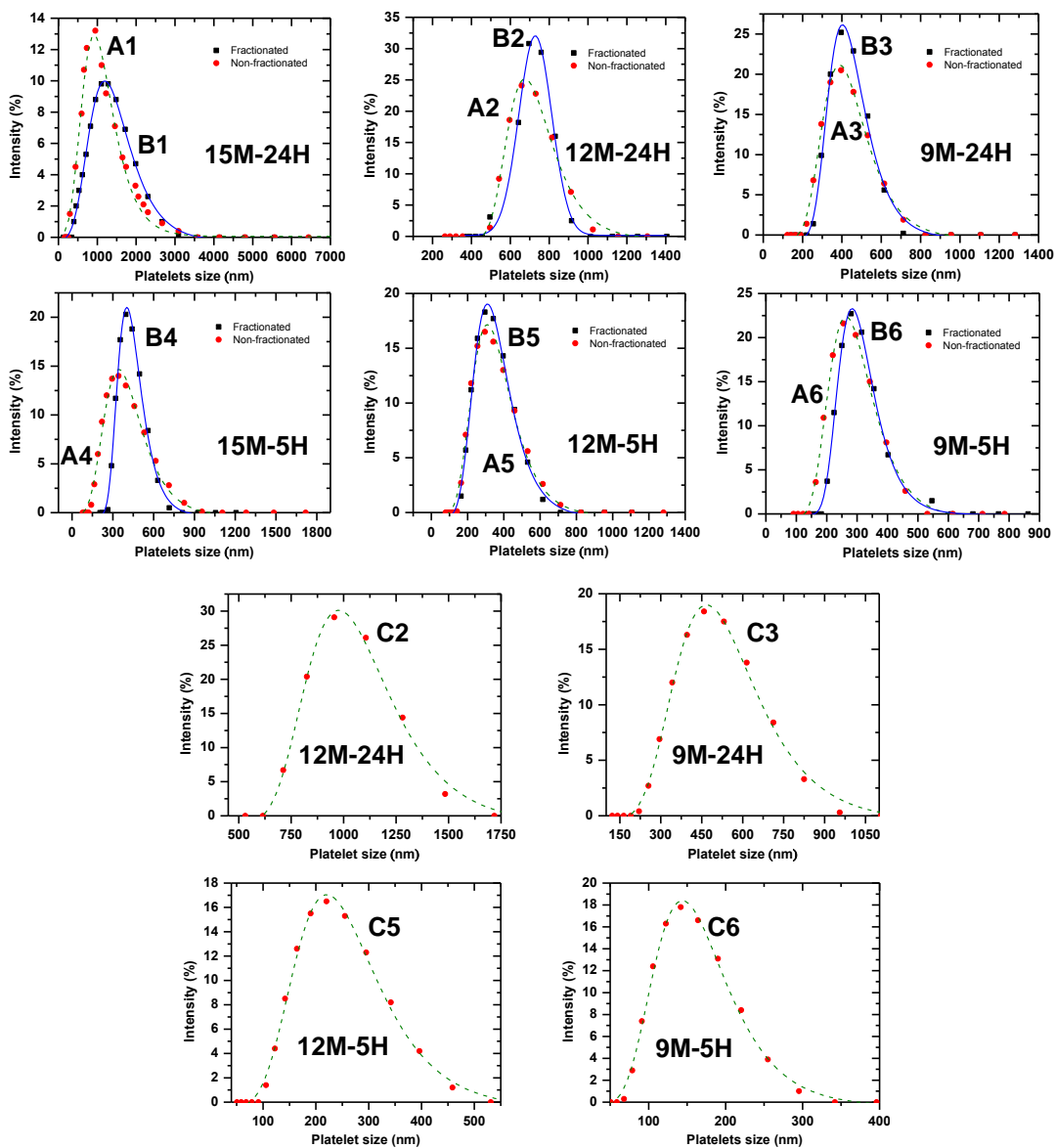


Figure 28. Size distribution for exfoliated ZrP platelets as measured by DLS. Aspect ratio and polydispersity obtained are listed in **Table 3**. The non-fractionated and the fractionated samples are represented by the green-dashed (gray-dashed) red circles and the blue-lined (black-lined) black squares, respectively. The lines are fit to the extreme distribution function.

Table 3. Characterization of the exfoliated ZrP platelets

Sample	Nanoplate size (nm)			Polydispersity (σ)			Inversed aspect ratio (ξ^*)		
	A	B	C	A	B	C	A	B	C
ZrP(9M-5H) (6)	331 ± 87	367 ± 107	214 ± 62	25 ± 1%	24 ± 1%	29 ± 2%	0.0081 ± 0.0020	0.0073 ± 0.0020	0.013 ± 0.004
ZrP(12M-5H) (5)	400 ± 146	536 ± 162	377 ± 121	31 ± 2%	28 ± 1%	32 ± 2%	0.0067 ± 0.0030	0.0050 ± 0.0020	0.0071 ± 0.0020
ZrP(15M-5H) (4)	653 ± 206	687 ± 132	-	35 ± 2%	26 ± 1%	-	0.0041 ± 0.0010	0.0039 ± 0.0010	-
ZrP(9M-24H) (3)	957 ± 147	992 ± 173	776 ± 225	27 ± 2%	22 ± 2%	29 ± 2%	0.0028 ± 0.0005	0.0027 ± 0.0005	0.0035 ± 0.0010
ZrP(12M-24H) (2)	1276 ± 303	1410 ± 369	1604 ± 320	23 ± 1%	18 ± 1%	20 ± 1%	0.0021 ± 0.0005	0.0019 ± 0.0005	0.0017 ± 0.0004
ZrP(15M-24H) (1)	2233 ± 807	2436 ± 562	-	39 ± 2%	28 ± 1%	-	0.0012 ± 0.0005	0.0011 ± 0.0003	-

Polarized photographs of completely phase-separated suspensions are shown in **Figure 29**. As the concentration of exfoliated layers of ZrP increases, a birefringent nematic phase starts to appear at the bottom of the samples. We confirmed the presence of the characteristic nematic Schlieren textures using an optical microscope (TE-2000U, Nikon) for each aspect ratio [**Figure 30(a-f)**]. The texture observed between cross polarizers displays dark brushes having irregular curved shapes corresponding to extinction positions of the nematic liquid. Disclinations of $s = \pm 1/2$ and $s = \pm 1$, characteristics of nematic textures were observable.⁴⁴² The nematic fraction increased as the platelet concentration increased in the coexistence region until full nematic phase is reached [**Figure 29**]. We measured the height of the nematic portion in the samples in **Figure 29** to determine the percentage of the nematic phase of each sample [**Figure 31**]. It was possible to determine ϕ_I and ϕ_N from data extrapolation fitting with a logistic function, $H=a/(1+\exp[-k(\phi-\phi_c)])$, where H is the relative fraction percentage of the nematic phase, a is the upper asymptote, k is the increase rate of the nematic height with respect to the increase of sample volume fraction, and ϕ_c is the concentration at the maximum rate. ϕ_I (set $H_I/a = 0.025$) and ϕ_N (set $H_N/a=0.98$) are the volume fractions on the boundaries of the I-N phase transition. The errors for ϕ_I , ϕ_N are $(\delta a + \delta H_{I,N})/(a - H_{I,N}) + \delta H_{I,N}/H_{I,N} + \delta \phi_c + \delta \phi_{\text{sample}}$, where $\delta \phi_{\text{sample}}$ is the error introduced via sample preparation. The error contribution from k was ignored. The biphasic gap was then calculated as $\Delta \phi_{I-N} = \phi_N - \phi_I$. The measured biphasic values ($\Delta \phi_{I-N}$) are listed in **Table 4**.

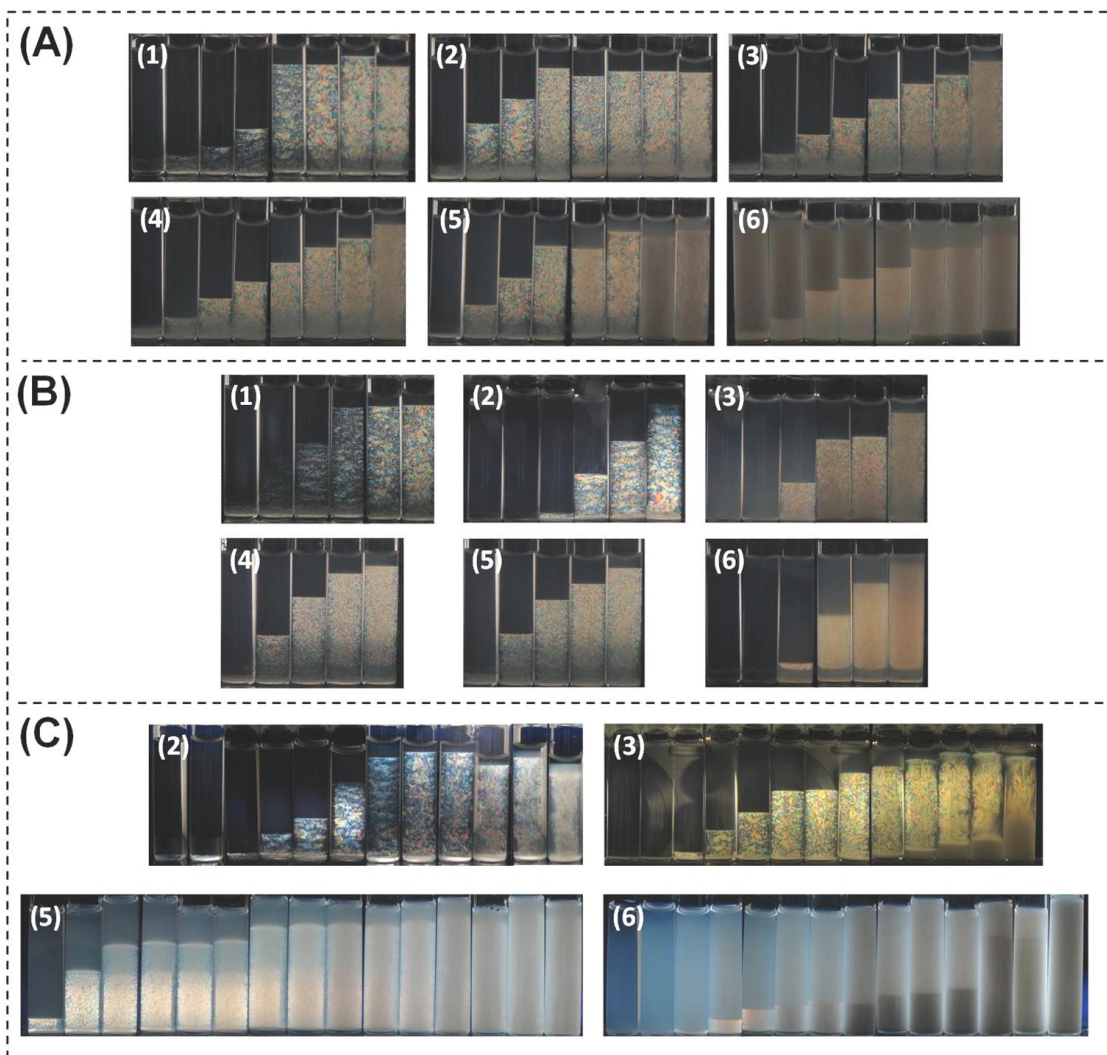


Figure 29. Suspensions of ZrP monolayers at various aspect ratios and different concentrations. (A1) through (A6) are the non-fractionated suspensions, and (B1) through (B6) are the fractionated suspensions. (C2) through (C6) are additional ZrP suspensions. Photographs were taken for samples set between cross polarizers to distinguish between upper isotropic and lower birefringent nematic liquid crystalline phase.

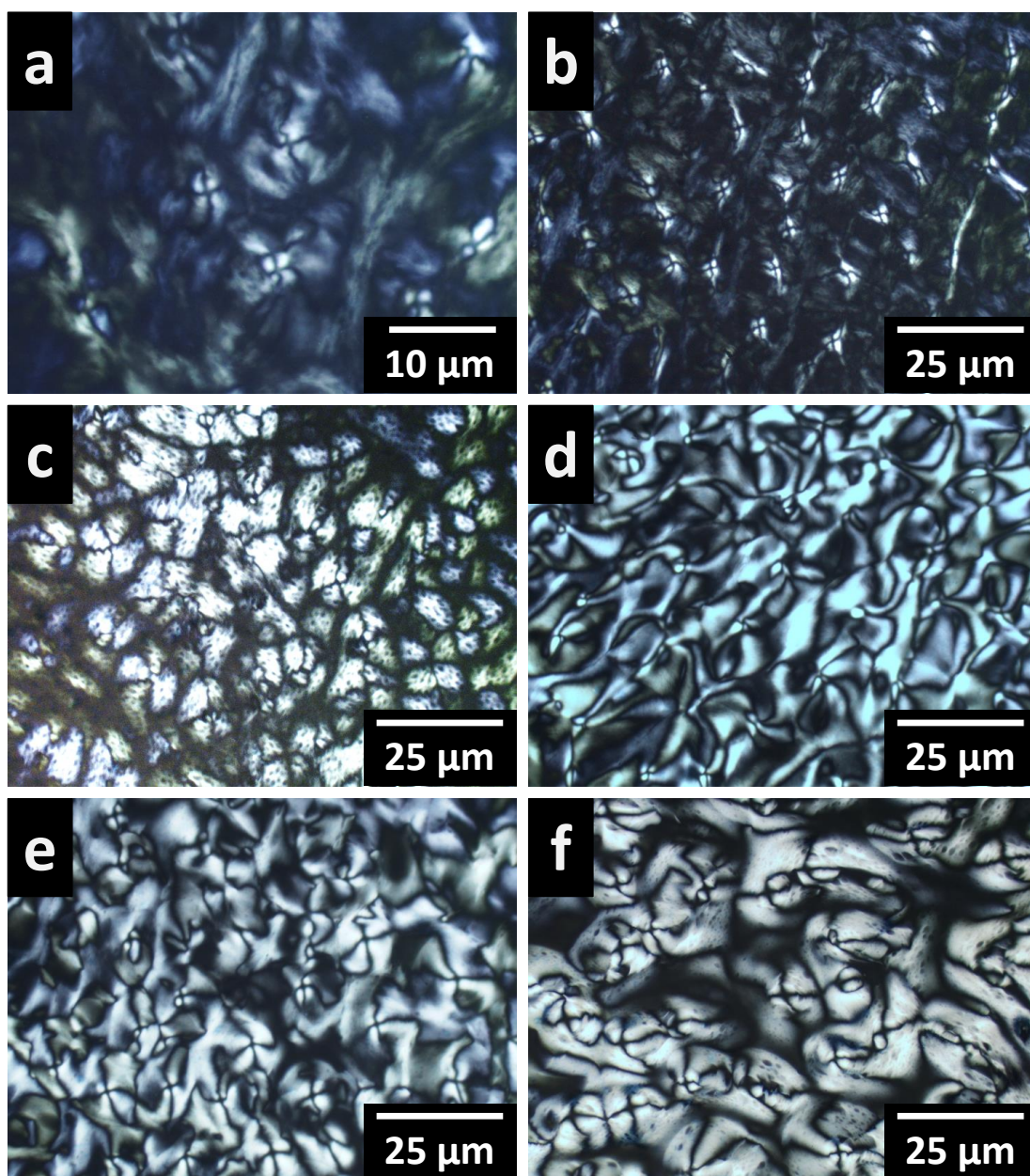


Figure 30. Cross-polarized optical microscopic images of nematic Schlieren textures at different aspect ratios. Inversed aspect ratio increases from (a) to (f) which are from samples of B1 to B6, and $\phi =$ (a) 0.0053, (b) 0.01, (c) 0.014, (d) 0.02, (e) 0.0420, and (f) 0.06. The micrographs were taken using a Nikon microscope TE-2000U with crossed polarizers. Picture of (a) was taken using 10x magnification and pictures of (b to f) using 4x magnification.

Table 4. The biphasic gap ($\Delta\phi_{I-N} = \phi_N - \phi_I$) values for different aspect ratios and polydispersities.

Sample	ϕ_I			ϕ_N			$\Delta\phi_{I-N}$		
	A	B	C	A	B	C	A	B	C
ZrP(9M-5H)(6)	$.023^{+0.003}_{-0.010}$	$.024^{+0.004}_{-0.008}$	$.062^{+0.010}_{-0.020}$	$.081^{+0.070}_{-0.012}$	$.055^{+0.045}_{-0.008}$	$.23^{+0.06}_{-0.03}$	$.058^{+0.070}_{-0.015}$	$.031^{+0.045}_{-0.011}$	$.17^{+0.06}_{-0.04}$
ZrP(12M-5H)(5)	$.017^{+0.003}_{-0.005}$	$.020^{+0.003}_{-0.006}$	$.028^{+0.004}_{-0.010}$	$.044^{+0.035}_{-0.007}$	$.042^{+0.020}_{-0.006}$	$.13^{+0.05}_{-0.02}$	$.028^{+0.035}_{-0.008}$	$.022^{+0.020}_{-0.008}$	$.10^{+0.05}_{-0.02}$
ZrP(15M-5H)(4)	$.0092^{+0.0014}_{-0.0030}$	$.010^{+0.002}_{-0.003}$	-	$.038^{+0.030}_{-0.006}$	$.020^{+0.010}_{-0.003}$	-	$.028^{+0.030}_{-0.006}$	$.01^{+0.010}_{-0.004}$	-
ZrP(9M-24H)(3)	$.0073^{+0.0010}_{-0.0030}$	$.0077^{+0.0012}_{-0.0020}$	$.012^{+0.002}_{-0.005}$	$.027^{+0.025}_{-0.004}$	$.014^{+0.007}_{-0.002}$	$.045^{+0.040}_{-0.007}$	$.020^{+0.025}_{-0.005}$	$.0066^{+0.0070}_{-0.0030}$	$.033^{+0.040}_{-0.008}$
ZrP(12M-24H)(2)	$.0068^{+0.0010}_{-0.0020}$	$.0060^{+0.0009}_{-0.0010}$	$.0045^{+0.0007}_{-0.0010}$	$.018^{+0.010}_{-0.003}$	$.010^{+0.002}_{-0.002}$	$.010^{+0.005}_{-0.002}$	$.011^{+0.010}_{-0.003}$	$.0044^{+0.0020}_{-0.0020}$	$.0055^{+0.0050}_{-0.0020}$
ZrP(15M-24H)(1)	$.0041^{+0.0006}_{-0.0010}$	$.0033^{+0.0005}_{-0.0010}$	-	$.010^{+0.007}_{-0.002}$	$.0052^{+0.0030}_{-0.0008}$	-	$.0059^{+0.0070}_{-0.0020}$	$.0019^{+0.0030}_{-0.0010}$	-

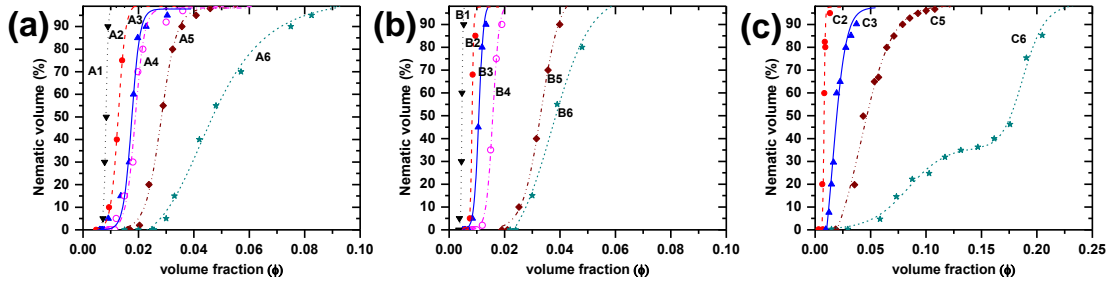


Figure 31. The relative fraction percentage of the nematic phase as a function of the monolayer volume fraction ϕ . (a) The non-fractionated suspensions, (b) the fractionated suspensions, and (c) the additional ZrP suspensions. Inversed aspect ratio increases from A1 to A6, from B1 to B6 and from C2 to C6. The values for inversed aspect ratio and polydispersity can be found in Table 1.

3.2.3.3 The Effect of Polydispersity on the I-N Transition at a Fixed Aspect Ratio

The effect of disk size polydispersity on the I-N transition was studied and compared to computer simulation results. Two inversed aspect ratio groups of 0.010 ± 0.003 and 0.0020 ± 0.0005 of ZrP samples were used. From **Table 3** we selected A6, B6, and C6 for group 1; and A2, B2, and C2 for group 2. For $\sigma=0$, we used the results obtained by Fartaria.¹⁵⁸ The isotropic (ϕ_I) and nematic (ϕ_N) volume fractions at inversed aspect ratios of 0.010 and 0.0020 were calculated to be $\phi_I = 0.026$ and $\phi_N = 0.027$, and $\phi_I = 0.0052$, and $\phi_N = 0.0056$, respectively, using $\phi = (9/8)(\xi^*)(\rho D^3)(1/3)^{1/2}$.¹⁹³ **Table 5** contains the volume fraction concentrations (ϕ_I , ϕ_N) and the polydispersity (σ) values. We plotted ϕ_I and ϕ_N as a function of polydispersity for 0.010 ± 0.003 and 0.0020 ± 0.0005 groups in **Figure 32(a)** and **Figure 32(b)**, respectively. It was observed that polydispersity has a great influence on the position of the I-N transition. As the polydispersity of suspensions increases, the biphasic gap broadens. In a recent publication¹⁶⁸ and in Bates *et al.*,³³⁵ it was shown from density functional theory (DFT)

calculation and computer simulations that an increase in polydispersity slightly decreases ϕ_I , but increases ϕ_N ; therefore the I-N transition widens with polydispersity, in agreement with our observation here. The DFT calculation there also showed a large biphasic gap at $\sigma = 0$, in contrast with the narrow gap reported by Bates *et al.*,³³⁵ at an inversed aspect ratio around zero. **Figure 32** also shows that DFT theory predicted a slower variation with size polydispersity compared to our experimental results. Fartaria¹⁵⁸ studied the dependence of the biphasic gap in the low inversed aspect ratio region. In comparison, the simulation is consistent with our experimental ZrP results for ϕ_I , however differs for ϕ_N due to polydispersity in our experiments (**Table 5**). Therefore, we can conclude that polydispersity does not affect ϕ_I values, but has a large effect on the ϕ_N values. In simulations, the I-N transition is weakly first order when polydispersity is zero.⁴⁴ But in our experiments, fractionation occurs due to polydispersity, where the large platelets populate the nematic phase and the smaller platelets stay in the isotropic phase. As a result, the biphasic gap becomes strongly first order.^{168, 335}

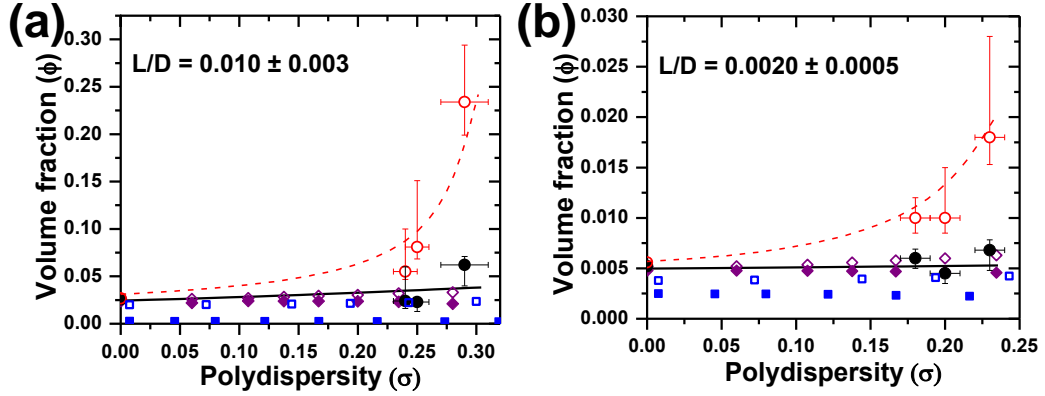


Figure 32. Volume fraction (ϕ) of the isotropic (solid black circles) and nematic (open red (gray) circles) volume fraction of the cloud phases as a function of polydispersity (σ) at fixed inverted aspect ratios of around (a) 0.010 and (b) 0.0020. The concentrations at zero polydispersity for both graphs were obtained from simulations of Fartaria *et al.*¹⁵⁸

The lines are guides for the eye. The solid and open blue (black) squares are the theoretical ϕ_I and ϕ_N , respectively, from Martinez-Raton *et al.*, using a DFT calculation with Zwanzig approximation.¹⁶⁸ The solid and the open purple (black) diamonds are the theoretical ϕ_I and ϕ_N , respectively, from Frenkel *et al.*, for infinitely thin plates.³³⁵

Table 5. Isotropic (ϕ_I) and nematic (ϕ_N) volume fractions for inverted aspect ratios (ξ^*) of 0.010 ± 0.003 and 0.0020 ± 0.0005 at different polydispersity (σ). The concentrations at zero polydispersity for both graphs were obtained from simulations of Fartaria and Sweatman.¹⁵⁸

Inversed aspect ratio (ξ^*)	Polydispersity (σ)	Isotropic (ϕ_I)	Nematic (ϕ_N)
0.010 \pm 0.003	0%	0.026	0.027
	24 \pm 1%	.024 ^{+0.004} _{-0.008}	.055 ^{+0.045} _{-0.008}
	25 \pm 1%	.023 ^{+0.003} _{-0.010}	.081 ^{+0.070} _{-0.012}
	29 \pm 2%	.062 ^{+0.010} _{-0.020}	.23 ^{+0.06} _{-0.03}
0.0020 \pm 0.0005	0%	0.0052	0.0056
	18 \pm 1%	.0060 ^{+0.0009} _{-0.0010}	.010 ^{+0.002} _{-0.002}
	20 \pm 1%	.0045 ^{+0.0007} _{-0.0010}	.010 ^{+0.005} _{-0.002}
	23 \pm 1%	.0068 ^{+0.0010} _{-0.0020}	.018 ^{+0.010} _{-0.003}

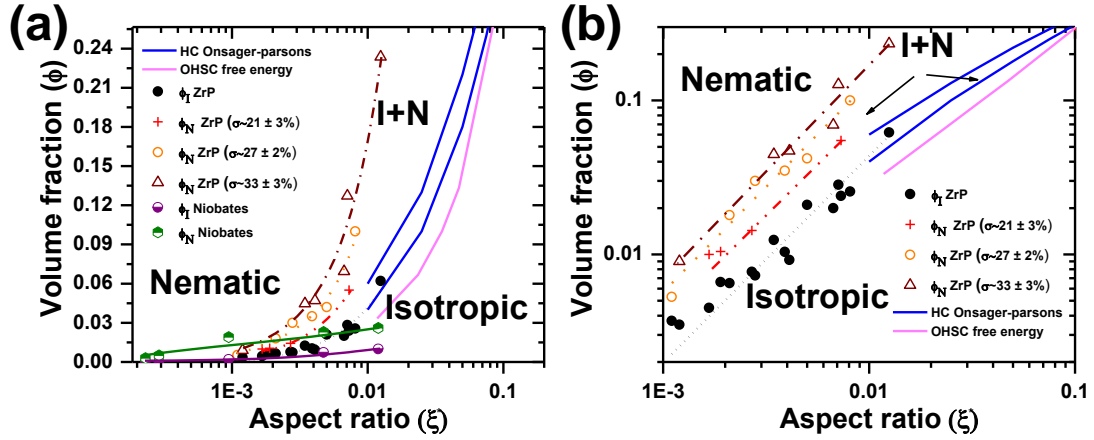


Figure 33. Comparison of the experimental ϕ_I and ϕ_N and simulation data. a) Linear-log diagram illustrating the correspondence of the ϕ_I with the Onsager-Parson theory and the OHSC free energy calculations. The difference in ϕ_N is due to effect of polydispersity of the ZrP platelets. The lines are guides for the eye. b) Log-log diagram showing power law scaling of inversed aspect ratio for ϕ_I , i, ii and $iii=23.1 \pm 8.1(\xi^*)^{1.36 \pm 0.10}$, and $\phi_{N, i}=115.5 \pm 78.6(\xi^*)^{1.41 \pm 0.20}$, $\phi_{N, ii}=68.6 \pm 48.3(\xi^*)^{1.36 \pm 0.10}$, and $\phi_{N, iii}=36.9 \pm 6.9(\xi^*)^{1.32 \pm 0.04}$ for groups i, ii and iii, confirming that the width of the biphasic transition is affected by aspect ratio and polydispersity.

3.2.3.4 The Effect of Aspect Ratio and Polydispersity on the I-N Transition

The combinational effect of aspect ratio and polydispersity on the I-N transition was evaluated. The isotropic transition volume fractions (ϕ_I) of all ZrP samples were analyzed together since they were only slightly affected by polydispersity. In contrast, the nematic volume fractions (ϕ_N) of the ZrP samples were studied in groups because they depended strongly on polydispersity. The samples were classified into groups i, ii, and iii for polydispersities of $33 \pm 3\%$, $27 \pm 2\%$ and $21 \pm 3\%$, respectively, as shown in **Table 6**. The transition boundaries are plotted in **Figure 33(a)**, where the solid black circles represent the isotropic phases and the red wine (dim gray) open triangles, orange (light gray) open circles, and red (dark gray) crosses represent the nematic phases for

group i, ii, and iii, respectively. **Figure 33(a)** shows that the biphasic gap ($\Delta\phi_{I-N}$) broadens as influenced by aspect ratio and polydispersity, implying that the nematic phase is favored at small inversed aspect ratios and higher concentrations.^{4, 6} The values can be found in **Table 4**. This behavior agrees with simulations from Bates *et al.*,³³⁵ where disks having a low aspect ratio were found to have a higher nematic orientation compared to disks having a higher inversed aspect ratio for a fixed concentration. In addition, Fartaria¹⁵⁸ affirmed that the first-order behavior of the I-N transition is more noticeable for larger inversed aspect ratio (ξ^*) values. In **Figure 33(a)** we also compare our study with the isotropic and nematic volume fractions obtained from niobate nanosheets represented as purple (dark gray) half-open circles and green (gray) half-open hexagons, respectively.²⁰⁶ The niobates isotropic line, except the data point around $L/D \approx 0.01$, is in agreement with ZrP. On the other hand, the nematic line does not overlap with the ZrP volume fractions.

Table 6. Classification of ZrP suspensions according to polydispersity.

Polydispersity group	A	B	C
i ($33 \pm 3\%$)	1, 4, 5	N/A	3, 5, 6
ii ($27 \pm 2\%$)	2, 3, 6	1, 4, 5	N/A
iii ($21 \pm 3\%$)	N/A	2, 3, 6	2

Also, our experimental results are comparable with the Onsager-Parson theory for flat cylinders¹³⁷ and OHSC^{159, 160} illustrated as blue (black) lines and a light pink (light gray) line, respectively, in **Figure 33(a,b)**. The discrepancies of the ZrP from

computer simulations might be due to change of ϕ_I and ϕ_N by the particle shape and uniformity.¹⁸⁰ For instance, for different non-circular shapes (regular hexagons, pentagons, squares, triangles, ellipses, and rectangles), the width of the biphasic gap was found to be the same. However, the I-N transition decreases in volume fraction if the shape differs from circular.¹⁸⁰

In **Figure 33(b)**, a further analysis was obtained from a log-log plot of the experimental data in comparison to simulations and theory. The isotropic (ϕ_I) and nematic (ϕ_N) lines for the experiments and simulations^{137, 139} were fitted using a power law function, $\phi = m(\xi^*)^n$, and compared in **Table 7**. In **Figure 33(b)**, it was observed that the I-N transition volume fractions for ZrP scales with the aspect ratio with a power law $\phi_{I,N} \sim (\xi^*)^{1.36 \pm 0.07}$. This result demonstrates that the broadening of the I-N transition strongly depends on polydispersity. As a result, the difference in the values of the parameters obtained from our experimental results from the simulations can be attributed to polydispersity,³³⁵ shape,¹⁸⁰ and the inter-particle interactions, since simulations did not consider these factors. Assuming the shape of the platelets affects ϕ_I and ϕ_N in the same way,¹⁸⁰ the biphasic gap ($\Delta\phi_{I-N}$) is essentially a function of polydispersity only. The position parameter (m) in the power law function depends on polydispersity and shape. **Table 7** and **Figure 33** show that the exponent (n) slightly depends on polydispersity. Therefore, it becomes interesting to see why similar colloidal systems, such as clay, having a large size polydispersity and large inversed aspect ratio ($\xi^* \sim 0.01$), commonly do not exhibit a nematic, but rather a gel phase, where some orientational order should be present.^{187, 188, 192, 443} We observed in this study that it is polydispersity that widens

$\Delta\phi_{I-N}$. Large size polydispersity could be one of the factors preventing a fully nematic phase suspension for clay.

3.2.4 Summary

In summary, our experiments revealed the effect of aspect ratio and polydispersity on the isotropic-nematic transition of colloidal suspensions of nanoplates that are uniform in thickness at the low thickness-to-diameter ratio limit. The aspect ratio of the nanoplates can be tailored by varying the size of ZrP crystals, and a subsequent exfoliation with intercalation of tetrabutylammonium cations between the interlayers. The I-N transition widens as inverted aspect ratio and polydispersity increase. The experimental data were compared to previous simulations, and the dissimilarities were attributed to size polydispersity and shape of the platelets. Extension of the present methodology can be applied to similar layered structures like montmorillonite,²⁸¹ layered double hydroxides,⁹² and niobates.^{81-83, 93-98, 218} The study of the I-N transition will allow further studies on liquid crystals dependence on aspect ratio, which will be a factor in tailoring optical, electrical, and mechanical properties of self-assembled discotic materials.

Table 7. Comparison of experimental and simulations isotropic (ϕ_I) and nematic (ϕ_N) lines on power law ξ^* scaling.

Research		Present work (ZrP)			Onsager-Parson theory ¹³⁷ (Short cylinders)	NVT Monte Carlo ¹³⁹ (cut spheres)
Polydispersity groups		i ($\sigma_i \sim 33 \pm 3\%$)	ii ($\sigma_{ii} \sim 27 \pm 2\%$)	iii ($\sigma_{iii} \sim 21 \pm 3\%$)	$\sigma=0$	$\sigma=0$
ϕ_I	m		23.1 ± 8.1		1.87 ± 0.10	4.94 ± 0.03
	n		1.36 ± 0.1		0.72 ± 0.03	1.20 ± 0.04
ϕ_N	m	115.5 ± 78.6	68.6 ± 48.3	36.9 ± 6.9	2.11 ± 0.20	Same as ϕ_I
	n	1.41 ± 0.20	1.36 ± 0.10	1.32 ± 0.04	0.83 ± 0.03	

3.3 Thermo-responsive Discotic Nematic Hydrogels

3.3.1 Introduction

Liquid crystals are intermediate states of materials with symmetry between liquid and crystalline ones. They are characterized by spontaneous orientation order.^{6, 7, 15, 335} Liquid crystals can be obtained from various colloidal systems such as spheres, rods, and disks.¹ Although numerous disk-like fluids exist in nature, fewer studies of disks than of rods have been undertaken.^{3, 4} In 1938, Langmuir reported the liquid crystalline state of disk-like, lath-like natural hectorite clay particles (*i.e.*, California bentonite).⁵ Partially influenced from Langmuir's observations, Onsager predicted the capability of rods and disks interacting by hard-core repulsions to form a liquid that is crystalline at high concentration on excluded volume effects.⁶ The discotic isotropic-nematic (I-N) transition has attracted enormous attention in the past decades.^{15, 16, 122, 168, 192, 198, 200} Lekkerkerker *et al.*,^{16, 193, 201} reported I-N transitions using gibbsite plate-like suspensions having an aspect ratio ($\xi = \text{diameter/thickness}$) around 11. These plate-like particles were suspended in toluene¹⁶ or water^{193, 201} via steric and electrostatic interactions, respectively. Stable nematic states have been obtained from Mg/Al layered double hydroxides (LDH) particles dispersed in water²⁰² or toluene.²⁰³

Inorganic nano-sheet suspensions stabilized by diffuse layers of large-sized charges have gained great interest as *lyotropic* liquid crystals.^{101, 122, 198, 199, 206, 207} They are obtained via exfoliation of layered materials in solvent and are characterized by a high anisotropy (*i.e.*, large aspect ratio). An extensive number of layered materials have been exfoliated to obtain inorganic nano-sheet suspensions,¹⁰⁴ such as clay,^{5, 187-189}

layered double hydroxides,⁹² niobates,^{81-83, 93-98} titanium oxides,^{81, 84} phosphates,^{81, 82, 99-101} and graphite.⁴³⁹ These inorganic nano-sheet suspensions are distinguished by large diameters, thin and uniform thicknesses, and exceptional electrical,²⁹⁵ optical,²⁹⁵ and magnetic^{305, 306} properties. In fact, highly anisotropic inorganic nano-sheets possess a higher nematic orientation compared with low-aspect-ratio disk-like colloidal systems^{158, 335} and are ready to evolve into a nematic state at extremely low nano-sheet concentrations.^{80, 206} The high fluidity (*i.e.*, low viscosity) of these suspensions allows macroscopic alignment via electrical³¹⁵⁻³¹⁷ or magnetic^{21, 101, 308-314} forces.

Zirconium phosphate (ZrP) nano-sheets are inorganic, acidic and cation exchange materials. They are obtained from the exfoliation of different phases of ZrP lamellar crystals, which differ in interlayer spacing and crystalline structure.^{79, 110} ZrP nano-sheets are indeed just the thickness of a single layer of O, P, and Zr atoms. The most widely known phase of ZrP is the α phase,^{79, 110} where the crystal lateral size, morphology and aspect ratio can be tailored by varying the parameters of the synthesis.^{80, 111} In the last decades, extensive work on the ZrP chemistry has been undertaken.⁴⁴⁴⁻⁴⁴⁷ A myriad of applications have started such as fuel cells,^{444, 448} biosensors,⁴⁴⁷ catalysis,⁴⁴⁹ and drug delivery.^{445, 446} We recently reported the use of amphiphilic ZrP nano-sheets as Pickering foams²⁵⁹ and emulsions²⁶⁰ stabilizers. Another possible way to exploit the ZrP extraordinary properties would be the incorporation of these nano-sheets into polymer matrix. For instance, mechanical properties of ZrP-epoxy nanocomposites^{285, 286} were enhanced²⁸⁷⁻²⁸⁹ by loading different amount of ZrP nano-sheets at various aspect ratios.²⁹⁰

We recently investigated the I-N transition at high aspect ratios ($\xi > 10$) and various polydispersities using ZrP nano-sheets.⁸⁰ The ZrP crystal lateral size was obtained in an extensive range^{80, 111} and subsequently exfoliated using tetrabutylammonium cations (TBA⁺) cations.⁸⁸ We found that the location of the I-N transition strongly depends on nano-sheet aspect ratio and lateral-size polydispersity. We indeed demonstrate that the biphasic gap ($\Delta\phi_{I-N} = \phi_N - \phi_I$) transition decreases along with the increase of nano-sheet aspect ratio.⁸⁰

Stimuli-responsive hydrogels have the ability to change with the system surroundings. The response to stimuli, such as temperature,⁴⁵⁰ pH,⁴⁵¹ photons,^{452, 453} and antigens,⁴⁵⁴ suggests potential applications in fields of drug delivery,⁴⁵⁵ optical microlenses,⁴⁵⁶ and sensors,⁴⁵⁷ amongst others. In particular, thermo-responsive hydrogels are promising ones that they present a first-order phase transitions at its lower critical solution temperature (LCST).⁴⁵⁸⁻⁴⁶⁰ To date, poly (N-isopropylacrylamide) (PNIPAm) is the most studied thermo-sensitive polymer in the literature. PNIPAm can evolve from an expanded to a collapsed state triggered by temperature rise.⁴⁶¹⁻⁴⁶³ A thermo-responsive polymer matrix is a good candidate for fabrication of inorganic liquid crystal nanocomposites, where the system volume can be easily contracted, therefore effectively increasing the nano-sheet volume fraction.⁴⁶⁴⁻⁴⁶⁶ A nematic hydrogel composed of inorganic ZrP nano-sheets embedded into a thermo-sensitive polymer matrix might make it a good candidate material for technological applications, including artificial muscles,^{467, 468} actuators,⁴⁶⁹ and electro-optical devices.⁴⁷⁰

Here, we make use of high-aspect-ratio zirconium phosphate (ZrP) nano-sheets to obtain thermo-responsive polymer hydrogels of a high nematic ordering. The nano-sheets were dispersed into a solution composed of N-isopropylacrylamide (NIPAm) along with acrylamide (AAm) as constituent monomers. In situ solvent polymerization leads to the formation of nematic hydrogels, as shown in **Figure 34a**. The nematic liquid crystal phase formation of ZrP nano-sheets enables ordering inside the hydrogels. These discotic nematic hydrogels have remarkable transparency, as well as thermo-sensitivity, allowing study of the discotic I-N transition and liquid crystalline nematic textures not only by increasing the initial nano-sheet concentration, but also by volume compression from the polymer matrix. In the literature, nematic states of calamitic^{464, 465, 471} and discotic⁴⁷² fluids in polymer nanocomposites have been reported. However, nematic ordering within the nanocomposites was obtained only at particle concentrations above 5 %wt. Our study is unique, since the nematic hydrogels fabricated here required a much lower particle concentration ($\phi_{\text{ZrP}} < 0.5$ %wt.). As previously mentioned, the intrinsic high anisotropy of the ZrP nano-sheets enables the formation of highly ordered liquid crystalline states at much reduced particle amounts.^{80, 158, 335} In nature, opals, nacre, bone, and enamel are highly ordered nanocomposites; the study of analogous materials is of particular interest.

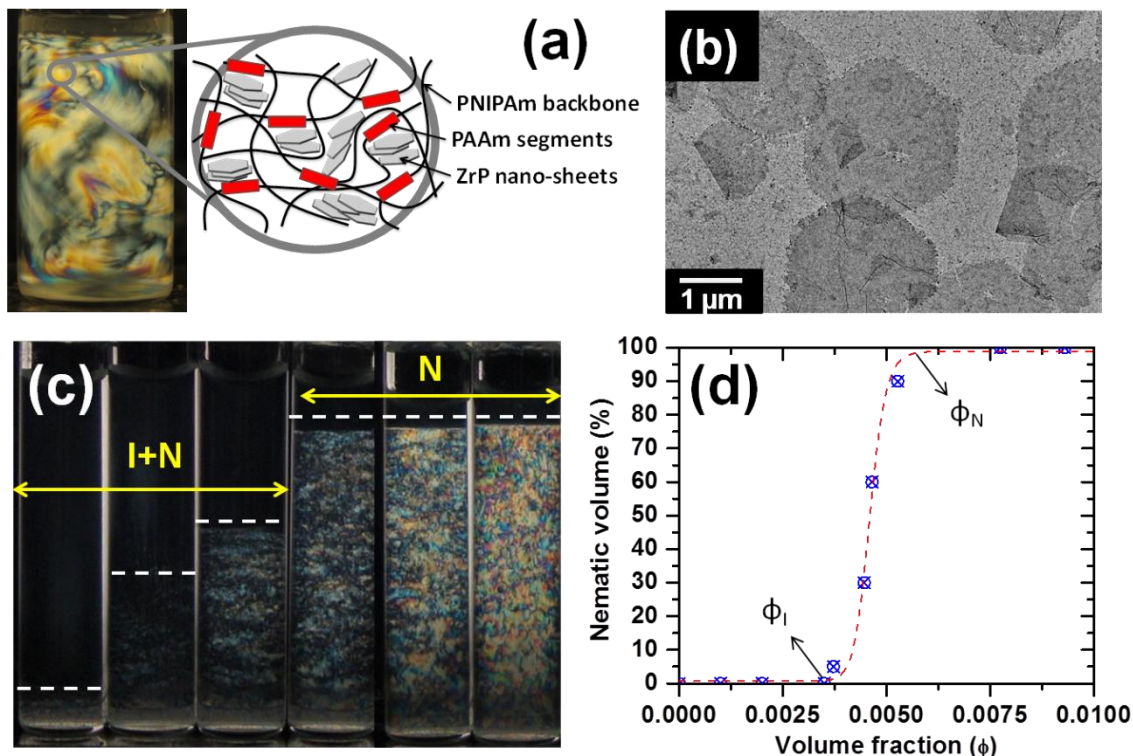


Figure 34. The study of ZrP isotropic-nematic (I-N) transition (a) ZrP-embedded PAAm-PNIPAM hydrogel. Schematic representation of ZrP nano-sheets dispersed in solvent between PAAm and PNIPAM polymer networks. (b) Transmission electron micrographs (TEM) of ZrP nano-sheets. (c) The discotic I-N phase diagram of ZrP nano-sheets. The sequence, left to right, corresponds to nano-sheet volume fractions of $\phi_{\text{ZrP}} = 0.0037, 0.0045, 0.0047, 0.0053, 0.0078, \text{ and } 0.0093$ respectively. (d) The nematic percentage as a function of volume fraction depicting the I-N transition. The arrows indicate the isotropic (ϕ_{I}) and nematic (ϕ_{N}) volume fraction transitions.

3.3.2 Experimental

3.3.2.1 Synthesis and Exfoliation of ZrP Crystals

α -ZrP crystals were fabricated in a phosphoric acid solution of 15 M for 24 h via hydrothermal method.¹¹¹ α -ZrP is a crystal composed of layers having the same thickness ($\sim 2.68 \pm 0.01$ nm).^{79, 100, 110} The ZrP nano-sheets were obtained by delaminating the crystals using tetrabutylammonium hydroxide (TBA^+OH^- , Sigma Aldrich, 40 %wt. in water) at a molar ratio of 1:1 in deionized (DI) water at 0°C.⁸⁸ The

suspension was treated under sonication for 3 h and left for 5 days to assure a complete exfoliation of the crystals. From this procedure, we obtained ZrP nano-sheets of 2436 ± 562 nm. The size and polydispersity of the nano-sheets were calculated using a dynamic light scattering instrument (DLS, ZetaPALS, Brookhaven Instruments Corporation, Holtsville, NY). From the translational and rotational diffusion of the nano-sheets,^{48, 440} the average particle size can be estimated, since they are characterized by having the same thickness ($\sim 2.68 \pm 0.01$ nm).¹⁰⁰ **Figure 34b** shows a transmission electron microscope (TEM) micrograph of ZrP nano-sheets after exfoliation of pristine ZrP crystals, confirming the characteristic hexagonal shapes of the nano-sheets.

3.3.2.2 Analysis of the Discotic I-N Transition

The discotic I-N transition was analyzed by diluting a concentrated mother suspension into borosilicate glass vials at various nano-sheet concentrations.⁸⁰ As the concentration of nano-sheet increased, a liquid crystalline texture (*i.e.*, nematic) starts to develop at the bottom of the suspensions until a full nematic suspension is obtained (**Figure 34c**). The vials were placed between two crossed polarizers and photographed using a Sony DSC-W220 digital camera as shown in **Figure 34c**. We measured the height of the nematic portion in the samples to determine the percentage of the nematic phase of each suspension (**Figure 34d**) driven by sedimentation.⁴⁷³ From **Figure 34d**, we determined the isotropic and nematic transition volume fractions, ϕ_I and ϕ_N , as $0.0033^{+0.0005}_{-0.0010}$ and $0.0052^{+0.0030}_{-0.0008}$, respectively. A more detailed procedure to determine the transition concentrations can be found in Mejia *et al.*⁸⁰.

The liquid crystalline texture was observed between crossed polarizers using an optical microscope (TE-2000U, Nikon). A ZrP nano-sheet suspension having a volume fraction of 0.010 was loaded into a rectangular-thin capillary of 0.1 x 1 mm and sealed using epoxy glue (5 Minute, Devcon) to prevent water evaporation. As expected, we confirmed the presence of nematic Schlieren textures as shown in **Figure 35a**. The nematic texture displays typical curved-dark brushes that merge into center points (*i.e.*, singularity).⁴⁷⁴

3.3.2.3 Preparation of ZrP Nematic Hydrogels

In general, a ZrP nano-sheet suspension was added to an aqueous monomer solution of acrylamide (AAm, 0.00235 ± 0.00010 g/mL), N-isopropylacrylamide (NIPAm, 0.00942 ± 0.00010 g/mL), N,N'-methylene bisacrylamide (cross-linker agent, 0.00045 ± 0.00001 g/mL), and urea (0.0348 ± 0.0001 g/mL). Subsequently, 0.11–20 μ L from a fresh aqueous solution of ammonium persulfate (APS, initiator, 0.10 ± 0.01 g/mL) and 5–20 μ L of N,N,N',N'-tetramethylethylenediamine (TEMED, catalyst) were added into 1 mL of the ZrP-monomer suspension. Finally, after mild shaking for a few minutes, nano-sheet-monomer suspension was loaded into a rounded borosilicate glass cylinder (Fisher Scientific, Pittsburgh, PA) and left to initiate the radical polymerization for 24 h at room temperature. The nematic hydrogels reported in this paper were fabricated using the same monomer, cross-linker and urea concentrations. **Figure 34a** illustrates a ZrP hydrogel consisting of homogeneously dispersed ZrP nano-sheets and two types of flexible polymer chain segments: PAAm and PNIPAm. For optical

characterization between crossed polarizers, the nano-sheet-monomer suspension was injected into a rectangular-thin capillary, sealed, and then concurrently polymerized and cross-linked at 295 K. **Figure 35b** shows distinctive discotic nematic textures of the produced ZrP-hydrogels having a ZrP nano-sheet volume fraction of 0.023 ± 0.001 .

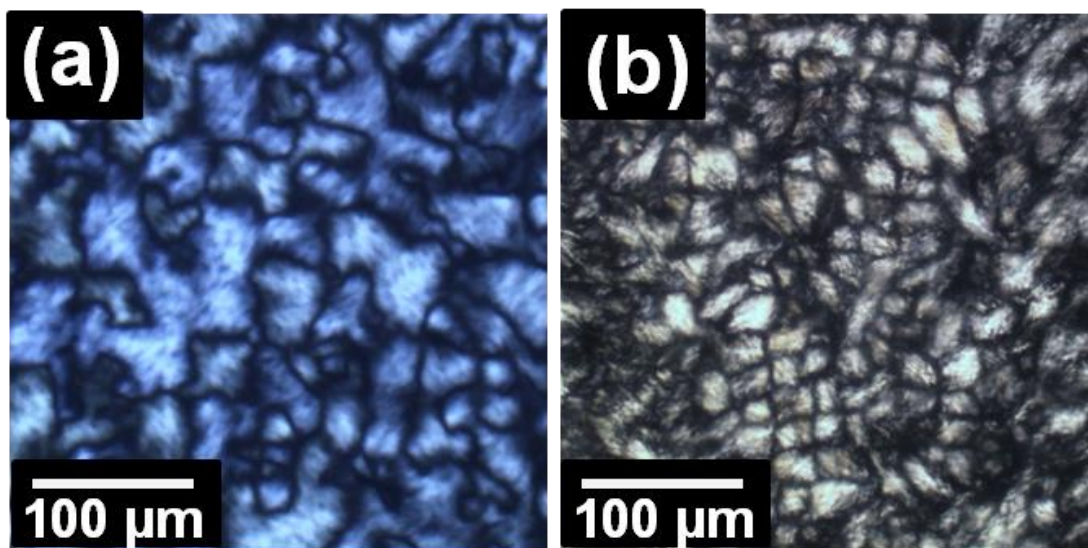


Figure 35. Schlieren texture of ZrP nano-sheet having a size of 2436 ± 562 nm (a) in aqueous suspension at $\phi_{\text{ZrP}}=0.010 \pm 0.001$ and (b) in PNIPAm-PAAm hydrogel at $\phi_{\text{ZrP}}=0.023 \pm 0.001$.

3.3.3 Results and Discussion

3.3.3.1 The Effect of Initiator and Accelerator on the Nematic Domains

We systematically varied the concentration of the initiator (APS) and the catalyst (TEMED) at a fixed ϕ_{ZrP} of 0.0035 ± 0.0005 . Since APS and TEMED is an initiator/catalyst system that provides free radicals to the vinyl polymerization, increasing TEMED concentration will increase the homolytic cleavage on moieties of APS.⁴⁷⁵ On the other hand, increasing the initiator (APS) concentration will introduce

hydroxyl radical group (-OH) termination on the polymer chains obtained by the cleavage of the persulfate initiator.^{475, 476} The nano-sheet concentration here, $\phi_{ZrP} = 0.0035 \pm 0.0005$, is slightly above the starting point of the I-N transition ($\phi_I = 0.0033_{-0.0010}^{+0.0005}$). Although samples at the beginning of the isotropic-nematic transition are mostly dark between crossed polarizers (**Figure 34c**), gently mixing the hydrogel during polymerization allows the nano-sheet aligning in the resulted flow.

Each sample was loaded into rounded borosilicate glass. Pictures of nematic hydrogel texture were obtained by positioning the vials between crossed polarizers, as shown in **Figure 36a**. The nematic hydrogel texture of each sample allowed us to qualitatively characterize the effect of the initiator and catalyst on the quantity and magnitude of the liquid crystalline domains. Interestingly, we identified a stronger initiator (APS) effect compared with the catalyst (TEMED) on the resultant polymeric matrix. From left to right in **Figure 36a**, by increasing catalyst concentration, a roughly constant number of nematic domains are observed. However, from top to bottom, as the initiator concentration increased in **Figure 36a**, an abrupt effect on the number and magnitude of nematic domains is observed. This behavior might be explained from the number of free radicals, R^* , that increment along with the initiator concentration. In fact, R^* is strongly proportional to $[\text{initiator}]^{1/2}$, that eventually leads to the formation of a larger number of polymer segments in the network.⁴⁷⁷ APS has a strong effect on the polymer chain length and the cross-linking density of the polymer matrix.⁴⁷⁷ Polymerization and cross-linking varies the liquid crystal orientation along the normal director of the nano-sheets, increasing the amount of extinction points in the nematic

texture. As a result, the primary polymer chains configuring the hydrogel network break the large nematic domains into smaller ones (**Figure 36a**).

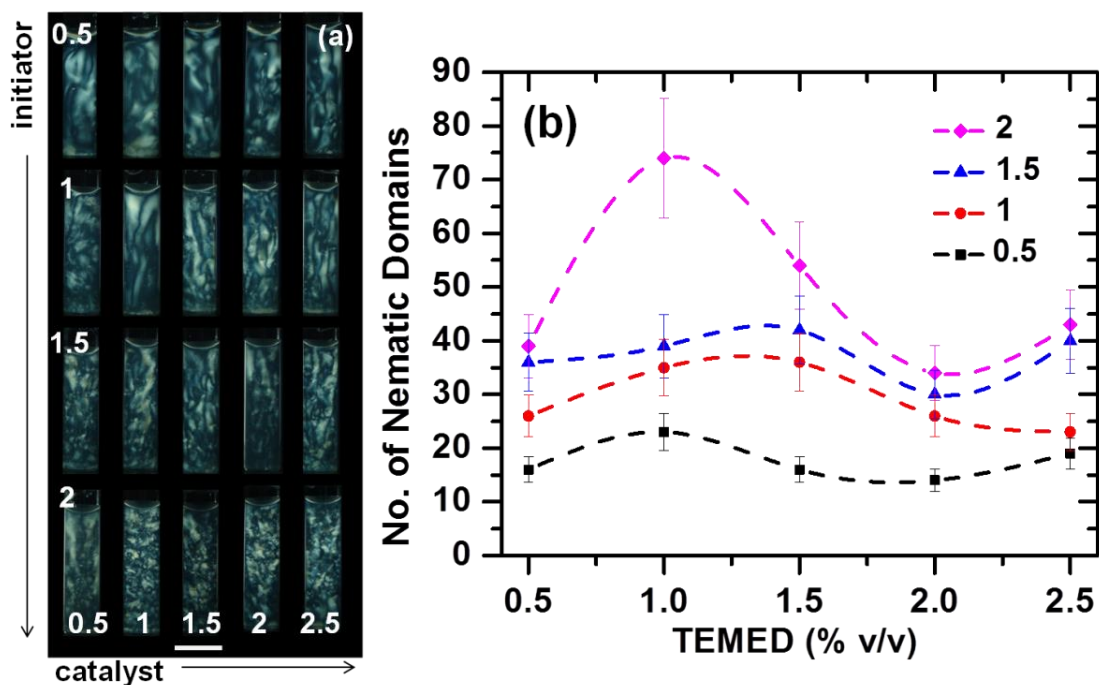


Figure 36. The effect of initiator (APS) and catalyst (TEMED) on the texture of the nematic hydrogels. (a) Crossed polarized pictures of the nematic hydrogels at various initiator and catalyst concentrations. The ZrP nano-sheet volume fraction is $\phi_{\text{ZrP}}=0.0035 \pm 0.0005$. The scale bar is 1 cm. (b) Plot of the number of nematic domains as a function of catalyst concentration. The black squares, red circles, blue triangles and pink diamonds correspond to an initiator concentration of 0.5 ± 0.1 , 1.0 ± 0.1 , 1.5 ± 0.1 and 2.0 ± 0.1 %wt., respectively.

To obtain quantitative details from the crossed polarized pictures, **Figure 36a** was processed and analyzed using ImageJ software (v1.43, National Institutes of Health). The number of nematic domains was extracted as a parameter to characterize the effect of initiator and catalyst during the nematic hydrogel formation. **Figure 36b** plots the number of nematic domains as a function of catalyst at several initiator concentrations. Similarly to our qualitative observations, the number of nematic domains

does not dramatically vary with catalyst concentration as it does with the presence of various amounts of the initiator.

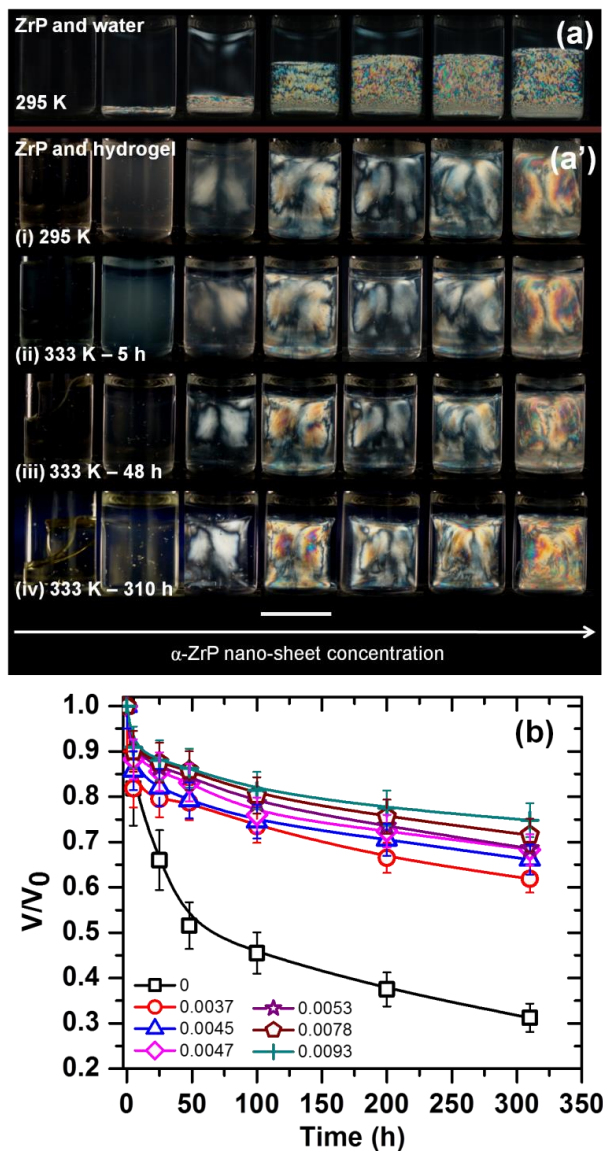


Figure 37. Crossed polarizing images of several nematic ZrP suspensions and hydrogels at different ZrP nano-sheet concentrations. (a) Discotic I-N phase transition of ZrP nano-sheet in aqueous suspensions. From left to right, the ZrP nano-sheet concentration corresponds to $\phi_{ZrP}=0, 0.0037, 0.0045, 0.0047, 0.0053, 0.0078,$ and 0.0093 . (a') Nematic hydrogels at the same concentration as (a). (i) At room temperature. (ii-iv) Volume shrinking of the nematic hydrogels at 333 K after 5, 48, and 310 h, respectively. The scale bar is 2 cm. (b) Normalized hydrogel volume as a function of time for samples in (a').

3.3.3.2 The Effect of Nano-sheet Concentration on Thermo-responsive Hydrogel

Deswelling

We studied the effect of ZrP nano-sheet concentration and temperature on the nematic hydrogels. **Figure 37a** presents a typical ZrP I-N transition phase diagram in aqueous suspensions. The fabricated nematic hydrogels shown in **Figure 37a'** used the exact same set of nano-sheet concentrations as those in **Figure 37a**. The nematic hydrogels were subjected to a temperature of 333 K. At this temperature, the PNIPAm polymers inside the hydrogel network should become hydrophobic, and the hydrogels experienced a volume compression, expelling water as they were shrinking. From these qualitative observations we obtained several noteworthy features:

- (i) the control hydrogel (PNIPAm and PAAm only, the first sample from the left, from (i) to (iv) in time sequence in **Figure 37**) presented a higher deswelling compared to the ones filled with the ZrP nano-sheets. In fact, the control hydrogel shrank 70% of its initial volume going from room temperature to 333 K. Interestingly, the nematic hydrogels presented a volume collapsing in a range of 35 to 25%, where the shrinkage was lowered by increasing the ZrP nano-sheet concentration
- (ii) the hydrogels exhibit weak color birefringence at low ZrP nano-sheet concentration. By increasing the particle concentration, the birefringent patterns of the samples became substantially more colorful

- (iii) the negligible variation in nematic domains demonstrates their limited degree of freedom during hydrogel collapsing, which infers that the ZrP nano-sheets are trapped inside the polymer network.

As observed in **Figure 37b**, when the temperature was raised above the LCST of PNIPAm (LCST \sim 305 K), the reference and the discotic nematic hydrogels presented similar temperature dependence on hydrogel shrinking and water deswelling. However, during the hydrogel hydrophilic-to-hydrophobic transition, the control hydrogel presented a sharp decrease in the hydrogel volume compared to nematic hydrogels. Interestingly, the ZrP nano-sheets introduced an increment in the hydrogel *rigidity*.⁴⁷⁸ According to Hou *et al.*,^{479, 480} the introduction of fillers, such as polysiloxane nanoparticles, will reduce the equilibrium swelling of the polymer hydrogels. Interestingly, in our experiments, as the amount of hydrophilic ZrP nano-sheets increased, the nematic hydrogels became more hydrophilic, therefore enhancing retention of water in the polymer matrix.

3.3.3.3 The Effect of Volume Compression on Nematic Hydrogel Textures

3.3.3.3.1 Birefringent Color Pattern Manipulation via Hydrogel Shrinking

Suspensions of highly anisometric disk-like particles are characterized by a strong birefringence at relatively low particle concentration due to their high anisotropy. The birefringence displayed in these high-aspect-ratio particle suspensions is a result of the high orientational ordering within the system.⁴⁸¹ The birefringence is defined as $\Delta\eta =$

$\eta_e - \eta_o$, where η_e and η_o are the refractive indices of the extraordinary and the ordinary rays, respectively, when polarized light enters into a uniaxial material.⁴⁸¹ The maximum intensity (I_{\max}) of the polarized light is defined as $I_{\max} = E^2 \sin^2(\delta/2)$, where E is the amplitude of the electromagnetic vector, and δ is the phase difference, $\delta = (2\pi/\lambda)\Delta\eta t$. δ is dependent on the wavelength of the incident white light, λ , sample birefringence, $\Delta\eta$, and sample thickness, t . Due to the dependence of δ on λ of white light, striking color patterns composed of constructive or destructive wavelengths can be visualized. These colors are reported in the literature in the form of a Michel-Levy chart.⁴⁸²

Figure 38a, b, and c show zoomed-in photographs of nematic hydrogels from **Figure 37a'** having ϕ_{ZrP} of 0.0045, 0.0047, and 0.0093, respectively, after 0, 5, 22, 48, 190, and 310 h. By placing the samples between crossed polarizers, each sample presented a sequence of birefringent pattern intensification during hydrogel volume shrinkage. As observed in **Figure 38a** to **Figure 38c**, the intensity of the birefringent colors depends strongly on the ZrP nano-sheet concentration. In fact, the birefringence of the ZrP nano-sheet hydrogel can be approximated by $\Delta\eta_{\text{ZrP-hydrogel}} = \Delta\eta_{\text{ZrP}}\phi_{\text{ZrP}}S_2$, where $\Delta\eta_{\text{ZrP}}$ is the intrinsic birefringence of a ZrP nano-sheet and S_2 is the nematic order parameter in the suspension.⁴⁸¹ During the collapse of nematic volume, parameter values of ϕ_{ZrP} and S_2 increment upward, therefore enriching the color patterns. For instance, **Figure 38a** shows a low ϕ_{ZrP} nematic hydrogel (*i.e.*, low S_2), where the gel appears white-yellowish and become whiter as the hydrogel shrinks (*i.e.*, S_2 and ϕ_{ZrP} increment).

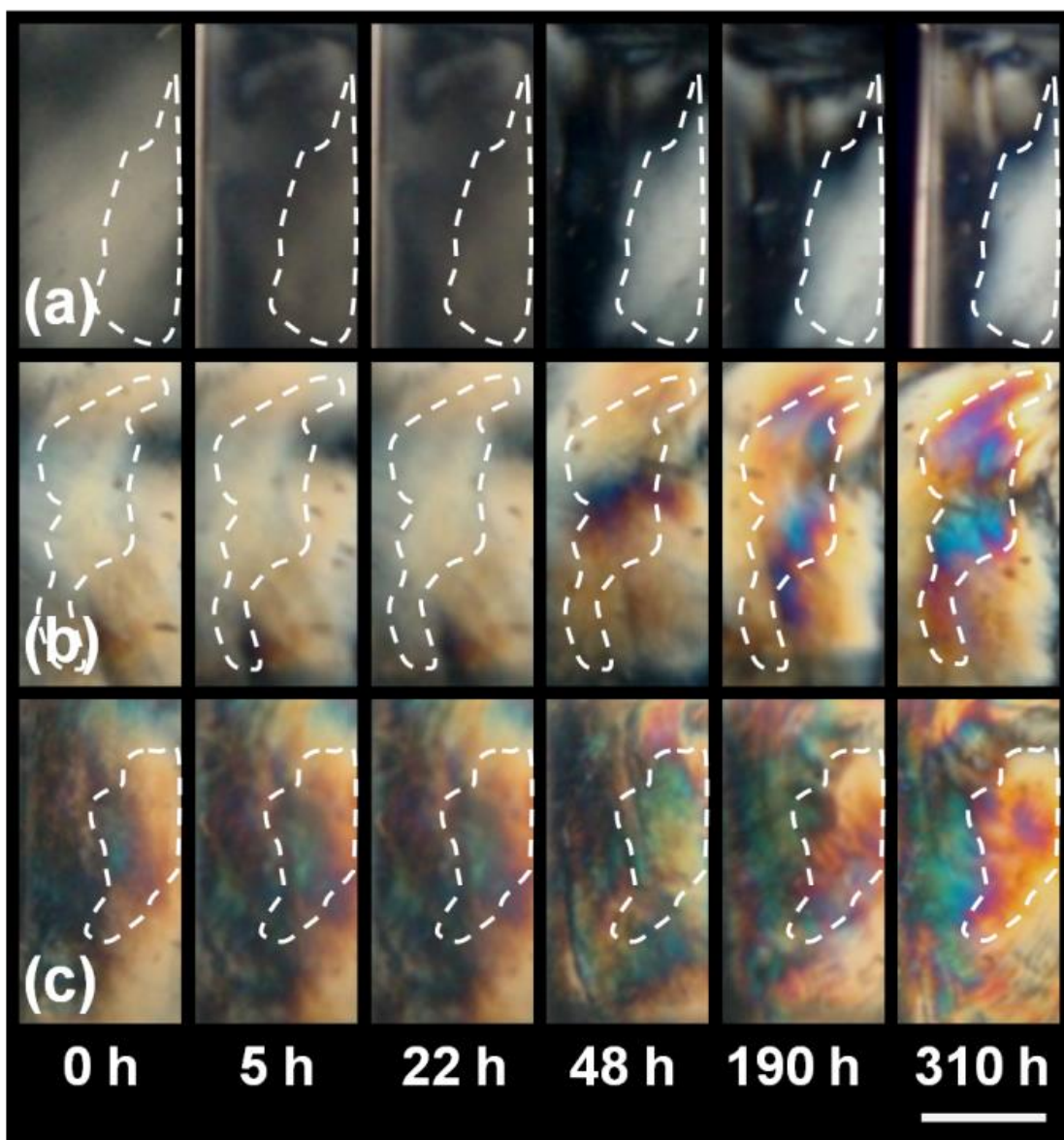


Figure 38. Birefringent color pattern variation due to temperature-shrinkage of the polymer hydrogels. The incrementing of ϕ_{ZrP} and S_2 during hydrogel collapsing initiated a birefringent color transition in the hydrogels. The samples contains a ZrP volume fraction (ϕ_{ZrP}) of: (a) 0.0045 (b) 0.0047, and (c) 0.0093. The scale bar is 0.5 cm. The samples were stored at 333 K.

3.3.3.3.2 Isotropic-nematic Transition during Hydrogel Edge-wrinkling at 333 K

We explored the possibility of observing an I-N transition at the edge due to hydrogel wrinkling similar to the one reported by Islam *et al.*,^{464, 465} The ZrP nano-

sheet concentration utilized here is $\phi_{\text{ZrP}} = 0.0030 \pm 0.0005$, which is slightly below ϕ_1 . After hydrogel preparation, the two ends of the capillary were sealed with optical glue to prevent water evaporation and stored at ambient temperature. The capillary was observed between crossed polarizers using an optical microscope with the temperature set to 333 K using thermal stage (HC561, Instec Inc.).

Figure 39 shows a series of crossed polarizing micrographs of the capillary-sealed nematic hydrogel during shrinking at 333 K. At the beginning, the hydrogel remained isotropic and the edge remained relatively straight along with some minor wrinkling (**Figure 39a**). Thereafter, the sample began to present instabilities as evidence from folding and creasing,⁴⁸³ commonly observed on the edge of polymer hydrogels (**Figure 39b, c**). From these instabilities, an increase in the birefringence of the edges was observed (**Figure 39c**). As visualized from **Figure 39(b-f)**, the undulation of the hydrogel sidewalls became stronger, which resulted in a sinusoidal bending of the whole sample, exhibiting undulations and cusps similar to Islam *et al.*,^{464, 465} resulting in an increment of the defect number on the edge. From these observations, the strength of the defects are +1 or -1 as suggested from the four bright lobes.⁴⁷⁴ As mentioned in the previous section, during hydrogel edge-wrinkling, $\Delta\eta_{\text{ZrP-hydrogel}}$ increases, as does nematic ordering (S_2).⁴⁸¹ In our study, since $\Delta\eta_{\text{ZrP}}$, and ϕ_{ZrP} ($\phi_{\text{ZrP}} < \phi_1$) are fixed parameters in our system during hydrogel shrinking, it is clear that S_2 increments are due to a higher alignment of the ZrP nano-sheets on the edge.⁴⁶⁴ Interestingly, although the nematic hydrogels fabricated in this report are composed of disk-like inorganic nano-sheets of ZrP, they possess a similar behavior to the ones made with carbon nanotubes

from Islam *et al.*,^{464, 465} This observation confirms Onsager's prediction that applies cylindrical-like objects having a certain diameter (d) and thickness (t), where rods are $t \gg d$ and disks are $t \ll d$.^{6, 199}

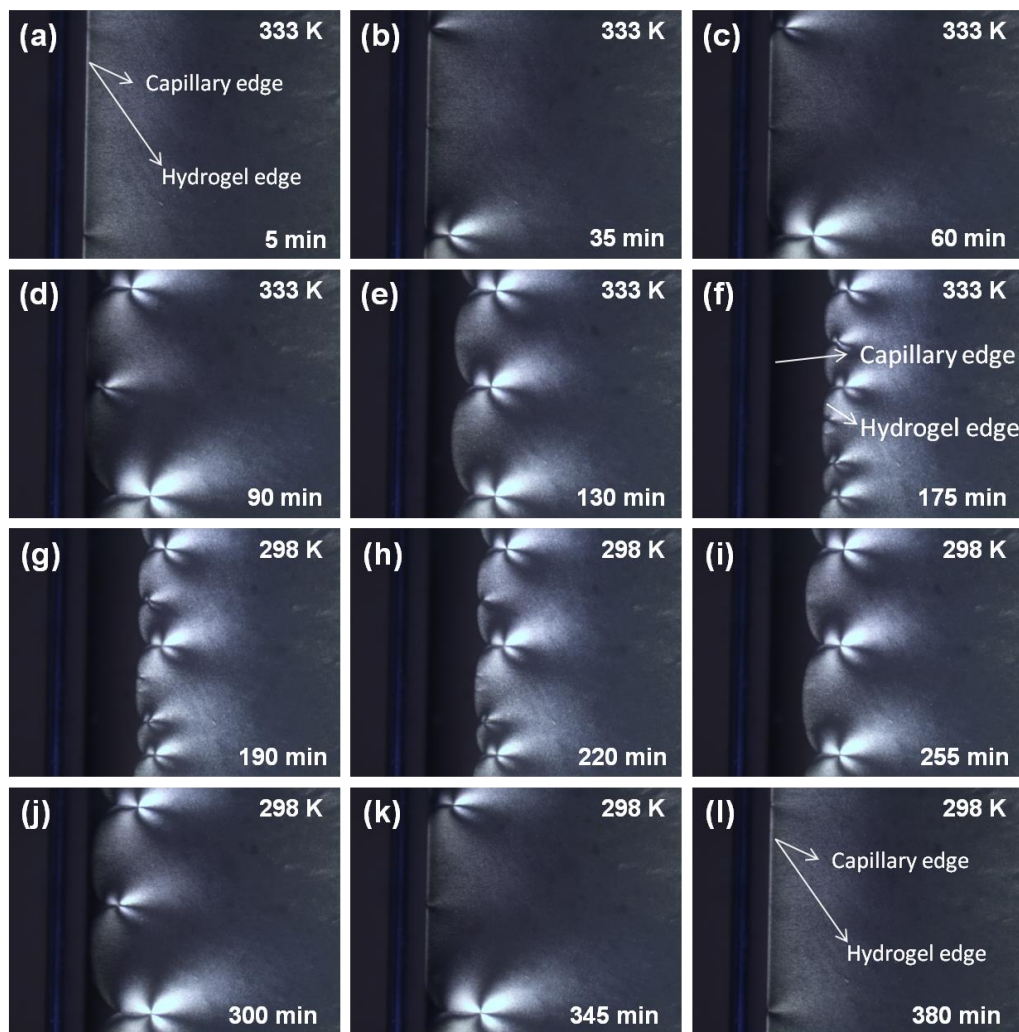


Figure 39. Time-sequential crossed polarized optical microscopy images of a sealed capillary tube containing ZrP nano-sheet hydrogels at $\phi_{\text{ZrP}} = 0.0030 \pm 0.0005$ during deswelling and swelling. (a-f) Deswelling of the nematic hydrogel at 333 K. At the edge, the isotropic-to-nematic transition takes place as evidenced from the visualization of nematic defects. Defects of +1 and -1 are characterized from their four lobes. (g-l) Swelling of the nematic hydrogel at ambient temperature. Reversible nematic-to-isotropic transition occurs as the concentration of ZrP nano-sheets on the hydrogel edge decrease during water absorption.

3.3.4 Summary

In summary, we have developed a new type of discotic nematic hydrogel from the polymerization/cross-linking of NIPAm and AAm monomer solutions containing high-aspect-ratio ZrP nano-sheets. These novel materials are highly ordered polymer hydrogels having low nano-sheet concentrations. The nematic hydrogels were characterized using crossed polarizing microscopy. The nematic domains in the hydrogel polymer network were studied by the variation of initiator (APS) and catalyst (TEMED) concentrations. We found that APS has a great influence on polymer chain length and cross-linking density, affecting the amount of extinction points in the nematic texture. However, no significant effect on the nematic texture was observed for TEMED at any concentration. We also studied the effect of ZrP nano-sheet concentration and temperature above the LCST on the hydrogels. Interestingly, the hydrogels containing ZrP nano-sheets presented an increment in the hydrogel rigidity compared to hydrogel only as evidenced from the low volume shrinking. This effect might come from the hydrophilic nano-sheets in assisting the water holding inside the polymer matrix. In addition, we observed that the concentration of ZrP nano-sheets possess a strong effect on the birefringent colors of the hydrogels during shrinking. This hydrogel behavior could be explained by the effect of ϕ_{ZrP} and S_2 on the birefringence of the system ($\Delta\eta_{\text{ZrP-hydrogel}}$). As the hydrogel volume collapses, ϕ_{ZrP} and S_2 increments could influence the birefringent color patterns. Finally, we observed the nematic hydrogel edge in rectangular-thin capillaries under optical microscope at a temperature above the LCST. The hydrophilic-to-hydrophobic transition of the hydrogel induced instabilities on the

polymer network matrix, resulting in edge-wrinkling. Wrinkling on the edge initiated an increase in the nematic order (S_2) of the nano-sheets. Interestingly, although the samples were prepared at a concentration nearly below the isotropic concentration (ϕ_I), the formation of four lobe nematic defects indicated an isotropic-to-nematic (I-N) transition at the edge.

We believe that the use of high-aspect-ratio ($\sim 10^3$) nano-sheets to induce highly ordered nematic liquid crystals at low particle concentration is a starting point for the formation of highly ordered polymer nanocomposites. The motivation for the combination of inorganic nano-sheets relies on the ability of these high-aspect-ratio particles to align at low concentrations due to their large excluded volumes. The addition of inorganic nano-sheets into polymer hydrogels provides a new and promising strategy to enhance stimuli-responsive soft composites with great mechanical properties and durability for their use in a wide range of industrial and medical fields, *e.g.*, chemical separation, food preservation, optical sensing, drug delivery, and wound dressing.

CHAPTER IV

INTERFACIAL STABILIZATION USING NANO-SHEETS*

4.1 Synopsis

We demonstrate the fabrication of amphiphilic nano-sheets, which are either surface- or edge-modified plates with a thickness at atomic scale, one of the thinnest amphiphilic particles reported so far. They are obtained by exfoliation of functionalized layered crystals, the first time that laminar structures have been utilized to produce such particles. Stable emulsions were made utilizing these nano-sheets. The adsorption of the amphiphilic nano-sheets to the oil-in-water interfaces and the reduction of surface tension between the PDMS and the amphiphilic nano-sheet suspensions were quantitatively characterized.

We also developed Pickering foams highly stabilized by high-aspect-ratio ($\xi =$ diameter/thickness) nano-sheets. The effects of particle aspect ratio, concentration, and hydrophobicity were also investigated. To our knowledge, our study provides the first experimental evidence of the effect of particle aspect ratio on particle-stabilized foams. The adsorption properties of these highly anisotropic nano-sheets are strongly affected

* Reprinted with permission from “Pickering emulsions stabilized by amphiphilic nano-sheets” by A. F. Mejia, A. Diaz, S. Pullela, Y.-W. Chang, M. Simonetty, C. Carpenter, J. D. Batteas, M. S. Mannan, A. Clearfield and Z. Cheng, 2012. *Soft Matter*, 8, 10245-10253, Copyright 2012 by The Royal Society of Chemistry.

Reprinted with permission from “Stabilization of Pickering foams by high-aspect-ratio nano-sheets” by J. S. Guevara, A. F. Mejia, M. Shuai, Y.-W. Chang, M. S. Mannan and Z. Cheng, 2013. *Soft Matter*, 9, 1327-1336, Copyright 2013 by The Royal Society of Chemistry.

by their small thickness and large lateral size (*i.e.*, two-dimensional). These high-aspect-ratio nano-sheets were obtained by exfoliation of α -Zirconium phosphate (ZrP) crystals with propylamine ($C_3H_7NH_2$, PA). The hydrophobicity of the nano-sheets was tailored by adjusting the PA:ZrP molar ratio in the suspension. The morphology and stability of the foam depend on the nano-sheet aspect ratio and concentration as well as the PA:ZrP molar ratio. Here, we found that using low and high aspect ratio nano-sheets having a high and an intermediate degree of hydrophobicity, respectively, is the successful formula to obtain high foam stability. The aqueous foams were characterized using optical and cross-polarized micrographs. Scanning electron microscopy (SEM) micrographs of dried foams revealed the adsorption of the PA-ZrP nano-sheets on the air-water interface. The foam stability was studied by measuring foam and water volume as a function of time to obtain the foam decay and water drainage rate, respectively. We also observed that the foams were stabilized by jammed layers of nano-sheets located in the bulk and at the air-water interface. These layers of particles prevent air diffusion between the bubbles, hence arresting Ostwald ripening and coalescence.

4.2 Pickering Emulsions Stabilized by Amphiphilic Nano-sheets

4.2.1 Introduction

Amphiphilic particles are both hydrophilic and hydrophobic. Acting as surfactants, they are able to stabilize liquid-liquid interfaces to form Pickering emulsions. Two types of amphiphilic particles are the so-called Janus and Gemini particles. Janus particles were named after the Roman god of doorways by Nobel

Laureate Pierre-Gilles de Gennes as they have two hemispheres or halves with distinguishable differences in chemical properties.⁴⁸⁴ Currently, there are several methods to prepare Janus particles.^{345, 485-494} For example, Janus particles can be obtained from double-emulsion droplets using microfluidics,⁴⁹⁰ electrohydrodynamic jetting of parallel polymer solutions,³⁴⁵ metal coating,⁴⁹¹ and a hierarchical self-assembly process.⁴⁹² Janus particles are also building blocks for supra-particle assemblies based on their anisotropy,^{1, 248, 495} which offers a gamut of other applications, such as drug delivery agents,⁴⁹⁶⁻⁴⁹⁸ photonic crystals,⁴⁹⁹ electronics,⁵⁰⁰ and photolithography.⁵⁰¹⁻⁵⁰³ Janus particles are strongly adsorbed to interfaces,^{248, 504} where they act as surfactants for the formation of stable Pickering emulsions (see Supplementary **Figure B1** and text.).^{244, 505, 506}

Gemini molecular surfactants can be described as molecules having a long hydrocarbon sequence, followed by a charged group (cationic, anionic, or nonionic), then a spacer (rigid or flexible) plus a second charged group, and another hydrocarbon chain segment. Rosen and Tracy listed more than 60 papers and more than 40 patents related to Gemini surfactants.⁵⁰⁷ Zana reviewed micellization thermodynamics, properties, and phase behaviors of aqueous micelles (*e.g.* size, shape, rheology, etc.).⁵⁰⁸ Regular surfactants are characterized by their critical micelle concentrations (CMCs), above which the molecules prefer to join the micelle rather than the interface. Gemini molecules are well known to possess lower CMC values than do the surfactants of equivalent chain length,^{509, 510} making them more efficient in lowering surface tension.⁵¹¹ Although Janus particles function as regular surfactants in terms of their function in stabilizing Pickering

emulsions, as the counterpart to the Gemini surfactants, the Gemini particles have not yet been fabricated. In this paper, we demonstrate the fabrication of surface and edge-modified amphiphilic nano-sheets, similar in configuration to Janus and Gemini nano-plates, respectively, using lamellar crystals. These particles have a small thickness; hence, large aspect ratio. In addition, we reveal theoretically and experimentally that high aspect ratio amphiphilic nano-sheets can provide good stabilization of liquid-liquid interfaces.^{234, 248} In the literature, amphiphilic nano-sheets have been obtained from block-copolymer cross-linking,^{249, 250} graphite exfoliation,^{251, 252} block-copolymer graphene modification,^{253, 254} and crushing of inorganic^{255, 256} and polymer-inorganic²⁵⁷ hollow silica spheres. They have served to emulsify immiscible liquids,^{251, 255, 258} and have been useful to fabricate polymer composites.²⁵⁸

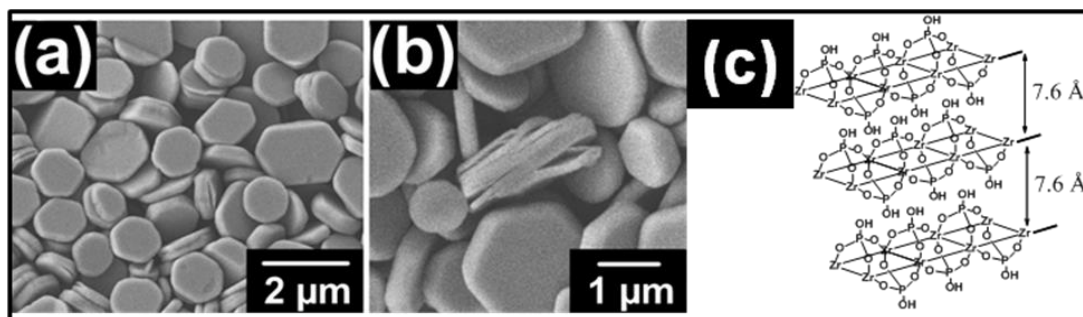


Figure 40. The α -zirconium phosphate crystals. (a) SEM micrograph. (b) Zoomed view of a particular crystal showing cracks along the lamellar layers. (c) Idealized structures of the alpha phase of zirconium phosphate (α -ZrP).

Pickering emulsions are emulsions stabilized by colloidal particles. Water-in-oil Pickering emulsions, formed using solid particles such as asphaltenes, are commonly the reason for the high stability of water droplets in crude oil. As solid particles are adsorbed onto the water-oil interface, the surface energy of the system is reduced and,

consequently, the emulsion is established. The overall Pickering emulsion stability process is governed by the macroscopic apparent interfacial energy, γ_a , which is defined as $\gamma_a = \gamma_{ow} - \Pi_s(\Gamma_p)$, where γ_{ow} is the oil-water interfacial energy and Π_s is the two-dimensional surface pressure, which depends on the particle adsorption on the oil-water interface Γ_p .²²⁷ As the particle concentration increments, Π_s approaches to γ_{ow} . Therefore, γ_a goes to zero, completely arresting the Ostwald ripening between the emulsion droplets (*i.e.*, low degree of coalescence). This effect can be explained due to the high desorption energy of the particles and the resulting capillary effects.²²⁷⁻²²⁹ The stability of Pickering emulsions depends on the size, shape, and wettability of particles at the interface.^{234, 242-245} Based on theory, spherical,²⁴⁶ rod-like,²⁴⁶ and discotic²⁴⁷ particles can be used as Pickering stabilizers to produce colloidosomes.²⁷¹⁻²⁷³ Colloidosomes²⁷¹⁻²⁷³ are microcapsules having a coagulated colloidal particle shell that can result from Pickering emulsions, as first synthesized by Velev *et al.*,²⁷⁴ For instance, platelet-like laponite clay has been used to prepare latex via Pickering miniemulsion polymerization.^{269, 270}

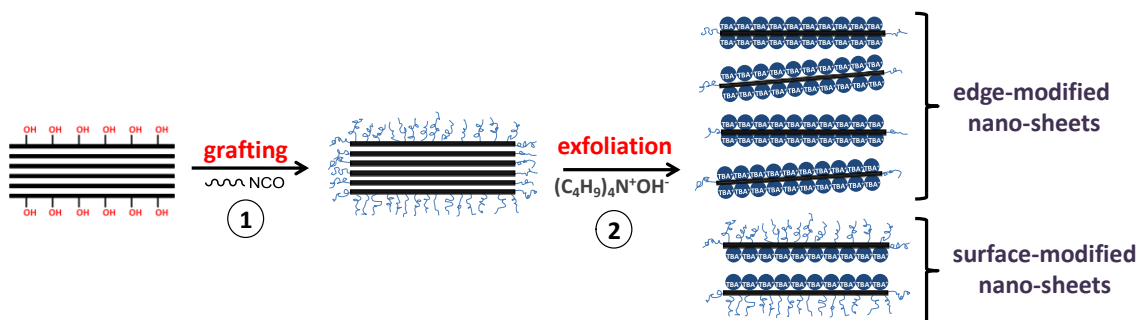
Anisotropic particles with high aspect ratio ($\zeta = 2R_d/h$) can be good emulsion stabilizers (see Supplementary *Particle-stabilized emulsions* section).²³⁴ In the past, Lagaly *et al.*, confirmed that large-aspect-ratio plate-shaped clay particles together with nonionic surfactants could be used as stabilizers for emulsions by creating a mechanical barrier to prevent coalescence.^{265, 266} Additionally, surfactant-free o/w emulsions can be stabilized by synthetic clay (laponites)²⁶⁷ and phase inversion can be present.²⁶⁸

Lamellar crystals are characterized by their layered structure. They can be inorganic crystals, such as clay,⁷⁶ α -zirconium phosphates (α -ZrP)⁷⁷⁻⁸⁰ (**Figure 40**), niobates,⁸¹⁻⁸³

titanates,⁸⁴⁻⁸⁶ or organic crystals, such as graphite, which is formed by stacks of graphene layers.⁸⁷ Lamellar crystals often exhibit the morphology of platelets (**Figure 40(a)**). They are used as rheological thickeners for drilling fluids, paint, cosmetics, and pharmaceutical products.^{105, 512} They have also been extensively investigated in polymer-clay nano-composites¹⁰⁶⁻¹⁰⁹ and electronics⁵¹³ over past decades. They are distinguished by strong bonds in the x and y directions in the plane of the flat crystal, but weaker interactions between the layers in the z direction. Lamellar crystals can, therefore, go through intercalation and exfoliation by guest molecules.⁸⁸ When interactions between the intercalated guest molecules are weak enough in the interlayer region, an exfoliation can take place. Among the most widely used lamellar crystals are the α phase of zirconium phosphate (α -ZrP) with chemical formulas $\text{Zr}(\text{HPO}_4)_2 \cdot \text{H}_2\text{O}$ (**Figure 40**). The α -ZrP crystal layer is composed of a ZrO_6 sheet coordinated with HPO_4^{2-} tetrahedrons forming a covalent network (**Figure 40(c)**).^{79, 110} The thickness of a monolayer of α -ZrP is about 0.66 nm (0.63 nm if the phosphate groups are deprotonated).⁸⁹

Here, we bridge these two thus far independently developing fields of amphiphilic particles and lamellar compounds, demonstrating the ability to create thin amphiphilic nano-sheets analogous to Janus (JPs) and Gemini (GPs) platelets, which are indeed just the thickness of a single layer of O, P, and Zr atoms, via the functionalization of lamellar crystals followed by exfoliation. In fact, functionalized nano-sheets belong to the general category of amphiphilic particles at the “zero” size limit (atomic scale) in one dimension. Within their particle family, they are the closest to conventional surfactant molecules. They are viewed best, however, as assembled clusters of

surfactants organized laterally. The single nano-plate layer is rigid when the nano-sheet size is about several tenths of a nanometer or less and become flexible when the size is larger than a hundred nanometers, depending on the bending elasticity of the layer.²⁸⁸ The impermeable nature of the crystalline layer serves as a barrier, preventing diffusion of small molecules, and, hence, the coalescence of emulsions “wrapped” by it.

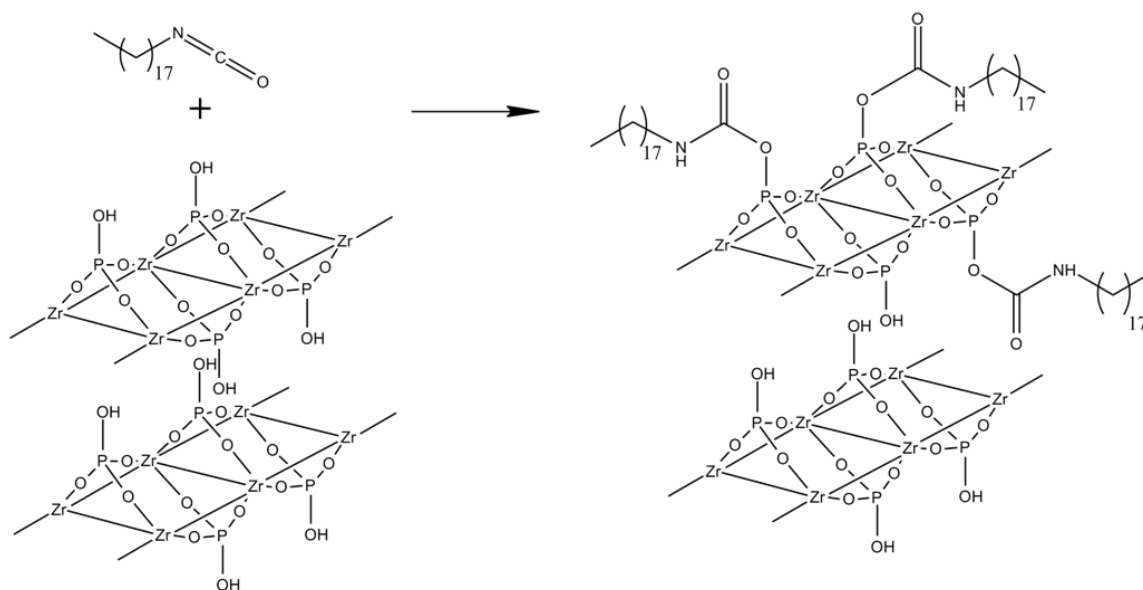


Scheme 1. The 2-D schematic representation of the fabrication of thin-surface and edge-modified amphiphilic nano-sheets. The initial step consists of the grafting of a coupling agent over the surface and the edges of α -ZrP. Subsequently, the exfoliation of the crystals is carried out to obtain the surface and edge-modified nano-sheets from their outer and inner layers, respectively.

4.2.2 Experimental

The α -ZrP is characterized by a strong hydrophilicity; hence, chemical modification is required to convert it to become hydrophobic. First, a coupling agent is grafted over the exposed edges and flat surfaces of the α -ZrP crystals (**Scheme 1**, grafting step). Subsequently, via the exfoliation of these crystals, a mixture of surface and edge-modified amphiphilic nano-sheets are obtained from the outer and the inner layers, respectively (**Scheme 1**, exfoliation step and Supplementary **Figure B2** for transmission electron microscope (TEM) images of the α -ZrP nano-sheets). The resulting nano-sheets are amphiphilic. Exfoliation of the lamellar crystals occurs when

enough tetra-(n-butylammonium) hydroxide (TBA^+OH^-) is added to exceed single-layer packing of TBA^+ ions in the interlayer region.^{77, 80, 89-91} The mono-layers obtained are atomically flat, mechanically strong, flexible, and chemically stable in common basic and acidic solvents. The α -ZrP crystals are easy to synthesize, and the crystal size and size polydispersity are highly tunable by varying phosphoric acid concentration, reaction time, and reaction temperature. In addition, α -ZrP crystals are able to achieve complete exfoliation (For size and thickness control, see Supplementary **Figure B3**).⁸⁹



Scheme 2. Reaction mechanism for the octadecyl isocyanate grafting the edge and the outer surfaces of α -ZrP crystals.

It is well known that α -ZrP presents low reactive hydroxyl groups on its surfaces.^{79, 110} Although numerous studies have reported intercalation of several compounds into α -ZrP,^{445, 447, 514-516} a direct grafting reaction on ZrP crystal surfaces had not been evaluated consistently, and just a few studies can be found in literature.^{444, 517, 518} The surface modification here consists of a chemical (covalent) reaction of the OH

groups on the surface of α -ZrP with octadecyl isocyanate (ODI) as a coupling agent. The particles created in the current study were synthesized by grafting ODI (**Scheme 2**) over the edges and the outer surfaces of α -ZrP crystals. The intercalation of the ODI into α -ZrP does not take place due to the high hydrophobicity of the ODI and the high hydrophilicity of the interlayer region. The ODI coupling agent is one of the most broadly used functional group reagents in synthesis reactions due to the high reactivity of its functional group, $-\text{NCO}$. It has been reported that the isocyanate group reacts with the hydroxyl groups of the hydroxyapatite ($\text{Ca}_5(\text{PO}_4)_3\text{OH}$) crystals.⁵¹⁹⁻⁵²² Liu *et al.*, confirmed the reactivity of the hydroxyapatite surface hydroxyl groups towards the organic isocyanate groups.⁵¹⁹ In addition, previous work also reported the grafting of different organic silane coupling agents on the surface of the calcium phosphate through the reaction with its surface hydroxyl groups.^{523, 524}

4.2.2.1 Synthesis and Functionalization of α -Zirconium Phosphate

The synthesis of the highly crystalline α -ZrP by the hydrothermal method has been described in previous publications.^{78, 80, 91} Particularly, 6 g $\text{ZrOCl}_2 \cdot 8\text{H}_2\text{O}$ were mixed with 60 mL (9 M) H_3PO_4 and heated at 200 °C for 24 h in a high-pressure autoclave. After the reaction, the product was centrifuged and washed three times with deionized (DI) H_2O and dried overnight at 60 °C. The dried product was ground with a mortar and pestle into a fine powder. Highly crystalline α -ZrP was used to avoid the intercalation of the modifier in the surface and edge modification step. Finally, the crystals were reacted with octadecyl isocyanate (Aldrich, 98%) in a 1:10 (ODI:ZrP)

molar ratio at 65 °C, using o-xylene as a solvent, for 12 hours under nitrogen. The resulting product was washed with methanol three times and dried at 60 °C overnight in an oven.

4.2.2.2 Characterization of the Modified α -Zirconium Phosphate

The resulting powder was characterized by Fourier transform infrared (FTIR, Shimadzu IRAffinity-1 spectrometer in an ATR, attenuated total reflection mode with a ZnSe ATR Prism Model Pike MIRacle A, Columbia, MD), and thermogravimetric analysis (TGA, Q500 TA Instrument, New Castle, DE). X-ray photoelectron spectroscopy (XPS, Kratos Axis Ultra Imaging, Chestnut Ridge, NY) was conducted to analyze the elementary composition of the final compound. AFM images were collected with an Agilent/Molecular Imaging PicoSPM coupled with an RHK Technology SPM 1000 Electronics Revision 8.

4.2.3 Results and Discussion

4.2.3.1 Fourier Transform Infrared (FTIR)

The grafting reactions (*i.e.* the outer surface modification reactions) were analyzed by FTIR (**Figure 41**). The FTIR spectrum of pristine α -ZrP is shown in **Figure 41(1)**. We observed that the isocyanate band ($-\text{N}=\text{C}=\text{O}$) at 2260 cm^{-1} (**Figure 41(2)**) vanished after reaction (**Figure 41(3)**). In the meantime, a new band at 3375 cm^{-1} appeared, which corresponds to a secondary amine ($\text{R}'\text{R}-\text{N}-\text{H}$) (**Figure 41(3)**). In addition, the CH_2 and CH_3 symmetric and asymmetric stretching bands at $3000\text{--}2850\text{ cm}^{-1}$ were observed in the product. FTIR spectra contained two $\text{C}=\text{O}$ bands, at 1685 cm^{-1}

for the ester carbonyl ($-\text{RC}(\text{O})\text{O}-$) and 1525 cm^{-1} for amide II ($-\text{RR}'\text{C}(\text{O})\text{NH}$) as predicted in **Scheme 2**. The presence of amide bands and the disappearance of the isocyanate band indicated that the hydroxyl groups over the surface of α -ZrP reacted with the isocyanate groups and resulted in the formation of urethane linkage. The sharp bands located at 3510 cm^{-1} and 3590 cm^{-1} for pristine α -ZrP and the surface-modified product were attributed to the asymmetric and symmetric stretching of the intercalated water, while the one located at 1620 cm^{-1} was attributed to the bending vibration of water.⁵²⁵ The remains of the intercalated water, after completion of the grafting reaction, indicated that no intercalation of the lamellar crystals occurred during the grafting reactions because of the high crystallinity of the pristine ZrP crystals.

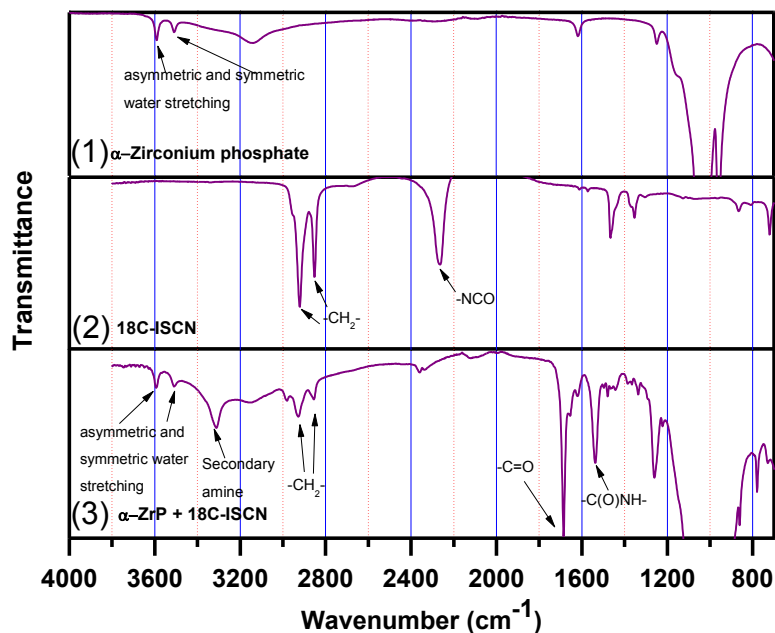


Figure 41. FTIR of α -Zirconium phosphate surface with grafted octadecylisocyanate groups. (1) α -ZrP, (2) octadecyl isocyanate, and (3) the grafted product.

4.2.3.2 X-ray Photoelectron Spectroscopy (XPS)

XPS analysis was conducted to measure the film composition that complements the infrared analysis. The binding energy of carbon (C(1s) : 285 eV) was used as the reference for data calibration. XPS is a highly diagnostic tool for the assessment of the chemical state of the elements; it has been used before to characterize α -ZrP and its organic derivatives.⁴⁴⁹ The XPS spectra of octadecyl isocyanate grafted to α -ZrP is shown in **Figure 42**. The C(1s) peak located at $E_b = 287.7$ eV corresponds to the carbons in the aliphatic chain, and the peak located at 289 eV corresponds to the carbon in the C(O)NH group (**Figure 42(a)**). As expected, the grafted lamellar crystals displayed a significant N(1s) band (**Figure 42(b)**). The N(1s) peak located at $E_b = 399$ eV was attributed to the nitrogen in the -C(O)NH group. The above FTIR and XPS characterization demonstrated that we have covalently attached an organic coupling agent to the hydroxyl groups of the phosphate on the surfaces of α -ZrP crystals.

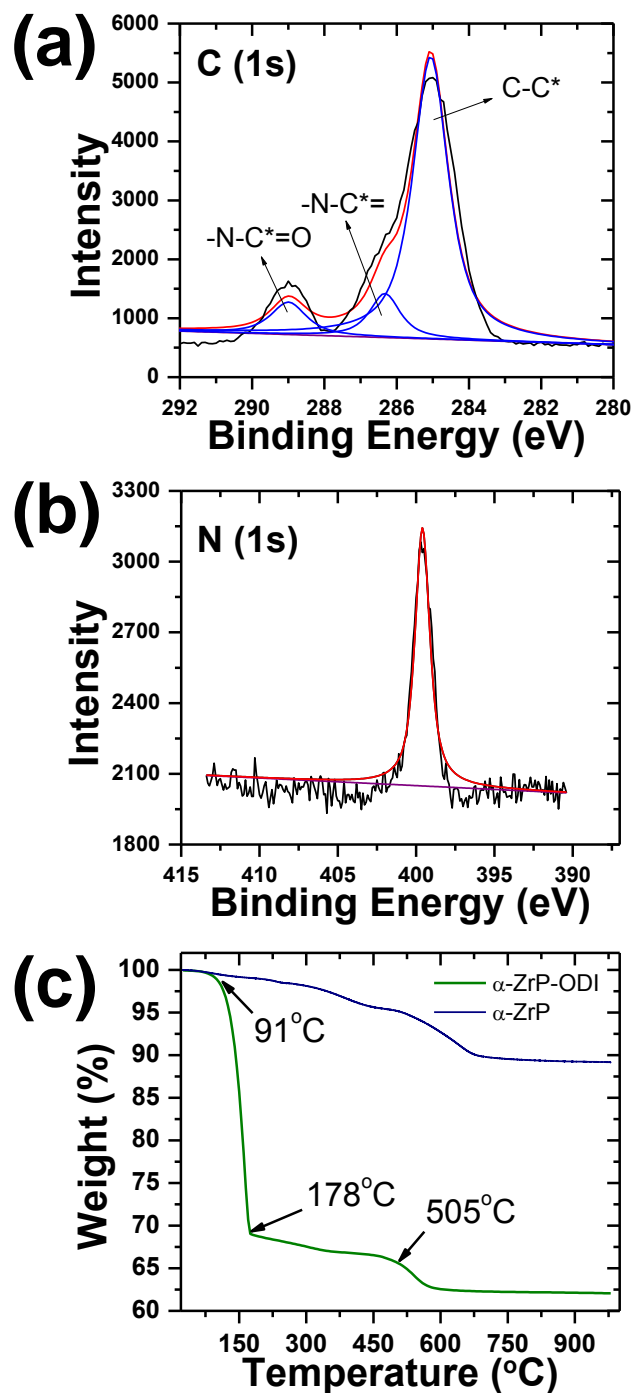


Figure 42. XPS and TGA spectra of the product obtained from the reaction of ODI with α -ZrP (a). Deconvolution of the C(1s) spectrum exhibits three peaks, consistent with the presence of the N-C(=O)- and carbon atoms. (b) N(1s) spectra. (c) The thermal stability of pristine α -ZrP (blue line) and α -ZrP grafted with ODI (green line) analyzed by TGA.

4.2.3.3 Thermogravimetric Analysis (TGA)

Figure 42(c) shows the TGA thermogram of pristine and grafted crystals. The final product of the thermo-decomposition of pristine α -ZrP is ZrP_2O_7 [$Zr(HPO_4)_2 \cdot H_2O(s) + \text{heat (700 } ^\circ\text{C)} \rightarrow ZrP_2O_7(s) + 2H_2O(g)$] exhibits a weight loss of about 12%. On the other hand, grafted crystals presented a weight loss of about 37%. The TGA spectrum showed four regions. The first one ranged from 25 $^\circ\text{C}$ to 91 $^\circ\text{C}$; the second one, from 91 $^\circ\text{C}$ to 178 $^\circ\text{C}$; the third one, from 178 $^\circ\text{C}$ to 505 $^\circ\text{C}$; and the last one, from 505 $^\circ\text{C}$ to 800 $^\circ\text{C}$. The first region shows slight loss of solvent from the surface of the crystals. The second region shows evaporation of the water contained between the layers of the α -ZrP. The third region shows the removal of the aliphatic chains grafted on the surface. Finally the fourth region shows condensation of the phosphates. The TGA indicated that about 25% of sample is from the surface modification.

4.2.3.4 Exfoliation of the Modified α -Zirconium Phosphate

The functionalized crystals were then exfoliated to obtain a mixture of surface and edge-modified amphiphilic nano-sheets. Exfoliated α -ZrP was obtained by adding tetra-(n-butylammonium) hydroxide (TBA^+OH^- , Aldrich, 40% in water) at a molar ratio of $ZrP:TBA = 1:1$ in DI water. During the intercalation reaction, the suspension was subject to sonication (Branson 8510, 40 kHz, Danbury, CT) to guarantee the intercalation of the TBA^+ . A complete exfoliation of the crystals might take several

minutes to hours.⁸⁹ A schematic representation of the α -ZrP crystal exfoliation is depicted in **Scheme 1**.

4.2.3.5 Emulsion Preparation

4.2.3.5.1 Mineral Oil in Water Emulsions

Our amphiphilic α -ZrP nano-sheets have a large aspect ratio ($\xi \sim 320$) due to their extremely thin thickness (about 2.8 nm) (See atomic force microscope (AFM) topography images and section analysis in **Figure B4**.)⁸⁹ As stated before, we predicted that high-aspect-ratio nano-sheets would be able to offer greater stability between liquid films to prevent coalescence.^{234, 526} Their large lateral surface area offers strong adsorption energy at the oil-water interface. Surfactant-free oil-in-water emulsions stabilized with exfoliated α -ZrP-ODI containing a mixture of surface- and edge-modified amphiphilic nano-sheets were prepared at room temperature. The preparation consisted of adding 700 μ L of the exfoliated nano-sheet suspension (0.05 g/mL) within 2 mL of H₂O and 300 μ L of light mineral oil (Sigma Aldrich). The mixture was treated by sonication for 10 minutes to allow the amphiphilic nano-sheets move to the oil-water interface. Dye was added to the oil phase to make the oil fluorescent for confocal microscopy observation. Optical and confocal micrographs of the oil-in-water emulsions are shown in **Figure 43(a)** and **Figure 43(b)**, respectively.

A control emulsion was prepared using the same procedure with an exfoliated non-modified α -ZrP suspension. **Figure 43(c)** and **Figure 43(f)** illustrate the o/w emulsion comparison of the use of non-modified and modified α -ZrP as surface-active

agents, respectively. The emulsion of the former lasted only for a couple hours, while the latter lasted for months. An optical microscope was used to observe in detail the o/w emulsions. **Figure 43(d)** and **Figure 43(g)** show the emulsions for both cases when freshly made just after sonication. In the case of **Figure 43(g)**, it should be noted that under white light, the α -ZrP-ODI nano-sheets are difficult to observe due to their extreme thin thickness.⁸⁹ After 24 days, optical micrographs were obtained for the emulsions. In comparison with **Figure 43(d)**, the control emulsion optical micrograph (**Figure 43(e)**) elucidates coalescence of the oil droplets. The micrographs for the emulsion stabilized using exfoliated α -ZrP-ODI can be found at **Figure 43(h)** (top of the emulsion) and **Figure 43(i)** (middle), where no significant coalescence was observed. In contrast to **Figure 43(i)**, no emulsion droplets were found at the 24th day in the middle of the sample shown in **Figure 43(c)** due to the coalescence and creaming in the emulsions made using non-modified α -ZrP nano-sheets.

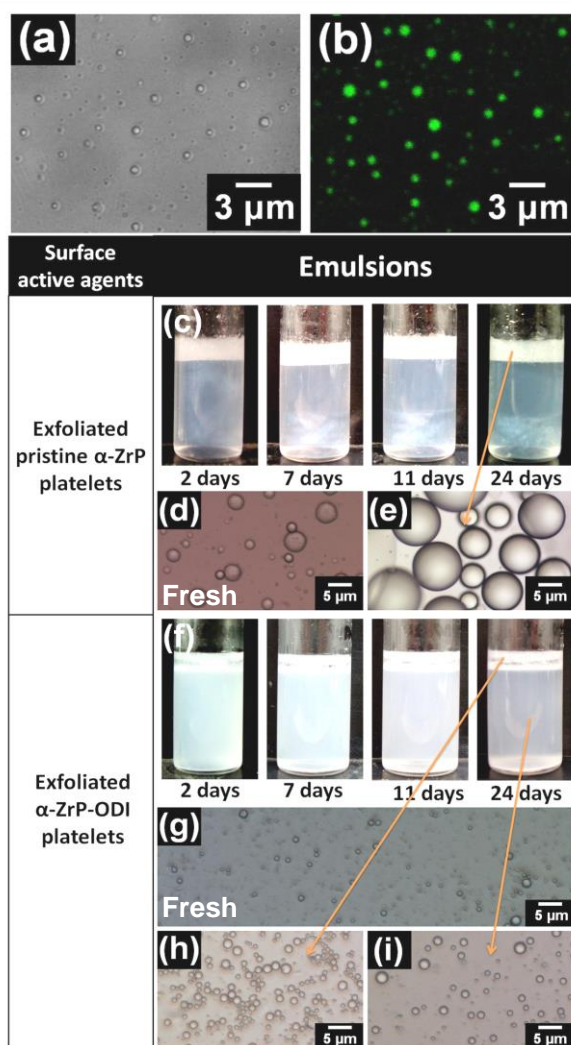


Figure 43. Characterization of stable emulsions stabilized by α -ZrP-ODI nano-sheets and unstable emulsions using non-modified α -ZrP nano-sheets. Representative (a) optical micrograph and (b) confocal laser scanning micrograph of o/w emulsions using α -ZrP-ODI as surface-active agents. (c) Observation of o/w emulsions stabilized by non-modified α -ZrP monolayers. The emulsion coalesced and quickly creamed. (d) Optical micrographs of the o/w emulsion right after emulsification and (e) after 24 days, which indicates that non-modified α -ZrP nano-sheets are not good emulsifiers due to the observed coalescence. (f) Creaming of o/w emulsions stabilized by α -ZrP-ODI nano-sheets. The emulsion presents less creaming compared to (c) due to the less degree of coalescence. (g) Micrograph showing the oil-in-water droplets after emulsification. (h) o/w emulsion micrograph from the top and (i) from the middle after 24 days, where no coalescence was observed. Pictures of (a, d, e, g, h, and i) were taken using a Nikon microscope TE-2000U with 20x magnification. (b) was taken using a Leica confocal microscope TCS SP5 with magnification of 100x. (c and f) digital photographs were taken using a Sony DSC-220W digital still camera.

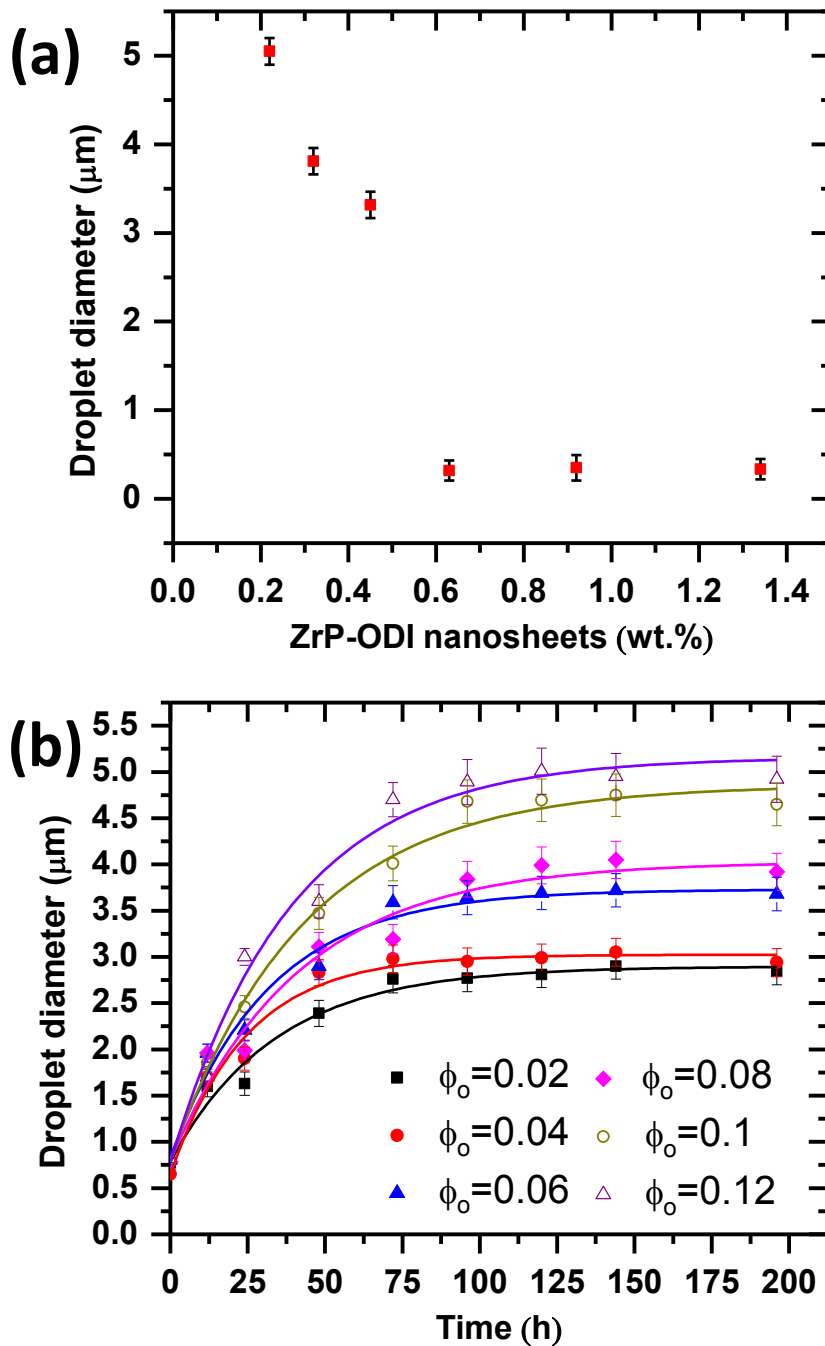


Figure 44. (a) Toluene-in-water emulsion droplet diameter as a function of α -ZrP-ODI nano-sheet concentration after one week. The toluene volume fraction is $\phi_o=0.085$. (b) Droplet diameter of toluene-in-water emulsions as a function of time. The concentration of α -ZrP-ODI nano-sheets is 0.45 wt. %.

4.2.3.5.2 Emulsion Stability of Aromatic Liquids in Water Emulsions

To study the capability of the α -ZrP-ODI nano-sheets to emulsify immiscible aromatic liquids, emulsions of toluene-in-water and styrene-in-water were evaluated. For the toluene-in-water emulsions, the droplet size dependence was studied by increasing the amphiphilic nano-sheet concentration as Ashby and Binks did using laponite clay.²⁶⁷ **Figure 44(a)** displays the toluene droplet diameters for samples with different amounts of α -ZrP-ODI nano-sheets. The droplet diameter decreased with an increase in α -ZrP-ODI nano-sheets in a range between 0.2 to 0.62 wt. % and became constant after that at a fixed oil concentration ($\phi_o=0.085$). In general, an increase in amphiphilic nano-sheets results in a decrease in emulsion droplet size. Also, the toluene-in-water emulsion droplet diameter and the emulsion stability were studied by varying the oil content. **Figure 44(b)** displays the toluene droplet diameters for six samples with varied toluene volume fractions for a fixed α -ZrP-ODI nano-sheet concentration (0.45 wt.%) over a period of a week. The toluene-in-water emulsion stability was measured for the six samples. All emulsions were stabilized after 100 h. It was found that droplet diameter increased with oil content (**Figure 44(b)**). In this experiment, a small size distribution for the droplets was detected, similar to previous Pickering emulsion observations (**Figure 45(a)**).⁵²⁷⁻⁵³⁰ Simply by changing the nano-sheet system from α -ZrP-ODI to non-modified α -ZrP nano-sheets, we obtained droplets from monodispersed to polydispersed as shown in **Figure 45(a, b)**. Visual observations of **Figure 45(c)** revealed that the toluene-in-water emulsion stabilized by non-modified nano-sheets (right) had undergone a much more evident creaming process than the emulsion stabilized by α -ZrP-

ODI nano-sheets (left). The image in **Figure 45(b)** had the same composition and had settled for the same amount of time as the samples with α -ZrP-ODI nano-sheets in **Figure 45(a)**.

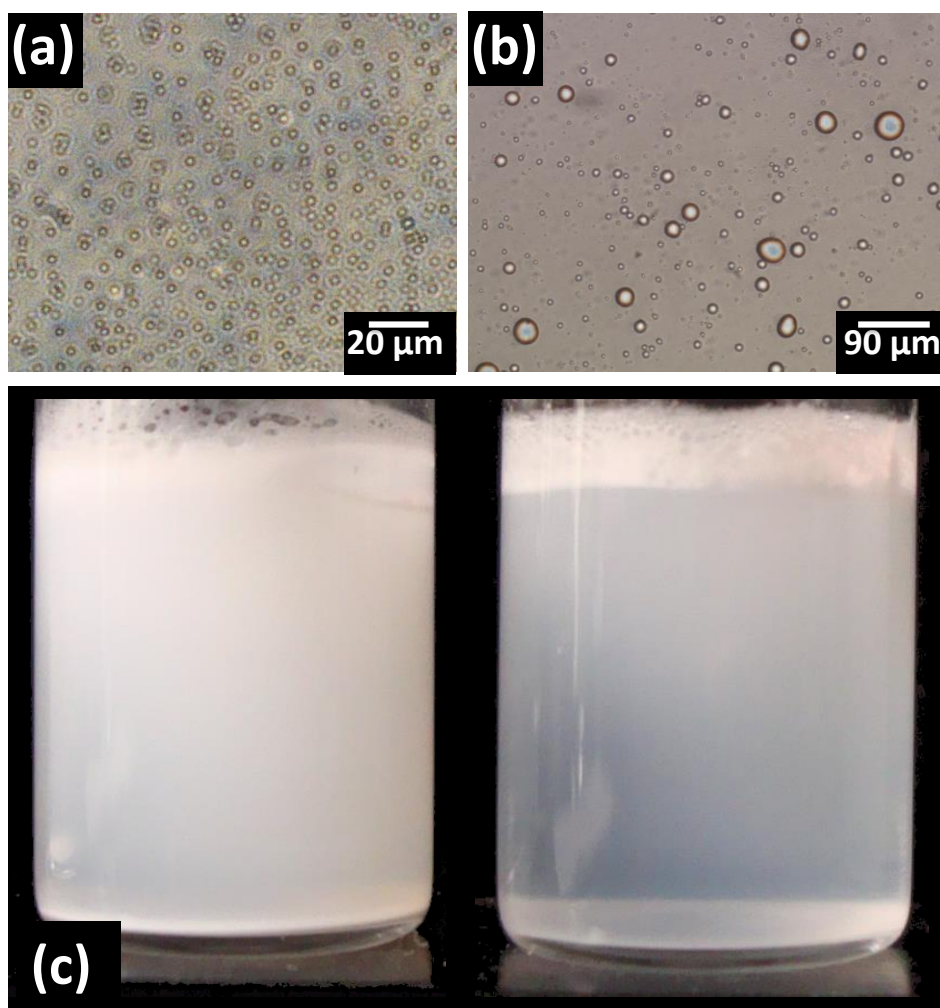


Figure 45. Toluene-in-water emulsions stabilized by α -ZrP-ODI and non-modified α -ZrP nano-sheets, where toluene concentration was $\phi_o=0.12$. (a) Micrograph of uniform toluene-in-water droplets stabilized by α -ZrP-ODI nano-sheets. The diameter of the droplets is $3.05 \pm 0.42 \mu\text{m}$. (b) Micrograph of polydispersed toluene-in-water emulsion droplets stabilized by non-modified α -ZrP nano-sheets. (c) Toluene-in-water emulsions stabilized by non-modified α -ZrP (right) showing strong creaming due to large drop size and stabilized by α -ZrP-ODI nano-sheets (left) with a less creaming effect. The picture is taken at 200 h after emulsification.

4.2.3.5.3 Pickering Miniemulsion Polymerization

The stable Pickering emulsions that we observed above established the viability of producing a Pickering miniemulsion polymerization of styrene using α -ZrP-ODI nano-sheets as stabilizers, generating armored latex particles similar to the armored latex suspensions of Bon and Colver.²⁷⁰ We performed six Pickering miniemulsion polymerizations of styrene by varying the quantity of α -ZrP-ODI nano-sheets from 0.22 to 1.32 wt. % in aqueous solutions at a constant monomer volume fraction of styrene, approximately $\phi_0=0.085$. Azobisisobutyronitrile (AIBN, Sigma Aldrich) was used as an initiator for the polymerization. Stable Pickering miniemulsions of submicron α -ZrP-ODI colloidosomes were generated via sonication and were subsequently polymerized at 65 °C for two days. It was observed that polystyrene particle diameter was decreased by increasing the amphiphilic nano-sheet content (**Figure 46**).

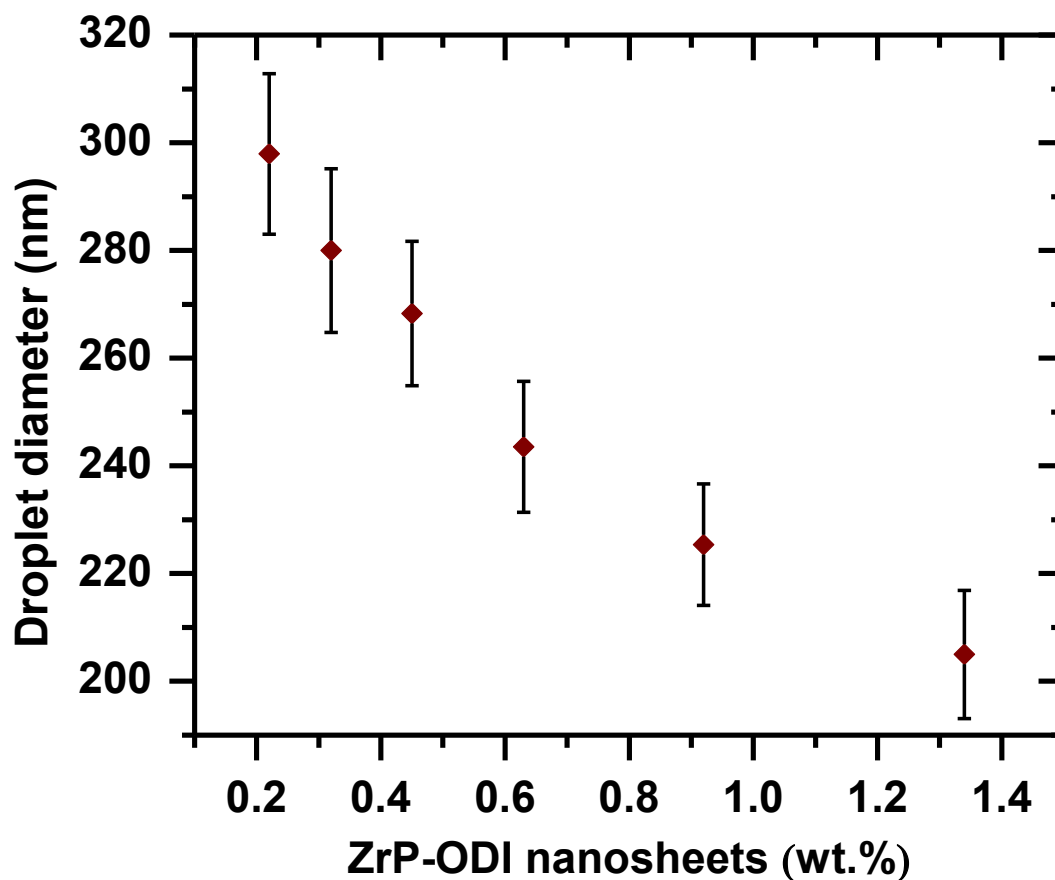


Figure 46. Pickering miniemulsion polymerization of styrene using α -ZrP-ODI nanosheets as stabilizers. Average polystyrene particle diameter as a function of weight percent of platelets.

Figure 47(a) shows an SEM image after polymerization of styrene in a Pickering miniemulsion using α -ZrP-ODI nano-sheets as stabilizers. It confirms the formation of polystyrene- α -ZrP-ODI-nano-sheets particles with a size 215 ± 52 nm. In addition, TEM images were also taken of the platelet-armored polystyrene particles (**Figure 47(b, c and d)**). **Figure 47(b, c)** shows that styrene emulsions were able to form non-spherical particles showing facet edges and non-smooth corners due to the location of the α -ZrP-ODI nano-sheets at the styrene-water interface. Also, as in the case of optical

microscopy for mineral oil-in-water and toluene-in-water, observation of the α -ZrP-ODI nano-sheets in SEM micrographs is difficult due to their atomic thickness and because the nano-sheets were fused on the polystyrene surface. From the TEM micrograph (**Figure 47(d)**), the α -ZrP-ODI nano-sheets constituted a layer about 2-nm thick surrounding the polystyrene core. The presence of Zr, P and O over the surface of the polystyrene- α -ZrP-ODI-nano-sheet particles was detected in the EDX spectra (**Figure B5**).

4.2.3.6 Evaluation of Surface Coverage

Since styrene emulsification utilized the strong adsorption properties of the nano-sheets at the styrene-water interface, the adsorption process was analyzed in a similar way as Bon and Colver.²⁷⁰ Calculations were made to determine the amount of nano-sheets on the polystyrene particle surface. The surface concentration was calculated from the following equation²⁷⁰: $C_{\text{surface}} = 3\pi/2 (\rho_{\text{ZrP-ODI nano-sheets}}/\rho_{\text{polystyrene}}) (h/d_{\text{polystyrene}}) C_{\text{polystyrene}}$, where h is the thickness of the nano-sheets, C_{surface} (gg^{-1}) is the concentration of amphiphilic nano-sheets, and C_o (gg^{-1}) is the total concentration of the amphiphilic nano-sheets. $\rho_{\text{ZrP-ODI nano-sheets}}$ and $\rho_{\text{polystyrene}}$ are the densities of the ZrP-ODI nano-sheets and the polystyrene, respectively. The values of $d_{\text{polystyrene}}$, the average diameter of the polystyrene particle suspensions, were obtained from **Figure 46**. The average diameter of each sample was applied to the equation above to find the surface concentration of α -ZrP-ODI nano-sheets. **Figure 48** displays a plot of the α -ZrP-ODI nano-sheets on the surface versus the total concentration of α -ZrP-ODI nano-sheets. The line of best fit has

an R^2 value of 0.99, which proves a strong linear relationship. From this relationship, it is demonstrated that the partition, Γ , of the amphiphilic nano-sheets *on* the surface versus *in* the continuous phase was a *constant* (**Figure 48**). By adding more α -ZrP-ODI nano-sheets in the emulsions, therefore, surface areas created by these nano-sheets produced smaller-sized emulsions (**Figure 46**) due to their high surface activity. For a fixed amount of styrene, the final particle diameter was set by the quantity of amphiphilic nano-sheets, M , if the size polydispersity of the resulted particles was not high, because the amount of nano-sheets on the surface would be $M \times \Gamma$, and only a single layer of nano-sheet was on the surface (**Figure 47(d)**).

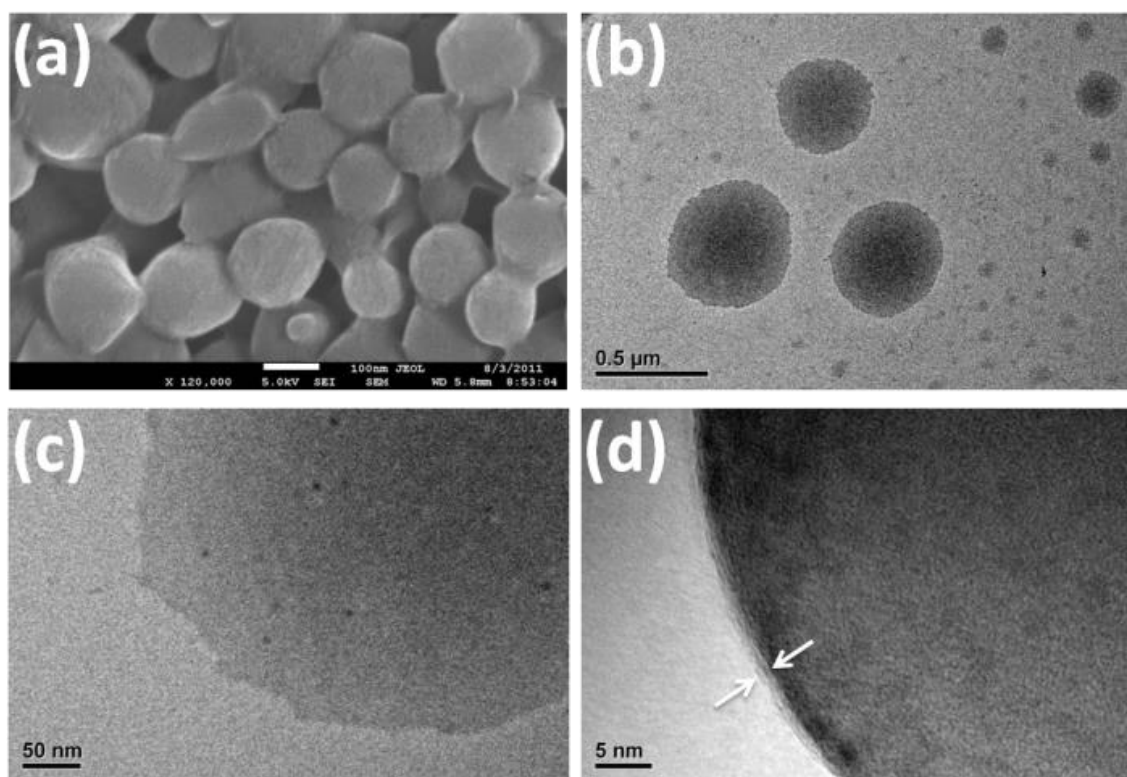


Figure 47. Polymerization of Pickering miniemulsions of styrene-in-water. (a) SEM image of platelet-armored-polystyrene particles. (b), (c) and (d) TEM images of nano-sheet-armored polystyrene particles.

4.2.3.7 Contact Angle Measurements

We also performed contact angle measurements of the α -ZrP-ODI nano-sheets suspensions on polydimethylsiloxane (PDMS) films using Young's equation to determine the surface tension between a hydrophobic surface of PDMS and the amphiphilic nano-sheet suspensions (see Supplementary **Figure B6** and text for explicit explanation of the surface tension methodology). Some authors have raised concerns about the reliability on the measurements of the static contact angles.^{243, 531} In our study, the contact angle is reported as a representative parameter of the partitioning of the amphiphilic nano-sheets at the PDMS-water interface. As α -ZrP-ODI nano-sheet concentration was increased from 0.2 to 0.6 wt. %, the contact angle decreased, hence the surface tension was indeed reduced (*i.e.*, the droplet wettability was increased). The reduction of the surface tension was in a good correlation with the emulsion size reduction in the above experiments of toluene and styrene emulsification. This correlation might indicate that the α -ZrP-ODI nano-sheets would reduce the oil-water interfacial tension, enabling them to create new surfaces. The underlying mechanism could be the high flexibility of α -ZrP-ODI nano-sheets (**Figure B2**).²⁸⁸ They can curve on to the surface of the oil droplets and make small emulsion droplets. In the case of Gemini nano-sheets, the hydrophobic tails can stick into (for the one on the oil side) or bend toward (for the ones on the other side, as the length of the ODI is about 2 nm) the oil phase.

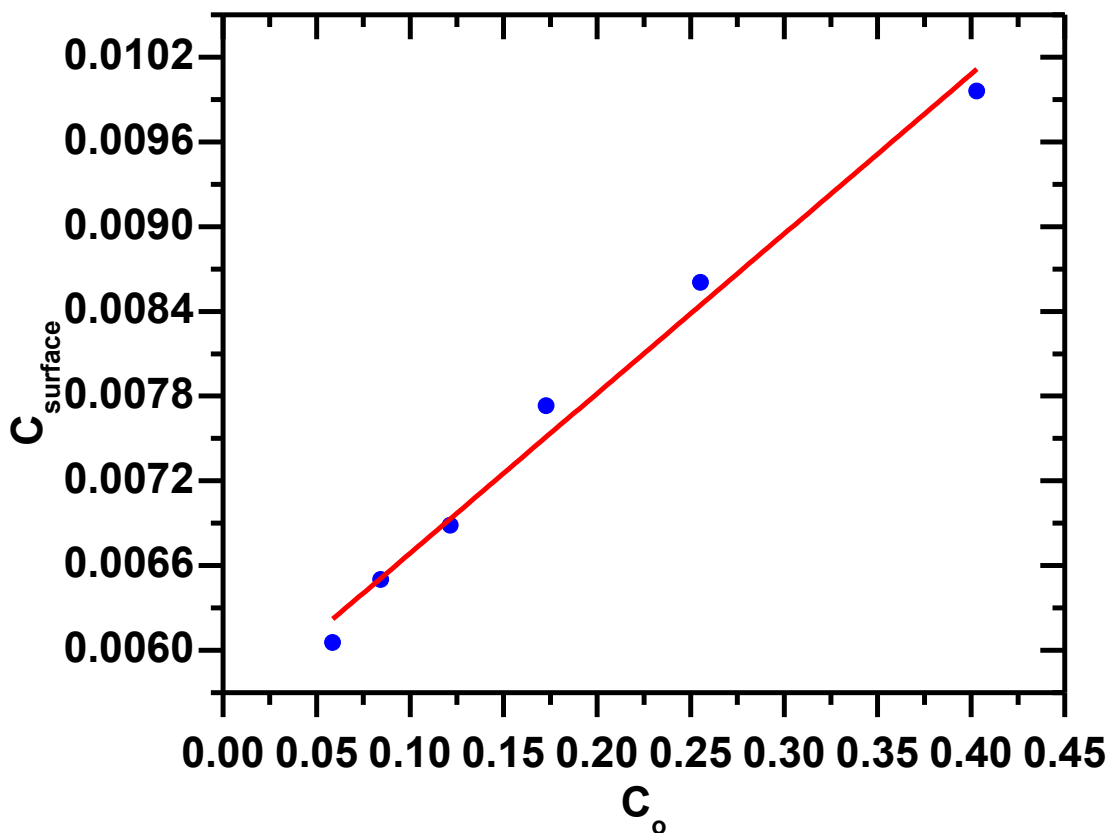


Figure 48. Concentration of amphiphilic nano-sheets on the surface ($C_{surface}$) vs. total concentration of platelets (C_o).

4.2.4 Summary

In summary, we have demonstrated the fabrication of thin amphiphilic nano-sheets by exfoliating α -ZrP crystals grafted with a coupling agent of hydrophobic molecules on their edges and outer surfaces. Their chemical structures were confirmed via XPS, TGA, and FTIR measurements. Octadecyl isocyanate is a powerful functionalization agent to initiate the surface reaction of α -ZrP. We anticipate that this functional group opens doors for further functionalization of α -ZrP to diversify applications.

These novel thin amphiphilic nano-sheets were used to stabilize surfactant-free oil-in-water emulsions. TEM revealed that there was only a single layer of nano-sheets on the interface. Stable *uniform* toluene-in-water emulsions were observed by using the amphiphilic nano-sheets as stabilizers. In contrast, controlled experiments using the non-modified nano-sheets produced highly polydispersed emulsions. It confirmed that α -ZrP-ODI nano-sheets were attracted to the oil-in-water interface. The polymerization of Pickering miniemulsions to produce polystyrene particles were performed similarly to the method of Bon and Colver.²⁷⁰ From the emulsion size measurements, it was found that the partition Γ of the amphiphilic nano-sheets *on* the surface was *constant*, and by adding more α -ZrP-ODI nano-sheets to the emulsions, surface areas were created by these nano-sheets, producing smaller sized emulsions. We also confirmed that the α -ZrP-ODI nano-sheets might be able to reduce the oil-in-water surface tension by using nano-sheets.

These two-dimensional amphiphiles introduce a new class of materials and applications of thin amphiphilic particles that are at nano-scale and possess a great amount of flexibility. They have practical applications for cosmetic and hygiene products for the personal care industry, and for oil extraction in the petroleum industry. They can improve paints and enhance the polymer nano-composites due to their affinity to the medium. We anticipate that the amphiphilic nano-sheets could be used to stabilize contrast agents for ultrasonic imaging of colloids, such as gas bubbles. The grafting of pH- and temperature-sensitive polymers to the nano-sheets will produce “smart” amphiphilic nano-sheets suitable for drug delivery and sensor applications. In the future,

two-dimensional amphiphiles could be also fabricated by grafting coupling agents over the surface of other materials, such as graphene or TiO₂ nano-sheets.

4.3 Stabilization of Pickering Foams by High-aspect-ratio Nano-sheets

4.3.1 Introduction

Aqueous foams are dispersions of gas in a continuous aqueous phase. They are characteristically metastable:⁵³² bubble size increases with time. The increment of the average bubble size is driven mainly by two processes, coarsening and coalescence. Coarsening occurs when gas diffuses from a small bubble to a larger one due to the higher Laplace pressure inside the small bubble. Simultaneously, coalescence takes place when two bubbles merge due to the rupture of the liquid film between them during the drainage of the liquid. Typically, molecular surfactants or proteins are used as stabilizers of these systems.

Gas-water interfaces can also be stabilized by particles. These types of foams are known as particle-stabilized foams or Pickering foams and are a subject of considerable attention recently. The ability of solid particles to stabilize gas-liquid and liquid-liquid interfaces has been fully investigated during the last decades.²²⁶ The use of foams stabilized with particles has gained attention due to its potential applications. Particle-stabilized foams have served as an alternative to proteins for enhancement of textures of foams in the food industry,⁵³³ rheological modifiers for oil recovery,⁵³⁴ recovery of minerals in the flotation processes,^{535, 536} and as novel porous templates of polymers and ceramics.⁵³⁷⁻⁵⁴¹

In the literature, it is possible to find aqueous foams stabilized with solid particles alone or along with surfactants.^{226, 245, 526, 542-545} Particle-stabilized foams have been obtained with surface-modified iron particles,⁵⁴⁶ silica spheres,^{239, 240, 547-549} metal oxides nanoparticles,^{550, 551} polymeric particles of PVC,⁵⁵² latex,⁵⁵³ polymeric rods,⁵⁵⁴ CaCO₃ rods,²³³ cellulose particles,⁵⁵⁵ and fine graphite and quartz particles,⁵⁵⁶ among others.

Synthetic clay platelets have also been used for foam stabilization. Laponite, along with amines and surfactants,^{232, 261, 262, 264} and layered double hydroxides (LDH) modified with sodium butyrate²⁶³ have served as foam stabilizers.

Different methodologies have been applied to produce particle-stabilized foams, such as bubbling, shaking, stirring, and sudden drop in pressure.⁵⁴⁸ The volume of foam obtained and bubble morphology varies with the method employed.

Although solid particles can be good foam stabilizers, there are some particular conditions that need to be satisfied for interfacial stabilization. Hydrophilic particles at nano scale can form agglomerations with the plateau borders of the foam,⁵⁵⁷ whereas partially hydrophobic particles can irreversibly adsorb into the air-water interface.²⁴⁵ There are several other factors affecting the particle role as interfacial stabilizers, such as hydrophobicity,²³⁸⁻²⁴¹ size,^{230, 231} shape,^{233, 263} aspect ratio,²³⁴ and concentration.²³⁵⁻²³⁸ Contradictory results related to the optimum particle size for foam stabilization, are reported in the literature.⁵⁵⁶ Tang *et al.*,⁵⁵⁷ used silica spheres and surfactants to stabilize foams, and concluded that stability could be enhanced using smaller particles, whereas

Hudales and Stein⁵⁵⁸ stated that a higher foam stability could be achieved with larger hydrophilic quartz particles.

Bubble morphology has also been intensively studied in foam stabilization.²³⁶ The presence of particles at the air-water interface might evolve into armored bubbles that display non-spherical shapes. Subramaniam *et al.*,^{559, 560} observed this phenomenon with mineral oil droplets and air bubbles, which were able to preserve their shape even within a thin layer of particles. Interfacial jamming accounts for these particular shapes, which have been observed in air-water interfaces stabilized with particles of polymethylmethacrylate, gold, and zirconium oxide. Interfacial jamming might explain the high mechanical strength and structural stability of systems, such as dirty air bubbles in the ocean,⁵⁶¹ gelled lipids on air bubbles,⁵⁶² and protein-coated vesicles.⁵⁶³

α -Zirconium phosphate ($\text{Zr}(\text{HPO}_4)_2 \cdot \text{H}_2\text{O}$, ZrP) is a synthetic layered compound with a well-defined disk-like structure.⁷⁹ A wide variety of synthetic layered materials are found in the literature, such as silicates, phosphates, phosphonates, phosphites, oxides, hydroxides, niobates, chalcogenides, and sulfides.⁵⁶⁴ In ZrP, zirconium atoms are coordinated with oxygen atoms of the phosphate group forming a layered structure. In the interlayer space, acid-base reactions can occur, where the free $-\text{OH}$ groups from the phosphate react with amines.^{99, 565, 566} From intercalation and exfoliation, ZrP can be delaminated into single thin layers.⁹⁹ High-aspect-ratio ($\zeta = \text{diameter} / \text{thickness}$) ZrP nano-sheets can be obtained by fabricating ZrP crystals of different sizes^{79, 80} followed by exfoliation with guest molecules (*e.g.* tetrabutylammonium hydroxide, propylamine, etc).^{88, 99, 565}

Suspensions of ZrP nano-sheets are not able to stabilize air-water or liquid-liquid interfaces, since these highly anisotropic particles are extremely hydrophilic due to the presence of hydroxyl ($-\text{OH}$) groups on the particle surface.⁷⁸ Recently, we stabilized oil-in-water emulsions using amphiphilic nano-sheets obtained from the exfoliation of ZrP crystals functionalized with octadecyl-isocyanate.²⁶⁰ Similarly, alkyl-amines in aqueous solutions cannot form stable foams. Amines with alkyl chains shorter than 12 carbons cannot form a stable floating layer on the surface of water due to their great affinity with the aqueous phase.²⁶³ Thus far, to the best of our knowledge, no thin and large lateral size disk-like particles (*i.e.*, nano-sheets) have been used as foam stabilizers. In our study, we exfoliated ZrP crystals of different sizes using propylamine ($\text{C}_3\text{H}_7\text{NH}_2$, PA) as the exfoliating agent. The exfoliation of ZrP crystals allows us to obtain nano-sheets of uniform thickness and high aspect ratio. The degree of hydrophobicity of the nano-sheets is controlled by varying the molar ratio of PA:ZrP in the suspensions.^{264, 547} We studied the possibility of obtaining aqueous foams using nano-sheets of ZrP of high-aspect-ratio with a varying degree of hydrophobicity.

4.3.2 Experimental

4.3.2.1 Materials

Zirconyl chloride ($\text{ZrOCl}_2 \cdot 8\text{H}_2\text{O}$, 98%, Aldrich), phosphoric acid (H_3PO_4 , 85%, Fisher Scientific), and propylamine ($\text{C}_3\text{H}_7\text{NH}_2$, 98%, Sigma Aldrich) were used as received. All the suspensions and solutions were made using high-purity Milli-Q water (Millipore).

4.3.2.2 Control of the Size of ZrP Crystals

Three batches of ZrP pristine crystals of different sizes were synthesized using reflux and hydrothermal method as described by Sun *et al.*,⁷⁸ The first batch, A, was prepared by the reflux method (RM) using a phosphoric acid solution of 3M for 24 h. The second and third batch, B and C, were prepared by the hydrothermal method (HM) using a phosphoric acid solution of 15M for 5 h and 24 h, respectively. **Figure 49(a-c)** show the ZrP crystals prepared at 3M-24h (RM), 15M-5h (HM), and 15M-24h (HM), respectively. **Figure 49(d)** shows the crystal size distribution of the three ZrP batches. **Table 8** contains the lateral size and polydispersity (σ) of the crystals obtained from dynamic light scattering measurements (DLS, ZetaPALS, Brookhaven Instruments Corporation, Holtsville, NY).

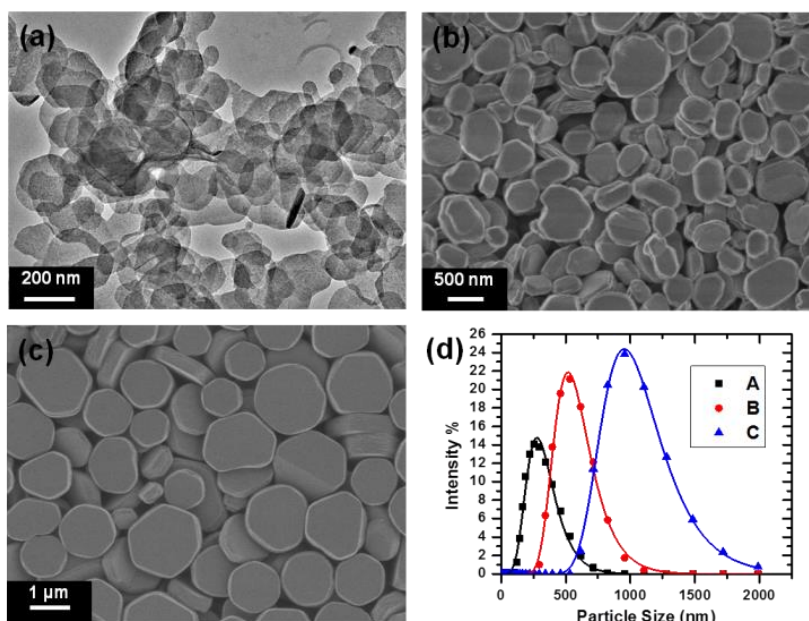


Figure 49. Pristine α -ZrP crystals. Transmission (a) and scanning (b, c) electron microscope micrographs of different ZrP sizes prepared at varying conditions (a) 3M-24 h (RM). (b) 15M-5h (HM), and (c) 15M-24 h (HM). (d) Size distribution of the ZrP crystals fabricated at different reaction conditions.

4.3.2.3 Exfoliation and Modification with Propylamine

To obtain thin nano-sheets of ZrP, the layered crystals in **Figure 49(a-c)** were exfoliated by dispersing the crystals in de-ionized (DI) water and subsequently adding a solution of PA (0.1M) at a molar ratio of 1:1 (PA:ZrP) under continuous stirring.⁹⁹ The concentrated suspensions were treated under sonication for 1 h, and left for 4 days to ensure full intercalation of the guest molecule and to achieve a complete crystal delamination. Finally, we obtained stable colloidal suspensions of ZrP-PA nano-sheets in water. After exfoliation, the nano-sheet aspect ratios for the three suspensions were calculated from estimated thickness, as described by Sun *et al.*,¹⁶⁸ (**Table 8**).

Table 8. Nano-sheet lateral size and aspect ratio

Batch	Lateral size (nm)	Aspect Ratio (ξ)
A	261 ± 36	97 ± 13
B	548 ± 77	204 ± 29
C	1142 ± 305	426 ± 114

4.3.2.4 Preparation of ZrP-PA Nano-sheet Suspensions

For each aspect ratio, the concentrated ZrP nano-sheet stock suspension was diluted to concentrations of 0.5 ± 0.1 , 1 ± 0.1 , 1.5 ± 0.1 , and 2 ± 0.1 %wt. In order to control the PA:ZrP ratio, a PA solution was added until ratios of 1.32 ± 0.05 , 1.53 ± 0.05 , 1.74 ± 0.05 , 1.95 ± 0.05 , and 2.16 ± 0.05 were obtained. From each PA-ZrP suspension, 7 mL were transferred into a 1.6-cm \times 12.5-cm stoppered glass tube (Fisher Scientific, Pittsburgh, PA). The prepared samples were left at room temperature for 24 h to achieve a full adsorption of PA onto the surface of the ZrP nano-sheets.

4.3.2.5 Preparation of Aqueous Foams Stabilized by ZrP-PA Nano-sheets

To obtain aqueous foams stabilized by ZrP-PA nano-sheets, each suspension was vigorously shaken by hand for a period of 30 s. The obtained foam was characterized taking digital photographs at several times using a Canon A3300 digital camera. The digital images were analyzed using ImageJ software (v1.43, National Institutes of Health). Optical and cross-polarized micrographs were taken using a Nikon TE-2000U microscope. The structure of dried foams was observed using a scanning electron microscope (SEM-JEOL JSM-7500F).

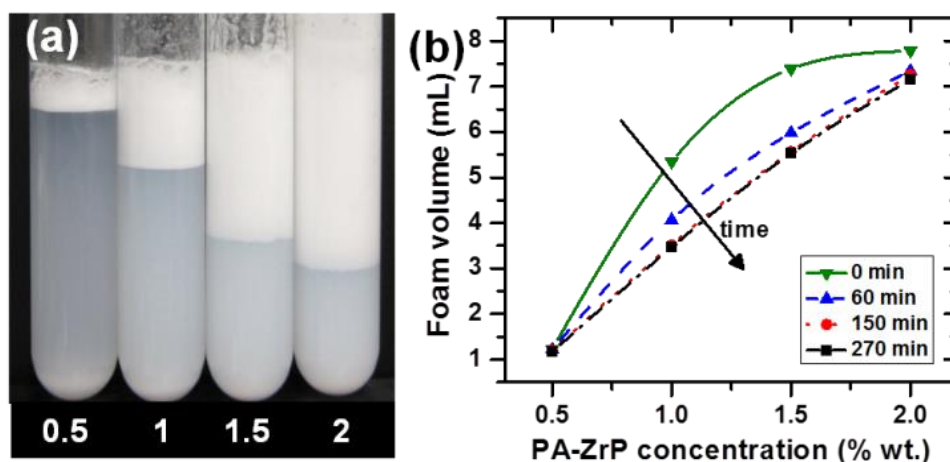


Figure 50. Effect of ZrP-PA nano-sheet concentration on foam stabilization. (a)

Aqueous foams 7 days after preparation as a function of ZrP-PA nano-sheet concentration. The nano-sheet suspension of batch A were used in this experiment at a PA:ZrP molar ratio of 2.16 ± 0.05 . The nano-sheet concentrations are 0.5 ± 0.1 , 1 ± 0.1 , 1.5 ± 0.1 and 2 ± 0.1 % wt. (b) Foam volume as a function of nano-sheet concentration at different times after preparation. The green apex-down triangles, blue triangles, red circles, and black squares correspond to 0, 60, 150, and 270 min., respectively. Lines are guide to the eye.

4.3.3 Results and Discussion

4.3.3.1 Effect of ZrP-PA Nano-sheet Concentration on the Aqueous Foam

To analyze the effect of ZrP-PA nano-sheet concentration on the aqueous foam stability, we created a set of suspensions using batch A having concentrations of 0.5 ± 0.1 , 1 ± 0.1 , 1.5 ± 0.1 , and 2 ± 0.1 %wt. The PA:ZrP molar ratio was set to 2.16 ± 0.05 . Initially, after shaking, the stabilized bubbles were present throughout the entire sample. Air bubbles rapidly started to accumulate at the top of the tube (*i.e.*, creaming), leaving a less turbid lower phase of ZrP-PA nano-sheets dispersed in water. As the ZrP-PA nano-sheet concentration incremented, we observed a growing trend in the aqueous foam as shown in **Figure 50(a)**. A higher nano-sheet concentration enabled the local adsorption of a greater amount of particles onto the air-water interface. As the nano-sheet

concentration increases, more air-water interface can be stabilized. Tang *et al.*,⁵⁵⁷ described the effect of silica spheres and sodium dodecyl sulfate (SDS) concentration on the amount of aqueous foam. They reported that an increase in particle concentration enhances the stability of aqueous foams. Similar results have been obtained using partially hydrophobic silica spheres,⁵⁴⁸ crystalline sodium chloride (NaCl) particles modified with cetyl trimethyl-ammonium bromide (CTAB),²³⁵ and modified disk-like particles.²⁶⁴ In our study, we observed that the amount of aqueous foams made with ZrP-PA nano-sheets of similar hydrophobicity and fixed aspect ratio was proportional to the concentration of particles in the bulk, as observed in **Figure 50(b)**. We also analyzed the foam stability for each suspension at different times after preparation **Figure 50(b, black arrow)**. Interestingly, at equilibrium, the foam volume became linearly dependent on nano-sheet concentration, as seen in **Figure 50(b, black squares)**. Hence, the ability to stabilize foam is proportional to the coverage of particles at the interface. An enhanced surface coverage prevents the diffusion of air molecules between the bubbles; therefore, as the nano-sheet concentration increases, so does the stability of the aqueous foams.

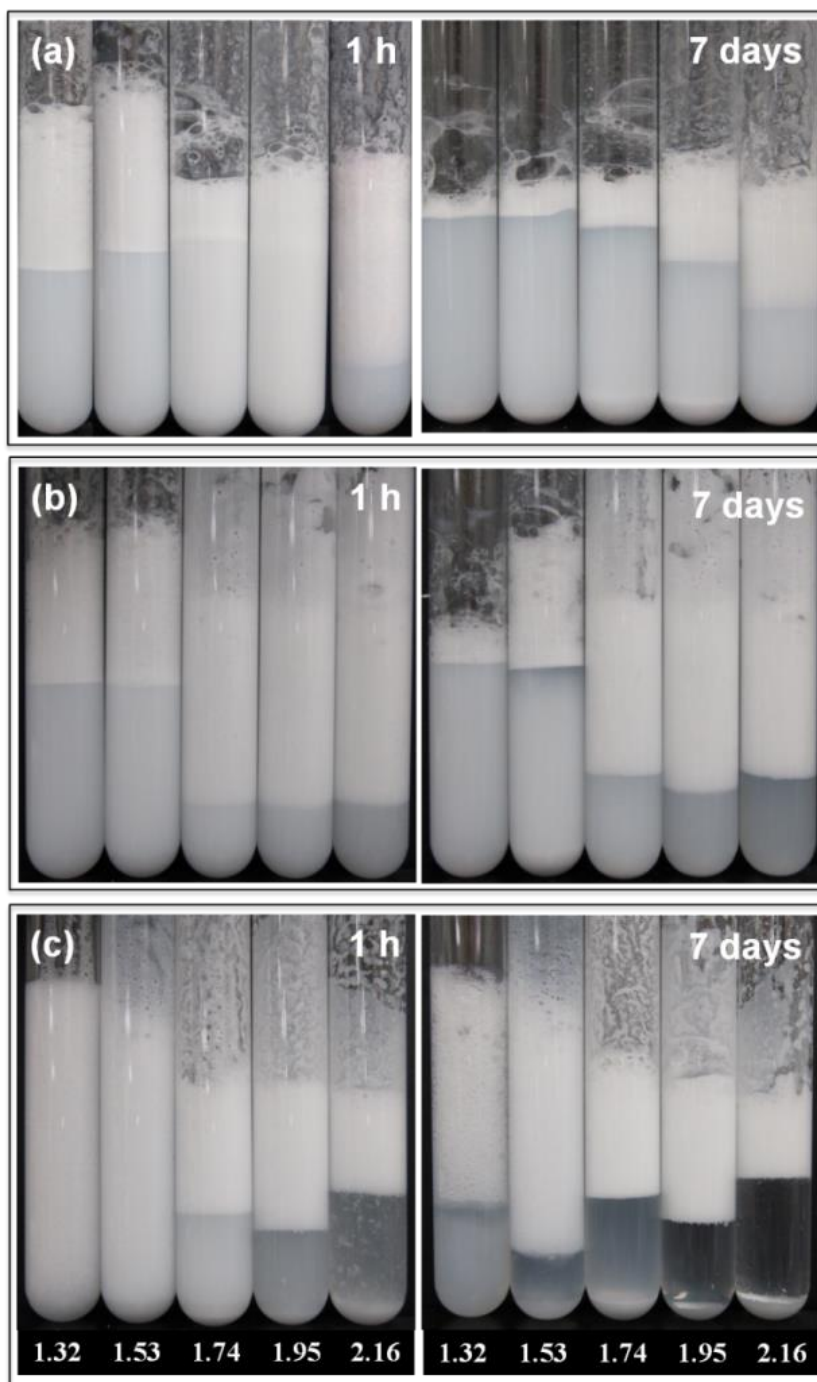


Figure 51. Foams stabilized by ZrP-PA nano-sheets using (a) batch A (b) batch B, and (c) batch C, for different PA:ZrP molar ratios at 1 h and 7 days after foam stabilization. The concentration of ZrP-PA nano-sheets is 2 ± 0.1 % wt.

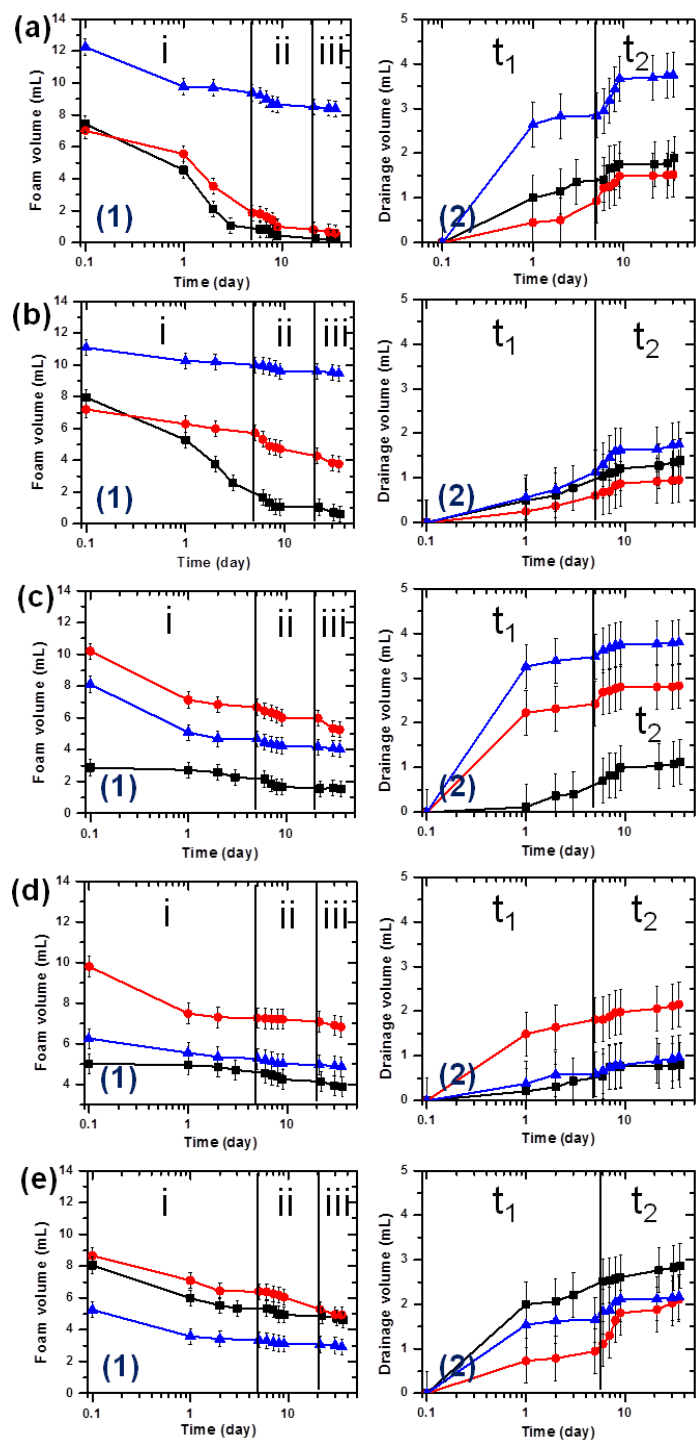


Figure 52. Aqueous foam stability at varying nano-sheet aspect ratio and PA:ZrP molar ratio. (a1–e1) Foam and (a2–e2) drainage volume as a function of time. The black squares, red circles and blue triangles correspond to batches A, B, and C, respectively. The PA:ZrP molar ratios were set to (a) 1.32 ± 0.05 , (b) 1.53 ± 0.05 , (c) 1.74 ± 0.05 , (d) 1.95 ± 0.05 , and (e) 2.16 ± 0.05 .

4.3.3.2 Effect of ZrP-PA Nano-sheet Aspect ratio and Hydrophobicity on Aqueous Foams

4.3.3.2.1 Macroscopic Observation of the Foams

To determine the effect of particle hydrophobicity and aspect ratio on the stabilized aqueous foams, ZrP-PA suspensions were prepared at 1.32 ± 0.05 , 1.53 ± 0.05 , 1.74 ± 0.05 , 1.95 ± 0.05 , and 2.16 ± 0.05 PA:ZrP molar ratios, at a concentration of ZrP-PA nano-sheets of $2\% \pm 0.1$ wt. **Figure 51** shows the aqueous foams made from nano-sheet suspensions of batches A, B, and C at different PA:ZrP molar ratios. In general, remarkable foam stability was obtained in all of the studied molar ratio range. Even at a low molar ratio, the nano-sheets are hydrophobic enough to stabilize bubbles after hand-shaking. The nano-sheets in the suspension adsorb on the air-water interface that is generated as they reduce the surface energy of the system. After foam preparation, the bubbles coarsen and the total bubble surface area covered by the nano-sheets decreases. This coarsening process continues until the total available surface area is covered by the nano-sheets (*i.e.*, limited coalescence).⁵⁶⁷ A critical nano-sheet aspect ratio for an optimal interfacial stabilization will depend on the surface chemistry, wetting, and the interaction interparticle forces.²³⁴ With an increment in the molar ratio, the hydrophobicity of the nano-sheets increases,^{264, 547} allowing more nano-sheets to be adsorbed on the air-water interface. Since we are varying the degree of hydrophobicity of the nano-sheets, different foam behaviour is expected.

The increase in the amount of adsorbed particles on the air-water interface also increases the amount of aqueous foam volume, as observed from batches A and B in **Figure**

51(a,b). Interestingly, an opposite behaviour was observed at the highest aspect ratio at a PA:ZrP molar ratio above 1.53 ± 0.05 . This could be explained by the large aggregates of nano-sheets that quickly settled to the bottom of the glass tube, as seen in **Figure 51(c, 1 h and 7 days)**. This particle aggregation indicates that the maximum nano-sheet concentration on the available air-water interface has been reached (*i.e.*, dense packing of nano-sheets). The nano-sheets in batch C possess a highly hydrophobic interaction that makes them prone to aggregate rather than to adsorb onto the air-water interface.

Dickinson *et al.*,⁵⁴⁸ explained that during particle aggregation, the ability to stabilize the air-water interface decreases due to the lack of particles that adsorb on it. The effect of particle size on the interface can be explained from the adsorption energy equation: $\Delta G = \pi R^2 \gamma_{aw} (1 \pm \cos \theta)$, where ΔG is the energy required to remove an adsorbed particle out from the air-water interface into the bulk, R is the size of the particle, γ_{aw} is the interfacial tension between the air and water, and θ is the wetting angle of the particle at the interface.²⁴³ From the described equation, the detachment energy is proportional to the surface area of the particle; therefore, larger particles have a larger energy of attachment to interfaces relative to the thermal energy kT . Thus, when a particle is at an interface, it can be thought of as it being irreversibly adsorbed.²⁴⁵ In fact, batch C and batch B nano-sheets at the same degree of hydrophobicity possess particle energies of adsorption to the air-water interface of 21 and 5 times greater than batch A nano-sheets, respectively.

However, as previously stated, particle aggregation driven by hydrophobic interaction has a negative effect in the availability of particles at the interface and cannot

be neglected as it prevents particles to be effectively adsorbed on the air-water interface.⁵⁶⁸ Therefore, for large nano-sheets, a maximum in foam production is expected as a result of these two competing effects: hydrophobic nano-sheet aggregation and adsorption on the air-water interface.^{235, 569} In our case, a maximum shows up for batch C platelets at a molar ratio of ~ 1.53 . A similar behaviour using spherical silica particles and increasing particle hydrophobicity was experienced by Kruglyakov *et al.*,²³⁸

4.3.3.2.2 Analysis of the Stability of the Aqueous Foams

To analyze the stability of the aqueous foam, we tracked the foam volume as a function of time, as shown in **Figure 52(a1–e1)** and the drainage volume (*i.e.*, volume of water) as a function of time, as shown in **Figure 52(a2–e2)** from the foam pictures obtained in **Figure 51**.

Very interestingly, we observe that the reduction of foam volume occurred in a three-step process (**Figure 52(a1–e1)**); (i) creaming and draining, (ii) coarsening and draining, and (iii) foam collapsing. These three stages were identified based on the change in slope of foam volume with time (**Figure 52(a1–e1)**). In general, bubble creaming occurred right after foam preparation and lasted for about 4 days. During the next 6 days, the foam volume decreased due to water drainage and coarsening. After the 10th day, the foam presented little variation in volume. Since the foam is holding little or no water in the system, the burst of large bubbles dominated and some foam collapsing was observed.

In our research, for nano-sheets of batch C and at a low PA:ZrP molar ratio (<1.53), we obtained a large foam volume of high stability (**Figure 52(a1–b1)**). At this molar ratio region, it is interesting to note that the foam volume stability is dependent on the nano-sheet aspect ratio. As particle aspect ratio is increased, as shown in **Figure 51**, the foams become more stable. Similar to the method described by Madivala *et al.*,²³⁴ increasing the nano-sheet aspect ratio is a practical method to increase stability at low particle concentration. At molar ratios of PA:ZrP larger than 1.74, in spite of the initial foam volume, a similar foam stability was observed for all batches (**Figure 52(c1–e1)**). In general, a significantly high stability was found for our nano-sheet stabilized system, in contrast to surfactant-stabilized foams. Alargova *et al.*,⁵⁵⁴ explained that foam volume may be initially larger in foams stabilized by surfactants, but stability is outstanding for foams made with partially hydrophobic particles. In our experiments, foam volume was preserved at least 36 days after stabilization, whereas SDS foams lasted up to only 2 days.⁵⁵⁴

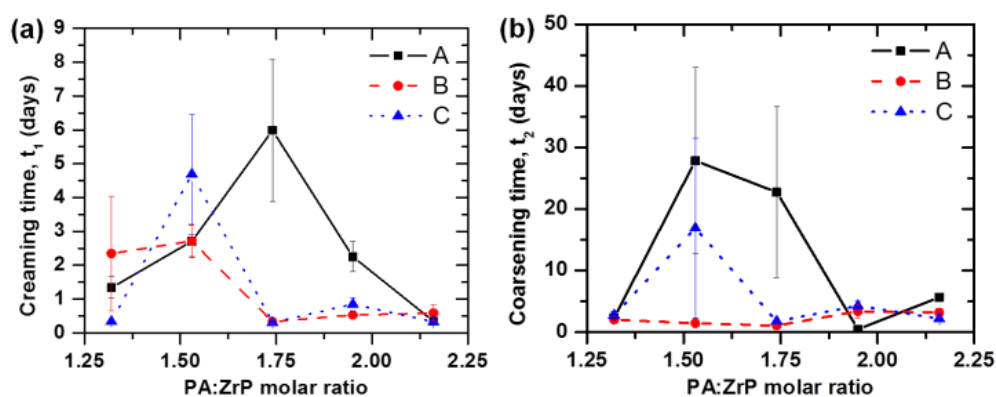


Figure 53. The two-time scales, t_1 and t_2 , observed during water drainage as a function of the PA:ZrP molar ratio at different aspect ratios. (a) Creaming and (b) Coarsening time. The black squares, red circles, and blue triangles correspond to batches A, B, and C, respectively.

We also observed that water drainage takes place in a two-time-scale process, t_1 and t_2 (**Figure 52(a2–e2)**). These two time scales observed during the water drainage are attributed to creaming, coarsening, and water draining and are plotted as a function of the PA:ZrP molar ratio at a fixed nano-sheet aspect ratio (**Figure 53**). t_1 is mainly proportional to the effect of bubble creaming and water draining from the foam structure, whereas t_2 is proportional to water draining and coarsening. Creaming is controlled by the bubbles' size, gravity, suspension viscosity, and the density difference between the discontinuous and the continuous phase. Draining is the free flow of water driven by gravity through the foam's random network of plateau borders. In our case, draining is influenced by the hydrophobicity of the nano-sheets. Hydrophobic nano-sheets aggregate and create clusters at the air-water interface, whereas hydrophilic nano-sheets stay at the plateau borders, preventing water drainage. During draining, the liquid borders between adjacent bubbles become too thin and coalesce. Surprisingly, in our system, coarsening becomes practically negligible after draining, as evidenced by the arrested bubble coalescence. Water drainage observations for foams stabilized by proteins were reported by Elizalde *et al.*,⁵⁷⁰ In such system, the drainage volume reached a plateau in a couple of hours, compared to our study, where this plateau was reached several days after preparation. Such preservation of the foam volume and slow drainage occurs due to the formation of a nano-sheet layer at the bubble surface. This layer of nano-sheets is able to maintain the bubble shape by forming a shell-like structure on the air-water interface.^{240, 553} In **Figure 53a** and **b**, it was observed that the aqueous foams created with nano-sheet suspensions of batch A presented longer t_1 and t_2 compared to

the ones stabilized by nano-sheet suspensions of batches B and C. This observation is in agreement with the lowest stability presented in the aqueous foams stabilized using nano-sheets of batch A (*i.e.*, low aspect ratio).

Figure 54(a–c) displays the foam decay rate (red line with squares) and the water drainage rate (blue line with triangles) for foams obtained in **Figure 51(a–c)**, respectively. These rates were obtained by calculating the variation in foam volume and drainage volume during the first 10 days after foam stabilization. The rates are plotted as a function of the PA:ZrP molar ratio for batches A, B, and C, respectively.

In our experiments, we observed a constant water drainage rate with the variation of nano-sheet aspect ratio and PA:ZrP molar ratio (*i.e.*, different hydrophobicity). In the case of the foam decay rate, aqueous foams stabilized using batch C presented constant rates at different molar ratios. However, for aqueous foams stabilized by batches A and B, constant rates were reached only above a PA:ZrP molar ratio of 1.74 and 1.53, respectively. These results indicate a dependence of the foam decay rate plateau values on nano-sheet hydrophobicity and aspect ratio. In general, for molar ratios higher than 1.74, the nano-sheets at different aspect ratios are hydrophobic enough to create highly stable aqueous foams. In addition, the obtained foams presented reduced water drainage and foam decay with time. Intriguingly, at molar ratios larger than 1.74, aqueous foams stabilized by nano-sheet suspensions of batch A presented a lower foam decay rate (~ 0.05 mL/day) compared to batches B and C (~ 0.1 mL/day). This suggests that an efficient manner to stabilize air-water interfaces consists in using low and high aspect

ratio nano-sheets having a high and an intermediate degree of hydrophobicity, respectively.

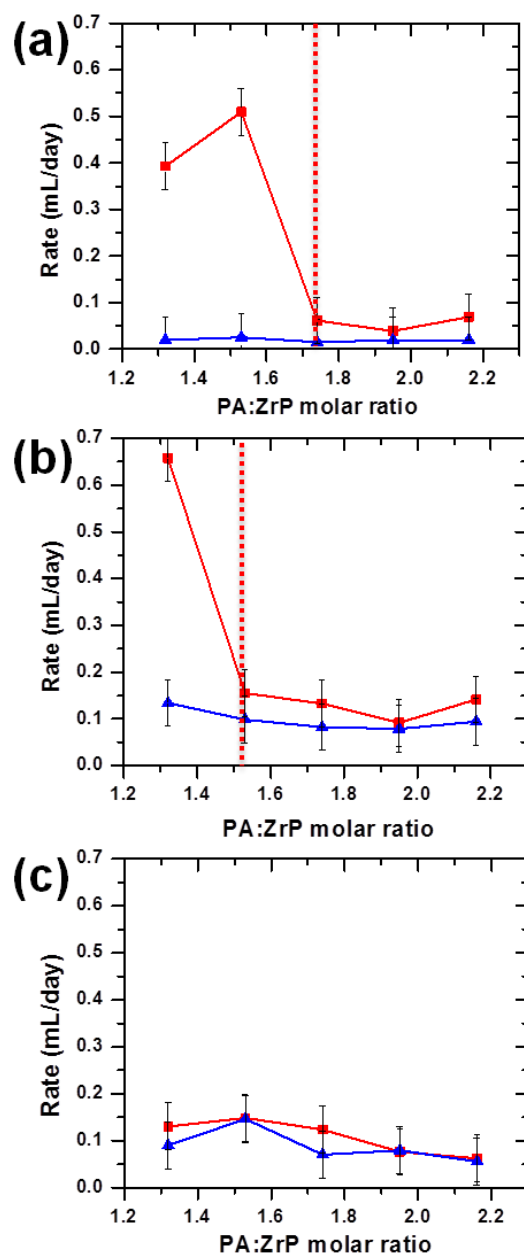


Figure 54. Foam decay (red squares) and water drainage rate (blue triangles) as a function of PA:ZrP molar ratio of aqueous foams obtained from nano-sheet suspensions of batch (a) A (b) B, and (c) C. The foam decay and water drainage rate were calculated from the foam and water volume at the 10th day with respect to the volume right after preparation, respectively.

4.3.3.2.3 Microscopic Analysis of the Aqueous Foams

The optical micrographs in **Figure 55** reveal the variation of the bubble size and shape as a function of PA:ZrP molar ratio of the foams obtained from the three different aspect ratio nano-sheet suspensions. Using nano-sheet suspensions of batch A (*i.e.*, low aspect ratio) (**Figure 55(a1–a4)**), at low PA:ZrP molar ratios (≤ 1.53), the apparent bubble size is in a range between 50 and 250 μm (**Figure 55(a1–a2)**). At intermediate PA:ZrP molar ratios (~ 1.74), the apparent bubble size decreases to a range between 50 and 200 μm , and non-spherical bubbles are observed (**Figure 55(a3)**). Further increase in the PA:ZrP molar ratios (~ 2.16), resulted in a slightly reduced bubble size in a range between 50 and 150 μm (**Figure 55(a4)**).

Using nano-sheet suspensions of batch B (*i.e.*, intermediate aspect ratio) as shown in **Figure 55(b1–b4)**, at low PA:ZrP molar ratios (~ 1.32), the bubbles are spherical and tend to squeeze due to the presence of surrounding bubbles (**Figure 55(b1)**). Upon increase of the PA:ZrP molar ratio, a larger number of non-spherical bubble shapes is observed (**Figure 55(b2–b3)**). At high PA:ZrP molar ratio (~ 2.16), particle aggregation caused by hydrophobic interactions is evident, as seen in **Figure 55(b4)**.

Finally, using nano-sheet suspensions of batch C (*i.e.*, large aspect ratio) (**Figure 55(c1–c4)**), at low PA:ZrP molar ratios (~ 1.32), the bubble are spherical and nearly uniform in shape (**Figure 55(c1)**). Upon increase of the PA:ZrP molar ratio and similar to foams stabilized by nano-sheet suspensions of batch B, a larger number of non-spherical bubbles is observed (**Figure 55(c2–c3)**). At molar ratios of 2.16, the creation

of nano-sheet aggregates is evident, as seen in **Figure 55(c4)**. Cluster formation is more noticeable for high nano-sheet aspect ratio and high PA:ZrP molar ratios. This observation is in agreement with Kobayashi *et al.*,⁵⁶⁸ where large particles are more prone to aggregate compared to smaller ones. The variation of bubble size by increasing the PA:ZrP molar ratio can be understood from an increment in the suspension apparent viscosity. This increase in viscosity impedes air incorporation during the foam production process.⁵⁵⁰ Other studies using particles such as modified silica²³⁶ and LDH platelets,²⁶³ also found that smaller average bubble size was observed at high surface-modifying agent concentration, mainly due to a reduction in the suspension surface tension along with an increase in the foam viscosity. This effect can be explained by the increase of PA adsorption on the ZrP nano-sheet surface. This adsorption produces an increase in the apparent viscosity from the screening of the particle surface charges by the oppositely charged PA molecules in the system.⁵⁵⁰ Nano-sheets of a larger diameter possess a larger contact area, thus increasing the suspension viscosity more noticeably compared to the smaller particles.⁴⁴⁰ The observation of the non-spherical bubble shape might be attributed to the formation of a particle-jammed bubble surface. Such shapes can be preserved due to non-uniform external stresses from jammed-like nano-sheets located at the air-water interface.⁵⁵⁹ In addition, jamming of nano-sheets in the bulk can occur due to the increment of the particle local concentration in the plateau borders during creaming, water draining, and coarsening.

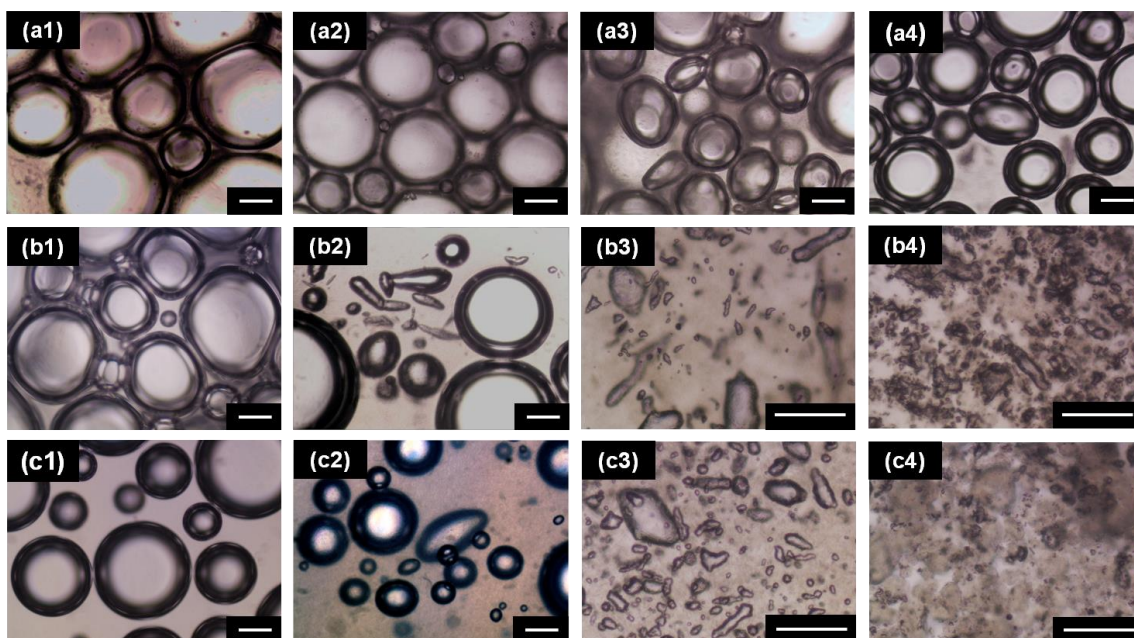


Figure 55. Optical micrographs of bubbles extracted from the aqueous foams in **Figure 51**. The micrographs were taken 1 h after foam stabilization. The aqueous foams were obtained by shaking suspensions containing nano-sheets from (a) batch A, (b) batch B, and (c) batch C. From (1) to (4) the molar ratios were set to (1) 1.32 ± 0.05 , (2) 1.53 ± 0.05 , (3) 1.74 ± 0.05 , and (4) 2.16 ± 0.05 , respectively. The scale bar is 100 μm .

4.3.3.2.4 Pickering Foam Structures as Water Barriers

In our system, we observed an interesting foam behaviour that has not yet been reported. After two months of foam preparation at a high ZrP-PA nano-sheet concentration (2 wt.%), the foam tubes were placed upside down. Intriguingly, we observed that the aqueous foams were able to prevent water from flowing down, as shown in **Figure 56**, at PA:ZrP molar ratios above 1.74 for batch B and C and 1.95 for batch A. Assuming a water Poiseuille flow behavior, liquid-blockage might occur due to water flow resistance, which depends on the plateau border geometry, $R \sim L/D^4$, where R is the hydrodynamic resistance, L is the length of the plateau border, and D is the distance between the plateau borders' surfaces.⁵⁷¹ During foam drainage, the plateau

borders surfaces approached and rested in an immobile position.⁵⁷¹ Since $D \ll L$, water flow resistance is extremely high and prevents the flow of water downward the foam. Also, a further contribution might come from the closed-packed rigid-structure created from the packing of nano-sheets at the air-water interface and in the plateau borders.

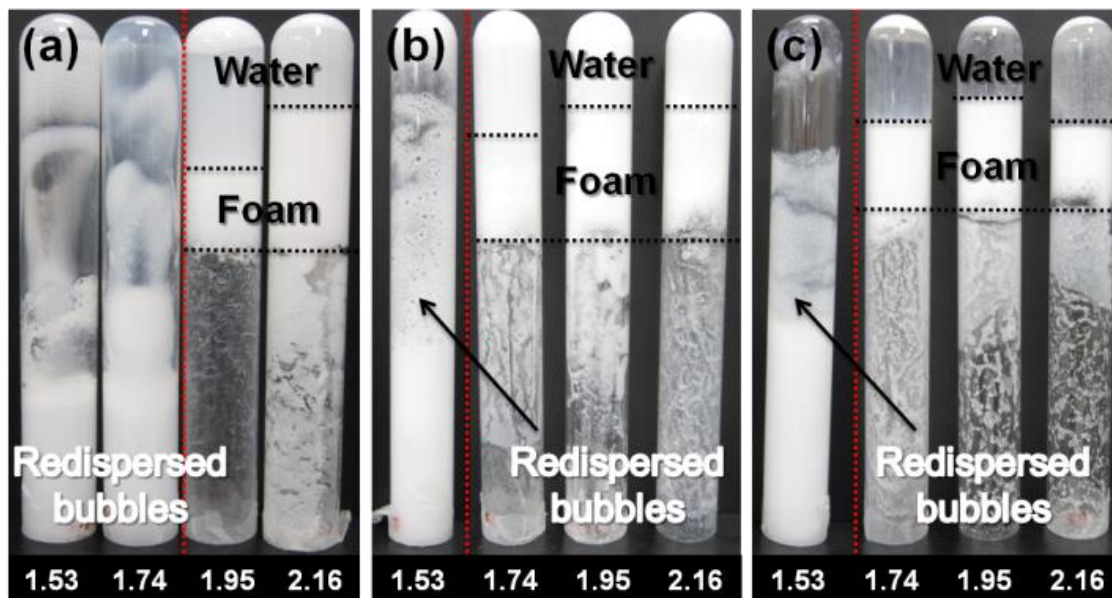


Figure 56. Aqueous foams obtained from nano-sheet suspensions at varying aspect ratios and PA:ZrP molar ratios. (a) batch A, (b) batch B, and (c) batch C. The water is blocked at the top of the tube due to the jammed ZrP-PA nano-sheets in the bulk and on the air bubbles.

4.3.3.3 The Structure of the Foam Stabilized by ZrP-PA Nano-sheets at Varying Aspect Ratio

To verify the presence and adsorption of ZrP-PA nano-sheets in the bulk and on the air-water interface, we compared optical and cross-polarized micrographs taken at different PA:ZrP molar ratios, as shown in **Figure 57**. Highly anisotropic particles (*i.e.*, large aspect ratio) such as ZrP nano-sheets are well known for being birefringent under

crossed polarizers.^{48, 80, 572} As expected, a strong birefringence was observed on the surface of the bubbles at varying molar ratios as seen in **Figure 57(b, d)**. This is direct evidence that the ZrP-PA nano-sheets adsorb on the air-water interface. Birefringent zones were also observed in the bulk, indicating the presence of non-adsorbed nano-sheets. **Figure 57b** shows the homogeneous nano-sheet distribution in the bulk suspension at a molar ratio of 1.32. By increasing the molar ratio to 1.95, we observed a stronger birefringence on the surface of the bubbles, as shown in **Figure 57d**. The adsorption of a large quantity of nano-sheets at the interface increases the birefringence intensity at that region. In addition, we found evidence of nano-sheet aggregation due to hydrophobic interactions from the brightest clusters in the bulk. An increment in the number of nano-sheets at the interface and the plateau borders will increase the rigidity and the strength of the foam, as previously shown in **Figure 56**. This is consistent with the stability observations in **Figure 52** and **Figure 54**, which demonstrated that at high PA:ZrP molar ratio (≥ 1.74) foam volume is preserved in time.

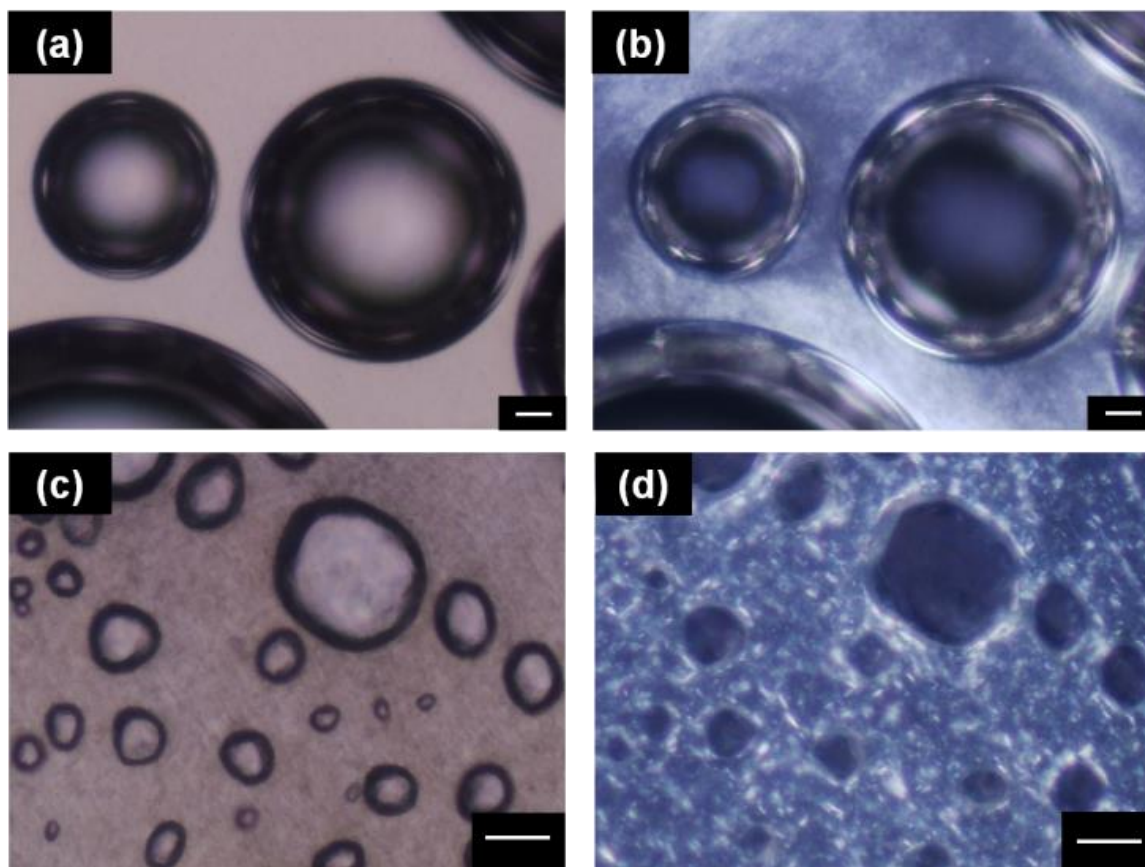


Figure 57. The contrast between optical and crossed-polarized micrographs of the foams. The micrographs were taken 1 h after foam stabilization. The foams are obtained from suspensions of batch C. (a) and (c) are optical micrographs at a molar ratio of PA:ZrP of 1.32 and 1.95, respectively. (b) and (d) are cross-polarized micrographs at a molar ratio of PA:ZrP of 1.32 and 1.95, respectively. The nano-sheet concentration is fixed at 2 ± 0.1 % wt. The scale bar is 50 μm .

Figure 58(a–c) shows scanning electron micrographs (SEM) of foam dried at room temperature. **Figure 58(a1–c1)** show the dried structure of foams obtained with the batches containing the nano-sheets of the smallest (batch A), intermediate (batch B), and largest (batch C) sizes at low PA:ZrP molar ratio (1.32). Zoom-in micrographs of **Figure 58(a1–c1)** are shown in **Figure 58(a1x–c1x)**. For each nano-sheet aspect ratio, we observed that a thin film of ZrP-PA nano-sheets was present at the air-water interface.

A very interesting behaviour was also observed during the drying of the aqueous foam. The foam bubbles obtained with nano-sheet suspensions of batch A, evolved from a spherical into a typical polyhedral shape. On the other hand, for foams stabilized by nano-sheet suspensions of batch B and batch C, the bubble structure was more dry resistant, preventing the burst of the bubbles and preserving its spherical shape.

By increasing the molar ratio to 2.16 (**Figure 58(a2-c2)**) and looking into the zoom-in images (**Figure 58(a2x-c2x)**), we observed a large increase in the thickness of the nano-sheet film over the bubble surface. As the PA:ZrP molar ratio increased, the nano-sheets became more hydrophobic; hence, the particles tended to aggregate and adsorb over the air-water interface. This increment in the nano-sheet aggregation results in a thicker layer of particles. These layers of fused particles are the main reason for the low gas diffusion between the air bubbles. However, there are a more reasons to explain why aqueous foams stabilized by high-aspect-ratio nano-sheets can present shapes other than spherical. For instance, layers of ZrP are able to bend ⁷⁸ due to inhomogeneous stress distribution, shear at foam formation or possible defects in the ZrP structure.

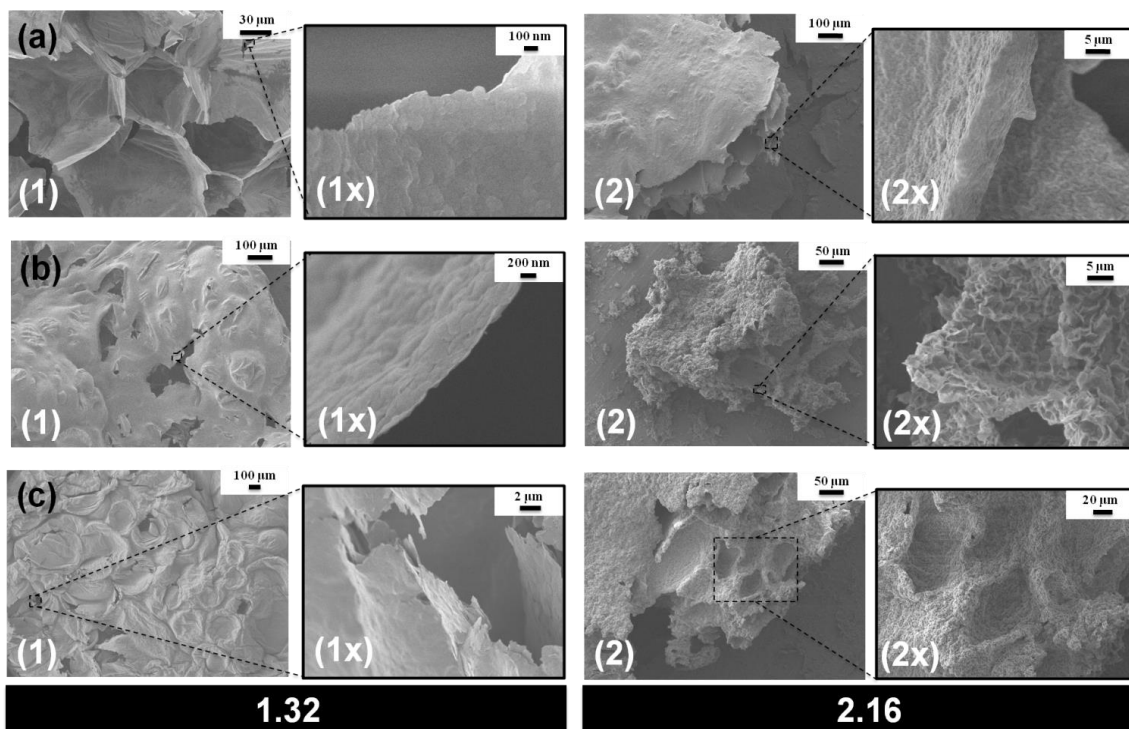


Figure 58. SEM micrographs of dried aqueous foam stabilized by ZrP-PA nano-sheets of different batches as labelled. (a) Batch A, (b) batch B, and (c) batch C. The zoomed-in images show the nano-sheets at the air-water interface. The PA:ZrP molar ratios were set as labelled.

4.3.4 Summary

We developed highly stable Pickering foams using high-aspect-ratio ZrP nano-sheets. The effect of nano-sheet aspect ratio, concentration, and hydrophobicity to stabilize air-water interfaces was elucidated. We found that using low and high aspect ratio nano-sheets having a high and an intermediate degree of hydrophobicity, respectively, is the successful formula to obtain high foam stability. ZrP nano-sheet suspensions of varying aspect ratios were obtained by fabricating crystals of different sizes followed by exfoliation with PA. The degree of hydrophobicity of the nano-sheets was modified by adjusting the PA:ZrP molar ratio. Foam stabilization was achieved by

vigorously hand-shaking the nano-sheet suspensions. We observed that the produced foam volume was proportional to the nano-sheet concentration. For all nano-sheet aspect ratios, at sufficiently high PA:ZrP molar ratios, the foam volume does not vary after the initial water drainage, lasting at least 36 days. Exceptional foaminess and stability was found using the nano-sheet suspension of highest aspect ratio at PA:ZrP molar ratios lower or equal to 1.53. Also, these nano-sheets displayed better stability in terms of foam decay and water drainage rate compared to the other two nano-sheet suspensions. At high hydrophobicity, however, nano-sheets of the highest aspect ratio are prone to create clusters on the interface and in the bulk, whereas low-aspect-ratio nano-sheets attach more readily to the air-water interface and tend to stabilize larger bubbles. We also found that collapsing of foam volume occurs in a three-step process. In addition, water drainage takes place in a two-time-scale process, t_1 and t_2 . These foam behavioral differences in time are dependent on creaming, draining, and coarsening. Scanning electron microscopy (SEM) micrographs showed that several layers of nano-sheets in a jammed-like structure stabilized each air bubble. These layers form a rigid structure in the air interface, which slows down coarsening, coalescence, and water drainage inside the foams. Since the layers between bubbles determine foam stability, a more detailed study about their internal configuration will be presented in the future. This work will assist to elucidate in a more profound level the effect of high aspect ratio nano-sheets on the stability of aqueous foams.

CHAPTER V

CONCLUSIONS AND FUTURE WORK

5.1 Summary

This work focuses on two main areas: the study of the discotic colloidal liquid crystal phase transitions and the application of disk-like colloidal systems as interfacial stabilizers. Research on discotic liquid crystals has just resumed after a long intermission and little efforts have been devoted to the control of their size and size distribution. The main goals of this dissertation were to fabricate novel discotic fluids with unprecedented uniformity in size and shape and understand how the liquid crystalline phase transitions of disk-like colloidal fluids depend on factors such as shape, aspect ratio, lateral size polydispersity, and particle concentration. We also studied the ability of disk-like nano-sheets to stabilize gas-liquid and liquid-liquid interfaces and investigated the effect of particle aspect ratio, concentration, and hydrophobicity.

In **Chapter II**, we produced discotic colloids via electrospray of melted wax. Using a stable cone-jet mode and by controlling density and surface tension mismatching between the wax and the collection solution, uniform emulsions were obtained. Anisotropic wax particles were achieved by inducing the formation of the rotator phase of the wax emulsions. Alkenes go through surface freezing that their surfaces crystallize at temperature right above their bulk melting temperature. At the melting temperature, surface freezing created a crystalline monolayer around our wax droplets that would act as the nuclei of the rotator phase as temperature decreased. Then

rotator phase grew from the surface towards the center, fabricating the disks. The shape of the resultant particles is adjusted by two control parameters, the anchoring and the spontaneous curvature c_0 . The aspect ratio of the flat disks can be varied by setting the magnitude of the surface tension anisotropy using different ratios of surfactant and co-surfactants at the interface. The wax disk self-assembling was analyzed via solvent evaporation to induce depletion attraction. We found that the morphology of anisotropic particles is vital to their self-assembling behaviors. Along with evaporation, phases such as isotropic, condensed, columnar stacking, and self-assembly of columnar rods are revealed.

Subsequently, in **Chapter III** we revealed the effect of aspect ratio and polydispersity on the isotropic-nematic transition of colloidal suspensions of nanoplates that are uniform in thickness at the low thickness-to-diameter ratio limit. The aspect ratio of the nanoplates can be tailored by varying the size of ZrP crystals, and a subsequent exfoliation with intercalation of TBA cations between the interlayers. The I-N transition widens as aspect ratio and polydispersity increase. The experimental data were compared to previous simulations, and the dissimilarities were attributed to size polydispersity and shape of the platelets.

We also described the formation of thermo-responsive and highly-ordered ZrP nano-sheets in bulk polymer at low nano-sheet concentration. These ZrP/polymer nanocomposites were obtained via the polymerization/cross-linking of N-isopropylacrylamide and acrylamide monomer solutions with high aspect ratio ZrP nano-sheets. At a temperature above the polymer LCST, edge-wrinkling was observed.

This wrinkling induced an increment in the nematic order of the nano-sheets evolving in an I-N transition. The evolution of the discotic nematic defects on the edge is further discussed.

In **Chapter IV**, we have demonstrated the fabrication of thin amphiphilic Janus and Gemini nano-sheets by exfoliating α -ZrP crystals grafted with a coupling agent of hydrophobic molecules on their edges and outer surfaces. These novel thin amphiphilic Janus and Gemini nano-sheets were used to stabilize surfactant-free oil-in-water emulsions. Similarly, analogous high-aspect-ratio ZrP amphiphilic nano-sheets were utilized to develop highly stable Pickering foams. The effect of nano-sheet aspect ratio, concentration, and hydrophobicity to stabilize air-water interfaces was elucidated. We found that using low and high aspect ratio nano-sheets having a high and an intermediate degree of hydrophobicity, respectively, is the successful formula to obtain high foam stability. Scanning electron microscopy (SEM) micrographs revealed that several layers of nano-sheets in a jammed-like structure stabilized each air bubble. These layers form a rigid structure in the air interface, which slows down coarsening, coalescence, and water drainage inside the foams.

5.2 Future Research and Ongoing Projects

Based on the results of this dissertation, there are many possible directions that could be taken. Future work may be focused in the study of disk lateral size polydispersity, particle interactions, gravity, and external fields on the liquid crystalline phase behaviors. In the discussions below, preliminary results and future work in terms of the effect of small depletants on the phase behavior of discotic liquid crystals and discotic self-assembly is discussed.

5.2.1 Liquid Crystalline Phase Behavior of Zirconium Phosphate - Silica Suspensions

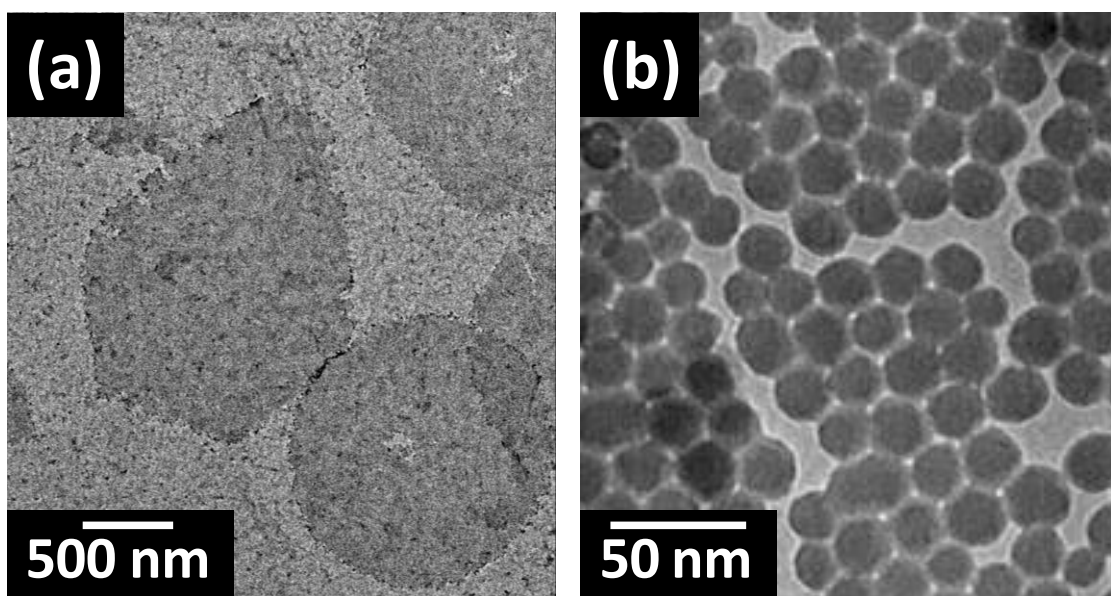


Figure 59. Transmission electron micrographs of (a) ZrP nano-sheets and (b) silica spheres.

Discotic systems are particularly sensitive to a depletion attraction since the overlap volume of depletion zones for parallel platelets are large compared to the case of spheres and rods. Here, we demonstrated that depletion attraction in the colloidal ZrP

nano-sheet system can be brought by the addition of colloidal spheres. We are currently studying the phase behavior of high aspect ratio ZrP nano-sheets mixed with silica spheres. The nano-sheets and the spheres are 1500 and 20 nm in diameter, respectively (**Figure 59**). By mixing silica spheres into nano-sheet suspensions, the spheres can act as depletants, resulting in a variation of the ZrP nano-sheet phase diagram.

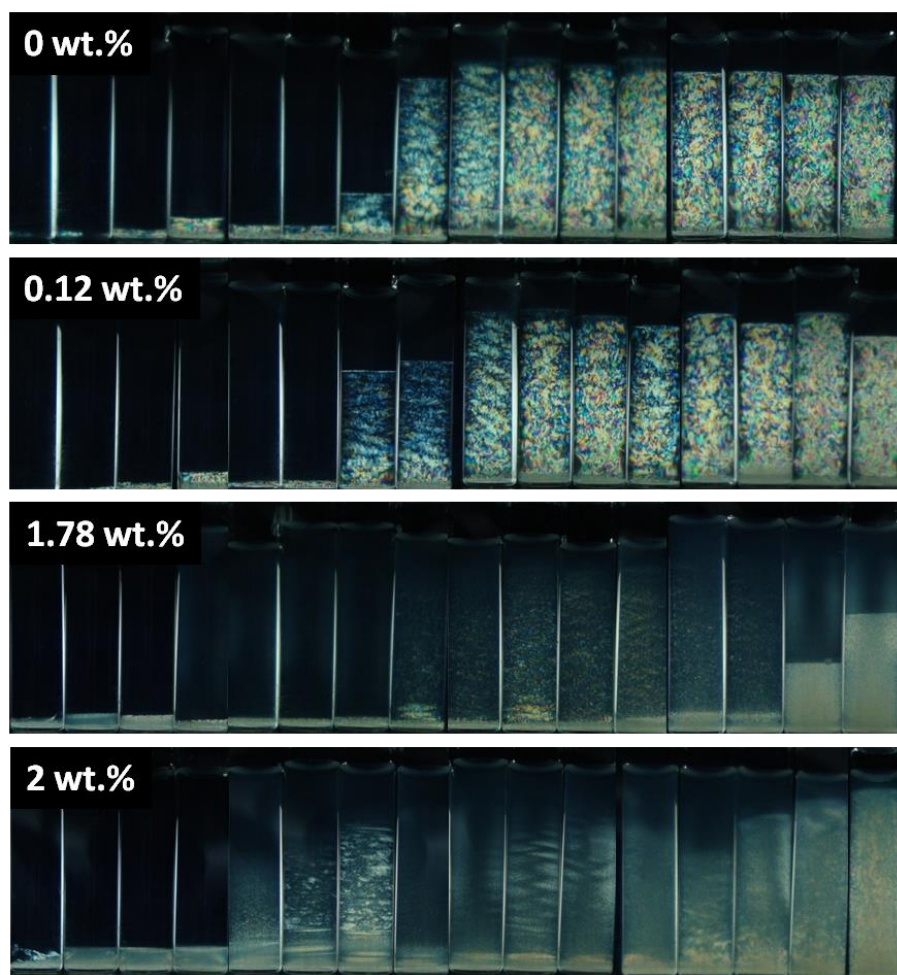


Figure 60. Photographs of ZrP/silica suspensions between crossed polarizers. From left to right, ZrP volume fraction corresponds to 0.0009, 0.0018, 0.0027, 0.0036, 0.0045, 0.0054, 0.0063, 0.0070, 0.0081, 0.009, 0.01, 0.0108, 0.0117, 0.0126, 0.0153, and 0.018, respectively. From top to bottom, silica concentration corresponds to 0, 0.12, 1.78, and 2 wt.%, respectively.

Figure 60 shows photographs of the phase separated samples at fixed silica concentration and varying ZrP volume fractions. Typically, the nematic fraction grows as the ZrP nano-sheet volume fraction increases. Surprisingly, at a relatively high silica concentration, the demixing of the nematic phase into two nematic phases, N_1 and N_2 was observed. For a further analysis, N_1 was visualized under an optical microscope coupled with crossed polarizers and compared with N_2 . The texture of N_1 observed between cross polarizers displays dark brushes having irregular curved shapes corresponding to extinction positions of the nematic liquid. Disclinations of $s = \pm 1/2$ and $s = \pm 1$, characteristics of nematic textures are observable (**Figure 61a**).⁴⁴² The texture of N_2 displays a uniform domain and strong birefringence (**Figure 61b**).

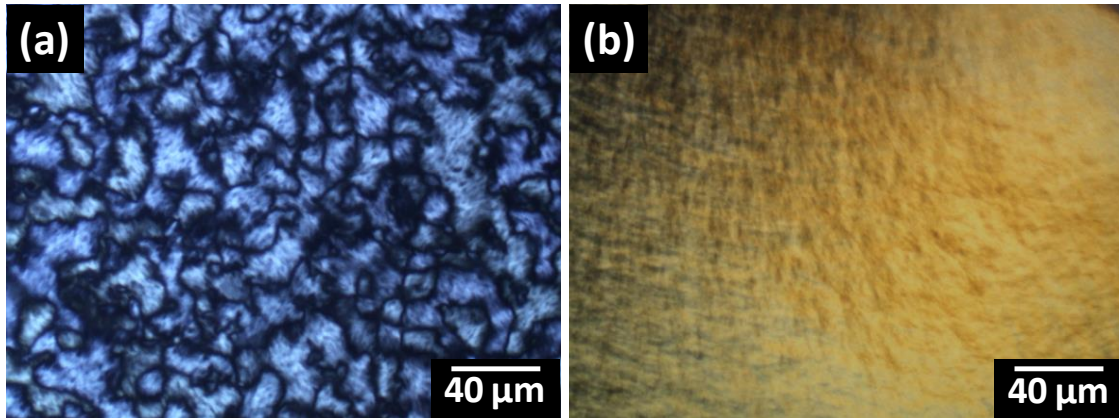


Figure 61. Cross-polarized optical microscopic images of nematic Schlieren textures (a) N_1 , $\phi_d = 0.0081$ and silica concentration of 0 wt.%. and (b) N_2 , $\phi_d = 0.018$ and silica concentration of 1.78 wt.%. The micrographs were taken using a Nikon microscope TE-2000U with crossed polarizers. Pictures were taken using 4 \times magnification.

We observed a pronounced broadening of the isotropic-nematic (I-N) transition as shown in **Figure 62** as concentration of silica spheres increases. The broadening implies that fully nematic samples re-enter into an I-N coexistence region (*i.e.*, biphasic

state). This phase separation occurs due to depletion attraction forces inside the suspensions. Interestingly, we also found that at a certain region of the ZrP/silica phase diagram, a biphasic (N_1 - N_2) and triphasic (I- N_1 - N_2) region.

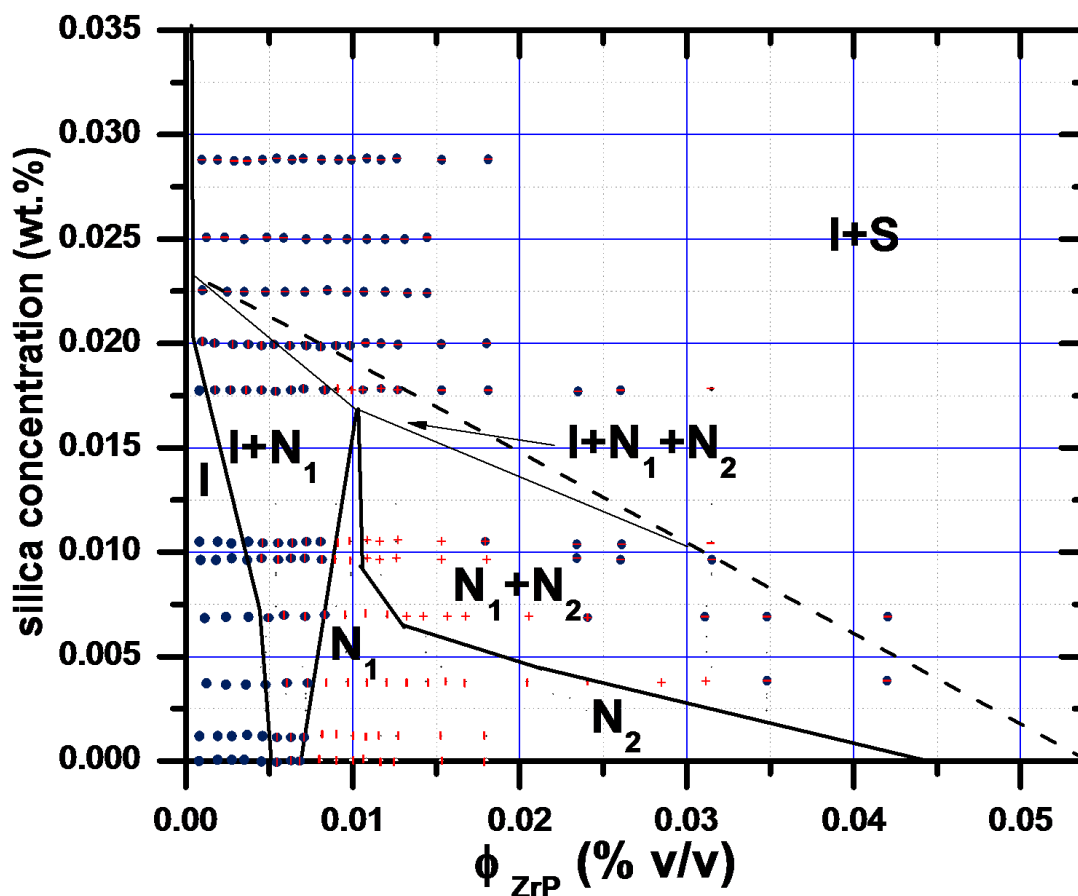


Figure 62. Phase diagram as a function of ZrP and silica concentration. Phase states include isotropic (I, blue circle), nematic-1(N_1 , red-vertical rectangle), nematic-2(N_2 , red-horizontal rectangle), and smectic (S).

In summary, we are studying the experimental phase diagram of suspensions containing ZrP nano-sheets and silica spheres. The phase diagram shows the enriching of liquid crystalline phases at different ZrP nano-sheet and silica sphere concentrations. As predicted by Lekkerkerker *et al.*,⁵⁷³, the N_1 - N_2 coexistence is originated from a

competition among translational and orientational entropy (favoring mixed state) and excluded volume entropy (favoring demixing).⁵⁷³ N_1 is a phase characterized of smaller liquid crystal domains in contrast to N_2 , which is a birefringent closed-packed phase. The understanding of the depletion attraction forces in colloidal suspensions are of technological interest, not only for colloid science but also for industrial systems, such as food dispersions and the paint industry.

5.2.2 Phase Behavior and Self-assembly of Wax Disks and SDS Micelles

There is a need in the literature of methodologies to create 3D structures on the colloidal scale. A typical approach consists in forming structures of discotic particles by varying the concentration in the bulk. Low aspect ratio wax disks (~4 to 5) are of great interest due to their self-assembly into a great variety of structures. However, wax disks made of α -eicosene possess low thermal and mechanical stability due to the low melting temperature of the wax ($T_m \sim 26-28$ °C) and disk concentration cannot be controlled (**Table 9**). To solve this issue, we fabricated uniform alkane (nonadecane, a wax) emulsions by electrospraying melted nonadecane at 60 °C and collecting the emulsions in 10mM sodium dodecyl sulfate (SDS) solution producing micron-sized emulsions. The emulsions were cooled down to room temperature and kept at 4 °C in a refrigerator. Once the wax disk colloids are solidified, the suspension was left at room temperature, and visualized through confocal microscopy (**Figure 63a,b**).

Table 9. Melting temperature (T_m) and rotator phase range of different waxes

Wax	T_m ($^{\circ}\text{C}$)	Rotator phase range
α -Eicosene	26	$3\text{ }^{\circ}\text{C} < T < 22\text{ }^{\circ}\text{C}$
n-Nonadecane	32	$20\text{ }^{\circ}\text{C} < T < 31\text{ }^{\circ}\text{C}$

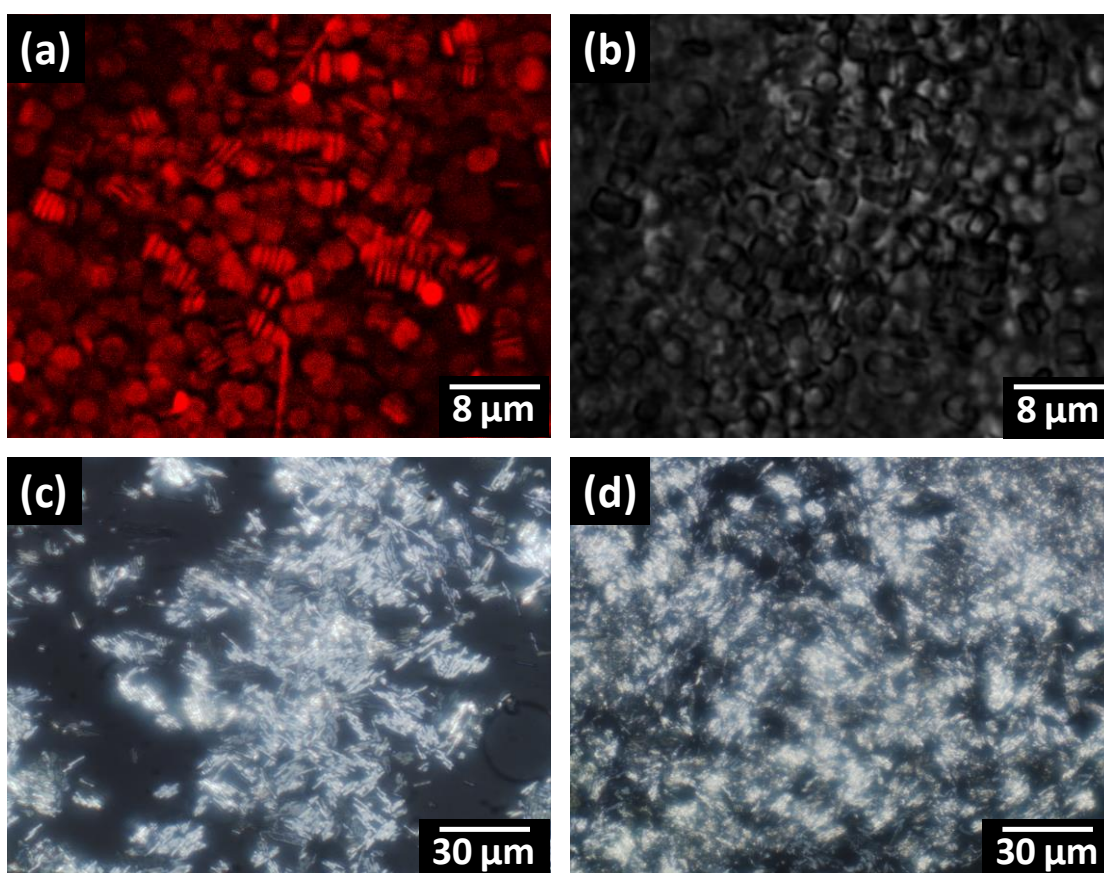


Figure 63. Nonadecane wax disks. (a) Confocal micrographs. Wax disks coated with Nile red. Magnification 100x. (b) Confocal reflective image at the same position as (a). (c, d) Self-assembling of wax disks in an evaporating droplet observed under cross-polarizing microscopy. Magnification 20x.

Alkanes go through surface freezing that their surfaces crystallize at temperature right above their bulk melting temperature. At the melting temperature of nonadecane ($T_m \sim 32 \text{ }^\circ\text{C}$), surface freezing created a crystalline monolayer around our wax droplets that would act as the nuclei of the rotator phase as temperature decreased. Then rotator phase grew from the surface towards the center, fabricating the disks. Since n-nonadecane rotator phase is present in a temperature range between 20 and 31 $^\circ\text{C}$ (Table 9), therefore, these novel wax disks can be manipulated at room temperature (23 $^\circ\text{C}$). Figure 63c,d show the self-assembly of n-nonadecane wax disks by introducing inter-particle depletion interactions via SDS micelles and increasing the wax disk concentration through solvent evaporation.

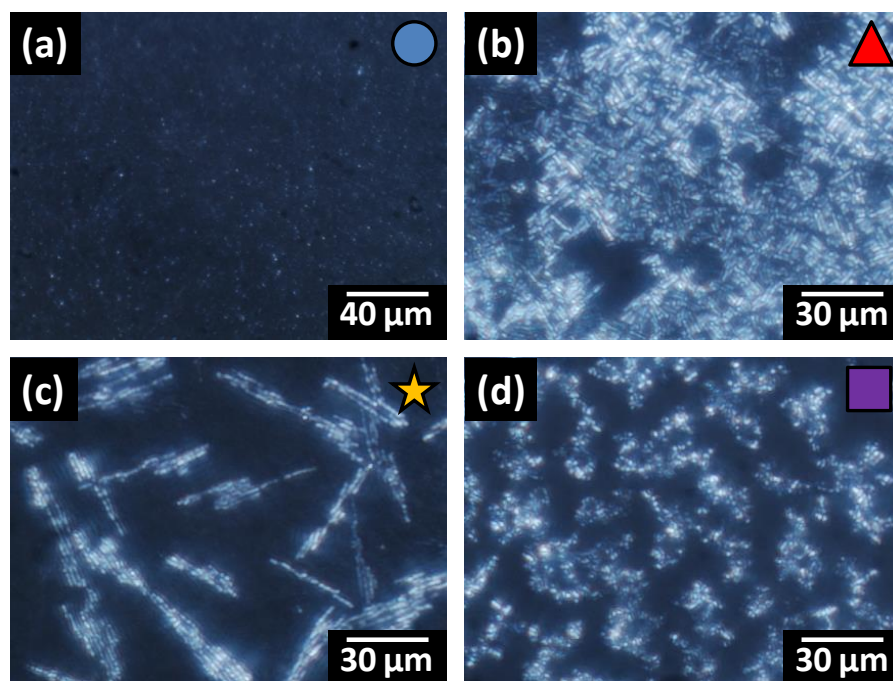


Figure 64. Different states observed for nonadecane wax disks of aspect ratio around 5. Isotropic (blue circle), short rods (red triangle), long rods (yellow star), and random aggregations (purple square).

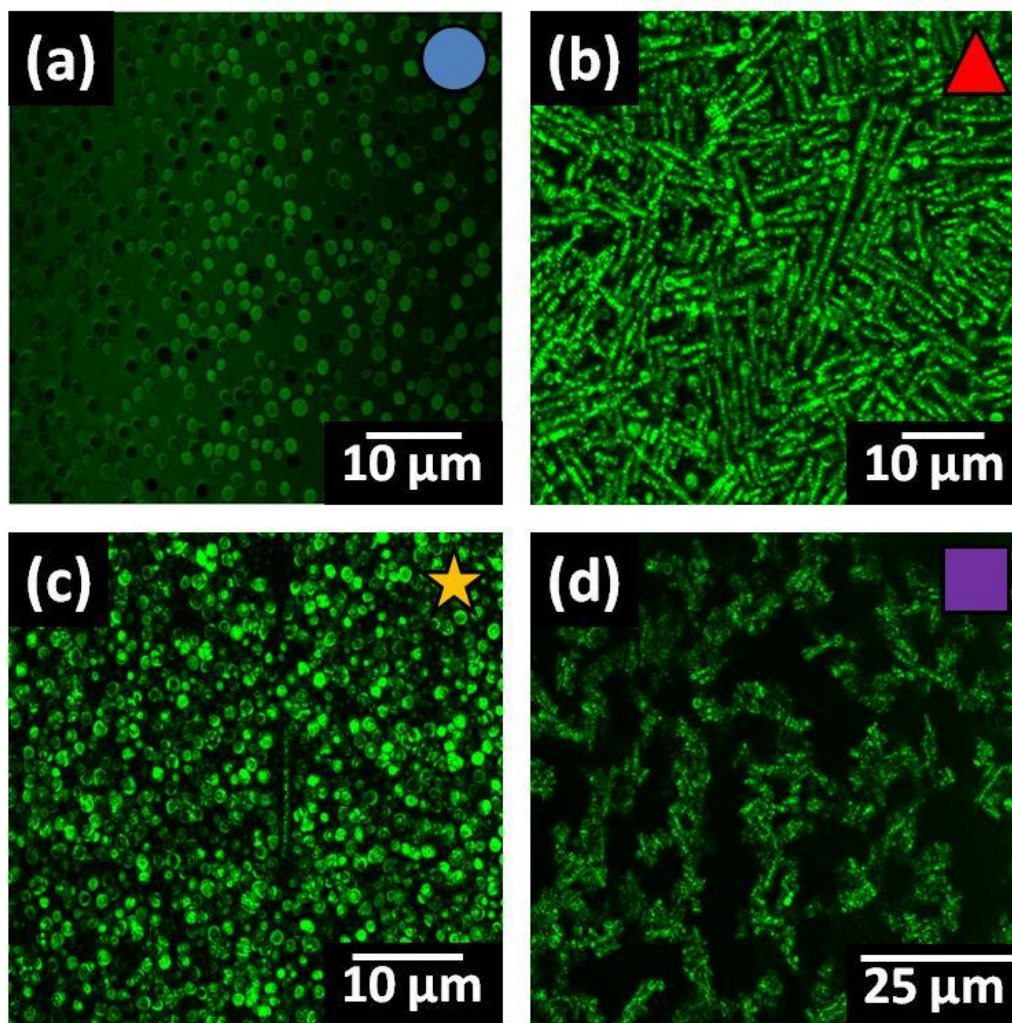


Figure 65. Different states observed for nonadecane wax disks of aspect ratio around 5. Isotropic (blue circle), short rods (red triangle), long rods (yellow star), and random aggregations (purple square).

We are systematically studying the phase behavior and the self-assembly of the n-nonadecane wax disks. The wax disks were coated with Nile red. Subsequently, tube dialysis was performed to remove excess of SDS micelles and Nile red. The wax disk concentration in the suspension was increased via filtration and creaming. In our experiments, we obtained wax disk concentrations of 1, 3, 6, 13, 16, 24, and 30 %w/w.

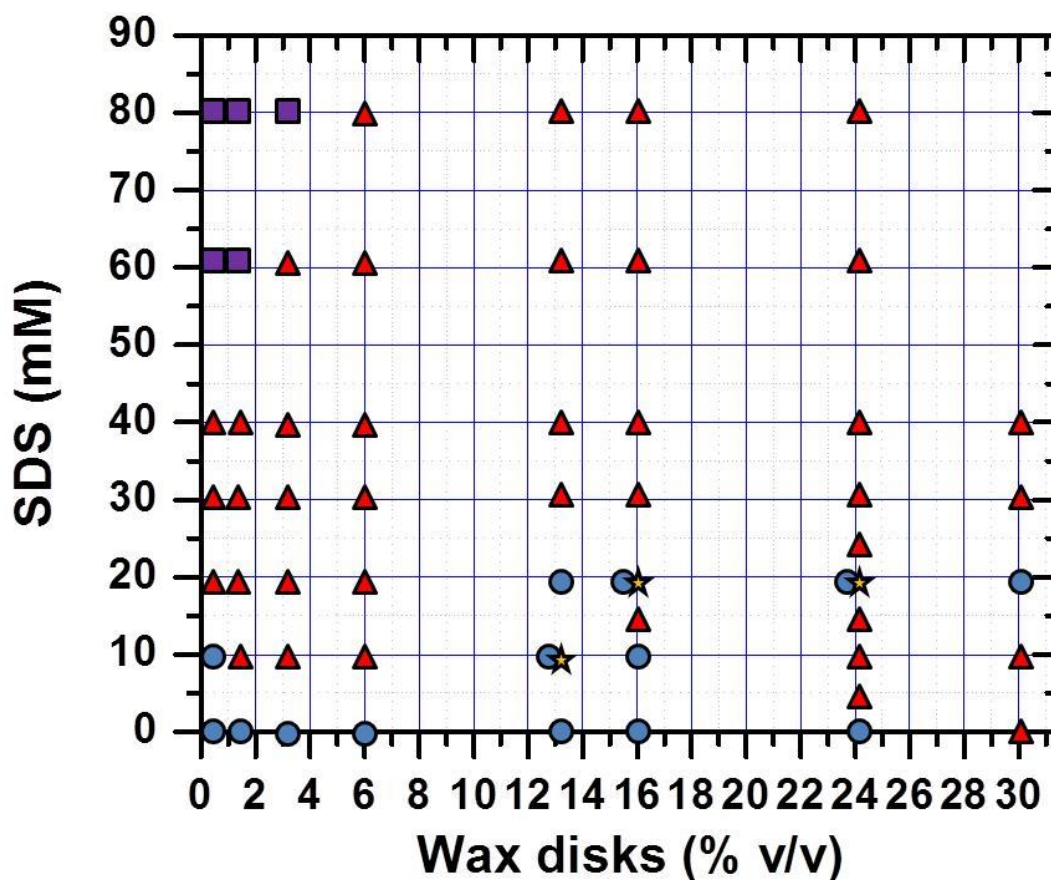


Figure 66. Selective interaction tuned with depletion attraction from SDS micelles. Diagram of the different states observed in suspensions of wax disks of aspect ratio around 4, at various concentrations of SDS. We identified states such as isotropic (blue circle), short rods (red triangle), long rods (yellow star), and random aggregations (purple square).

The wax disks suspensions were enclosed inside flat glass capillaries at varying SDS concentrations. Finally, we observed the dispersions by optical microscopy coupled with crossed polarizers to identify characteristic structural states of the liquid crystalline phases as a function of the wax disk and depletant concentrations as shown in **Figure 64(a-d)**. Interestingly, at various wax disk and SDS micelle concentration, we observed isotropic (blue circle, ●), short rods (red triangle, ▲), long rods (yellow star, ★), and

random aggregations (purple square, ■). **Figure 65** shows micrographs using confocal microscopy.

To sum, we observed self-assembled high aspect ratio stacks of disks, which implies that the face-to-face interactions are stronger than side-to-side interactions. A state diagram is shown in **Figure 66**, where summarizes the observed states at varying wax disk and SDS micelle concentrations. Our method of controlling depletion interactions offers the possibility to overcome the outstanding challenges of 3D assembly in the micrometer scale, such as the formation of the discotic columnar and cubic phases.

REFERENCES

1. S. C. Glotzer and M. J. Solomon, *Nature Materials*, 2007, **6**, 557-562.
2. W. G. Hoover and F. H. Ree, *J. Chem. Phys.*, 1968, **49**, 3609-3617.
3. S. C. McGrother, D. C. Williamson and G. Jackson, *J. Chem. Phys.*, 1996, **104**, 6755-6771.
4. G. J. Vroege and H. N. W. Lekkerkerker, *Rep. Prog. Phys.*, 1992, **55**, 1241-1309.
5. I. Langmuir, *J. Chem. Phys.*, 1938, **6**, 873-896.
6. L. Onsager, *Ann. NY. Acad. Sci.*, 1949, **51**, 627-659.
7. P. A. Forsyth, S. Marcelja, D. J. Mitchell and B. W. Ninham, *J. Chem. Soc. Farad. T2.*, 1977, **73**, 84-88.
8. J. J. Hao, K. V. Subbarao and J. M. Duniway, *Phytopathology*, 2003, **93**, 443-450.
9. M. Moan, *Physical chemistry of colloids and interfaces in oil production*, Institute Francais Du Petrole, Reuil, Paris, 1992.
10. E. S. Boek, P. V. Coveney, H. N. W. Lekkerkerker and P. vanderSchoot, *Phys. Rev. E.*, 1997, **55**, 3124-3133.
11. S. Priyanto, G. A. Mansoori and A. Suwono, *Chemical Engineering Science*, 2001, **56**, 6933-6939.
12. M. D. Lobato, J. M. Pedrosa, A. R. Hortal, B. Martínez-Haya, R. Lebrón-Aguilar and S. Lago, *Colloid. Surface. A.*, 2007, **298**, 72-79.
13. J. Bednar, R. A. Horowitz, S. A. Grigoryev, L. M. Carruthers, J. C. Hansen, A. J. Koster and C. L. Woodcock, *Proc. Natl. Acad. Sci. U. S. A.*, 1998, **95**, 14173-14178.
14. M. Stefanini, W. Dameshek, J. B. Chatterjea, E. Adelson and I. B. Mednicoff, *Blood*, 1953, **8**, 26-64.
15. F. M. van der Kooij, K. Kassapidou and H. N. W. Lekkerkerker, *Nature*, 2000, **406**, 868-871.
16. F. M. van der Kooij and H. N. W. Lekkerkerker, *Journal of Physical Chemistry B*, 1998, **102**, 7829-7832.

17. A. V. Petukhov, D. van der Beek, R. P. A. Dullens, I. P. Dolbnya, G. J. Vroege and H. N. W. Lekkerkerker, *Physical Review Letters*, 2005, **95**, 077801.
18. M. Morvan, D. Espinat, J. Lambard and T. Zemb, *Colloids and Surfaces a-Physicochemical and Engineering Aspects*, 1994, **82**, 193-203.
19. L. M. Zhang, C. Jahns, B. S. Hsiao and B. Chu, *Journal of Colloid and Interface Science*, 2003, **266**, 339-345.
20. J. C. Baird and J. Y. Walz, *Journal of Colloid and Interface Science*, 2006, **297**, 161-169.
21. L. J. Michot, I. Bihannic, S. Maddi, S. S. Funari, C. Baravian, P. Levitz and P. Davidson, *Proc. Natl. Acad. Sci. U. S. A.*, 2006, **103**, 16101-16104.
22. T. Nicolai and S. Cocard, *Journal of Colloid and Interface Science*, 2001, **244**, 51-57.
23. P. Mongondry, J. F. Tassin and T. Nicolai, *Journal of Colloid and Interface Science*, 2005, **283**, 397-405.
24. J. O. Fossum, *Physica A*, 1999, **270**, 270-277.
25. L. Y. Sun, W. J. Boo, D. H. Sun, A. Clearfield and H. J. Sue, *Chemistry of Materials*, 2007, **19**, 1749-1754.
26. A. E. Saunders, A. Ghezelbash, D. M. Smilgies, M. B. Sigman and B. A. Korgel, *Nano Letters*, 2006, **6**, 2959-2963.
27. H. M. Birch, *Nature*, 2007, **446**, 940-940.
28. C. J. Hernandez and T. G. Mason, *J. Phys. Chem. C*, 2007, **111**, 4477-4480.
29. S. Badaire, C. Cottin-Bizonne, J. W. Woody, A. Yang and A. D. Stroock, *J. Am. Chem. Soc.*, 2007, **129**, 40-41.
30. H. A. Baghdadi, H. Sardinha and S. R. Bhatia, *Journal Of Polymer Science Part B-polymer Physics*, 2005, **43**, 233-240.
31. A. Knaebel, M. Bellour, J. P. Munch, V. Viasnoff, F. Lequeux and J. L. Harden, *Europhysics Letters*, 2000, **52**, 73-79.
32. J. O. Fossum, H. H. Bergene, A. Hansen, B. O'Rourke and G. Manificat, *Phys. Rev. E.*, 2004, **69**, 036108.

33. N. B. Wilding, P. Sollich, M. Fasolo and M. Buzzacchi, *J. Chem. Phys.*, 2006, **125**, 01490.
34. M. Adams and S. Fraden, *Biophysical Journal*, 1998, **74**, 669-677.
35. N. Urakami and M. Imai, *J. Chem. Phys.*, 2003, **119**, 2463-2470.
36. M. Fasolo and P. Sollich, *J. Chem. Phys.*, 2005, **122**, 074904.
37. P. Sollich, *Journal Of Physics-condensed Matter*, 2002, **14**, R79-R117.
38. V. Germain and M. P. Pileni, *Advanced Materials*, 2005, **17**, 1424-1429.
39. D. A. Kofke and P. G. Bolhuis, *Phys. Rev. E.*, 1999, **59**, 618-622.
40. H. H. Wensink and G. J. Vroege, *J. Chem. Phys.*, 2003, **119**, 6868-6882.
41. N. Clarke, J. A. Cuesta, R. Sear, P. Sollich and A. Speranza, *J. Chem. Phys.*, 2000, **113**, 5817-5829.
42. F. M. van der Kooij, D. van der Beek and H. N. W. Lekkerkerker, *Journal of Physical Chemistry B*, 2001, **105**, 1696-1700.
43. J. A. C. Veerman and D. Frenkel, *Physical Review A*, 1990, **41**, 3237-3244.
44. M. A. Bates and D. Frenkel, *J. Chem. Phys.*, 1998, **109**, 6193-6199.
45. T. G. Mason, *Phys. Rev. E.*, 2002, **66**, 060402.
46. Z. Cheng, P. M. Chaikin and T. G. Mason, *Physical Review Letters*, 2002, **89**, 108303.
47. A. F. Mejia, P. He, D. Luo, M. Marquez and Z. Cheng, *J. Colloid Interface Sci.*, 2009, **334**, 22-28.
48. A. F. Mejia, P. He, M. Netemeyer, D. W. Luo, M. Marquez and Z. D. Cheng, *Soft Matter*, 2010, **6**, 4885-4894.
49. S. Badaire, C. Cottin-Bizonne and A. D. Stroock, *Langmuir*, 2008, **24**, 11451-11463.
50. J. H. Moon, A. J. Kim, J. C. Crocker and S. Yang, *Advanced Materials*, 2007, **19**, 2508-2512.
51. K. Zhao and T. G. Mason, *Phys. Rev. Lett.*, 2007, **99**, 4.

52. D. Dendukuri, S. S. Gu, D. C. Pregibon, T. A. Hatton and P. S. Doyle, *Lab on a Chip*, 2007, **7**, 818-828.
53. D. Dendukuri, D. C. Pregibon, J. Collins, T. A. Hatton and P. S. Doyle, *Nature Materials*, 2006, **5**, 365-369.
54. T. J. Merkel, K. P. Herlihy, J. Nunes, R. M. Orgel, J. P. Rolland and J. M. DeSimone, *Langmuir*, 2009, **26**, 13086-13096.
55. T. J. Merkel, S. W. Jones, K. P. Herlihy, F. R. Kersey, A. R. Shields, M. Napier, J. C. Luft, H. L. Wu, W. C. Zamboni, A. Z. Wang, J. E. Bear and J. M. DeSimone, *Proc. Natl. Acad. Sci. U. S. A.*, 2011, **108**, 586-591.
56. J. P. Rolland, B. W. Maynor, L. E. Euliss, A. E. Exner, G. M. Denison and J. M. DeSimone, *J. Am. Chem. Soc.*, 2005, **127**, 10096-10100.
57. B. G. Wang, H. C. Shum and D. A. Weitz, *ChemPhysChem*, 2009, **10**, 641-645.
58. C. H. Park, N. O. Chung and J. Lee, *Journal of Colloid and Interface Science*, 2011, **361**, 423-428.
59. M. Okubo, T. Fujibayashi and A. Terada, *Colloid and Polymer Science*, 2005, **283**, 793-798.
60. C. H. M. Weber, A. Chiche, G. Krausch, S. Rosenfeldt, M. Ballauff, L. Harnau, I. Göttker-Schnetmann, Q. Tong and S. Mecking, *Nano Letters*, 2007, **7**, 2024-2029.
61. Y. N. Xia, Y. J. Xiong, B. Lim and S. E. Skrabalak, *Angew. Chem.-Int. Edit.*, 2009, **48**, 60-103.
62. A. M. Wierenga, T. A. J. Lenstra and A. P. Philipse, *Colloids and Surfaces A: Physicochemical and Engineering Aspects*, 1998, **134**, 359-371.
63. A. B. D. Brown, S. M. Clarke and A. R. Rennie, *Langmuir*, 1998, **14**, 3129-3132.
64. A. B. D. Brown, C. Ferrero, T. Narayanan and A. R. Rennie, *Eur. Phys. J. B*, 1999, **11**, 481-489.
65. L. Durand-Keklikian, I. Haq and E. Matijević, *Colloids and Surfaces A: Physicochemical and Engineering Aspects*, 1994, **92**, 267-275.
66. V. F. Puentes, D. Zanchet, C. K. Erdonmez and A. P. Alivisatos, *J. Am. Chem. Soc.*, 2002, **124**, 12874-12880.

67. G. D. Zhang, X. Chen, J. K. Zhao, Y. C. Chai, W. C. Zhuang and L. Y. Wang, *Mater. Lett.*, 2006, **60**, 2889-2892.
68. Y. W. Zhang, X. Sun, R. Si, L. P. You and C. H. Yan, *J. Am. Chem. Soc.*, 2005, **127**, 3260-3261.
69. M. B. Sigman, A. Ghezelbash, T. Hanrath, A. E. Saunders, F. Lee and B. A. Korgel, *J. Am. Chem. Soc.*, 2003, **125**, 16050-16057.
70. A. Ghezelbash and B. A. Korgel, *Langmuir*, 2005, **21**, 9451-9456.
71. K. H. Park, K. Jang and S. U. Son, *Angew. Chem.-Int. Edit.*, 2006, **45**, 4608-4612.
72. S. Ithurria, M. D. Tessier, B. Mahler, R. Lobo, B. Dubertret and A. Efros, *Nature Materials*, 2011, **10**, 936-941.
73. C. Vonk, S. M. Oversteegen and J. Wijnhoven, *Journal of Colloid and Interface Science*, 2005, **287**, 521-525.
74. J. Wijnhoven, *Chemistry of Materials*, 2004, **16**, 3821-3828.
75. J. Wijnhoven, *Journal of Colloid and Interface Science*, 2005, **292**, 403-409.
76. E. Balnois, S. Durand-Vidal and P. Levitz, *Langmuir*, 2003, **19**, 6633-6637.
77. W. J. Boo, L. Sun, J. Liu, A. Clearfield and H.-J. Sue, *J. Phys. Chem. C*, 2007, **111**, 10377-10381.
78. L. Y. Sun, W. J. Boo, H. J. Sue and A. Clearfield, *New J. Chem.*, 2007, **31**, 39-43.
79. A. Clearfield and G. D. Smith, *Inorg. Chem.*, 1969, **8**, 431-436.
80. A. F. Mejia, Y.-W. Chang, R. Ng, M. Shuai, M. S. Mannan and Z. Cheng, *Phys. Rev. E.*, 2012, **85**, 061708.
81. S. W. Keller, H. N. Kim and T. E. Mallouk, *J. Am. Chem. Soc.*, 1994, **116**, 8817-8818.
82. D. M. Kaschak, J. T. Lean, C. C. Waraksa, G. B. Saupe, H. Usami and T. E. Mallouk, *J. Am. Chem. Soc.*, 1999, **121**, 3435-3445.
83. M. M. J. Treacy, S. B. Rice, A. J. Jacobson and J. T. Lewandowski, *Chemistry of Materials*, 1990, **2**, 279-286.

84. T. Sasaki, M. Watanabe, H. Hashizume, H. Yamada and H. Nakazawa, *J. Am. Chem. Soc.*, 1996, **118**, 8329-8335.
85. T. Sasaki and M. Watanabe, *J. Am. Chem. Soc.*, 1998, **120**, 4682-4689.
86. T. Sasaki, S. Nakano, S. Yamauchi and M. Watanabe, *Chemistry of Materials*, 1997, **9**, 602-608.
87. S. Park and R. S. Ruoff, *Nat Nano*, 2009, **4**, 217-224.
88. A. A. Marti and J. L. Colon, *Inorg. Chem.*, 2003, **42**, 2830-2832.
89. H. N. Kim, S. W. Keller, T. E. Mallouk, J. Schmitt and G. Decher, *Chemistry of Materials*, 1997, **9**, 1414-1421.
90. D. M. Kaschak, S. A. Johnson, D. E. Hooks, H. N. Kim, M. D. Ward and T. E. Mallouk, *J. Am. Chem. Soc.*, 1998, **120**, 10887-10894.
91. Y.-W. Chang, A. F. Mejia, Z. Cheng, X. Di and G. B. McKenna, *Physical Review Letters*, 2012, **108**, 247802.
92. M. Adachi-Pagano, C. Forano and J. P. Besse, *Chem. Commun.*, 2000, 91-92.
93. G. B. Saupe, C. C. Waraksa, H. N. Kim, Y. J. Han, D. M. Kaschak, D. M. Skinner and T. E. Mallouk, *Chemistry of Materials*, 2000, **12**, 1556-1562.
94. R. Abe, M. Hara, J. N. Kondo, K. Domen, K. Shinohara and A. Tanaka, *Chemistry of Materials*, 1998, **10**, 1647-1651.
95. R. Abe, K. Shinohara, A. Tanaka, M. Hara, J. N. Kondo and K. Domen, *Chemistry of Materials*, 1997, **9**, 2179-2184.
96. R. E. Schaak and T. E. Mallouk, *Chemistry of Materials*, 2000, **12**, 3427-3434.
97. N. Miyamoto, H. Yamamoto, R. Kaito and K. Kuroda, *Chem. Commun.*, 2002, **20**, 2378-2379.
98. F. E. Osterloh, *J. Am. Chem. Soc.*, 2002, **124**, 6248-6249.
99. G. Alberti, M. Casciola and U. Costantino, *Journal of Colloid and Interface Science*, 1985, **107**, 256-263.
100. H.-N. Kim, S. W. Keller, T. E. Mallouk, J. Schmitt and G. Decher, *Chemistry of Materials*, 1997, **9**, 1414-1421.

101. J. C. P. Gabriel, F. Camerel, B. J. Lemaire, H. Desvaux, P. Davidson and P. Batail, *Nature*, 2001, **413**, 504-508.
102. P. Joensen, R. F. Frindt and S. R. Morrison, *Mater. Res. Bull.*, 1986, **21**, 457-461.
103. H. S. S. Ramakrishna Matte, A. Gomathi, A. K. Manna, D. J. Late, R. Datta, S. K. Pati and C. N. R. Rao, *Angewandte Chemie International Edition*, 2010, **49**, 4059-4062.
104. J. N. Coleman, M. Lotya, A. O'Neill, S. D. Bergin, P. J. King, U. Khan, K. Young, A. Gaucher, S. De, R. J. Smith, I. V. Shvets, S. K. Arora, G. Stanton, H. Y. Kim, K. Lee, G. T. Kim, G. S. Duesberg, T. Hallam, J. J. Boland, J. J. Wang, J. F. Donegan, J. C. Grunlan, G. Moriarty, A. Shmeliov, R. J. Nicholls, J. M. Perkins, E. M. Grievson, K. Theuwissen, D. W. McComb, P. D. Nellist and V. Nicolosi, *Science*, 2011, **331**, 568-571.
105. J. Dau and G. Lagaly, *Croat. Chem. Acta*, 1998, **71**, 983-1004.
106. E. P. Giannelis, *Advanced Materials*, 1996, **8**, 2935.
107. A. Usuki, N. Hasegawa and M. Kato, in *Inorganic Polymeric Nanocomposites and Membranes*, Springer-Verlag, Berlin, 2005, vol. 179, pp. 135-195.
108. M. W. Weimer, H. Chen, E. P. Giannelis and D. Y. Sogah, *J. Am. Chem. Soc.*, 1999, **121**, 1615-1616.
109. H. J. Sue, K. T. Gam, N. Bestaoui, N. Spurr and A. Clearfield, *Chemistry of Materials*, 2003, **16**, 242-249.
110. J. M. Troup and A. Clearfield, *Inorg. Chem.*, 1977, **16**, 3311-3314.
111. M. Shuai, A. F. Mejia, Y.-W. Chang and Z. Cheng, *CrystEngComm*, 2013, 1970-1977.
112. Z. P. Xu, G. Stevenson, C.-Q. Lu and G. Q. Lu, *Journal of Physical Chemistry B*, 2006, **110**, 16923-16929.
113. K. S. Novoselov, A. K. Geim, S. V. Morozov, D. Jiang, Y. Zhang, S. V. Dubonos, I. V. Grigorieva and A. A. Firsov, *Science*, 2004, **306**, 666-669.
114. K. S. Novoselov, D. Jiang, F. Schedin, T. J. Booth, V. V. Khotkevich, S. V. Morozov and A. K. Geim, *Proc. Natl. Acad. Sci. U. S. A.*, 2005, **102**, 10451-10453.
115. N. Behabtu, J. R. Lomeda, M. J. Green, A. L. Higginbotham, A. Sinitskii, D. V. Kosynkin, D. Tsentelovich, A. N. G. Parra-Vasquez, J. Schmidt, E. Kesselman,

- Y. Cohen, Y. Talmon, J. M. Tour and M. Pasquali, *Nature Nanotechnology*, 2010, **5**, 406-411.
116. B. Dan, N. Behabtu, A. Martinez, J. S. Evans, D. V. Kosynkin, J. M. Tour, M. Pasquali and I. I. Smalyukh, *Soft Matter*, 2011, **7**, 11154-11159.
117. Z. Xu and C. Gao, *Acs Nano*, 2011, **5**, 2908-2915.
118. Z. Xu and C. Gao, *Nature Communications*, 2011, **2**.
119. P. N. Pusey and W. Vanmegen, *Nature*, 1986, **320**, 340-342.
120. D. Frenkel, *Statistical Mechanics of Liquid Crystals*, North-Holland, Amsterdam, 1991.
121. W. C. K. Poon and P. N. Pusey, in *Observation, Prediction and Simulation of Phase Transitions in Complex Fluids*, eds. M. Baus, L. F. Rull and J. P. Ryckaert, 1995, vol. 460, pp. 3-51.
122. P. Davidson and J. C. P. Gabriel, *Curr. Opin. Colloid Interface Sci.*, 2005, **9**, 377-383.
123. Y. Min, M. Akbulut, K. Kristiansen, Y. Golan and J. Israelachvili, *Nature Materials*, 2008, **7**, 527-538.
124. M. Adams, Z. Dogic, S. L. Keller and S. Fraden, *Nature*, 1998, **393**, 349-352.
125. E. Barry and Z. Dogic, *Proc. Natl. Acad. Sci. U. S. A.*, 2010, **107**, 10348-10353.
126. L. Rossi, S. Sacanna, W. T. M. Irvine, P. M. Chaikin, D. J. Pine and A. P. Philipse, *Soft Matter*, 2011, **7**, 4139-4142.
127. E. V. Shevchenko, D. V. Talapin, N. A. Kotov, S. O'Brien and C. B. Murray, *Nature*, 2006, **439**, 55-59.
128. K. Miszta, J. de Graaf, G. Bertoni, D. Dorfs, R. Brescia, S. Marras, L. Ceseracciu, R. Cingolani, R. van Roij, M. Dijkstra and L. Manna, *Nature Materials*, 2011, **10**, 872-876.
129. M. E. Leunissen, C. G. Christova, A. P. Hynninen, C. P. Royall, A. I. Campbell, A. Imhof, M. Dijkstra, R. van Roij and A. van Blaaderen, *Nature*, 2005, **437**, 235-240.
130. J. Lahiri, L. Isaacs, B. Grzybowski, J. D. Carbeck and G. M. Whitesides, *Langmuir*, 1999, **15**, 7186-7198.

131. A. M. Kalsin, M. Fialkowski, M. Paszewski, S. K. Smoukov, K. J. M. Bishop and B. A. Grzybowski, *Science*, 2006, **312**, 420-424.
132. S. Sacanna, W. T. M. Irvine, P. M. Chaikin and D. J. Pine, *Nature*, 2010, **464**, 575-578.
133. A. P. Alivisatos, K. P. Johnsson, X. G. Peng, T. E. Wilson, C. J. Loweth, M. P. Bruchez and P. G. Schultz, *Nature*, 1996, **382**, 609-611.
134. G. P. Mitchell, C. A. Mirkin and R. L. Letsinger, *J. Am. Chem. Soc.*, 1999, **121**, 8122-8123.
135. M. R. Jones, R. J. Macfarlane, B. Lee, J. Zhang, K. L. Young, A. J. Senesi and C. A. Mirkin, *Nature Materials*, 2010, **9**, 913-917.
136. R. J. Macfarlane, B. Lee, M. R. Jones, N. Harris, G. C. Schatz and C. A. Mirkin, *Science*, 2011, **334**, 204-208.
137. H. H. Wensink and H. N. W. Lekkerkerker, *Molecular Physics*, 2009, **107**, 2111-2118.
138. S. D. Peroukidis, A. G. Vanakaras and D. J. Photinos, *Journal of Materials Chemistry*, 2010, **20**, 10495-10502.
139. J. A. C. Veerman and D. Frenkel, *Physical Review A*, 1992, **45**, 5632-5648.
140. D. Frenkel and R. Eppenga, *Physical Review Letters*, 1982, **49**, 1089-1092.
141. L. Harnau, *Molecular Physics*, 2008, **106**, 1975-2000.
142. D. L. Cheung, L. Anton, M. P. Allen, A. J. Masters, J. Phillips and M. Schmidt, *Phys. Rev. E.*, 2008, **78**, 041201.
143. D. Costa, J. P. Hansen and L. Harnau, *Molecular Physics*, 2005, **103**, 1917-1927.
144. L. Harnau, D. Costa and J. P. Hansen, *Europhysics Letters*, 2001, **53**, 729-734.
145. A. Esztermann, H. Reich and M. Schmidt, *Phys. Rev. E.*, 2006, **73**, 011409.
146. L. Harnau, D. Rowan and J. P. Hansen, *J. Chem. Phys.*, 2002, **117**, 11359-11365.
147. H. Hansen-Goos and K. Mecke, *Physical Review Letters*, 2009, **102**, 018302.
148. A. J. Masters, *Journal Of Physics-condensed Matter*, 2008, **20**, 283102.

149. P. D. Duncan, M. Dennison, A. J. Masters and M. R. Wilson, *Phys. Rev. E.*, 2009, **79**, 031702.
150. X. M. You, A. Y. Vlasov and A. J. Masters, *J. Chem. Phys.*, 2005, **123**, 034510.
151. K. L. Savithramma and N. V. Madhusudana, *Molecular Crystals and Liquid Crystals*, 1981, **74**, 243-259.
152. S. D. Lee, *J. Chem. Phys.*, 1987, **87**, 4972-4974.
153. S. D. Lee, *J. Chem. Phys.*, 1988, **89**, 7036-7037.
154. J. D. Parsons, *Physical Review A*, 1979, **19**, 1225-1230.
155. M. Franco-Melgar, A. J. Haslam and G. Jackson, *Molecular Physics*, 2008, **106**, 649-678.
156. A. A. Verhoeff, H. H. Wensink, M. Vis, G. Jackson and H. N. W. Lekkerkerker, *Journal of Physical Chemistry B*, 2009, **113**, 13476-13484.
157. M. M. Pineiro, A. Galindo and A. O. Parry, *Soft Matter*, 2007, **3**, 768-778.
158. R. P. S. Fartaria and M. B. Sweatman, *Chem. Phys. Lett.*, 2009, **478**, 150-154.
159. A. Cuetos and B. Martinez-Haya, *J. Chem. Phys.*, 2008, **129**, 214706.
160. M. Marechal, A. Cuetos, B. Martinez-Haya and M. Dijkstra, *J. Chem. Phys.*, 2011, **134**, 094501.
161. H. N. W. Lekkerkerker, P. Coulon, R. Vanderhaegen and R. Deblieck, *J. Chem. Phys.*, 1984, **80**, 3427-3433.
162. S. D. Zhang, P. A. Reynolds and J. S. van Duijneveldt, *J. Chem. Phys.*, 2002, **117**, 9947-9958.
163. D. van der Beek, T. Schilling and H. N. W. Lekkerkerker, *J. Chem. Phys.*, 2004, **121**, 5423-5426.
164. M. A. Bates and D. Frenkel, *Phys. Rev. E.*, 1998, **57**, 4824-4826.
165. L. Wu, H. H. Wensink, G. Jackson and E. A. Mueller, *Molecular Physics*, 2012, **110**, 1269-1288.
166. Y. Martinez-Raton and E. Velasco, *J. Chem. Phys.*, 2011, **134**, 124904.
167. Y. Martinez-Raton and E. Velasco, *J. Chem. Phys.*, 2012, **137**, 134906.

168. D. Sun, H.-J. Sue, Z. Cheng, Y. Martinez-Raton and E. Velasco, *Phys. Rev. E.*, 2009, **80**, 041704.
169. P.-F. Lenne and A. Nicolas, *Soft Matter*, 2009, **5**, 2841-2848.
170. F. Sciortino and E. Zaccarelli, *Current Opinion in Solid State and Materials Science*, 2011, **15**, 246-253.
171. M. A. Bates and G. R. Luckhurst, *J. Chem. Phys.*, 1996, **104**, 6696-6709.
172. D. Chakrabarti and D. J. Wales, *Physical Review Letters*, 2008, **100**, 127801.
173. E. M. del Rio, A. Galindo and E. de Miguel, *Phys. Rev. E.*, 2005, **72**, 051707.
174. D. Frenkel, B. M. Mulder and J. P. McTague, *Physical Review Letters*, 1984, **52**, 287-290.
175. J. L. Lebowitz and J. W. Perram, *Molecular Physics*, 1983, **50**, 1207-1214.
176. B. Martinez-Haya and A. Cuetos, *J. Chem. Phys.*, 2009, **131**, 074901.
177. B. Martinez-Haya and A. Cuetos, *Mol. Simul.*, 2009, **35**, 1077-1083.
178. A. Chamoux and A. Perera, *J. Chem. Phys.*, 1998, **108**, 8172-8181.
179. B. Martinez-Haya and A. Cuetos, *Phys. Rev. E.*, 2010, **81**, 020701
180. M. A. Bates, *J. Chem. Phys.*, 1999, **111**, 1732-1736.
181. L. Morales-Anda, H. H. Wensink, A. Galindo and A. Gil-Villegas, *J. Chem. Phys.*, 2012, **136**, 034901.
182. L. Filion, M. Marechal, B. van Oorschot, D. Pelt, F. Smalenburg and M. Dijkstra, *Physical Review Letters*, 2009, **103**, 188302.
183. R. Blaak, D. Frenkel and B. M. Mulder, *J. Chem. Phys.*, 1999, **110**, 11652-11659.
184. S. J. S. Qazi, G. Karlsson and A. R. Rennie, *Journal of Colloid and Interface Science*, 2010, **348**, 80-84.
185. P. D. Duncan, A. J. Masters and M. R. Wilson, *Phys. Rev. E.*, 2011, **84**, 011702.
186. M. Marechal, A. Patti, M. Dennison and M. Dijkstra, *Physical Review Letters*, 2012, **108**, 206101.

187. A. Mourchid, A. Delville, J. Lambard, E. LeColier and P. Levitz, *Langmuir*, 1995, **11**, 1942-1950.
188. J.-C. P. Gabriel, C. Sanchez and P. Davidson, *J. Phys. Chem.*, 1996, **100**, 11139-11143.
189. B. J. Lemaire, P. Panine, J. C. P. Gabriel and P. Davidson, *Europhysics Letters*, 2002, **59**, 55-61.
190. I. Bihannic, L. J. Michot, B. S. Lartiges, D. Vantelon, J. Labille, F. Thomas, J. Susini, M. Salome and B. Fayard, *Langmuir*, 2001, **17**, 4144-4147.
191. F. Cousin, V. Cabuil and P. Levitz, *Langmuir*, 2002, **18**, 1466-1473.
192. H. Hemmen, N. I. Ringdal, E. N. De Azevedo, M. Engelsberg, E. L. Hansen, Y. Méheust, J. O. Fossum and K. D. Knudsen, *Langmuir*, 2009, **25**, 12507-12515.
193. D. van der Beek and H. N. W. Lekkerkerker, *Langmuir*, 2004, **20**, 8582-8586.
194. F. R. C. Chang and G. Sposito, *Journal of Colloid and Interface Science*, 1994, **163**, 19-27.
195. J. P. Hansen and E. Trizac, *Physica A*, 1997, **235**, 257-268.
196. E. Trizac, L. Bocquet, R. Agra, J. J. Weis and M. Aubouy, *Journal Of Physics-condensed Matter*, 2002, **14**, 9339-9352.
197. A. Delville, *Journal of Physical Chemistry B*, 1999, **103**, 8296-8300.
198. J. C. P. Gabriel and P. Davidson, in *Colloid Chemistry I*, Springer-Verlag Berlin, Berlin, 2003, vol. 226, pp. 119-172.
199. N. Miyamoto and T. Nakato, *Israel Journal of Chemistry*, 2012, **52**, 881-894.
200. D. van der Beek, H. Reich, P. van der Schoot, M. Dijkstra, T. Schilling, R. Vink, M. Schmidt, R. van Roij and H. Lekkerkerker, *Physical Review Letters*, 2006, **97**, 087801.
201. D. van der Beek and H. N. W. Lekkerkerker, *Europhysics Letters*, 2003, **61**, 702-707.
202. S. Y. Liu, J. Zhang, N. Wang, W. R. Liu, C. G. Zhang and D. J. Sun, *Chemistry of Materials*, 2003, **15**, 3240-3241.
203. M. C. D. Mourad, E. J. Devid, M. M. van Schooneveld, C. Vonk and H. N. W. Lekkerkerker, *Journal of Physical Chemistry B*, 2008, **112**, 10142-10152.

204. N. Miyamoto and T. Nakato, *Adv. Mater.*, 2002, **14**, 1267-1270.
205. H. H. Wensink, G. J. Vroege and H. N. W. Lekkerkerker, *Journal of Physical Chemistry B*, 2001, **105**, 10610-10618.
206. N. Miyamoto and T. Nakato, *Journal of Physical Chemistry B*, 2004, **108**, 6152-6159.
207. T. Nakato, N. Miyamoto and A. Harada, *Chem. Commun.*, 2004, 78-79.
208. T. Nakato, N. Miyamoto, A. Harada and H. Ushiki, *Langmuir*, 2003, **19**, 3157-3163.
209. S. H. Aboutalebi, M. M. Gudarzi, Q. B. Zheng and J.-K. Kim, *Advanced Functional Materials*, 2011, **21**, 2978-2988.
210. J. E. Kim, T. H. Han, S. H. Lee, J. Y. Kim, C. W. Ahn, J. M. Yun and S. O. Kim, *Angew. Chem.-Int. Edit.*, 2011, **50**, 3043-3047.
211. M. C. D. Mourad, A. V. Petukhov, G. J. Vroege and H. N. W. Lekkerkerker, *Langmuir*, 2010, **26**, 14182-14187.
212. D. van der Beek, A. V. Petukhov, S. M. Oversteegen, G. J. Vroege and H. N. W. Lekkerkerker, *European Physical Journal E*, 2005, **16**, 253-258.
213. A. B. G. M. Leferink Op Reinink, J. M. Meijer, D. Kleshchanok, D. V. Byelov, G. J. Vroege, A. V. Petukhov and H. N. W. Lekkerkerker, *Journal Of Physics-condensed Matter*, 2011, **23**, 194110.
214. A. A. Verhoeff and H. N. W. Lekkerkerker, *Soft Matter*, 2012, **8**, 4865-4868.
215. M. C. D. Mourad, D. V. Byelov, A. V. Petukhov, D. A. M. de Winter, A. J. Verkleij and H. N. W. Lekkerkerker, *Journal of Physical Chemistry B*, 2009, **113**, 11604-11613.
216. A. Speranza and P. Sollich, *J. Chem. Phys.*, 2002, **117**, 5421-5436.
217. D. Kleshchanok, P. Holmqvist, J. M. Meijer and H. N. W. Lekkerkerker, *J. Am. Chem. Soc.*, 2012, **134**, 5985-5990.
218. D. Yamaguchi, N. Miyamoto, T. Fujita, T. Nakato, S. Koizumi, N. Ohta, N. Yagi and T. Hashimoto, *Phys. Rev. E.*, 2012, **85**, 011403.
219. D. Bonn, H. Kellay, H. Tanaka, G. Wegdam and J. Meunier, *Langmuir*, 1999, **15**, 7534-7536.

220. H. Tanaka, J. Meunier and D. Bonn, *Phys. Rev. E.*, 2004, **69**, 031404.
221. D. Kleshchanok, J.-M. Meijer, A. V. Petukhov, G. Portale and H. N. W. Lekkerkerker, *Soft Matter*, 2011, **7**, 2832-2840.
222. D. Kleshchanok, J.-M. Meijer, A. V. Petukhov, G. Portale and H. N. W. Lekkerkerker, *Soft Matter*, 2012, **8**, 191-197.
223. J. Wijnhoven, D. D. van't Zand, D. van der Beek and H. N. W. Lekkerkerker, *Langmuir*, 2005, **21**, 10422-10427.
224. M. C. D. Mourad, A. A. Verhoeff, D. V. Byelov, A. V. Petukhov and H. N. W. Lekkerkerker, *Journal Of Physics-condensed Matter*, 2009, **21**, 474218.
225. J. Perrin, *Annales De Chimie Et De Physique*, 1909, **18**, 5-114.
226. T. S. Horozov, *Curr. Opin. Colloid Interface Sci.*, 2008, **13**, 134-140.
227. S. Tcholakova, N. D. Denkov and A. Lips, *Physical Chemistry Chemical Physics*, 2008, **10**, 1608-1627.
228. T. S. Horozov and B. P. Binks, *Angew. Chem. Int. Edit.*, 2006, **45**, 773-776.
229. C. Zeng, H. Bissig and A. D. Dinsmore, *Solid State Commun.*, 2006, **139**, 547-556.
230. A. Dippenaar, *Int. J. Miner. Process.*, 1982, **9**, 15-22.
231. G. Johansson and R. J. Pugh, *Int. J. Miner. Process.*, 1992, **34**, 1-21.
232. Q. Liu, S. Y. Zhang, D. J. Sun and J. Xu, *Colloids and Surfaces a-Physicochemical and Engineering Aspects*, 2010, **355**, 151-157.
233. W. Z. Zhou, J. Cao, W. C. Liu and S. Stoyanov, *Angew. Chem.-Int. Edit.*, 2009, **48**, 378-381.
234. B. Madivala, S. Vandebriel, J. Fransaer and J. Vermant, *Soft Matter*, 2009, **5**, 1717-1727.
235. K. Vijayaraghavan, A. Nikolov and D. Wasan, *Adv. Colloid Interface Sci.*, 2006, **123**, 49-61.
236. U. T. Gonzenbach, A. R. Studart, E. Tervoort and L. J. Gauckler, *Langmuir*, 2007, **23**, 1025-1032.

237. N. G. Vilкова, S. I. Elaneva, P. M. Kruglyakov and S. I. Karakashev, *Mendeleev Commun.*, 2011, **21**, 344-345.
238. P. M. Kruglyakov, S. I. Elaneva and N. G. Vilкова, *Adv. Colloid Interface Sci.*, 2011, **165**, 108-116.
239. B. P. Binks and T. S. Horozov, *Angew. Chem.-Int. Edit.*, 2005, **44**, 3722-3725.
240. T. Kostakis, R. Ettelaie and B. S. Murray, *Langmuir*, 2006, **22**, 1273-1280.
241. N. G. Vilкова, S. I. Elaneva and S. I. Karakashev, *Mendeleev Commun.*, 2012, **22**, 227-228.
242. S. Melle, M. Lask and G. G. Fuller, *Langmuir*, 2005, **21**, 2158-2162.
243. B. P. Binks and S. O. Lumsdon, *Langmuir*, 2000, **16**, 8622-8631.
244. B. P. Binks and S. O. Lumsdon, *Langmuir*, 2001, **17**, 4540-4547.
245. B. P. Binks, *Curr. Opin. Colloid Interface Sci.*, 2002, **7**, 21-41.
246. L. C. Dong and D. T. Johnson, *Langmuir*, 2005, **21**, 3838-3849.
247. Y. Nonomura, S. Komura and K. Tsujii, *Journal of Physical Chemistry B*, 2006, **110**, 13124-13129.
248. J. Hu, S. X. Zhou, Y. Y. Sun, X. S. Fang and L. M. Wu, *Chem. Soc. Rev.*, 2012, **41**, 4356-4378.
249. A. Walther, X. Andre, M. Drechsler, V. Abetz and A. H. E. Muller, *J. Am. Chem. Soc.*, 2007, **129**, 6187-6198.
250. A. Walther, M. Drechsler and A. H. E. Muller, *Soft Matter*, 2009, **5**, 385-390.
251. J. Kim, L. J. Cote, F. Kim, W. Yuan, K. R. Shull and J. X. Huang, *J. Am. Chem. Soc.*, 2010, **132**, 8180-8186.
252. D. W. Lee, T. Kim and M. Lee, *Chemical Communications*, 2011, **47**, 8259-8261.
253. X. Y. Qi, K. Y. Pu, H. Li, X. Z. Zhou, S. X. Wu, Q. L. Fan, B. Liu, F. Boey, W. Huang and H. Zhang, *Angew. Chem. Int. Edit.*, 2010, **49**, 9426-9429.
254. J. F. Shen, Y. H. Hu, C. Li, C. Qin and M. X. Ye, *Small*, 2009, **5**, 82-85.

255. F. X. Liang, K. Shen, X. Z. Qu, C. L. Zhang, Q. A. Wang, J. L. Li, J. G. Liu and Z. Z. Yang, *Angew. Chem. Int. Edit.*, 2011, **50**, 2379-2382.
256. S. J. Ding, B. Liu, C. L. Zhang, Y. Wu, H. F. Xu, X. Z. Qu, J. G. Liu and Z. Z. Yang, *Journal of Materials Chemistry*, 2009, **19**, 3443-3448.
257. Y. Chen, F. X. Liang, H. L. Yang, C. L. Zhang, Q. Wang, X. Z. Qu, J. L. Li, Y. L. Cai, D. Qiu and Z. Z. Yang, *Macromolecules*, 2012, **45**, 1460-1467.
258. M. M. Gudarzi and F. Sharif, *Soft Matter*, 2011, **7**, 3432-3440.
259. J. S. Guevara, A. F. Mejia, M. Shuai, Y.-W. Chang, M. S. Mannan and Z. Cheng, *Soft Matter*, 2013, **9**, 1327-1336.
260. A. F. Mejia, A. Diaz, S. Pullela, Y.-W. Chang, M. Simonetty, C. Carpenter, J. D. Batteas, M. S. Mannan, A. Clearfield and Z. Cheng, *Soft Matter*, 2012, 10245-10253.
261. S. Y. Zhang, D. J. Sun, X. Q. Dong, C. F. Li and J. Xu, *Colloids and Surfaces a-Physicochemical and Engineering Aspects*, 2008, **324**, 1-8.
262. S. Y. Zhang, Q. Lan, Q. Liu, H. Xu and D. J. Sun, *Colloids and Surfaces a-Physicochemical and Engineering Aspects*, 2008, **317**, 406-413.
263. Q. Liu, L. Y. Luan, D. J. Sun and J. Xu, *Journal of Colloid and Interface Science*, 2010, **343**, 87-93.
264. Q. Liu, S. Y. Zhang, D. J. Sun and J. Xu, *Colloids and Surfaces a-Physicochemical and Engineering Aspects*, 2009, **338**, 40-46.
265. G. Lagaly, M. Reese and S. Abend, *Applied Clay Science*, 1999, **14**, 83-103.
266. G. Lagaly, M. Reese and S. Abend, *Applied Clay Science*, 1999, **14**, 279-298.
267. N. P. Ashby and B. P. Binks, *Physical Chemistry Chemical Physics*, 2000, **2**, 5640-5646.
268. Y. Nonomura and N. Kobayashi, *Journal of Colloid and Interface Science*, 2009, **330**, 463-466.
269. T. Wang, P. J. Colver, S. A. F. Bon and J. L. Keddie, *Soft Matter*, 2009, **5**, 3842-3849.
270. S. A. F. Bon and P. J. Colver, *Langmuir*, 2007, **23**, 8316-8322.

271. A. D. Dinsmore, M. F. Hsu, M. G. Nikolaidis, M. Marquez, A. R. Bausch and D. A. Weitz, *Science*, 2002, **298**, 1006-1009.
272. G. McHale and M. I. Newton, *Soft Matter*, 2011, **7**, 5473-5481.
273. P. F. Noble, O. J. Cayre, R. G. Alargova, O. D. Velev and V. N. Paunov, *J. Am. Chem. Soc.*, 2004, **126**, 8092-8093.
274. O. D. Velev, K. Furusawa and K. Nagayama, *Langmuir*, 1996, **12**, 2374-2384.
275. G. Choudalakis and A. D. Gotsis, *European Polymer Journal*, 2009, **45**, 967-984.
276. S. C. Tjong, *Materials Science & Engineering R-Reports*, 2006, **53**, 73-197.
277. D. Porter, E. Metcalfe and M. J. K. Thomas, *Fire and Materials*, 2000, **24**, 45-52.
278. F. Hussain, M. Hojjati, M. Okamoto and R. E. Gorga, *Journal of Composite Materials*, 2006, **40**, 1511-1575.
279. J. Liu, W. J. Boo, A. Clearfield and H. J. Sue, *Materials and Manufacturing Processes*, 2006, **21**, 143-151.
280. A. Okada and A. Usuki, *Macromolecular Materials and Engineering*, 2006, **291**, 1449-1476.
281. D. R. Paul and L. M. Robeson, *Polymer*, 2008, **49**, 3187-3204.
282. P. C. LeBaron, Z. Wang and T. J. Pinnavaia, *Applied Clay Science*, 1999, **15**, 11-29.
283. J. K. Pandey, A. P. Kumar, M. Misra, A. K. Mohanty, L. T. Drzal and R. P. Singh, *Journal of Nanoscience and Nanotechnology*, 2005, **5**, 497-526.
284. S. S. Ray and M. Bousmina, *Progress in Materials Science*, 2005, **50**, 962-1079.
285. H. J. Sue, K. T. Gam, N. Bestaoui, N. Spurr and A. Clearfield, *Chemistry of Materials*, 2004, **16**, 242-249.
286. T. Lan and T. J. Pinnavaia, *Chemistry of Materials*, 1994, **6**, 2216-2219.
287. W. J. Boo, L. Sun, J. Liu, E. Moghbelli, A. Clearfield, H. J. Sue, H. Pham and N. Verghese, *Journal of Polymer Science, Part B: Polymer Physics*, 2007, **45**, 1459-1469.
288. W. J. Boo, L. Sun, G. L. Warren, E. Moghbelli, H. Pham, A. Clearfield and H. J. Sue, *Polymer*, 2007, **48**, 1075-1082.

289. W. J. Boo, L. Y. Sun, J. Liu, A. Clearfield, H. J. Sue, M. J. Mullins and H. Pham, *Composites Science and Technology*, 2007, **67**, 262-269.
290. L. Sun, W. J. Boo, D. Sun, A. Clearfield and H. J. Sue, *Chemistry of Materials*, 2007, **19**, 1749-1754.
291. X. Wan, G. Long, L. Huang and Y. Chen, *Advanced Materials*, 2011, **23**, 5342-5358.
292. D. A. Dikin, S. Stankovich, E. J. Zimney, R. D. Piner, G. H. B. Dommett, G. Evmenenko, S. T. Nguyen and R. S. Ruoff, *Nature*, 2007, **448**, 457-460.
293. X. Huang, X. Qi, F. Boey and H. Zhang, *Chem. Soc. Rev.*, 2012, **41**, 666-686.
294. G. C. Maitland, *Curr. Opin. Colloid Interface Sci.*, 2000, **5**, 301-311.
295. M. J. Shah, C. M. Hart and D. C. Thompson, *J. Phys. Chem.*, 1963, **67**, 1170-1178.
296. S. M. Jogun and C. F. Zukoski, *Journal of Rheology*, 1999, **43**, 847-871.
297. S. Jogun and C. F. Zukoski, *Journal of Rheology*, 1996, **40**, 1211-1232.
298. E. Paineau, L. J. Michot, I. Bihannic and C. Baravian, *Langmuir*, 2011, **27**, 7806-7819.
299. L. J. Michot, I. Bihannic, K. Porsch, S. Maddi, C. Baravian, J. Mougel and P. Levitz, *Langmuir*, 2004, **20**, 10829-10837.
300. W. Sugimoto, O. Terabayashi, Y. Murakami and Y. Takasu, *Journal of Materials Chemistry*, 2002, **12**, 3814-3818.
301. G. Schmidt, A. I. Nakatani, P. D. Butler and C. C. Han, *Macromolecules*, 2002, **35**, 4725-4732.
302. G. Schmidt, A. I. Nakatani, P. D. Butler, A. Karim and C. C. Han, *Macromolecules*, 2000, **33**, 7219-7222.
303. G. Schmidt, A. I. Nakatani and C. C. Han, *Rheologica Acta*, 2002, **41**, 45-54.
304. X. Wang, Y. Gao, K. Mao, G. Xue, T. Chen, J. Zhu, B. Li, P. Sun, Q. Jin, D. Ding and A.-C. Shi, *Macromolecules*, 2006, **39**, 6653-6660.
305. D. van der Beek, A. V. Petukhov, P. Davidson, J. Ferre, J. P. Jamet, H. H. Wensink, G. J. Vroege, W. Bras and H. N. W. Lekkerkerker, *Phys. Rev. E.*, 2006, **73**, 041402.

306. D. van der Beek, P. Davidson, H. H. Wensink, G. J. Vroege and H. N. W. Lekkerkerker, *Phys. Rev. E.*, 2008, **77**, 031708.
307. V. Peikov, R. Sasai and K. Yamaoka, *Chemistry Letters*, 1995, **3**, 177-178.
308. F. Camerel, J. C. R. Gabriel and P. Batail, *Advanced Functional Materials*, 2003, **13**, 377-381.
309. X. Commeinhes, P. Davidson, C. Bourgaux and J. Livage, *Advanced Materials*, 1997, **9**, 900-903.
310. H. Desvaux, J. C. P. Gabriel, P. Berthault and F. Camerel, *Angew. Chem.-Int. Edit.*, 2001, **40**, 373-376.
311. P. Porion, A. M. Faugere, L. J. Michot, E. Paineau and A. Delville, *J. Phys. Chem. C*, 2011, **115**, 14253-14263.
312. E. N. de Azevedo, M. Engelsberg, J. O. Fossum and R. E. de Souza, *Langmuir*, 2007, **23**, 5100-5105.
313. M. Eguchi, M. S. Angelone, H. P. Yennawar and T. E. Mallouk, *J. Phys. Chem. C*, 2008, **112**, 11280-11285.
314. J. Y. Kim, F. E. Osterloh, H. Hiramatsu, R. K. Dumas and K. Liu, *Journal of Physical Chemistry B*, 2005, **109**, 11151-11157.
315. I. Dozov, E. Paineau, P. Davidson, K. Antonova, C. Baravian, I. Bihannic and L. J. Michot, *Journal of Physical Chemistry B*, 2011, **115**, 7751-7765.
316. T. Nakato, K. Nakamura, Y. Shimada, Y. Shido, T. Houryu, Y. Iimura and H. Miyata, *J. Phys. Chem. C*, 2011, **115**, 8934-8939.
317. E. Paineau, K. Antonova, C. Baravian, I. Bihannic, P. Davidson, I. Dozov, M. Imperor-Clerc, P. Levitz, A. Madsen, F. Meneau and L. J. Michot, *Journal of Physical Chemistry B*, 2009, **113**, 15858-15869.
318. W.-g. Kim, X. Zhang, J. S. Lee, M. Tsapatsis and S. Nair, *Acs Nano*, 2012, **6**, 9978-9988.
319. K. Varoon, X. Zhang, B. Elyassi, D. D. Brewer, M. Gettel, S. Kumar, J. A. Lee, S. Maheshwari, A. Mittal, C.-Y. Sung, M. Cococcioni, L. F. Francis, A. V. McCormick, K. A. Mkhoyan and M. Tsapatsis, *Science*, 2011, **334**, 72-75.
320. X. Zhang, D. Liu, D. Xu, S. Asahina, K. A. Cychosz, K. V. Agrawal, Y. Al Wahedi, A. Bhan, S. Al Hashimi, O. Terasaki, M. Thommes and M. Tsapatsis, *Science*, 2012, **336**, 1684-1687.

321. H. Y. Luo, L. Bui, W. R. Gunther, E. Min and Y. Roman-Leshkoy, *Acs Catalysis*, 2012, **2**, 2695-2699.
322. H. Kambersky, 1965. *Base for cosmetics*. United States, 3122618, filed Jun 26, 1961, and issued Oct 12, 1965.
323. N. A. Okoyama, A. Yoshihiko, 1984. *Wax emulsion*. United States, 4468254, filed Apr 14, 1983, and issued Aug 28, 1984.
324. T. C. Claret, W. E. Church and R. S. Hodgson, 1997. *Wax-based emulsions and their use in gypsum products*. United States, 5695553, filed Aug 9, 1996, and issued Dec 9, 1997.
325. B. M. Peek, B. W. Sewell, R. S. Johnson and D. DiCarlo, 2000. *Composites prepared with ready-to-use resin/wax emulsion adhesives*. United States, 6132885, filed Aug 30, 1996, and issued Oct 17, 2000.
326. F. H. Siegele, 1969. *Oil well fracturing method using emulsions*. United States, 3477512, filed Dec 15, 1967, and issued Nov 11, 1969.
327. J. Lange, O. Malitschek and F. Mader, 1972. *Method of improving wax-containing self-polishing emulsions and product*. United States, 3666500, filed Jul 22, 1968, and issued May 30, 1972.
328. R. D. Hagenmaier and R. A. Baker, *Journal of Agricultural and Food Chemistry*, 1994, **42**, 899-902.
329. R. Montenegro and K. Landfester, *Langmuir*, 2003, **19**, 5996-6003.
330. Y. Shinohara, N. Kawasaki, S. Ueno, I. Kobayashi, M. Nakajima and Y. Amemiya, *Physical Review Letters*, 2005, **94**, 097801.
331. A. B. Herhold, H. E. King and E. B. Sirota, *J. Chem. Phys.*, 2002, **116**, 9036-9050.
332. B. Q. Xie, H. F. Shi, S. C. Jiang, Y. Zhao, C. C. Han, D. F. Xu and D. J. Wang, *Journal of Physical Chemistry B*, 2006, **110**, 14279-14282.
333. F. Pinel, E. Leclerc-Cessac and S. Staunton, *Plant and Soil*, 2003, **255**, 619-629.
334. F. M. van der Kooij and H. N. W. Lekkerkerker, *Philosophical Transactions of the Royal Society of London Series a-Mathematical Physical and Engineering Sciences*, 2001, **359**, 985-995.
335. M. A. Bates and D. Frenkel, *J. Chem. Phys.*, 1999, **110**, 6553-6559.

336. W. W. Deng, J. F. Klemic, X. H. Li, M. A. Reed and A. Gomez, *Journal of Aerosol Science*, 2006, **37**, 696-714.
337. K. Q. Tang and A. Gomez, *Journal of Colloid and Interface Science*, 1996, **184**, 500-511.
338. D. Fantini, M. Zanetti and L. Costa, *Macromolecular Rapid Communications*, 2006, **27**, 2038-2042.
339. C. H. Chen, E. M. Kelder and J. Schoonman, *Journal of Power Sources*, 1997, **68**, 377-380.
340. I. Taniguchi, R. C. van Landschoot and J. Schoonman, *Solid State Ionics*, 2003, **160**, 271-279.
341. H. Kim, D. W. Luo, D. Link, D. A. Weitz, M. Marquez and Z. D. Cheng, *Applied Physics Letters*, 2007, **91**, 133106.
342. C. H. Chen, E. M. Kelder, P. vanderPut and J. Schoonman, *Journal of Materials Chemistry*, 1996, **6**, 765-771.
343. J. E. Diaz, A. Barrero, M. Marquez and I. G. Loscertales, *Advanced Functional Materials*, 2006, **16**, 2110-2116.
344. A. Jaworek, *Powder Technology*, 2007, **176**, 18-35.
345. K. H. Roh, D. C. Martin and J. Lahann, *Nature Materials*, 2005, **4**, 759-763.
346. J. B. Fenn, M. Mann, C. K. Meng, S. F. Wong and C. M. Whitehouse, *Science*, 1989, **246**, 64-71.
347. X. P. Chen, L. B. Jia, X. Z. Yin, J. S. Cheng and J. Lu, *Physics Of Fluids*, 2005, **17**, 032101.
348. I. G. Loscertales, A. Barrero, I. Guerrero, R. Cortijo, M. Marquez and A. M. Ganan-Calvo, *Science*, 2002, **295**, 1695-1698.
349. L. Y. Yeo, Z. Gagnon and H. C. Chang, *Biomaterials*, 2005, **26**, 6122-6128.
350. D. C. Kyritsis, B. Coriton, F. Faure, S. Roychoudhury and A. Gomez, *Combustion and Flame*, 2004, **139**, 77-89.
351. G. Muschiolik, *Curr. Opin. Colloid Interface Sci.*, 2007, **12**, 213-220.
352. S. Arumuganathar, S. Irvine, J. R. McEwan and S. N. Jayasinghe, *Biomedical Materials*, 2007, **2**, 158-168.

353. P. B. Deotare and J. Kameoka, *Nanotechnology*, 2006, **17**, 1380-1383.
354. J. U. Park, M. Hardy, S. J. Kang, K. Barton, K. Adair, D. K. Mukhopadhyay, C. Y. Lee, M. S. Strano, A. G. Alleyne, J. G. Georgiadis, P. M. Ferreira and J. A. Rogers, *Nature Materials*, 2007, **6**, 782-789.
355. A. Barrero, J. M. Lopez-Herrera, A. Boucard, I. G. Loscertales and M. Marquez, *Journal of Colloid and Interface Science*, 2004, **272**, 104-108.
356. R. Bocanegra, D. Galan, M. Marquez, I. G. Loscertales and A. Barrero, *Journal of Aerosol Science*, 2005, **36**, 1387-1399.
357. A. M. Ganan-Calvo, R. Gonzalez-Prieto, P. Riesco-Chueca, M. A. Herrada and M. Flores-Mosquera, *Nature Physics*, 2007, **3**, 737-742.
358. O. A. Basaran and R. Suryo, *Nature Physics*, 2007, **3**, 679-680.
359. F. J. Higuera, *Physics Of Fluids*, 2007, **19**, 012102.
360. A. G. Marin, I. G. Loscertales, M. Marquez and A. Barrero, *Physical Review Letters*, 2007, **98**, 014502.
361. Z. X. Li, J. R. Lu, D. A. Styrkas, R. K. Thomas, A. R. Rennie and J. Penfold, *Molecular Physics*, 1993, **80**, 925-939.
362. X. Li, T. J. Wang and Y. Jin, *Chemical Engineering & Technology*, 2006, **29**, 1273-1280.
363. H. Gang, O. Gang, H. H. Shao, X. Z. Wu, J. Patel, C. S. Hsu, M. Deutsch, B. M. Ocko and E. B. Sirota, *Journal of Physical Chemistry B*, 1998, **102**, 2754-2758.
364. R. C. Daniel and J. C. Berg, *Langmuir*, 2002, **18**, 5074-5082.
365. T. G. Mason and J. Bibette, *Physical Review Letters*, 1996, **77**, 3481-3484.
366. K. Sotoyama, Y. Asano, K. Ihara, K. Takahashi and K. Doi, *Journal of Food Science*, 1999, **64**, 211-215.
367. R. W. Samsel and A. S. Perelson, *Biophysical Journal*, 1982, **37**, 493-514.
368. R. W. Samsel and A. S. Perelson, *Biophysical Journal*, 1984, **45**, 805-824.
369. H. Hu and R. G. Larson, *Journal of Physical Chemistry B*, 2006, **110**, 7090-7094.
370. T. Thorsen, R. W. Roberts, F. H. Arnold and S. R. Quake, *Physical Review Letters*, 2001, **86**, 4163-4166.

371. A. S. Utada, E. Lorenceau, D. R. Link, P. D. Kaplan, H. A. Stone and D. A. Weitz, *Science*, 2005, **308**, 537-541.
372. M. A. Leich and G. L. Richmond, *Faraday Discuss.*, 2005, **129**, 1-21.
373. S. L. Anna and H. C. Mayer, *Phys. Fluids*, 2006, **18**, 121512.
374. C. Bahr, *Phys. Rev. E.*, 2006, **73**, 030702.
375. X. S. Kou, S. Z. Zhang, C. K. Tsung, Z. Yang, M. H. Yeung, G. D. Stucky, L. D. Sun, J. F. Wang and C. H. Yan, *Chem. Eur. J.*, 2007, **13**, 2929-2936.
376. V. Dugas, J. Broutin and E. Souteyrand, *Langmuir*, 2005, **21**, 9130-9136.
377. Q. Lei and C. D. Bain, *Phys. Rev. Lett.*, 2004, **92**, 176103.
378. Z. Dogic and S. Fraden, *Curr. Opin. Colloid Interface Sci.*, 2006, **11**, 47-55.
379. F. Livolant, A. M. Levelut, J. Doucet and J. P. Benoit, *Nature*, 1989, **339**, 724-726.
380. A. L. Hitt, A. R. Cross and R. C. Williams, *J. Biol. Chem.*, 1990, **265**, 1639-1647.
381. B. Wiley, Y. G. Sun, B. Mayers and Y. N. Xia, *Chem. Eur. J.*, 2005, **11**, 454-463.
382. J. W. Kim, R. J. Larsen and D. A. Weitz, *JACS*, 2006, **128**, 14374-14377.
383. S. Okamoto and S. Hachisu, *J. Colloid Interface Sci.*, 1973, **43**, 30-35.
384. F. M. van der Kooij, M. Vogel and H. N. W. Lekkerkerker, *Phys. Rev. E.*, 2000, **62**, 5397-5402.
385. P. Panda, K. P. Yuet, T. A. Hatton and P. S. Doyle, *Langmuir*, 2009, **25**, 5986-5992.
386. P. S. Drzaic, *Liquid Crystal Dispersions*, World Scientific, Singapore, 1995.
387. A. Adamczyk, *Mol. Cryst. Liq. Cryst.*, 1989, **170**, 53-69.
388. G. Toquer, T. Phou, S. Monge, A. Grimaldi, M. Nobili and C. Blanc, *Journal of Physical Chemistry B*, 2008, **112**, 4157-4160.
389. D. Rudhardt, A. Fernandez-Nieves, D. R. Link and D. A. Weitz, *Appl. Phys. Lett.*, 2003, **82**, 2610-2612.

390. M. Kleman and O. D. Lavrentovich, *Soft Matter Physics*, Springer, 2001.
391. D. K. Yoon, M. C. Choi, Y. H. Kim, M. W. Kim, O. D. Lavrentovich and H. T. Jung, *Nature Materials*, 2007, **6**, 866-870.
392. I. Dierking, *Textures of liquid crystals*, Wiley-VCH, Weinheim, 2003.
393. S. W. Bragg, *Supplement to Nature*, 1934, **3360**, 445.
394. S. Shojaei-Zadeh and S. L. Anna, *Langmuir*, 2006, **22**, 9986-9993.
395. M. C. Choi, T. Pfohl, Z. Y. Wen, Y. L. Li, M. W. Kim, J. N. Israelachvili and C. R. Safinya, *Proc. Natl. Acad. Sci. U. S. A.*, 2004, **101**, 17340-17344.
396. P. G. de Gennes and J. Prost, *The physics of liquid crystals*, Clarendon Press, Oxford, 1993.
397. G. P. Crawford and S. Zumer, (Eds.) *Liquid crystals in complex geometries*, Taylor and Francis, London, 1996.
398. J. Kuntsche, K. Westesen, M. Drechsler, M. H. J. Koch and H. Bunjes, *Pharm. Res.*, 2004, **21**, 1834-1843.
399. J. D. Bernal and D. Crowfoot, *Trans. Faraday Soc.*, 1933, **29**, 1032 - 1049.
400. Chandras.S and Madhusud.Nv, *Acta Crystallographica Section a-Crystal Physics Diffraction Theoretical and General Crystallography*, 1970, **A 26**, 153.
401. J. Bechhoefer and P. Oswald, *Europhysics Letters*, 1991, **15**, 521-526.
402. J. Bechhoefer, L. Lejcek and P. Oswald, *J. Phys. II.*, 1992, **2**, 27-44.
403. A. B. Croll, M. V. Massa, M. W. Matsen and K. Dalnoki-Veress, *Phys. Rev. Lett.*, 2006, **97**, 204502.
404. G. Friedel and F. Grandjean, *Bull. Soc. Fr. Mineral*, 1910, **33**, 409.
405. M. Todorokihara and H. Naito, *Mol. Cryst. .Liq. Cryst.*, 2004, **412**, 1679-1686.
406. J. B. Fournier and G. Durand, *Journal De Physique II*, 1991, **1**, 845-870.
407. W. E and P. Palffy-Muhoray, *J. .Nonlinear Sci.*, 1999, **9**, 417-437.
408. H. Naito, M. Okuda and O. Y. Zhongcan, *Phys. Rev. Lett.*, 1993, **70**, 2912-2915.
409. J. C. Earnshaw and C. J. Hughes, *Phys. Rev. A*, 1992, **46**, R4494-R4496.

410. A. Tulpar and W. A. Ducker, *Journal of Physical Chemistry B*, 2004, **108**, 1667-1676.
411. S. Asakura and F. Oosawa, *J. Chem. Phys.*, 1954, **22**, 1255-1256.
412. D. Vollhardt, G. Brezesinski, S. Siegel and G. Emrich, *Journal of Physical Chemistry B*, 2001, **105**, 12061-12067.
413. M. Malmsten and B. Lindman, *Langmuir*, 1989, **5**, 1105-1111.
414. P. T. Spicer and R. W. Hartel, *Aust. J. Chem.*, 2005, **58**, 655-659.
415. E. B. Sirota, H. E. King, D. M. Singer and H. H. Shao, *J. Chem. Phys.*, 1993, **98**, 5809-5824.
416. B. M. Ocko, X. Z. Wu, E. B. Sirota, S. K. Sinha, O. Gang and M. Deutsch, *Phys. Rev. E.*, 1997, **55**, 3164-3182.
417. E. B. Sirota, *Langmuir*, 1998, **14**, 3133-3136.
418. O. Y. Zhongcan and W. Helfrich, *Phys. Rev. Lett.*, 1987, **59**, 2486-2488.
419. Q. H. Liu, H. J. Zhou, J. X. Liu and O. Y. Zhong-Can, *Phys. Rev. E.*, 1999, **60**, 3227-3233.
420. P. A. Barneveld, D. E. Hesselink, F. A. M. Leermakers, J. Lyklema and J. Scheutjens, *Langmuir*, 1994, **10**, 1084-1092.
421. C. V. Teixeira, R. Itri and L. Q. do Amaral, *Langmuir*, 1999, **15**, 936-939.
422. O. D. Lavrentovich, M. Kleman and V. M. Pergamenschik, *Journal De Physique II*, 1994, **4**, 377-404.
423. P. Oswald and L. Lejcek, *European Physical Journal E*, 2006, **19**, 441-452.
424. Z. X. Li, J. R. Lu, D. A. Styrkas, R. K. Thomas, A. R. Rennie and J. Penfold, *Mol. Phys.*, 1993, **925**, 925-939.
425. P. He, A. F. Mejia, Z. D. Cheng, D. Z. Sun, H. J. Sue, D. S. Dinair and M. Marquez, *Phys. Rev. E.*, 2010, **81**, 7.
426. A. D. Ward, M. G. Berry, C. D. Mellor and C. D. Bain, *Chem. Commun.*, 2006, 4515-4517.
427. D. R. Nelson, *Nano Lett.*, 2002, **2**, 1125-1129.

428. S. Mondal, *Appl. Therm. Eng.*, 2008, **28**, 1536-1550.
429. D. Frenkel and B. M. Mulder, *Molecular Physics*, 1985, **55**, 1171-1192.
430. E. Yasuda, T. Enami, N. Hoteida, L. J. Lanticse-Diaz, Y. Tanabe and T. Akatsu, *Mat. Scie. Eng. A-Struct.*, 2008, **148**, 7-12.
431. R. Verdejo, F. Barroso-Bujans, M. A. Rodriguez-Perez, J. A. de Saja and M. A. Lopez-Manchado, *Journal of Materials Chemistry*, 2008, **18**, 2221-2226.
432. T. Odijk, *Macromolecules*, 1986, **19**, 2313-2329.
433. S. Ithurria, M. D. Tessier, B. Mahler, R. P. S. M. Lobo, B. Dubertret and A. L. Efros, *Nat Mater*, 2011, **10**, 936-941.
434. F. Camerel, J. C. P. Gabriel and P. Batail, *Chem. Commun.*, 2002, 1926-1927.
435. L. Kavan, J. H. Yum, M. K. Nazeeruddin and M. Gratzel, *Acs Nano*, 2011, **5**, 9171-9178.
436. K. L. Woon, M. P. Aldred, P. Vlachos, G. H. Mehl, T. Stirner, S. M. Kelly and M. O'Neill, *Chemistry of Materials*, 2006, **18**, 2311-2317.
437. M. Okazaki, K. Kawata, H. Nishikawa and M. Negoro, *Polym. Adv. Technol.*, 2000, **11**, 398-403.
438. L. S. Li, J. Walda, L. Manna and A. P. Alivisatos, *Nano Letters*, 2002, **2**, 557-560.
439. N. A. Kotov, I. Dekany and J. H. Fendler, *Adv. Mater.*, 1996, **8**, 637-641.
440. P. He, A. F. Mejia, Z. Cheng, D. Sun, H.-J. Sue, D. S. Dinair and M. Marquez, *Phys. Rev. E.*, 2010, **81**, 026310.
441. F. Gámez, P. J. Merkling and S. Lago, *Chem. Phys. Lett.*, 2010, **494**, 45-49.
442. P. G. Gennes, *The Physics of Liquid Crystals*, University Press, Oxford, 1974.
443. N. I. Ringdal, D. M. Fonseca, E. L. Hansen, H. Hemmen and J. O. Fossum, *Phys. Rev. E.*, 2010, **81**, 041702.
444. M. Casciola, D. Capitani, A. Donnadio, G. Munari and M. Pica, *Inorg. Chem.*, 2010, **49**, 3329-3336.
445. A. Díaz, A. David, R. Pérez, M. L. González, A. Báez, S. E. Wark, P. Zhang, A. Clearfield and J. L. Colón, *Biomacromolecules*, 2010, **11**, 2465-2470.

446. A. Diaz, V. Saxena, J. Gonzalez, A. David, B. Casanas, C. Carpenter, J. D. Batteas, J. L. Colon, A. Clearfield and M. D. Hussain, *Chemical Communications*, 2012, **48**, 1754-1756.
447. M. B. Santiago, M. M. Velez, S. Borrero, A. Díaz, C. Casillas, C. Hofmann, A. R. Guadalupe and J. L. Colón, *Electroanalysis*, 2006, **18**, 559-572
448. G. Vaivars, T. Mokrani, N. Hendricks and V. Linkov, *Journal of Solid State Electrochemistry*, 2004, **8**, 882-885.
449. J. L. Colón, D. S. Thakur, C.-Y. Yang, A. Clearfield and C. R. Martini, *J. Catal.*, 1990, **124**, 148-159.
450. G. H. Chen and A. S. Hoffman, *Nature*, 1995, **373**, 49-52.
451. Y. Qiu and K. Park, *Advanced Drug Delivery Reviews*, 2001, **53**, 321-339.
452. S. R. Sershen, G. A. Mensing, M. Ng, N. J. Halas, D. J. Beebe and J. L. West, *Advanced Materials*, 2005, **17**, 1366-1368.
453. X. Zeng and H. Jiang, *Applied Physics Letters*, 2008, **93**, 151101.
454. T. Miyata, N. Asami and T. Uragami, *Nature*, 1999, **399**, 766-769.
455. B. Jeong, Y. H. Bae, D. S. Lee and S. W. Kim, *Nature*, 1997, **388**, 860-862.
456. L. Dong and H. Jiang, *Soft Matter*, 2007, **3**, 1223-1230.
457. J. H. Holtz and S. A. Asher, *Nature*, 1997, **389**, 829-832.
458. F. Eeckman, A. J. Moes and K. Amighi, *European Polymer Journal*, 2004, **40**, 873-881.
459. F. Eeckman, A. J. Moes and K. Amighi, *International Journal of Pharmaceutics*, 2004, **273**, 109-119.
460. Y. Pan, H. Bao, N. G. Sahoo, T. Wu and L. Li, *Advanced Functional Materials*, 2011, **21**, 2754-2763.
461. K. Haraguchi and T. Takehisa, *Advanced Materials*, 2002, **14**, 1120-1124.
462. L. Liang, J. Liu and X. Y. Gong, *Langmuir*, 2000, **16**, 9895-9899.
463. H. G. Schild, *Prog. Polym. Sci.*, 1992, **17**, 163-249.

464. M. F. Islam, A. M. Alsayed, Z. Dogic, J. Zhang, T. C. Lubensky and A. G. Yodh, *Physical Review Letters*, 2004, **92**, 088303.
465. M. F. Islam, M. Nobili, F. F. Ye, T. C. Lubensky and A. G. Yodh, *Physical Review Letters*, 2005, **95**, 148301.
466. D. Lacoste, A. W. C. Lau and T. C. Lubensky, *European Physical Journal E*, 2002, **8**, 403-411.
467. M. Hebert, R. Kant and P. G. deGennes, *J. Phys. I*, 1997, **7**, 909-919.
468. D. L. Thomsen, P. Keller, J. Naciri, R. Pink, H. Jeon, D. Shenoy and B. R. Ratna, *Macromolecules*, 2001, **34**, 5868-5875.
469. W. Lehmann, H. Skupin, C. Tolksdorf, E. Gebhard, R. Zentel, P. Kruger, M. Losche and F. Kremer, *Nature*, 2001, **410**, 447-450.
470. C. C. Chang, L. C. Chien and R. B. Meyer, *Phys. Rev. E.*, 1997, **56**, 595-599.
471. C. Ozdilek, E. Mendes and S. J. Picken, *Polymer*, 2006, **47**, 2189-2197.
472. A. L. Troutier-Thuilliez, H. Hintze-Bruening, C. Taviot-Gueho, V. Verney and F. Leroux, *Soft Matter*, 2011, **7**, 4242-4251.
473. Z. Cheng, P. M. Chaikin, W. B. Russel, W. V. Meyer, J. Zhu, R. B. Rogers and R. H. Ottewill, *Materials & Design*, 2001, **22**, 529-534.
474. J. Nehring and A. Saupe, *Journal of the Chemical Society-Faraday Transactions II*, 1972, **68**, 1-15.
475. X. D. Feng, X. Q. Guo and K. Y. Qiu, *Makromolekulare Chemie-Macromolecular Chemistry and Physics*, 1988, **189**, 77-83.
476. M. R. Guilherme, R. da Silva, A. F. Rubira, G. Geuskens and E. C. Muniz, *Reactive & Functional Polymers*, 2004, **61**, 233-243.
477. O. Okay, *Polymer*, 1994, **35**, 2613-2618.
478. R. Fei, J. T. George, J. Park and M. A. Grunlan, *Soft Matter*, 2012, **8**, 481-487.
479. Y. Hou, R. Fei, J. C. Burkes, S. D. Lee, D. Munoz-Pinto, M. S. Hahn and M. A. Grunlan, *Journal of Biomaterials and Tissue Engineering*, 2011, **1**, 93-100.
480. Y. Hou, A. R. Matthews, A. M. Smitherman, A. S. Bulick, M. S. Hahn, H. Hou, A. Han and M. A. Grunlan, *Biomaterials*, 2008, **29**, 3175-3184.

481. A. A. Verhoeff, R. P. Brand and H. N. W. Lekkerkerker, *Molecular Physics*, 2011, **109**, 1363-1371.
482. N. H. Hartshorne, *The microscopy of liquid crystals*, London, 1974.
483. B. Li, Y. P. Cao, X. Q. Feng and H. J. Gao, *Soft Matter*, 2012, **8**, 5728-5745.
484. P. G. de Gennes, *Reviews of Modern Physics*, 1992, **64**, 645.
485. S. Jiang, Q. Chen, M. Tripathy, E. Luijten, K. S. Schweizer and S. Granick, *Advanced Materials*, 2010, **22**, 1060-1071.
486. J. Z. Du and R. K. O'Reilly, *Chem. Soc. Rev.*, 2011, **40**, 2402-2416.
487. A. Perro, S. Reculosa, E. Bourgeat-Lami, S. Ravaine and E. Duguet, *Actual Chim.*, 2010, **340**, 14-17.
488. A. B. Pawar and I. Kretzschmar, *Macromolecular Rapid Communications*, 2009, **31**, 150-168.
489. A. Walther and A. H. E. Muller, *Soft Matter*, 2008, **4**, 663-668.
490. C. H. Chen, R. K. Shah, A. R. Abate and D. A. Weitz, *Langmuir*, 2009, **25**, 4320-4323.
491. S. R. Ye and R. L. Carroll, *ACS Appl. Mater. Interfaces*, 2010, **2**, 616-620.
492. M. D. McConnell, M. J. Kraeutler, S. Yang and R. J. Composto, *Nano Letters*, 2010, **10**, 603-609.
493. R. K. Shah, J. W. Kim and D. A. Weitz, *Advanced Materials*, 2009, **21**, 1949-1953.
494. T. T. Chastek, S. D. Hudson and V. A. Hackley, *Langmuir*, 2008, **24**, 13897-13903.
495. A. van Blaaderen, *Nature*, 2006, **439**, 545-546.
496. K. H. Roh, M. Yoshida and J. Lahann, *Materialwiss. Werkstofftech.*, 2007, **38**, 1008-1011.
497. J. A. Champion, Y. K. Katare and S. Mitragotri, *Proc. Natl. Acad. Sci. U. S. A.*, 2007, **104**, 11901-11904.
498. R. Langer and D. A. Tirrell, *Nature*, 2004, **428**, 487-492.

499. C. M. Liddell, C. J. Summers and A. M. Gokhale, *Mater. Charact.*, 2003, **50**, 69-79.
500. M. Gratzel, *Nature*, 2001, **414**, 338-344.
501. M. Boncheva and G. M. Whitesides, *MRS Bull.*, 2005, **30**, 736-742.
502. M. Brust and C. J. Kiely, *Colloid. Surface. A.*, 2002, **202**, 175-186.
503. T. Ito and S. Okazaki, *Nature*, 2000, **406**, 1027-1031.
504. D. Dendukuri, T. A. Hatton and P. S. Doyle, *Langmuir*, 2007, **23**, 4669-4674.
505. Y. K. Takahara, S. Ikeda, S. Ishino, K. Tachi, K. Ikeue, T. Sakata, T. Hasegawa, H. Mori, M. Matsumura and B. Ohtani, *J. Am. Chem. Soc.*, 2005, **127**, 6271-6275.
506. A. Walther, M. Hoffmann and A. H. E. Muller, *Angew. Chem. Int. Edit.*, 2008, **47**, 711-714.
507. M. Rosen and D. Tracy, *J. Surfactants Deterg.*, 1998, **1**, 547-554.
508. R. Zana, *Adv. Colloid Interface Sci.*, 2002, **97**, 205-253.
509. F. M. Menger and C. A. Littau, *J. Am. Chem. Soc.*, 1993, **115**, 10083-10090.
510. F. M. Menger and J. S. Keiper, *Angew. Chem. Int. Edit.*, 2000, **39**, 1907-1920.
511. K. M. Layn, P. G. Debenedetti and R. K. Prud'homme, *J. Chem. Phys.*, 1998, **109**, 5651-5658.
512. E. S. Boek, P. V. Coveney, H. N. W. Lekkerkerker and P. van der Schoot, *Phys. Rev. E.*, 1997, **55**, 3124.
513. M. Osada and T. Sasaki, *Journal of Materials Chemistry*, 2009, **19**, 2503-2511.
514. M. E. B. Santiago, C. Declet-Flores, A. Díaz, M. M. Vélez, M. Z. Bosques, Y. Sanakis and J. L. Colón, *Langmuir*, 2007, **23**, 7810-7817.
515. A. A. Martí, N. Rivera, K. Soto, L. Maldonado and J. L. Colón, *J. Chem. Soc. Dalton Trans.*, 2007, 1713-1718.
516. R. A. Bermúdez, Y. Colón, G. A. Tejada and J. L. Colón, *Langmuir*, 2005, **21**, 890-895.

517. C. Y. Ortizavila and A. Clearfield, *J. Chem. Soc.-Dalton Trans.*, 1989, 1617-1623.
518. C. Y. Ortizavila and A. Clearfield, *Inorg. Chem.*, 1985, **24**, 1773-1778.
519. Q. Liu, J. R. de Wijn and C. A. van Blitterswijk, *Journal of Biomedical Materials Research*, 1998, **40**, 358-364.
520. Q. Liu, J. R. de Wijn, K. de Groot and C. A. van Blitterswijk, *Biomaterials*, 1998, **19**, 1067-1072.
521. Q. Liu, J. R. de Wijn and C. A. van Blitterswijk, *Journal of Biomedical Materials Research*, 1998, **40**, 257-263.
522. Q. Liu, J. R. de Wijn and C. A. van Blitterswijk, *Journal of Biomedical Materials Research*, 1998, **40**, 490-497.
523. R. Labella, M. Braden and S. Deb, *Biomaterials*, 1994, **15**, 1197-1200.
524. K. Nishizawa, M. Toriyama, T. Suzuki, Y. Kawamoto, Y. Yokugawa and F. Nagata, *Chem. Soc. Japan*, 1995, **1**, 63-67.
525. A. Clearfield, *Inorganic Ion Exchange Materials*, CRC Press, Boca Raton, 1982.
526. T. N. Hunter, R. J. Pugh, G. V. Franks and G. J. Jameson, *Adv. Colloid Interface Sci.*, 2008, **137**, 57-81.
527. D. J. Kraft, J. W. J. de Folter, B. Luigjes, S. I. R. Castillo, S. Sacanna, A. P. Philipse and W. K. Kegel, *Journal of Physical Chemistry B*, 2010, **114**, 10347-10356.
528. S. Sacanna, W. K. Kegel and A. P. Philipse, *Physical Review Letters*, 2007, **98**, 158301.
529. S. Sacanna, W. K. Kegel and A. P. Philipse, *Langmuir*, 2007, **23**, 10486-10492.
530. W. K. Kegel and J. Groenewold, *Phys. Rev. E.*, 2009, **80**, 030401.
531. N. X. Yan and J. H. Masliyah, *Journal of Colloid and Interface Science*, 1996, **181**, 20-27.
532. A. Colin, in *Foam Engineering*, John Wiley & Sons, Ltd, 2012, pp. 75-90.
533. E. Dickinson, *Curr. Opin. Colloid Interface Sci.*, 2010, **15**, 40-49.
534. B. P. Binks, A. Rocher and M. Kirkland, *Soft Matter*, 2011, **7**, 1800-1808.

535. S. Ata and P. D. Yates, *Colloids and Surfaces a-Physicochemical and Engineering Aspects*, 2006, **277**, 1-7.
536. O. Paulson and R. J. Pugh, *Langmuir*, 1996, **12**, 4808-4813.
537. R. Murakami and A. Bismarck, *Advanced Functional Materials*, 2010, **20**, 732-737.
538. A. R. Studart, U. T. Gonzenbach, I. Akartuna, E. Tervoort and L. J. Gauckler, *Journal of Materials Chemistry*, 2007, **17**, 3283-3289.
539. J. C. H. Wong, E. Tervoort, S. Busato, U. T. Gonzenbach, A. R. Studart, P. Ermanni and L. J. Gauckler, *Journal of Materials Chemistry*, 2010, **20**, 5628-5640.
540. J. C. H. Wong, E. Tervoort, S. Busato, L. J. Gauckler and P. Ermanni, *Langmuir*, 2011, **27**, 3254-3260.
541. J. C. H. Wong, E. Tervoort, S. Busato, U. T. Gonzenbach, A. R. Studart, P. Ermanni and L. J. Gauckler, *Journal of Materials Chemistry*, 2009, **19**, 5129-5133.
542. R. J. Pugh, *Adv. Colloid Interface Sci.*, 1996, **64**, 67-142.
543. B. S. Murray and R. Ettelaie, *Curr. Opin. Colloid Interface Sci.*, 2004, **9**, 314-320.
544. M. Vignes-Adler and D. Weaire, *Curr. Opin. Colloid Interface Sci.*, 2008, **13**, 141-149.
545. G. Kaptay and N. Babcsán, in *Foam Engineering*, John Wiley & Sons, Ltd, 2012, pp. 121-143.
546. S. Lam, E. Blanco, S. K. Smoukov, K. P. Velikov and O. D. Velev, *J. Am. Chem. Soc.*, 2011, **133**, 13856-13859.
547. U. T. Gonzenbach, A. R. Studart, E. Tervoort and L. J. Gauckler, *Angew. Chem.-Int. Edit.*, 2006, **45**, 3526-3530.
548. E. Dickinson, R. Ettelaie, T. Kostakis and B. S. Murray, *Langmuir*, 2004, **20**, 8517-8525.
549. T. N. Hunter, E. J. Wanless and G. J. Jameson, *Colloids and Surfaces a-Physicochemical and Engineering Aspects*, 2009, **334**, 181-190.

550. U. T. Gonzenbach, A. R. Studart, E. Tervoort and L. J. Gauckler, *Langmuir*, 2006, **22**, 10983-10988.
551. R. J. Pugh, *Langmuir*, 2007, **23**, 7972-7980.
552. B. M. Somosvari, N. Babcsan, P. Barczy and A. Berthold, *Colloids and Surfaces a-Physicochemical and Engineering Aspects*, 2007, **309**, 240-245.
553. S. Fujii, P. D. Iddon, A. J. Ryan and S. P. Armes, *Langmuir*, 2006, **22**, 7512-7520.
554. R. G. Alargova, D. S. Warhadpande, V. N. Paunov and O. D. Velev, *Langmuir*, 2004, **20**, 10371-10374.
555. H. A. Wege, S. Kim, V. N. Paunov, Q. X. Zhong and O. D. Velev, *Langmuir*, 2008, **24**, 9245-9253.
556. D. N. H. Tran, C. P. Whitby, D. Fornasiero and J. Ralston, *Journal of Colloid and Interface Science*, 2010, **348**, 460-468.
557. F. Q. Tang, Z. Xiao, J. A. Tang and J. A. Long, *Journal of Colloid and Interface Science*, 1989, **131**, 498-502.
558. J. B. M. Hudales and H. N. Stein, *Journal of Colloid and Interface Science*, 1990, **140**, 307-313.
559. A. B. Subramaniam, M. Abkarian, L. Mahadevan and H. A. Stone, *Nature*, 2005, **438**, 930-930.
560. A. B. Subramaniam, M. Abkarian and H. A. Stone, *Nature Materials*, 2005, **4**, 553-556.
561. B. D. Johnson and R. C. Cooke, *Science*, 1981, **213**, 209-211.
562. D. H. Kim, M. J. Costello, P. B. Duncan and D. Needham, *Langmuir*, 2003, **19**, 8455-8466.
563. P. Ratanabanangkoon, M. Gropper, R. Merkel, E. Sackmann and A. P. Gast, *Langmuir*, 2003, **19**, 1054-1062.
564. H. Nathan, B. Akhilesh and K. Challa, in *Handbook of Layered Materials*, CRC Press, 2004.
565. M. Casciola, G. Alberti, A. Donnadio, M. Pica, F. Marmottini, A. Bottino and P. Piaggio, *Journal of Materials Chemistry*, 2005, **15**, 4262-4267.

566. R. M. Tindwa, D. K. Ellis, G. Z. Peng and A. Clearfield, *Journal of the Chemical Society-Faraday Transactions I*, 1985, **81**, 545-552.
567. S. Arditty, C. P. Whitby, B. P. Binks, V. Schmitt and F. Leal-Calderon, *European Physical Journal E*, 2003, **11**, 273-281.
568. M. Kobayashi, F. Juillerat, P. Galletto, P. Bowen and M. Borkovec, *Langmuir*, 2005, **21**, 5761-5769.
569. G. N. Sethumadhavan, A. D. Nikolov and D. T. Wasan, *Journal of Colloid and Interface Science*, 2001, **240**, 105-112.
570. B. E. Elizalde, D. Giaccaglia, A. M. R. Pilosof and G. B. Bartholomai, *Journal of Food Science*, 1991, **56**, 24-26.
571. A. Saint-Jalmes, *Soft Matter*, 2006, **2**, 836-849.
572. A. F. Mejia, P. He, D. W. Luo, M. Marquez and Z. D. Cheng, *Journal of Colloid and Interface Science*, 2009, **334**, 22-28.
573. F. M. van der Kooij and H. N. W. Lekkerkerker, *Physical Review Letters*, 2000, **84**, 781-784.
574. Y. Nonomura, S. Komura and K. Tsujii, *Langmuir*, 2004, **20**, 11821-11823.
575. N. P. Pardhy and B. M. Budhlall, *Langmuir*, 2010, **26**, 13130-13141.
576. S. Berger, A. Synytska, L. Ionov, K. J. Eichhorn and M. Stamm, *Macromolecules*, 2008, **41**, 9669-9676.
577. A. Perro, S. Reculosa, S. Ravaine, E. B. Bourgeat-Lami and E. Duguet, *Journal of Materials Chemistry*, 2005, **15**, 3745-3760.
578. X. Y. Ling, I. Y. Phang, C. Acikgoz, M. D. Yilmaz, M. A. Hempenius, G. J. Vancso and J. Huskens, *Angew. Chem. Int. Edit.*, 2009, **48**, 7677-7682.
579. S. Jiang and S. Granick, *J. Chem. Phys.*, 2007, **127**, 161102.
580. E. M. Herzig, K. A. White, A. B. Schofield, W. C. K. Poon and P. S. Clegg, *Nature Materials*, 2007, **6**, 966-971.
581. B. P. Binks and P. D. I. Fletcher, *Langmuir*, 2001, **17**, 4708-4710.
582. C. Casagrande, P. Fabre, E. Raphael and M. Veyssie, *Europhysics Letters*, 1989, **9**, 251-255.

583. G. Kaptay, *Colloid. Surface. A.*, 2006, **282-283**, 387-401.
584. N. D. Denkov, I. B. Ivanov, P. A. Kralchevsky and D. T. Wasan, *Journal of Colloid and Interface Science*, 1992, **150**, 589-593.
585. A. F. Stalder, G. Kulik, D. Sage, L. Barbieri and P. Hoffmann, *Colloid. Surface. A.*, 2006, **286**, 92-103.
586. M. K. Chaudhury and G. M. Whitesides, *Langmuir*, 1991, **7**, 1013-1025.
587. G. Vazquez, E. Alvarez and J. M. Navaza, *J. Chem. Eng. Data*, 1995, **40**, 611-614.

APPENDIX A

ADDITIONAL FIGURES FOR CHAPTER II

Section I: Disk Morphology

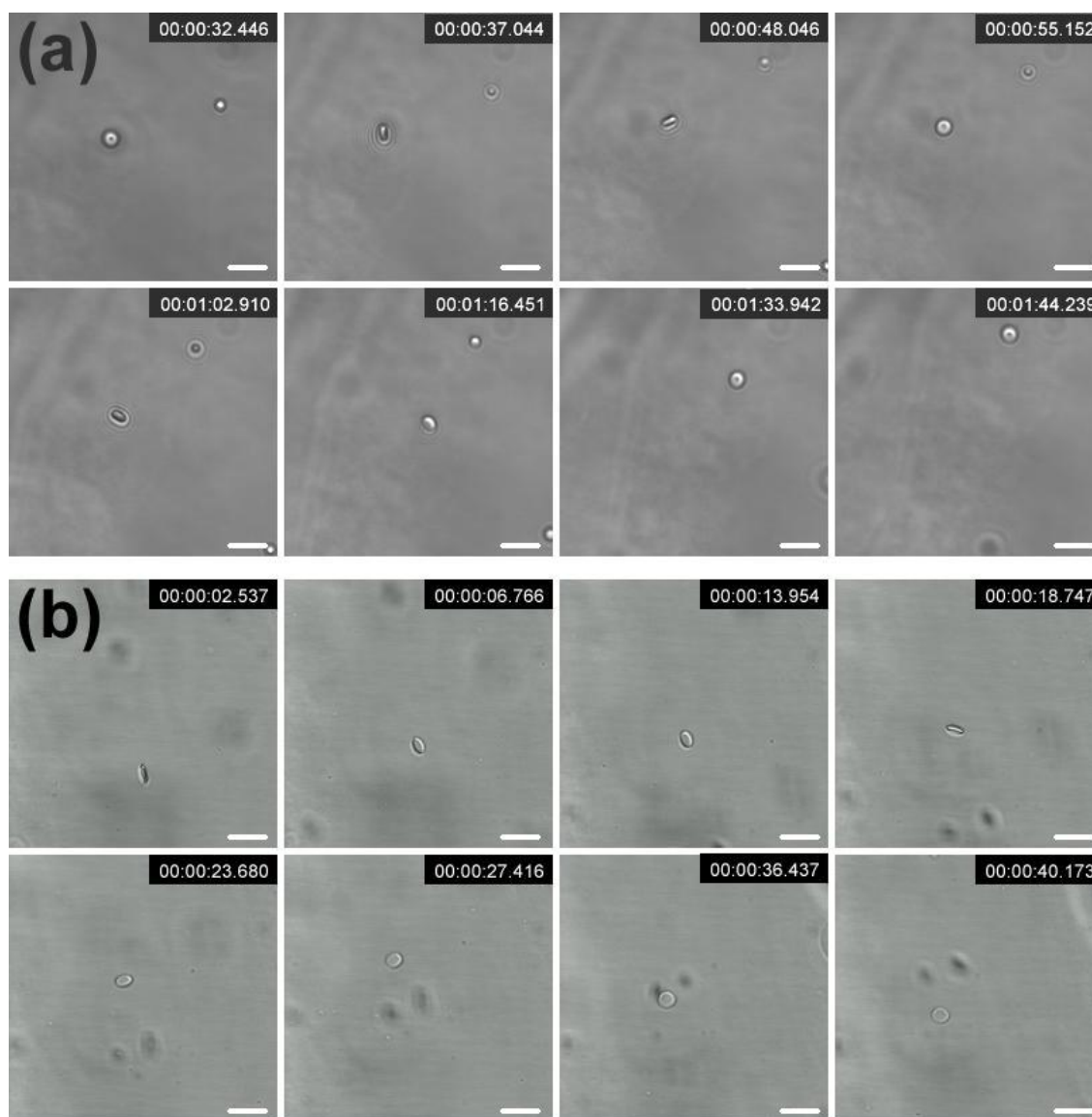


Figure A1. Time sequences of Brownian motions from the supplementary movies. (a) Biconcave disk. The dimples on the circular faces can be examined from various view-angles. (b) Flat disk. The flat surfaces and the increased aspect ratio compared to the biconcave disk are evident. The scale bars are 8 μm .

Section II. Disk Structure: Focal Conic Domain and $+\pi$ edge Disclination.

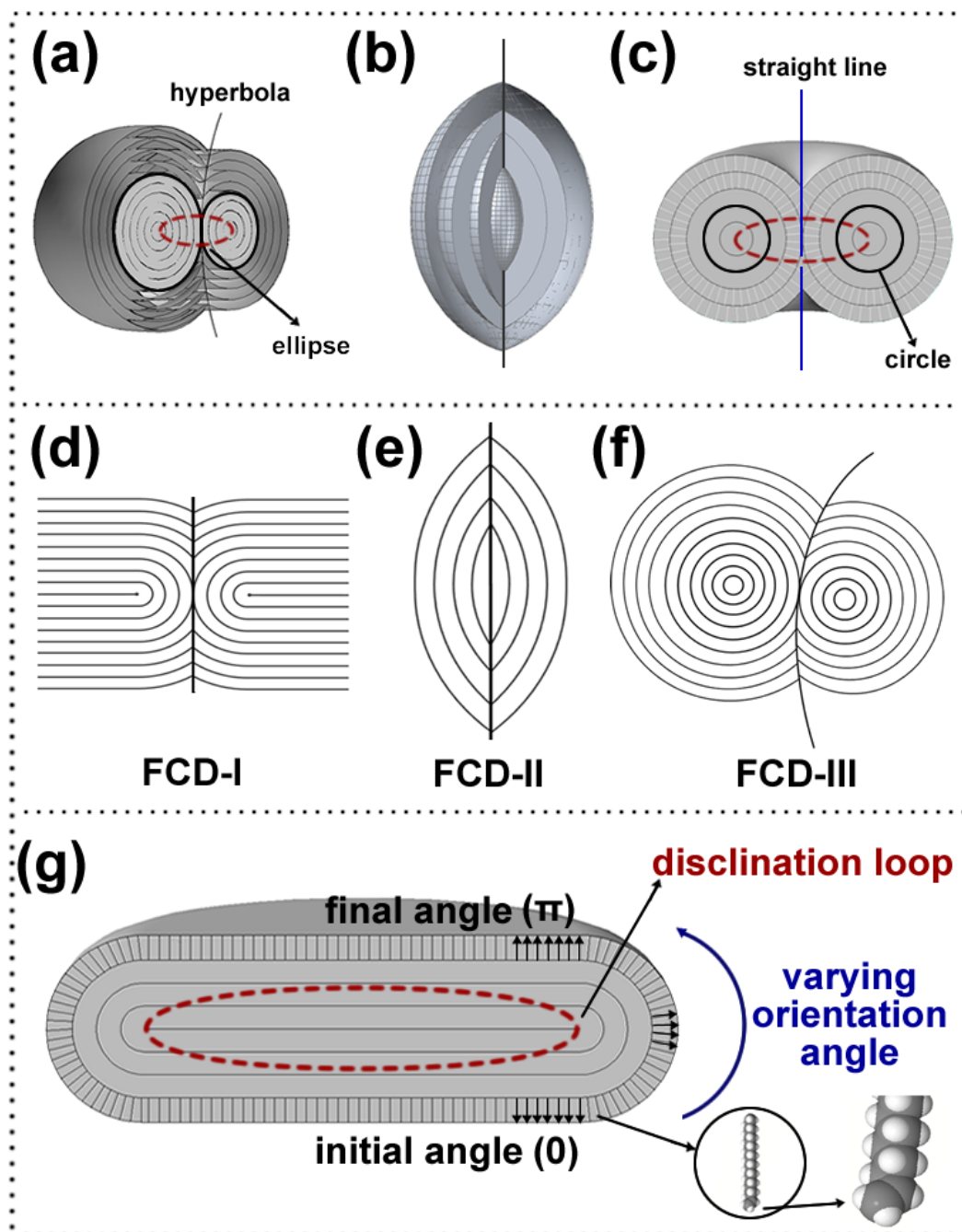


Figure A2. Defects of a layered structure. (a) A focal conic domain (FCD) defect with cores as a pair of an ellipse and a hyperbola. FCD is one type of defect typically observed in smectic liquid crystals. The general structure is made up of layers of molecules as illustrated. The α -eicosene molecules in the rotator phase organize into layers where the arranged molecules are perpendicular to the layers. (b) 3D structure for

FCD-II. (c) For the case of a symmetric FCD, the ellipse becomes a circle and the hyperbola becomes a straight line. (d) FCD-I, which is formed by cyclides with negative Gaussian curvature (curved part of the drawing). (e) FCD-II, which is formed by cyclides with positive Gaussian curvature. (f) FCD-III, which is formed by cyclides of both positive and negative Gaussian curvature. (d),(e) and (f) are the cut-views of the defects. For example, (f) is the cut view of (a) as well as (e) for (b). (d) is the central part of (c). (c) is rotationally symmetric about the line, which is drawn straight and can be curved as the hyperbola in (a). (f) The $+\pi$ disclination loop. The orientation of the α -eicosene molecules inside the flat disks has a topological defect: disclination loop. One cycling around the core, the integral change of the molecular orientation is π and changing in the same direction as the cycling, so it is called a $+\pi$ disclination loop. The arrays in the layer stand for the orientation of the α -eicosene molecules, which is not symmetric: one end has a c=c bond and the other is a c-c bond.

Section III: Disk Self-assembly

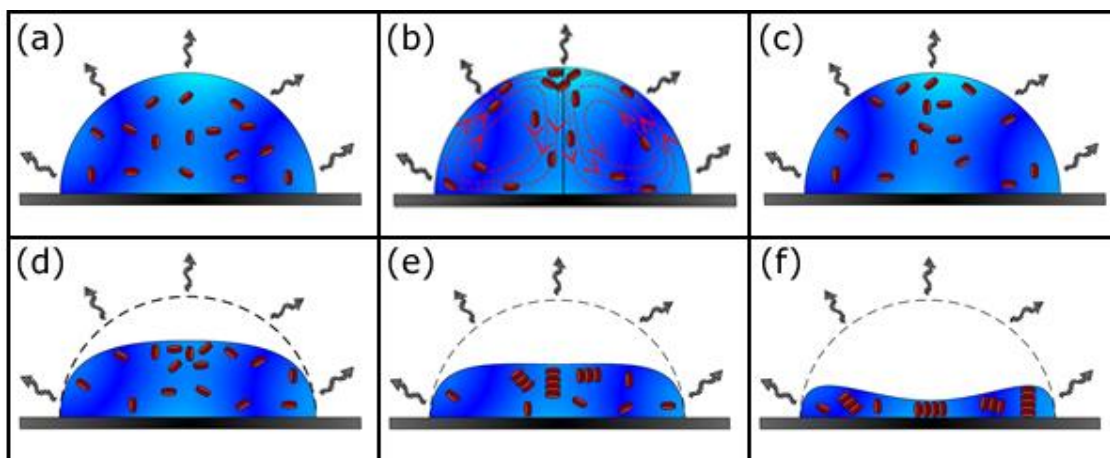


Figure A3. Schematic representation of the self-assembly of disks in an evaporating droplet (side view).

APPENDIX B

ADDITIONAL FIGURES FOR CHAPTER IV

Adsorption of Homogeneous and Amphiphilic Particles at Liquid-liquid Interfaces

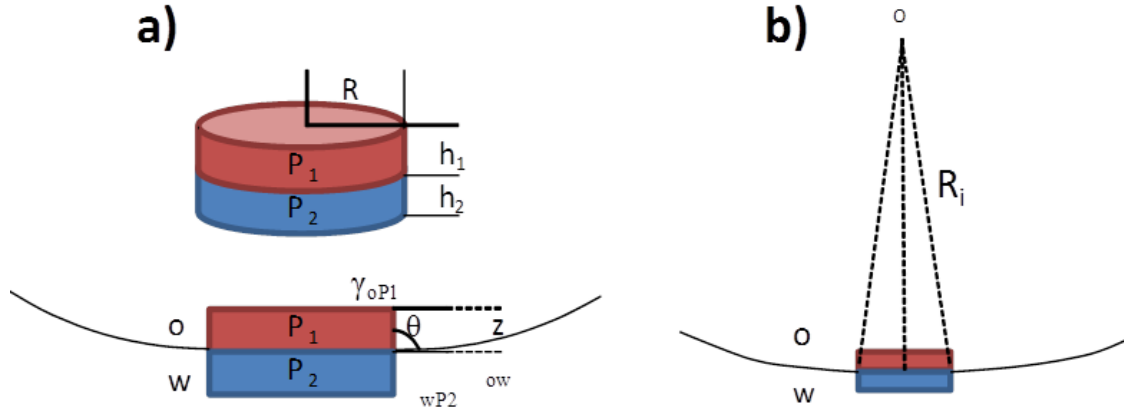


Figure B1. Illustrations of (a) a disk-shaped Janus particle and (b) its interfacial adsorption. Modified according to Nonomura *et al.*,⁵⁷⁴

Using homogeneous spheres, the highest stability of the resulting Pickering emulsion occurs when the three-phase contact angle among the particle, hydrophobic, and hydrophilic fluids is around 90° .^{242, 245, 575-578} Hydrophobic particles will stabilize water-in-oil emulsions having a contact angle slightly greater than 90° , whereas hydrophilic particles will stabilize oil-in-water emulsions having a contact angle slightly less than 90° .²⁴² In the case of Janus spheres, the stability is measured using the energy required to remove a particle from equilibrium into the hydrophobic fluid and normalized by the energy of removing it from the hydrophilic fluid, which is the so called Janus balance J , $J = (\sin^2\alpha + 2\cos\theta_p(\cos\alpha - 1)) / (\sin^2\alpha + 2\cos\theta_a(\cos\alpha + 1))$, where α is the angle from the center of the sphere to the hydrophilic-hydrophobic boundary, θ_p is

the contact angle of the hydrophilic side, and θ_a is the contact angle of the hydrophobic side. The highest stability of the Pickering emulsion stabilized by Janus particles is achieved when $J=1$, which can be obtained via tuning the parameter α .⁵⁷⁹⁻⁵⁸¹

The energy necessary to remove a disk-shaped Janus particle from its equilibrium position at the oil-water interface along the boundary between the hydrophobic and hydrophilic hemispheres is defined by⁵⁷⁴ $\Delta G_{\min} = \pi R_d^2 (\gamma_{oP1} + \gamma_{wP2} - \gamma_{ow}) + 2\pi R_d (h_1 \gamma_{oP1} + h_2 \gamma_{wP2})$, where πR_d^2 is the cross-sectional area of the particle, h_1 and h_2 are thickness of the hydrophobic and the hydrophilic regions, respectively, and the sum of them is equal to the thickness of the disk. P_1 indicates the hydrophobic region and P_2 , the hydrophilic region. γ_{oP1} and γ_{wP2} are the interfacial energies between the hydrophobic or hydrophilic regions and the oil or water interfaces, respectively (**Figure B1**). A similar behavior is presented for spherical⁵⁸² Janus particles.

Possible Mechanism of Emulsion Stabilization by Large Aspect Ratio Nano-sheets

However, two opposite effects are at work in the stabilization of Pickering emulsions using spherical particles, which have only one length scale, the diameter of the spheres $2r_s$. First, the interfaces of two adjacent emulsions will endure a maximum capillary pressure⁵⁸³ right before coalescence (P_c^{\max}), which can be expressed as $P_c^{\max} = \pm p(2\gamma_{ow}/r_s)(\cos\theta \pm z)$, where p is a theoretical parameter used to link the influence of particle concentration (with a “+” sign referring to oil-in-water (o/w) emulsions and with a “-” sign referring to water-in-oil (w/o) emulsions), and z is a constant dependent upon on the arrangement of particles in the interface.⁵⁸³ γ_{ow} is the interfacial energy between

the oil and the water, θ is the three-phase contact angle at the interface and r_s is the radius of the spheres.^{526, 583, 584} Assuming that θ is inside the stability intervals⁵⁸³ and the inter-particle distance is fixed,²²⁷ hence, the smaller the size of the spheres, the larger P_c^{\max} can be.^{227, 583} Spheres with a smaller radius r_s , therefore, prevent emulsion coalescence better than do larger spheres. Secondly, in the opposite effect, it is well known that small particles tend to escape from the interface by thermal fluctuations. The free energy to remove a sphere from the interface is defined by $\Delta G_{\text{remove}} = \pi r_s^2 \gamma_{ow}(1+\cos\theta)^2$. Therefore, spheres with a smaller radius r_s , escape more easily from the interface by thermal fluctuation than do the larger spheres.

The highly anisotropic particles we used here could reconcile these two effects due to the existence of two length scales, thickness h and lateral size $2R_d$. When considering the capillary interaction between two nano-sheets, an amphiphilic nano-sheet in the interface is equivalent to a closed packing of spheres with the interstitial space filled, where $2r_s$ (diameter of each sphere) corresponds to the thickness of the nano-sheet h . Also, the total area covered by these spheres is equal to the area covered by the nano-sheet. The interfaces of two adjacent emulsions will endure a maximum capillary pressure as $P_c^{\max} \approx \pm p(2\gamma_{ow}/r_s)(\cos\theta \pm z) \approx \pm p(4\gamma_{ow}/h)(\cos\theta \pm z)$. The nano-sheet thickness h can serve as a proxy for sphere diameter in the role of preventing emulsion coalescence. The capillary interaction between two nano-sheets with thickness h , with two edges parallel to each other, the meniscus between them is similar to that between two parallel cylinders of length h . The extremely small value of h offers a good capability to stabilize emulsions. Simultaneously, the nano-sheets' large lateral size $2R_d$ offers strong adsorption towards

the interface, preventing its escape due to thermal motion. Thus, particles with a large cross-sectional area, πR_d^2 , can be strongly adsorbed to the interface. Since $\Delta G_{\text{remove}} \sim R_d^2$ and $P_c^{\text{max}} \sim 1/h$, anisotropic particles with high aspect ratio ($\xi = 2R_d/h$) can be good emulsion stabilizers.²³⁴ However, large nano-sheets in diameter result in larger interstitial spaces compared with smaller nano-sheets. But, the emulsion droplets are stable because the nano-sheets are drawn into the region of inter-droplet forming a dense bridging monolayer as a result of strong capillary attraction.^{228, 229}

As Pickering stabilizers, high aspect ratio nano-sheets are more efficient than spheres. A nano-sheet has lower volume compared to a sphere of the same radius, hence less weight if the density is the same. For the same volume, a nano-sheet has a larger cross section on the interface, and adsorb stronger to the interface than a sphere. Therefore, fewer nano-sheets are required to cover the same liquid-liquid interface compared to their spherical counterparts.²⁵⁵ In addition, a nano-sheet presents a lower diffusivity of molecules compared to a close-packed structure of spheres of the same area; hence, blocking the process of Ostwald ripening that result in a lower degree of coalescence.²²⁷

Synthesis and Characterization of Zirconium Phosphate (ZrP)

Visualization of ZrP Nano-sheets

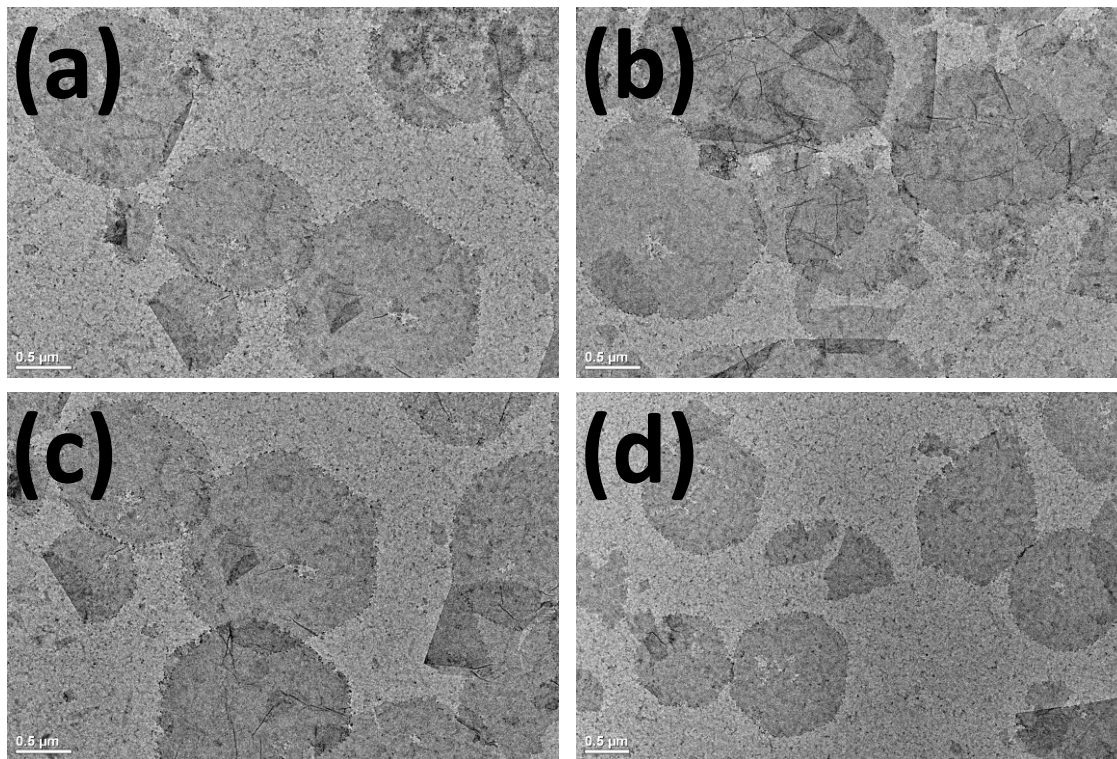


Figure B2. Transmission electron microscope (TEM) micrographs of several non-modified α -ZrP nano-sheets.

The α -ZrP nano-sheets in **Figure B2** are thin and flexible, and can present wrinkles as shown in **Figure B2(b,c)**. This demonstrates that the nano-sheets can bend on the oil-water interface to stabilize the emulsions. It has been proven that the single nano-plate layer is rigid when the nano-sheet size is about several tenths of a nanometer or less and becomes flexible when the size is larger than a hundred nanometers, depending on the bending elasticity of the layer.²⁸⁸

Control of the Size of ZrP Crystals via Hydrothermal Method

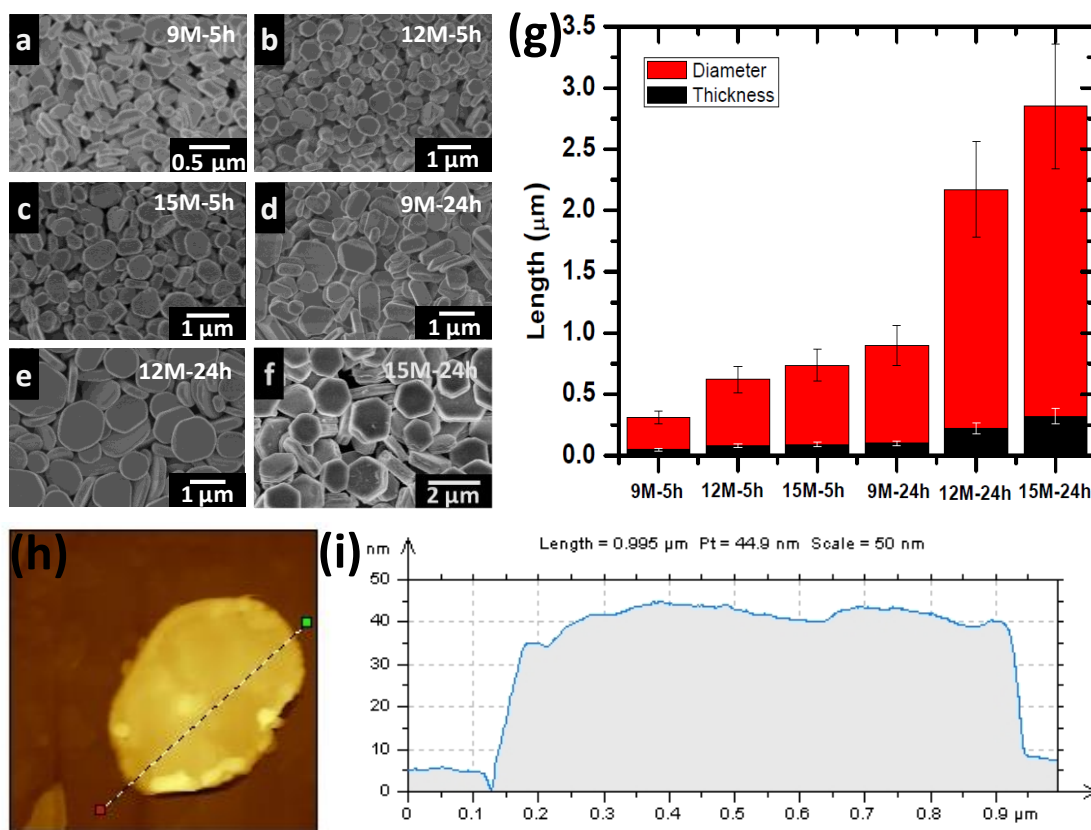


Figure B3. Pristine α -zirconium phosphate crystals. Scanning electron microscope (SEM) micrographs of different α -ZrP sizes synthesized via the hydrothermal method at 200 °C under different conditions (phosphoric acid concentration – reaction time). (a) 9M-5h, (b) 12M-5h, (c) 15M-5h, (d) 9M-24h, (e) 12M-24h, and (f) 15M-24h. (g) Quantification of the diameter (red bar) and the thickness (black bar) of the α -ZrP crystals.⁷⁸ (h) Atomic force microscope (AFM) contact mode topography image of a pristine α -ZrP crystal fabricated using 9M phosphoric acid for 24 h over a Si(100) surface modified with 3-aminopropyl trichlorosilane (APTES). (i) Section analysis for the cross-section white line seen in (h) gives a thickness of around 38 nm.

Characterization of the Thickness of ZrP Crystals via Atomic Force Microscopy (AFM)

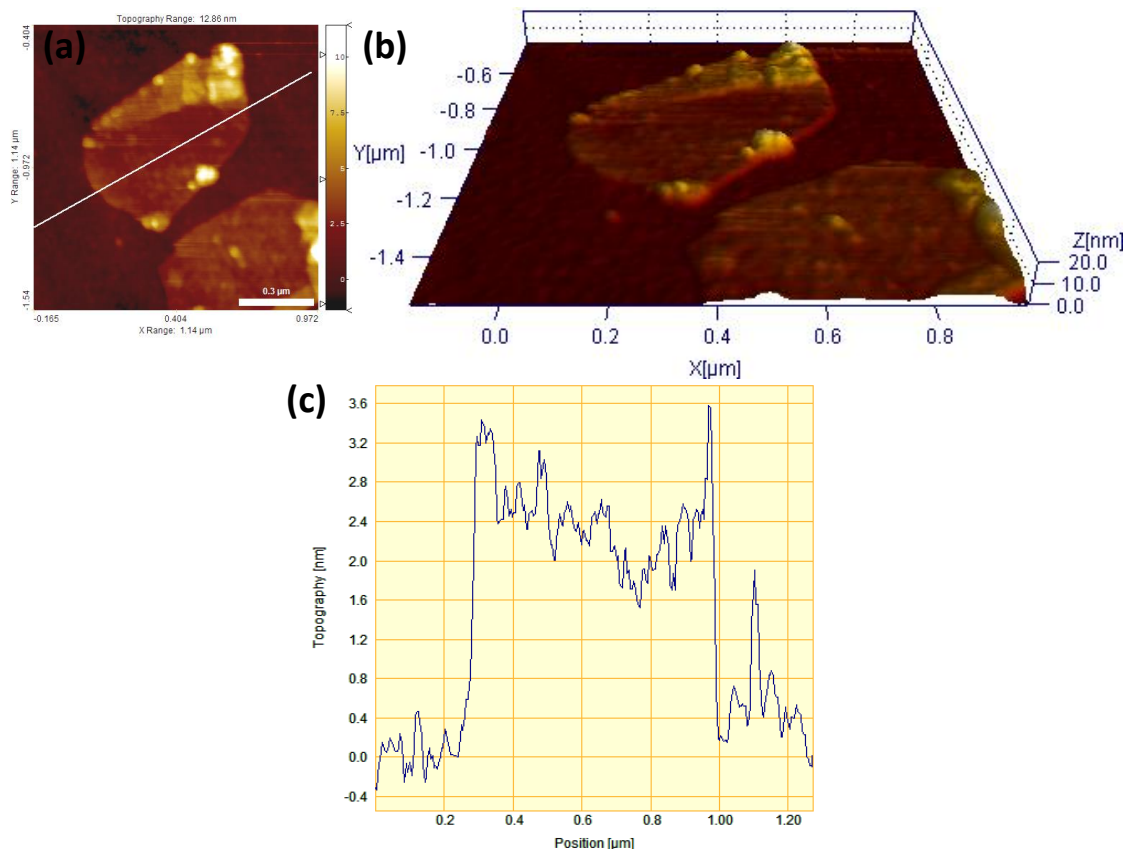


Figure B4. Modified α -ZrP-ODI nano-sheet. AFM contact mode topography image and section analysis of an amphiphilic α -ZrP-ODI nano-sheet over a Si(100) surface modified with octadecyltrichlorosilane (OTS). (a) 2D, and (b) 3D topography images. (c) Section analysis gives a thickness of around 2.8 nm (0.63 nm of a α -ZrP monolayer and 2.17 nm of the aliphatic chain) for the cross-section white line seen in (a).

Monolayer films of the desired alkylsilanes (APTES or OTS) were first prepared on cleaned and oxidized Si(100) and then ZrP nano-plates (or nano-sheets) were deposited through self-assembly using a suspension of the ZrP nano-sheets (nano-sheets) in a suitable solvent (EtOH for APTES and toluene for OTS). Si(100) substrates were cleaned and hydroxylated with a basic piranha solution (4:1:1) (v:v:v) mixture of high

purity H₂O: H₂O₂(30%):NH₄OH) at 80°C for 30 min. The substrates were rinsed under high-purity water for 60 s, then with ethanol, and finally dried under streaming nitrogen. Then the substrate was incubated in 1 wt % solutions of desired alkylsilanes (APTES or OTS) in a suitable solvent (EtOH for APTES and toluene for OTS) for ca. 15 h. The modified substrates were rinsed under high-purity water for 60 s, then with ethanol, and finally dried under streaming nitrogen. Finally, the ZrP nano-plates (or nano-sheets) were deposited through self-assembly using a suspension of the ZrP nano-sheets in a suitable solvent (EtOH for APTES and toluene for OTS) for 5 h. The final obtained substrate were rinsed under high-purity water for 60 s, then EtOH, and finally dried under streaming nitrogen.

Surface Characterization of Polystyrene Particles Stabilized by ZrP-ODI Nano-sheets

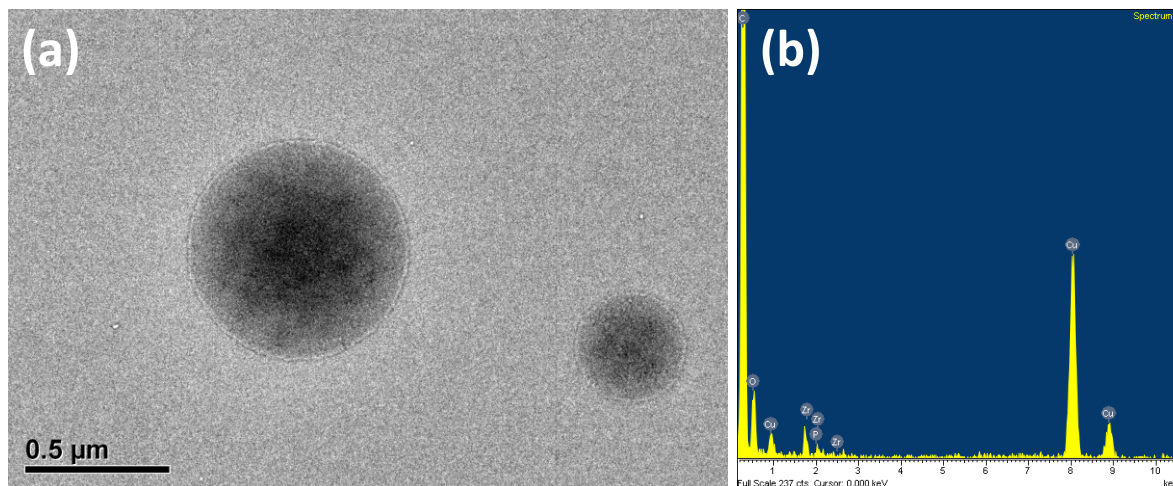


Figure B5. TEM and EDX elemental mapping analysis of the polystyrene- α -ZrP-ODI-nano-sheet particles. (a) TEM micrograph (b) Surface EDX spectra.

Static Contact Angle Measurements

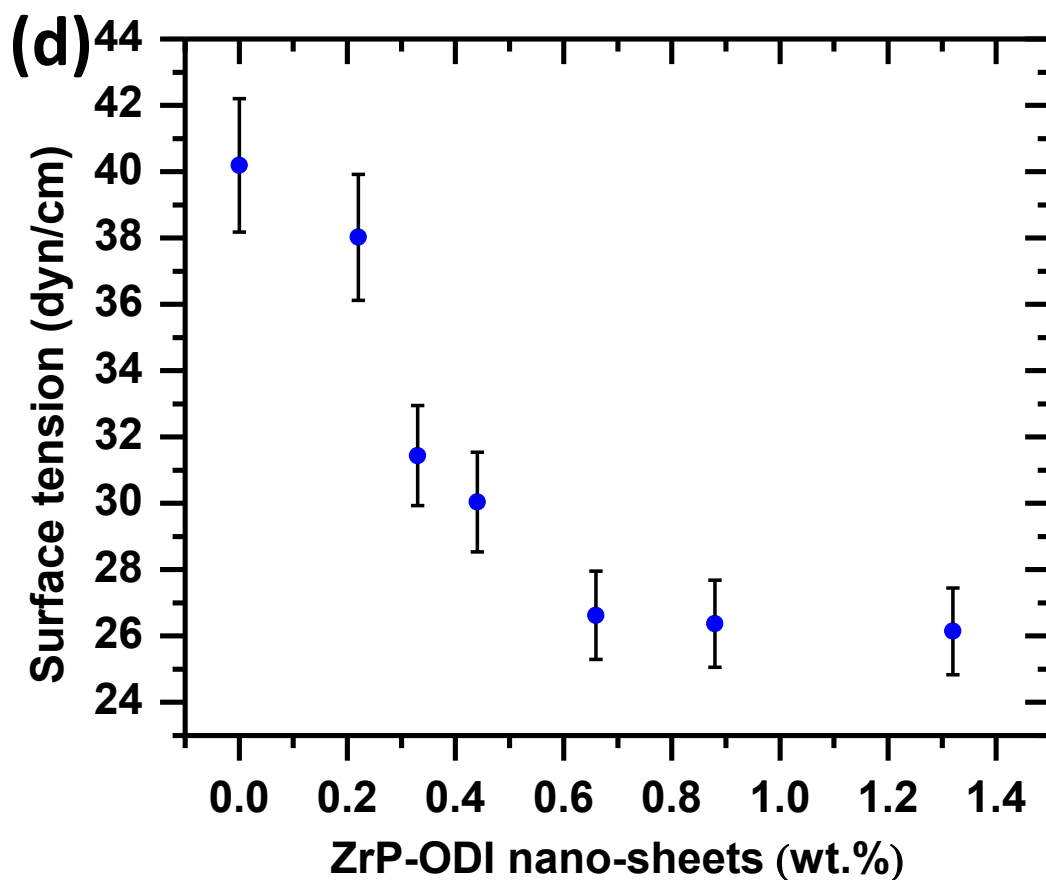
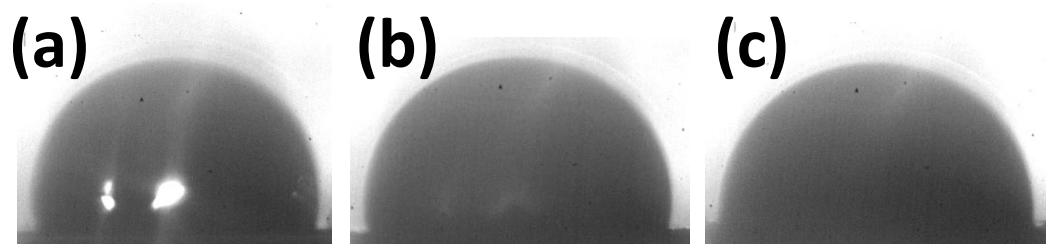


Figure B6. Suspension droplets at different α -ZrP-ODI nano-sheet concentrations. (a) Water only, (b) 0.44 wt% α -ZrP-ODI nano-sheets, and (c) 1.32 wt% α -ZrP-ODI nano-sheets. (d) Plot of the PDMS/suspensions interfacial tension against α -ZrP-ODI nano-sheet concentration.

A Phantom V4.2 camera (Vision Research, Wayne, NJ) with a high-magnification lens, together with the active contours method for measuring high-

accuracy contact angles using ImageJ⁵⁸⁵ was used to measure the surface tension of the PDMS-water interface. A glass slide was coated with PDMS to simulate similar surface tension interactions as in a PDMS-in-water suspension. The static contact angles were measured for seven different samples at different α -ZrP-ODI nano-sheet concentrations, as shown in **Figure B6**. Using Young's equation, $\gamma_{sl} = \gamma_{sa} - \gamma_{la} \cos\theta$, where γ_{sl} , γ_{sa} and γ_{la} correspond to the PDMS-liquid, PDMS-air and liquid-air surface tensions, respectively. The values taken for γ_{sa} was 21.8 dyn/cm⁵⁸⁶ and for γ_{la} was 72.8 dyn/cm⁵⁸⁷. **Figure B6** shows a similar tendency when compared to **Figure 44** and **Figure 46**, where α -ZrP-ODI nano-sheet concentration between 0.2 to 0.62 wt. % caused a decrease in surface tension and polystyrene particle diameter.

APPENDIX C

PEER-REVIEWED PUBLICATIONS

This dissertation is based on the following publications:

1. **Andres F. Mejia**, Agustin Diaz, Srinivas Pullela, Ya-Wen Chang, Michael Simonetty[#], Carrie Carpenter, James D. Batteas, M. Sam Mannan, Abraham Clearfield, and Zhengdong Cheng. *Pickering Emulsions Stabilized by Amphiphilic Nano-sheets*. *Soft Matter*, 8, 10245, (2012), Paper highlighted on front cover (**Chapter IV**)
2. **Andres F. Mejia**, Ya-Wen Chang, Ratna Ng[#], Min Shuai, M. Sam Mannan, and Zhengdong Cheng. *Aspect ratio and polydispersity dependence of isotropic-nematic transition in discotic suspensions*. *Phys. Rev. E*, 85, 061708, (2012), (PRE Kaleidoscope Image for Vol. 85 Iss.6) (**Chapter III**)
3. **Andres F. Mejia**, Peng He, Mark Netemeyer[#], Dawei Luo, Manuel Marquez, and Zhengdong Cheng. *Surface-controlled shape design of discotic microparticles*. *Soft Matter*, 6, 4885-4894, (2010) (**Chapter II**)
4. **Andres F. Mejia**, Peng He, Dawei Luo, Manuel Marquez, and Zhengdong Cheng. *Uniform discotic wax particles via electrospray emulsification*. *Journal of Colloid and Interface Science*, 334, 1, 22-28, (2009) (**Chapter II**)
5. Juan S. Guevara^{*#}, **Andres F. Mejia**^{*}, Min Shuai, Ya-Wen Chang, M. Sam Mannan, and Zhengdong Cheng. *Stabilization of Pickering Foams by High-aspect-ratio Nano-sheets*. *Soft Matter*, 9, 1327, (2013) (**Chapter IV**)

6. **Andres F. Mejia**, Ratna Ng[#], Peter Nguyen[#], Min Shuai, Hugo Y. Acosta, M. Sam Mannan, and Zhengdong Cheng. *Thermo-Responsive Discotic Nematic Hydrogels*. Submitted (**Chapter III**)
7. **Andres F. Mejia**, Ya-Wen Chang, Ratna Ng[#], and Zhengdong Cheng. *Liquid Crystalline Phase Behavior of Zirconium Phosphate - Silica Suspensions*. In preparation (**Chapter V**)
8. **Andres F. Mejia**, Elliott Joo[#], and Zhengdong Cheng. *Phase Behavior and Self-assembly of Wax Disks and SDS micelles*. In preparation (**Chapter V**)

Other papers by the author:

1. Ya-Wen Chang, **Andres F. Mejia**, Zhengdong Cheng, Xiaojun Di, and Gregory B. McKenna. *Gelation via Ion Exchange in Discotic Suspensions*. *Phys. Rev. Lett.* 108, 247802 (2012)
2. Peng He, **Andres F. Mejia**, Dazhi Sun, Hung-Jue Sue, Dean S. Dinair, Manuel Marquez, and Zhengdong Cheng. *Hindrance Function for Sedimentation of Colloidal Disks*. *Phys. Rev. E*, 81, 026310 (2010)
3. Min Shuai, **Andres F. Mejia**, Ya-Wen Chang, and Zhengdong Cheng. *Hydrothermal Synthesis of Layered α -Zirconium Phosphate Disks: Control of Aspect Ratio and Polydispersity for Nano-architecture*. *CrystEngComm*, DOI: 10.1039/c2ce26402a, (2012)
4. Peng Lian, **Andres F. Mejia**, Zhengdong Cheng, and M. Sam Mannan. *Flammability of Heat Transfer Fluid Aerosols Produced by Electrospray and*

Measured by Laser Diffraction Analysis. Journal of Loss Prevention in the Process Industries, 337-345, (2010)

5. Peng Lian, Dedy Ng, **Andres F. Mejia**, Zhengdong Cheng, and M. Sam Mannan. *Study on Flame Characteristics in Aerosols of Industrial Heat Transfer Fluids*. Ind. Eng. Chem. Res., 50 (12), pp 7644–7652 (2011)
6. Matthew Clements[#], Srinivasa Rao Pullela, **Andres F. Mejia**, Jingyi Shen, Tieying Gong, and Zhengdong Cheng, *Thermosensitive hard spheres*. Journal of Colloid and Interface Science. 317, 96-100, (2008)

*Authors equally contributed

[#] Undergraduate